TECHNISCHE UNIVERSITÄT MÜNCHEN

Fakultät für Chemie

Professur für Strukturelle Membranbiochemie

Structural studies on the pore-forming mitochondrial membrane proteins Bak and MPV17

Laura Esther Sperl, M. Sc.

Vollständiger Abdruck der von der Fakultät für Chemie der Technischen Universität München zur Erlangung des akademischen Grades eines

Doktors der Naturwissenschaften (Dr. rer. nat.)

genehmigten Dissertation.

Vorsitzender: Priv.-Doz. Dr. Gerd Gemmecker

Prüfende der Dissertation:

1. Prof. Dr. Franz Hagn
2. Prof. Dr. Michael Sattler

Die Dissertation wurde am 09.08.2021 bei der Technischen Universität München eingereicht und durch die Fakultät der Chemie am 21.09.2021 angenommen.

Acknowledgments

First of all, I would like to thank my supervisor Prof. Dr. Franz Hagn for offering me the opportunity to do my PhD on a very interesting and versatile subject in his research group and for the great support and advice he has given me throughout my PhD studies. I am very grateful for the fruitful discussions, his constructive feedback and his positive attitude, which very much helped staying motivated also when things did not work out. I am also very grateful for the wide diversity of methods and topics, which I was able to learn and apply during my time in his group.

In addition, I would like to thank everyone at the BNMRZ for the nice working environment and all their support by sharing experience, chemicals and instruments. Thank you to Dr. Sam Asami and PD Dr. Gerd Gemmecker for the NMR support and thank you to Dr. Winfried Meining for the IT support.

Additionally, I would like to thank all my coworkers in the Hagn Lab. Special thanks go to Dr. Kai Fredriksson for introducing me to the world of membrane proteins already back in Tübingen and to the Hagn group for my PhD. A big thank you also to my current coworkers Melina, Kai, Umut and Mariam for the very nice atmosphere in the lab and office and all their support and advice. This past year has really been great!

Further thanks goes to all my collaborators: Florian Rührnößl for the HDX-MS measurements, Dr. Martin Haslbeck for his support in the HDX-MS measurements, Annika Strauch for her help with the HDX-MS for an overnight measurement, Dr. Andre Muorao for the insect cell expression and Dr. Tilak Gupta and Dr. Carsten Peters for the negative stain EM measurements. I would also like to thank Lara Hassan and Dr. Sandra Lampl for the productive collaboration accepting my work as part of their publications.

Furthermore, I'd like to extend my appreciation to all the interns that supported my work with their contributions during their practicals in our group. Thank you Mandana, Ludwig, Afayat, Maxi, Maximilian and Anita.

Special thanks goes to all of my family for always being there for me, encouraging me throughout my studies but at the same time reminding me that life doesn't only consist of work. Thank you to my husband Franz for all his support during the past five years. Thank you to my mother and father, Grandma and Grandpa and my sister for their continuous love, help and support, which helped me master all challenges life has brought on me so far.

Most of all, I want to thank God for leading me down this path, always opening doors at the right moment unexpectedly and blessing me with great opportunities.

Publications

Parts of this thesis have been published:

Sperl LE, Rührnößl F, Schiller A, Haslbeck M, Hagn F, High-resolution analysis of the conformational transition of pro-apoptotic Bak at the lipid membrane, EMBO Journal (2021): e107159. (10.15252/embj.2020107159)

Sperl LE and Hagn F, NMR structural and biophysical analysis of the disease-linked inner mitochondrial membrane protein MPV17, Journal of Molecular Biology (2021): 167098. https://doi.org/10.1016/j.jmb.2021.167098

Häusler E, Fredriksson K, Goba I, Peters C, Raltchev K, Sperl L, Steiner A, Weinkauf S and Hagn F, Quantifying the insertion of membrane proteins into lipid bilayer nanodiscs using a fusion protein strategy, BBA - Biomembranes, 1862 (2020), 183-190 (10.1016/j.bbamem.2020.183190)

Other publications:

Lampl S, Janas MK, Donakonda S, Brugger M, Lohr K, Schneider A, Manske K, Sperl LE, Wettmarshausen J, Müller C, Laschinger M, Hartmann D, Hüser N, Perrochi F, Schmitt-Kopplin P, Hagn F, Zender L, Hornung V, Borner C, Pichlmair A, Kashkar H, Klingenspor M, Prinz M, Schreiner S, Conrad M, Jost PJ, Zischka H, Steiger K, Krönke M, Zehn D, Protzer U, Heikenwälder M, Knolle PA and Wohlleber D, Reduced mitochondrial resilience enables non-canonical induction of apoptosis after TNF receptor signaling in virus-infected hepatocytes, J Hepat, https://doi.org/10.1016/j.jhep.2020.06.026

Hassan L, Lin L, Sorek H, Sperl LE, Goudoulas T, Hagn F, Germann N, Tian T and Benz JP, Cross-talk of cellulose and mannan perception pathways leads to inhibition of cellulase production in several filamentous fungi, mBio (2019) 10:e00277-19. doi.org/10.1128/mBio.00277-19

Abbreviations

AA	Amino acid
Apol	Amphipol
ATP	Adenosine triphosphate
Bak	Bcl-2-antagonist/killer 1
Bcl-2	B-cell lymphoma 2
BclxL	B-cell lymphoma-extra large
BH	Bcl-2-homology
BME	β-Mercaptoethanol
cBid	cleaved Bid
C12E8	Octaethylene glycol monododecyl ether
CD	Circular dichroism
CMC	Critical micellular concentration
CL	Cardiolipin
cryo-EM	cryo-electron microscopy
Cu/phen	Cu^{2+}-phenanthroline
CYMAL-7	7-Cyclohexyl-1-heptyl-β-D-maltoside
DDM	n-Dodecyl-β-D-maltoside
DIABOLO	Direct inhibitors of apoptosis protein [IAP]-binding protein with low pI
DMPC	1,2-Dimyristoyl-sn-glycero-3-phosphocholine
DMPG	1,2-Dimyristoyl-sn-glycero-3-phosphoglycerol
DOTA	Tetra-aza-cyclo-dodecane-tetra-acetic acid
DPC	n-Dodecylphosphocholine
DSA	Doxyl-stearic acid
DSC	Differential scanning calorimetry
DTT	Dithiothreitol
E. coli	Escherichia coli
ER	Endoplasmatic reticulum
GuHCl	Guanidine hydrochloride
HDL	High-density lipoprotein
HDX-MS	Hydrogen/deuterium exchange mass-spectrometry
IAP	Inhibitors of apoptosis
IMM	Inner mitochondrial membrane
IMS	Inter membrane space
IPTG	Isopropyl β-D-1-thiogalactopyranoside
ITC	Isothermal titration calorimetry
LMNG	Lauryl maltose neopentyl glycol
MDMD	Mitochondrial DNA maintenance defect
MMTS	Methyl-methanethiosulfonate
MSP	Membrane scaffold protein
mtDNA	Mitochondrial DNA
NMR	Nuclear magnetic resonance
OG	n-Octyl-β-D-glucoside
OGNG	Octyl glucose neopentyl glycol
OMM	Outer mitochondrial membrane
PDB	Protein data bank
PC	Phosphatidylcholine
PE	Phosphatidylethanolamine
PG	Phosphatidylglycerol
PI	Phosphatidylinositol
PS	Phosphatidylserine
Puma	P53 Upregulated Modulator of Apoptosis
ROS	Reactive oxygen species
SMAC	Second mitochondria-derived activator of caspases

SEC	Size exclusion chromatography
SMALP	Styrene maleic anhydride lipid particle
SRP	Signal recognition particle
TIM	Translocase of the inner membrane
TMH	Transmembrane helix
TOM	Translocase of the outer membrane
UV	ultra-violet

Abstract

Mitochondrial integrity is essential for cell homeostasis. Thus, proteins forming pores in mitochondrial membranes must be tightly regulated and their malfunction carries the potential to induce severe pathologies. This work contributes to the structural and functional comprehension of the disease-linked pore-forming mitochondrial membrane proteins Bak and MPV17.

Upon activation, the pro-apoptotic Bcl-2 family protein Bak permeabilizes the outer mitochondrial membrane. This step is crucial for the intrinsic pathway of apoptosis, which is essential in preventing cancer. Thereby, Bak must undergo major conformational changes from a membrane-attached to a membrane-inserted state. While a large set of data indicate global conformational changes during pore formation, high-resolution structural details remain sparse. Here, the high-resolution NMR structure of the Bak transmembrane helix is determined and, using NMR and HDX-MS, the soluble domain is structurally characterized in lipid nanodiscs in its inactive, membrane-attached and active, membrane-incorporated states. Once activated, α-helix 1 dissociates from the protein core and adopts an unfolded and dynamic partially membrane-bound conformation. In addition, protein folding experiments reveal marked differences in the folding landscape of Bak and anti-apoptotic BclxL and suggest that α-helix 1 in Bak is a metastable structural element defining its apoptotic functionality. Consequently, mutagenesis experiments aimed at stabilizing helix 1 yielded Bak variants with reduced pore forming activity supporting that the here resolved structural rearrangements in α-helix 1 are critical for Bak activation by facilitating the structural transformations required for pore formation. Furthermore, interaction studies with BclxL on a membrane surface revealed a novel binding site in Bak helix 1. As the binding of BclxL to Bak inhibits apoptosis, these findings further highlight the importance of the Bak helix 1 not only in the induction of apoptosis, but also during its inhibition.

The second protein investigated here is the integral inner mitochondrial membrane protein MPV17. Its loss-of-function is linked to mitochondrial DNA maintenance defects, which lead to a tissue-specific reduction or deletion of mitochondrial DNA and organ failure in infants. Several disease-causing mutations in MPV17 have been identified and earlier studies with reconstituted protein suggest that MPV17 forms a high conductivity channel in the membrane. However, the molecular and structural basis of the MPV17 functionality remains only poorly understood. Here, an efficient protocol for its high-level production in *E. coli* and its purification from inclusion bodies is presented making MPV17 accessible to high-resolution structural studies. Combining biophysical and NMR methods, MPV17 refolded into detergent micelles is shown to adopt a compact structure consisting of six membrane-embedded α-helices. Furthermore, MPV17 is shown to form oligomers in a lipid bilayer that are further stabilized by disulfide-bridges. In line with these findings, MPV17 could only be inserted into lipid nanodiscs of 8 to 12 nm in diameter if intrinsic cysteines were either removed by mutagenesis or blocked by chemical modification. By this nanodisc reconstitution approach, it was demonstrated that disease

linked MPV17 variants show reduced oligomerization properties in the membrane. These data suggest that, induced by oxidative stress, MPV17 can alter its oligomeric state from a monomer to a disulfide-stabilized oligomeric pore which might be required for the transport of metabolic DNA precursors into the mitochondrial matrix to compensate for the damage caused by reactive oxygen species, a byproduct of oxidative phosphorylation.

These studies reveal novel insights on two essential mitochondrial membrane proteins. As a full comprehension of the mechanisms behind pathological manifestations is a prerequisite for drug discovery, this work might facilitate future studies on developing therapeutics for cancer and MPV17-related mitochondrial DNA depletion defects.

Zusammenfassung

Unversehrte Mitochondrien sind für die Zellhomöostase essenziell. Daher unterliegen Poren-bildende Proteine in Mitochondrien einer strengen Regulation und ihre Fehlfunktion trägt das Potenzial schwere Erkrankungen hervorzurufen. Diese Doktorarbeit liefert neue strukturelle und funktionelle Erkenntnisse zu den Poren-bildenden mitochondrialen Membranproteinen Bak und MPV17.

Nach Aktivierung bildet das pro-apoptotische Protein Bak, welches der Familie der Bcl-2 Proteine angehört, Poren in der äußeren mitochondrialen Membran. Dieser Schritt ist essenziell für den intrinsischen Signalweg der Apoptose, mit der eine Zelle verhindert, dass sie entartet und Krebs entsteht. Bak ändert dabei seine Konformation, in dem das ursprünglich nur in der Membran verankerte Protein in die Membran eintaucht. Eine Vielzahl von Studien konnte bereits zeigen, dass dieser Schritt mit großen strukturellen Veränderungen einhergeht. Hoch aufgelöste Strukturdaten fehlen bisher jedoch. In dieser Doktorarbeit wurde die Struktur der Transmembranhelix gelöst, die inaktives Bak in der Membran verankert. Zusätzlich wurde die lösliche Domäne in Lipid Nanodiscs in ihrem inaktiven und ihrem aktiven, Membran-insertierten Zustand mittels NMR und HDX-MS strukturell charakterisiert. Diese Studien zeigen, dass die α-Helix 1 von Bak nach Aktivierung vom restlichen Protein dissoziiert und entfaltet. Dabei nimmt sie einen dynamischen und teilweise Membran-gebundenen Zustand ein. Zusätzlich zeigen Proteinfaltungsstudien große Unterschiede zwischen dem Faltungsverhalten von Bak und anti-apoptotischem BclxL auf, die darauf hinweisen, dass die α-Helix 1 in Bak ein metastabiles strukturelles Element bildet, welches die apoptotische Funktionalität eines Bcl-2 Proteins definiert. Folglich führten Mutagenesestudien mit dem Ziel die Helix 1 zu stabilisieren, zu Bak-Mutanten mit verringerter Porenbildung und unterstützen somit die These, dass die hier aufgelöste Umstrukturierung der α-Helix 1 essentiell für die Aktivierung von Bak ist, indem sie die strukturelle Transformation erleichtert, die zu Porenbildung führt. Darüber hinaus zeigen Interaktionsstudien mit BclxL auf einer Membranoberfläche, eine bisher unbekannte Bindungsstelle in der Bak α-Helix 1. Die Bindung von BclxL an Bak inhibiert die Apoptose, sodass die Bak α-Helix 1 nicht nur einen wichtigen Faktor für das Einleiten der Apoptose, sondern auch für ihre Inhibierung, darstellt.

Das zweite Protein, das hier studiert wird, ist MPV17, welches sich in der inneren mitochondrialen Membran befindet. Die Fehlfunktion dieses Membranproteins führt zur Reduktion und Deletion von mitochondrialer DNA und zu Organversagen bereits im Säuglingsalter. Mehrere pathologische Mutationen in MPV17 konnten bereits identifiziert werden. Zusätzlich weisen frühere Studien mit rekombinant hergestelltem Protein darauf hin, dass MPV17 einen leitenden Kanal in der Membran formt. Die molekulare und strukturelle Basis der MPV17-Funktionalität ist bisher allerdings wenig verstanden. In dieser Doktorarbeit wird ein effizientes Protokoll für die Herstellung in *E. coli* und die Aufreinigung aus Einschlusskörperchen aufgezeigt, wodurch MPV17 auch mittels hoch-auflösender Strukturbestimmungsmethoden untersucht werden kann. Durch die Kombination von biophysikalischen und NMR-basierten Methoden, wird gezeigt, dass in Detergenzmizellen rückgefaltetes MPV17 eine

kompakte Struktur aufweist, die sechs Membran-gebundene α-Helices enthält. Darüber hinaus wird gezeigt, dass MPV17 in einer Lipiddoppelschicht Oligomere bildet, die durch Disulfidbrücken stabilisiert werden. Dementsprechend konnte MPV17 nur dann in Lipid Nanodiscs mit einem Durchmesser von 8-12 nm insertiert werden, wenn die Cysteine vorher entweder durch Mutagenese entfernt oder durch chemische Modifikation blockiert wurden. Mittels dieses Vorgehens, konnte gezeigt werden, dass pathologische Mutanten eine verringerte Tendenz zur Oligomerisierung aufweisen. Diese Daten weisen darauf hin, dass oxidativer Stress dazu führt, dass monomeres MPV17 sich in eine Disulfid-verbrückte oligomere Pore umwandelt. Diese Pore könnte für den Transport von metabolischen DNA-Ausgangsstoffen in die mitochondriale Matrix nötig sein, um Schaden durch reaktive Sauerstoffspezies, einem Nebenprodukt der oxidativen Phosphorylierung, zu verhindern.

Diese Studien liefern neue Erkenntnisse über zwei essenzielle mitochondriale Membranproteine. Da das vollumfängliche Verständnis der Mechanismen hinter einem Krankheitsbild eine wichtige Voraussetzung für die gezielte Arzneimittelentwicklung sind, könnte diese Arbeit zukünftige Studien unterstützen, die Medikamente gegen Krebs oder MPV17-induzierte Defekte der mitochondrialen DNA entwickeln.

Table of contents

1 Introduction

Mitochondria are the "powerhouse of the cell"[1,2]. This is enabled by the inner and outer mitochondrial membranes that allow a potential to form, which is controlled by the mitochondrial respiratory chain complexes[3,4]. Pores in these membranes have a high potential to harm or even kill the cell. Thus, proteins forming these pores must be tightly regulated. Deficiencies in these proteins are prone to act pathogenic making these pore-forming proteins interesting drug targets. However, the basis to develop specific drugs is to understand the underlying structural and functional relationships[5]. This thesis sheds new light onto the structural and functional features of Bak and MPV17, two distinct mitochondrial membrane protein systems located in the outer and inner mitochondrial membrane, respectively.

1.1 Membrane proteins

In contrast to soluble proteins, membrane proteins require stabilization by a membrane. Membrane proteins take over important functions including enzymatic reactions and the transport of signals or metabolites[6]. Thus, they are essential for communication and transport across the membrane barriers and important drug targets. However, while ~70 % of the currently marketed drugs target membrane proteins, they constitute only ~3 % of the structures deposited in the protein data bank (PDB)[7]. This highlights the need to structurally characterize membrane proteins and make them accessible to structure-based drug design[5].

1.1.1 The lipid bilayer membrane stabilizing membrane proteins

Membranes are lipid bilayers not only surrounding cells, but also compartmentalizing several cell organelles, e.g. the nucleus, mitochondria, endoplasmatic reticulum (ER) and Golgi apparatus in eukaryotes. They are constituted by amphipathic lipids, which form a lipid bilayer with two hydrophilic surfaces formed by the lipid head groups and a hydrophobic core consisting of the attached fatty acids[9]. Both the composition of the lipid head groups and the fatty acids largely influences the membrane characteristics and can be important for the functionality of the membrane proteins stabilized in the membrane. Therefore, they must also be taken into account when studying these proteins.

Three types of lipids form the lipid bilayer, namely phospholipids, glycolipids and sterols **(Fig. 1.1)**[9]. In phospholipids, the hydrophobic tail is formed by two fatty acids and is connected to the hydrophilic headgroup by a glycerol moiety. The hydrophilic headgroup is formed by a phosphate group linked to a hydrophilic group such as choline (PC), glycerol (PG), serine (PS), ethanolamine (PE) or inositol (PI). In glycolipids, the phosphatidyl-group is exchanged for a sugar. Both phospholipids and glycolipids can also be based on sphingosine instead of glycerol. Sterols contain a steroid structure and a hydroxyl group forming the hydrophilic headgroup. They are mainly found in mammalian membranes in form of cholesterol or in plant membranes as stigmasterol.

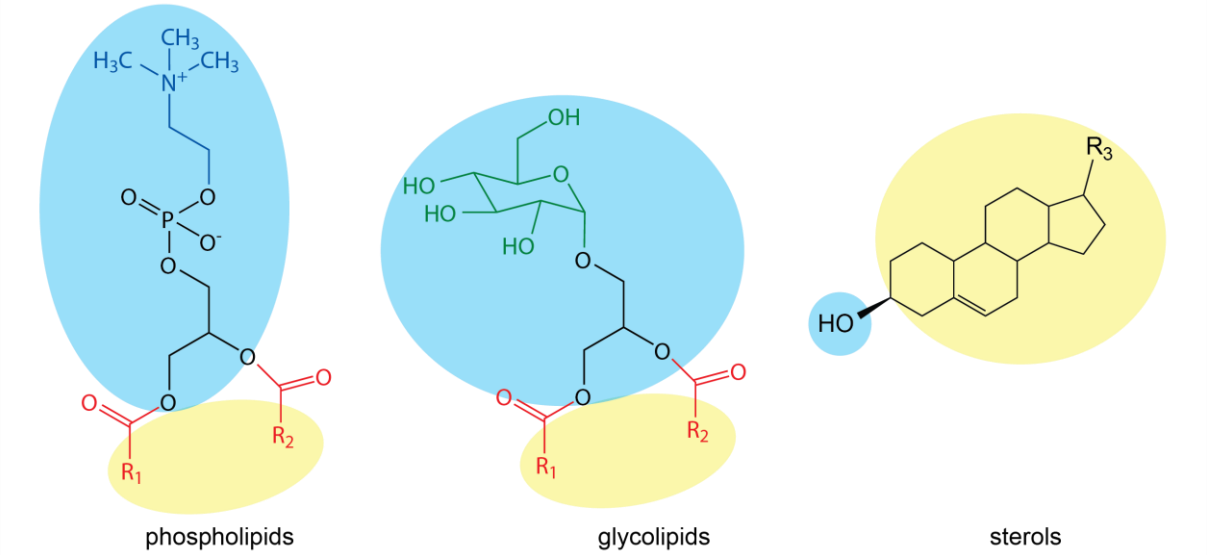

Figure 1.1: Three types of membrane lipids. In phospholipids, glycerol links the fatty acids (red) to a phosphatidyl group. The choline (blue) can be replaced by glycerol, serine, ethanolamine or inositol. In glycolipids, glycerol links the fatty acids (red) to a sugar moiety, here α-D-glucose (green). Sterols contain a steroid structure. R = hydrocarbon moiety with R_1/R_2 formed by fatty acid chains. The hydrophilic lipid headgroups are highlighted in blue and the hydrophobic tails in yellow.

Not only lipids can be glycosylated but also proteins, which are then named glycoproteins[8,10]. Glycosylation takes place in the ER and Golgi apparatus. Therefore, it is only found on the non-cytosolic side of the membrane. Due to the large diversity of sugars, these can function as markers, e.g. antigens recognized by antibodies[9].

As described by the fluid mosaic model, membranes are dynamic with laterally diffusing lipids and proteins[9,11]. In general, lipids diffuse faster than proteins. Vertical movements, also known as "flip-flop", of either lipids or proteins usually do not occur spontaneously due to the high activation energy necessary to force the hydrophilic regions through the hydrophobic membrane core. Therefore, the inner and outer leaflets of a membrane can be distinctly composed and membrane proteins can maintain their correct orientation. To enable an asymmetric lipid distribution between the individual membrane leaflets and the different membranes, which is essential for the membrane function, specific enzymes, such as flippases , catalyze the vertical movement of lipids in an ATP-dependent manner[12]. These enzymes are essential for the formation of membrane bilayers and, therefore, are found at the location of lipid synthesis, thus, at the inner leaflet of prokaryotes or the cytoplasmic leaflet of the ER in eukaryotes. In eukaryotes, the lipids must be transported from the ER to the other cell organelles. While this mainly takes place by vesicles, mitochondria acquire lipids through membrane contact sites to the ER[13]. Additionally, mitochondria produce specific lipids themselves[14].

1.1.2 The synthesis of membrane proteins

Membrane proteins are synthesized in ribosomes[9]. In yeast and prokaryotes, they are targeted to the membrane post-translationally. In higher eukaryotes, most membrane proteins are targeted to the ER

co-translationally. As membrane proteins contain an N-terminal signal sequence, they are recognized by the signal recognition particle (SRP) at an early stage during translation. This SRP has binding sites for the signal sequence, the ribosomes and the SRP receptor in the ER[9,15,16]. As soon as the ribosome interacts with the SRP, the protein synthesis is interrupted. Bound to the SRP, the synthesis machinery consisting of ribosomes, mRNA and the nascent protein is transported to the ER, where the SRP binds to its receptor located near the translocon. Only after the SRP binds to its receptor at the ER, it dissociates from the ribosome and the nascent protein enabling the protein synthesis to continue. Then the membrane protein is directly synthesized into the translocon, a protein pore through which the newly synthesized membrane protein is integrated into the ER membrane. If this is not its final destination, it is transported to the correct membrane by the secretory pathway in transport vesicles[10].

1.1.3 The structure of membrane proteins

Membrane proteins are very divers both structurally and functionally and are classified as peripheral, membrane bound and integral membrane proteins. **(Fig. 1.2)**[8,9]. Peripheral membrane proteins are only bound to the membrane surface. The binding can be achieved either by integral membrane proteins or lipid head groups. Membrane bound proteins are directly anchored to the membrane by either covalently bound fatty acid chains, a prenyl group or an amphipathic α-helix, which binds to the membrane surface peripherally. As many PI headgroups are glycophosphorylated, membrane proteins can also be attached to membranes by covalently binding to sugars[17]. The third group, which the membrane proteins studied in this work are classified as, are integral membrane proteins. Like the lipid bilayer, they have a hydrophobic core and hydrophilic flanking regions and span the membrane either as a β-barrel or as transmembrane helices (TMHs)[8]. The latter group is classified in three types[18]. Type 1 and 2 membrane proteins pass the membrane with a single α-helix. The N-terminus of a type 1 membrane protein is located in the cytosol, while type 2 membrane proteins are inserted into the membrane the opposite way. In both cases, a soluble domain can be attached to the TMH on either side of the membrane. Type 3 helical membrane proteins span the membrane as multiple α-helices. These membrane spanning regions mainly contain amino acids with nonpolar side chains, which interact with the lipid tails. TMHs consist of 20-30 residues, while ~10 amino acids are sufficient to span a membrane in an extended β-strand. Additionally, β-barrels predominantly form a hydrophilic pore, so that only every second amino acid is hydrophobic. Therefore, their transmembrane regions are very difficult to predict without an experimental structure. In contrast, transmembrane helices can be predicted quite well by hydrophobicity plots due to their large hydrophobic regions. In the membrane, the polar peptide bonds are driven to form hydrogen bonds with each other as water is absent. Since kinks in the transmembrane helices or the β-sheets would lead to insufficient hydrogen bonding, these rarely occur. A change in direction usually takes place outside the lipid bilayer by surface-exposed loops that can vary in size. Integral membrane proteins can also contain extramembranous soluble domains.

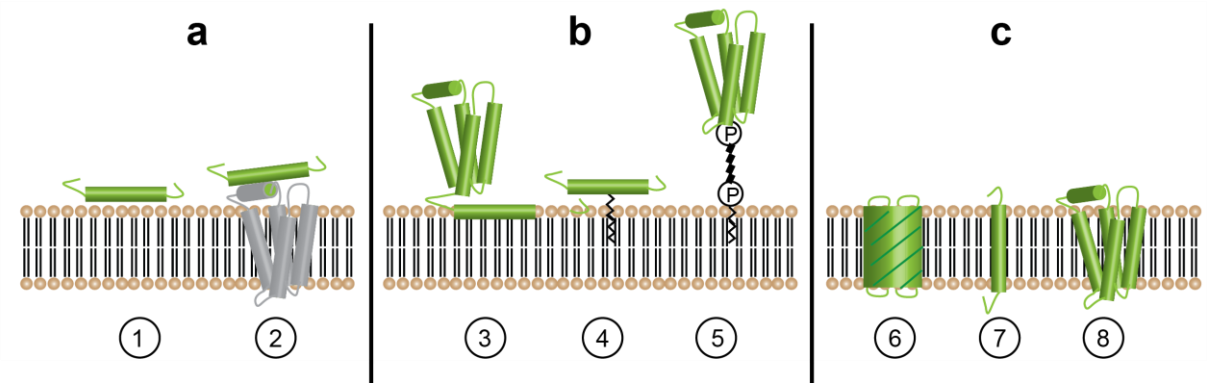

Figure 1.2: Overview on membrane protein classes. (a) Peripheral membrane proteins are bound to the membrane by interacting with lipid head groups (1) or an integral membrane protein (2). (b) Membrane bound proteins are covalently bound to the membrane by an amphipathic α-helix (3), a prenyl or fatty-acid chain (4) or a sugar moiety (5). (c) Integral membrane proteins span the membrane as β-barrels (6) or transmembrane helices (7+8).

As the function of each protein is determined by its three-dimensional structure, it can only be fully understood, if the structure is solved[19]. Despite efforts to structurally determine proteins in their cellular environment with in-cell NMR or cryo-electron tomography, the wide majority of structural studies requires their recombinant production and purification[20,21].

1.1.4 Recombinant production and purification of membrane proteins

Membrane proteins can be isolated directly from the native membrane[22,23]. However, the yields are often too low for structural studies. Therefore, they are usually overexpressed recombinantly in a host cell system, where they either integrate into a host membrane or are stored in inclusion bodies[24,25]. The insertion into a cellular membrane can be problematic, as a sufficient transport and insertion machinery is necessary and the lipid composition can be crucial for the successful stabilization as it can influence the inter- and intramolecular interactions between the membrane protein and lipids[26]. Additionally, an oversaturation of the membrane can lead to distress and even host cell death. If a membrane protein is successfully stabilized in a membrane, this has the advantage that it is usually properly folded. Then, it can be solubilized by an agent that disrupts the membrane, thereby offering an amphipathic environment that can stabilize the membrane protein instead[27]. In general, this is achieved with detergents, which are small amphipathic molecules that form micelles in water when the critical micellular concentration (CMC) is exceeded[28,29]. If the host cell stores the overexpressed membrane protein in inclusion bodies, these can be purified and the membrane protein extracted with chaotropic agents like urea or guanidine hydrochloride (GuHCl)[25]. With this approach the membrane protein must be refolded, which can be problematic in many cases. Once the membrane protein is successfully extracted in a membrane mimetic it can be purified in this environment using chromatographic methods. When the membrane protein is correctly folded and stabilized in the membrane mimetic of choice, a 3D structure can be determined using high-resolution methods such as nuclear magnetic resonance spectroscopy (NMR), X-ray crystallography or cryo-electron microscopy (cryo-EM)[30–32].

1.1.5 Membrane mimetics

In order to adopt a native structure and function, membrane proteins must be stabilized in a membrane-like environment[33,34]. Different membrane mimetics can be utilized for this purpose. Detergent micelles are the most widely used membrane mimetic[35]. They are easy to handle and the large variety of detergent scaffolds enables a wide screening for the best suited candidate for the membrane protein of interest. However, this membrane mimetic is not very native as no lipids are stabilizing the membrane protein. Additionally, detergents can lead to difficulties with downstream applications, for example the concentration of proteins cannot be detected by UV absorption in the presence of Triton X-100, detergents strongly interact with hydrophobic dyes influencing their fluorescence spectra and detergents are ionized during ESI-MS leading to strong signals[29]. Therefore, more native membrane mimicking systems are used whenever possible. An overview on membrane mimetics is given in the following subchapters starting from the least native to the most native membrane mimetic **(Fig. 1.3)**[35].

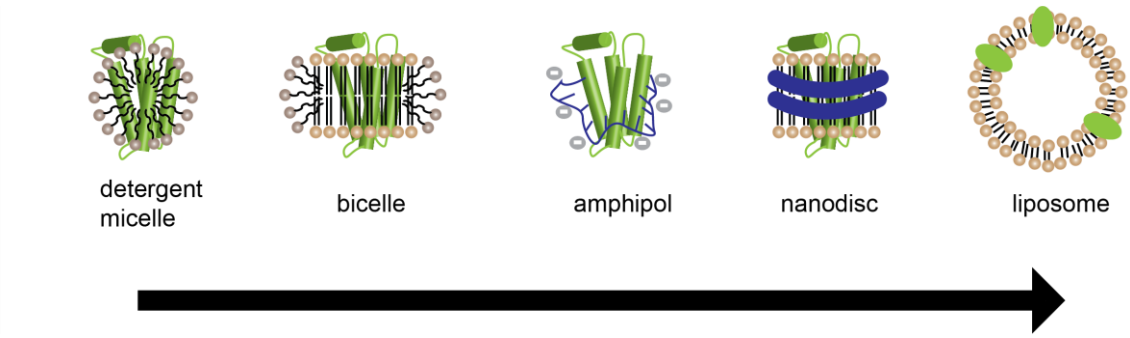

Figure 1.3: Overview of membrane mimetics commonly used in structural biology. The model membrane protein is shown in green. The arrow at the bottom indicates the increasing ability to resemble the native lipid bilayer membrane.

1.1.5.1 Detergent micelles

Detergents are surface active agents. Similar to lipids, they consist of a hydrophobic hydrocarbon tail and a hydrophilic headgroup[34]. According to their headgroup, they can be classified as nonionic, zwitterionic or ionic (cationic, anionic). Unlike lipids, which form lamellar bilayers, detergents form spherical aggregates of defined size, called micelles, after their individual concentration threshold, the CMC, is reached. In micelles, the hydrophobic moieties are buried in the micelle's core, while the hydrophilic headgroups form the surface that shields the core from the aqueous solution. The propensity to form micelles is determined by the shape of the amphiphilic molecule and expressed by the packing parameter P[28]:

$$P = \frac{v}{al}$$

Equation 1.1: The packing parameter P defines the shape into which amphiphiles self-organize in an aqueous solution. v = volume of the hydrophobic tail, a = cross-sectional area of the headgroup, l = length of the hydrophobic tail.

If $P < \frac{1}{3}$ micelles are formed, while lamellar structures are formed for $P \sim 1$. In order for a detergent to stabilize a membrane protein, it must be concentrated higher than the CMC. Then the hydrophobic parts of the membrane protein are stabilized in the micelle's core, while the hydrophilic extramembranous areas extend outside of the micelle and are surrounded by aqueous solution. Which detergent to use must be carefully tested, as not every detergent will stabilize every membrane protein. In general, ionic detergents are harsher than non-ionic detergents and short-chain detergents are harsher than those with a larger headgroup and tail[29]. As detergents can dissolve lipid membranes, this membrane mimetic is most often applied to extract membrane proteins from a lipid bilayer and for their purification. However, they can reduce the thermodynamic stability leading to an incorrect fold or even unfolding of the membrane protein and can hamper the functionality even if the membrane protein is correctly folded by interfering with the active site[34]. Furthermore, a detergent compatible with one membrane protein is not necessarily compatible with the interaction partner, rendering interaction studies on protein complexes difficult[36,37]. Depending on these functional aspects and the down-stream application, detergents can be exchanged for a more native membrane mimetic later.

1.1.5.2 Bicelles

Bicelles consist of a lipid-bilayer patch, which is stabilized by detergents or short-chain lipids on the rim. Their size can be adjusted by the ratio of the lipid/detergent concentration, defined as q-value[38] .

$$q = \frac{[lipid]}{[detergent]}$$

Equation 1.2: The q-value of bicelles.

The q-value can be used to calculate the radius R of the lipid bilayer, from which the diameter d of the bicelle can be derived as follows[39].

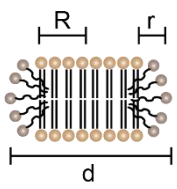

$$R = \frac{1}{2} krq(\pi + (\pi^2 + \frac{8k}{q})^{\frac{1}{2}})$$

$$d = 2 \cdot (R + r)$$

Equation 1.3: Calculation of the radius R of the lipid bilayer patch and the diameter d of the bicelle. $r = 1\ nm$; $k = \frac{A_{detergent}}{A_{lipid}}$; $A =$ surface area.

The membrane protein is embedded in the central lipid bilayer region, whose lipid content can be adjusted to the membrane protein. However, as detergents are also present in the assembly, they can still lead to the disadvantages encountered with detergent micelles.

1.1.5.3 Amphipols

Amphipols (apols) are amphipathic polymers that were developed to stabilize membrane proteins, in the absence of surfactants[40]. They consist of a chemically modified polyacrylic acid chain. Apols interact with the hydrophobic part of the membrane protein with a very low dissociation rate, stabilizing the membrane protein in an aqueous solution. Therefore, unlike detergents, the protein-bound apols are not in rapid exchange with free monomers and micelles and apols must not be added for further handling once the membrane protein is stabilized.

A8-35 is the most commonly used apol. In the nomenclature, the first letter stands for anionic (A)[41]. The following number refers to the monomeric molecular weight and the final number to the percentage of free carboxylic groups. Manifold chemical modifications have been introduced to change the properties of apols, e.g. the sensitivity to pH[42]. However, A8-35 is the only commercially available apol and is consequently used for most studies.

1.1.5.4 Nanodiscs

Nanodiscs are discoidal lipid bilayer patches stabilized by different components. The four most widely applied nanodisc systems will be described.

Membrane scaffold protein (MSP) nanodiscs utilize derivatives of apolipoprotein A-I, an amphipathic α-helical protein, which stabilizes high-density lipoprotein particles (HDL) in the blood[43]. Two MSPs wrap around the lipid bilayer patch to stabilize the hydrophobic lipid tails, which would be in direct contact with the aqueous solvent otherwise[44]. These discs are very homogenous, facilitating NMR studies[45]. The size is defined by the length of the MSP. Thus, by inserting or deleting one or more of the α-helices in the MSP, the nanodisc size can be adjusted to the requirements of the membrane protein of interest. More recently, circular MSPs were designed by applying different circularization methods, leading to even more stable and homogenous particles that are suitable for cryo-EM[46,47]. Furthermore, solid state NMR measurements on linear MSP nanodiscs have revealed a reduced lipid diffusion compared to liposomes caused by the interaction of the lipids with the MSP belt[48]. This is proposed to be even more native than the behavior in liposomes as lipid diffusion is also restricted in the cell due to proteins, rafts and the lipid composition. Drawbacks of this method are their interference with the spectroscopic absorbance of the membrane protein and the use of detergents for the initial solubilization of the membrane protein.

Peptide based nanodiscs utilize amphipathic peptides to stabilize the rim of the lipid discs[49]. Like MSP, the most commonly used peptide 18A is derived from Apolipoprotein A-I. Similar to bicelles, the size of these nanodiscs can be regulated by varying the ratio of peptide to lipids. Compared to other nanodisc systems, peptide nanodiscs are less stable due to their non-covalent interaction with each other and like MSP nanodiscs they interfere with absorbance-based spectroscopy.

Styrene maleic anhydride lipid particles (SMALPs) use an amphiphilic polymer with styrene as the hydrophobic and maleic acid as the hydrophilic moiety[7]. The phenyl groups interact with the hydrophobic lipid tails, while the maleic acid residues interact with the aqueous solution rendering the disc soluble. The size can be adjusted by varying the ratio of SMA to lipids. While solubility issues occur for the classical SMA at pH < 6.5 and in the presence of divalent cations, due to its chelating properties, chemically modified derivatives have been developed, which solve these difficulties[50,51]. An advantage of SMALPs is that they enable the direct extraction of membrane proteins out of a membrane, eliminating the use of detergents and synthetic lipids from the procedure

Most recently, saposin nanodiscs have been developed. The saposin protein family consists of a diverse group of lipid-interacting proteins[52,53]. The α-helical Saposin A has been shown to form lipid nanodiscs[54]. Disulfide bonds formed by the highly conserved six cysteines within saposins have been proposed to make this arrangement especially stable[54]. In contrast to MSP nanodiscs, the number of Saposin A molecules stabilizing the nanodisc is not defined. Similar to bicelles, peptide based nanodiscs and SMALPS, the particle size can be adjusted by varying the ratio of lipids to Saposin A. Additionally, like SMALPS this approach enables the direct extraction of membrane proteins[55].

1.1.5.5 Liposomes

When lipids are mixed with an aqueous solution, they form lamellar structures. These bilayers can also be forced into a spherical form encapsulating a second aqueous compartment by extrusion through a porous membrane or sonication[56]. Consisting purely of lipids, this membrane mimetic is the most native one. Depending on the pore size, extrusion yields liposome diameters starting from 30 nm, while sonication leads to small unilamellar vesicles (25-50 nm). As these liposomes are variable in size and lipid composition, they are applicable to most membrane proteins. The compartmentalization brings an additional advantage for the functional study of pore-forming membrane proteins and transporters[57,58]. By preparing the liposomes in one solution and washing them in another after the liposomes are formed, different environments can be created and transport can be monitored using a wide variety of methods. However, due to their large size liposomes are not compatible with all down-stream methods. Especially for solution NMR, where a larger system results in slower tumbling and consequently broad lines, and optical spectroscopy, where light scattering leads to unwanted interference, liposomes are not the first choice.

1.2 Mitochondria

Both protein systems studied in this work are located in mitochondrial membranes. Mitochondria are cell organelles surrounded by two membranes **(Fig. 1.4)**. The inner mitochondrial membrane (IMM) encompassing the matrix has a large surface, which is folded into cristae[59]. It is separated from the outer mitochondrial membrane (OMM) by an inter membrane space (IMS).

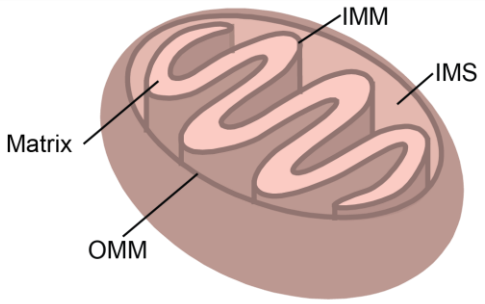

Figure 1.4: The mitochondrium is enveloped by two membranes. The matrix is surrounded by the inner mitochondrial membrane (IMM), the inter membrane space (IMS) and the outer mitochondrial membrane (OMM).

Mitochondria are essential for the energetics, metabolism and regulation of eukaryotic cells[60]. Thus, they take part in many metabolic processes such as the biosynthesis of lipids, amino acids, hem and Fe-S clusters, and are significantly involved in signaling pathways, quality control and apoptosis[60]. An important function is also the synthesis of ATP and the maintenance of the energy household. Located in the IMM are the protein complexes of the electron transfer chain and the ATP-synthase, which are the sites of energy production[61]. While the IMM has a very restricted permeability to allow for the generation of a proton gradient necessary for ATP synthesis, the OMM contains many protein-based pores, enabling the passage of ions, metabolites and even proteins[62].

The cytosol, the IMS and the matrix have different redox environments with the IMS being the most oxidizing and the matrix being more reducing than the cytosol[63]. Cells contain two primary redox regulatory systems comprising reduced/oxidized glutathione (GSH/GSSG) and reduced/oxidized thioredoxin, which keep the cysteine residues reduced at steady state levels[64]. These systems maintain the redox control in the cytosol and the matrix. However, in the IMS the redox state is controlled by a dedicated protein oxidation machinery formed by the oxidoreductase Mia40 and the sulfhydryl oxidase Erv1[65]. They introduce disulfide bonds into proteins containing specific signal sequences[64]. Consequently, the redox state of proteins in the IMS is independent from redox shifts occurring in the matrix and cytosol.

Unlike all other cell organelles, mitochondria have their own DNA and protein production machinery. While most mitochondrial proteins are produced by the nuclear DNA, thirteen mitochondrial proteins, as well as twenty-two transfer RNAs and 2 ribosomal RNAs for protein synthesis are encoded by the mitochondrial DNA (mtDNA)[66]. Unlike nuclear DNA, which is replicated only during cell division,

mtDNA synthesis is always active. Thus, a large machinery of proteins is necessary to maintain the mtDNA by regulating the mtDNA synthesis, the mitochondrial nucleotide pool and mitochondrial dynamics. These regulating proteins are encoded by the nuclear DNA and imported into the mitochondria by specific translocation machineries. All matrix proteins and many others have an N-terminal presequence (preprotein), which binds to the translocase of the outer membrane (TOM) [60,67,68]. This multimeric protein complex in the outer membrane contains an aqueous pore through which the preproteins are transported. Next, the presequence binds to the translocase of the inner membrane (TIM) 23[60,67,68], which transports the preprotein through the inner membrane into the matrix in an ATP- and membrane potential-dependent manner. Finally, the presequence is removed proteolytically and the protein is folded into its final structure supported by matrix chaperons. Inner membrane proteins are mainly shuttled by two distinct mechanisms. If they contain a presequence, their transport is stopped at TIM23 and they are laterally inserted into the membrane (=stop-transfer-mechanism). When no presequence is present, less defined internal signals target the proteins to the inner membrane by TIM22[67]. A third small group is first imported into the matrix and then inserted in the inner mitochondrial membrane in a membrane potential-dependent manner analogue to the proteins synthesized in mitochondria. This route is called the conservative sorting pathway[69].

The mitochondrial salvage pathways and specific transporters shuttling nucleotides from the cytosol into the mitochondrial matrix supply the nucleotide pool. If any of these proteins are mutated this can lead to defective mtDNA resulting in depletion or reduced quality, which further leads to a deficient synthesis of the encoded proteins mainly responsible for the energy supply of the cell. Thus, related diseases are often severe. This will be explained in more detail in **Chapter 1.4**.

In different cell types, the morphology of mitochondria varies strongly and is dynamic continuously changing by division (fission) and fusion events[70]. The different morphologies result from different ratios between the rates of fission and fusion. Mitochondrial fission and fusion are regulated by guanosine triphosphatases (GTPases) of the dynamin family, which enable the melting and division of the two membranes. These processes enable mitochondria to compensate for defects[71]. If the mutation load is below a critical threshold, mitochondria can rescue each other by exchanging the wild type versions of mtDNA, proteins and lipids, making fission and fusion important rescuing factors in response to toxic stress. If the damage is too great, mitochondria are targeted for autophagic elimination, termed mitophagy, during fission. In case the cell is damaged too severely and cannot be rescued, it undergoes apoptosis, a process governed by the Bcl-2 protein family, which will be discussed in the following **Chapter 1.3**.

Mitochondrial membranes contain a high level of PC, PE and cardiolipin (CL) phospholipids, while sphingolipids and sterols are rare[13]. The content of the individual lipids varies between the outer and inner mitochondrial membranes. Cardiolipin, which is only found in prokaryotes and the mitochondrial membrane of eukaryotes, constitutes 10-15 % of the mitochondrial lipids and is mainly found in the

IMM[72]. This lipid is produced in mitochondria and differs from other phospholipids, as it contains a double glycerophosphate backbone linked to four fatty acyl chains **(Fig. 1.5)**[73,74]. This conical structure induces a negative membrane curvature. Thus, cardiolipin is involved in the formation of the highly curved membrane regions found in the cristae. Additionally, it is involved in many mitochondrial processes, such as the maintenance of protein-protein and protein-membrane interactions[74]. It has been shown that CL is externalized on the OMM under stress conditions, where it functions as a signaling lipid for mitophagy and apoptosis[75,76]. Therefore, it is not surprising that it has been found to play a role also in Bcl-2 mediated apoptosis, which takes place on the OMM and will be described in the following chapter.

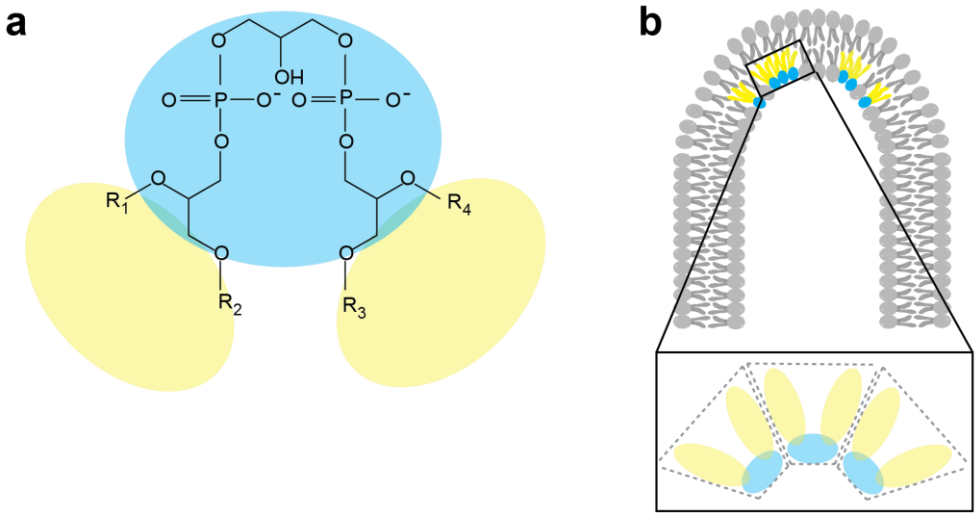

Figure 1.5: The mitochondrial lipid cardiolipin. (a) The hydrophilic headgroup (blue) in cardiolipin is formed by a double glycerophosphate backbone, which is linked to four fatty acid chains R_1-R_4 (yellow). This small headgroup with a bulky hydrophobic tail leads to a conical shape, which promotes a negative curvature (b).

1.3 The pro-apoptotic Bcl-2 family member Bak

Bak is a pro-apoptotic member of the Bcl2 protein family, which regulates the intrinsic pathway of apoptosis by controlling the permeability of the OMM [77,78]. Apoptosis, or programmed cell death, is an active and strongly regulated form of cell death, which occurs both as part of the normal cell turn over and as a defense mechanism when cells are damaged[79,80]. Thus, its regulation is very important for the overall tissue survival and can induce various diseases such as cancer or autoimmune and degenerative diseases, when it is not functioning correctly[81]. Therefore, controlling apoptosis and the players involved is a major therapeutic goal for curing these pathological conditions[82,83]. Venetoclax, a Bcl-2 inhibitor used for the therapy of chronic lymphocytic leukemia as well as other cancer types, was the first drug approved on the market targeting a Bcl-2 family member[84]. The development of further suitable drug candidates will be strongly facilitated by a better structural and functional understanding of the interacting proteins.

1.3.1 The role of Bcl-2 proteins in apoptosis

The Bcl-2 family comprises three subgroups classified as pro- and anti-apoptotic proteins, which regulate the intrinsic or mitochondrial pathway of apoptosis **(Fig. 1.6)**. The pro-apoptotic class includes both effectors and Bcl-2-homology (BH) 3-only proteins. Cytotoxic stress initiates the intrinsic pathway of apoptosis by upregulating the BH3-only proteins, which both activate the effectors and prevent the anti-apoptotic proteins from inhibiting the activation of effectors[85,86]. When the apoptotic threshold is exceeded, the effectors, such as Bak and Bax oligomerize and form pores in the OMM[81,87,88]. Through these pores, apoptogenic factors, like cytochrome c and SMAC/DIABOLO (second mitochondria-derived activator of caspases/direct inhibitors of apoptosis protein [IAP]-binding protein with low pI), are released into the cytosol[89,90]. While cytochrome c activates caspase 9 directly, SMAC/DIABOLO activate it indirectly by constraining the inhibitors of apoptosis (IAPs), which inhibit caspase 9. The activation of caspase 9 activates subsequent effector caspases and downstream apoptosis[82]. Additionally, the extrinsic or death receptor-mediated pathway can lead to apoptosis[82,90]. It is initiated by extracellular signals. After these death ligands bind to the death ligand receptor in the plasma membrane, caspase 8 is activated. This again results in the activation of effector caspases and downstream apoptosis and at the same time activates the BH3-only protein Bid engaging the intrinsic pathway of apoptosis to amplify the apoptotic response.

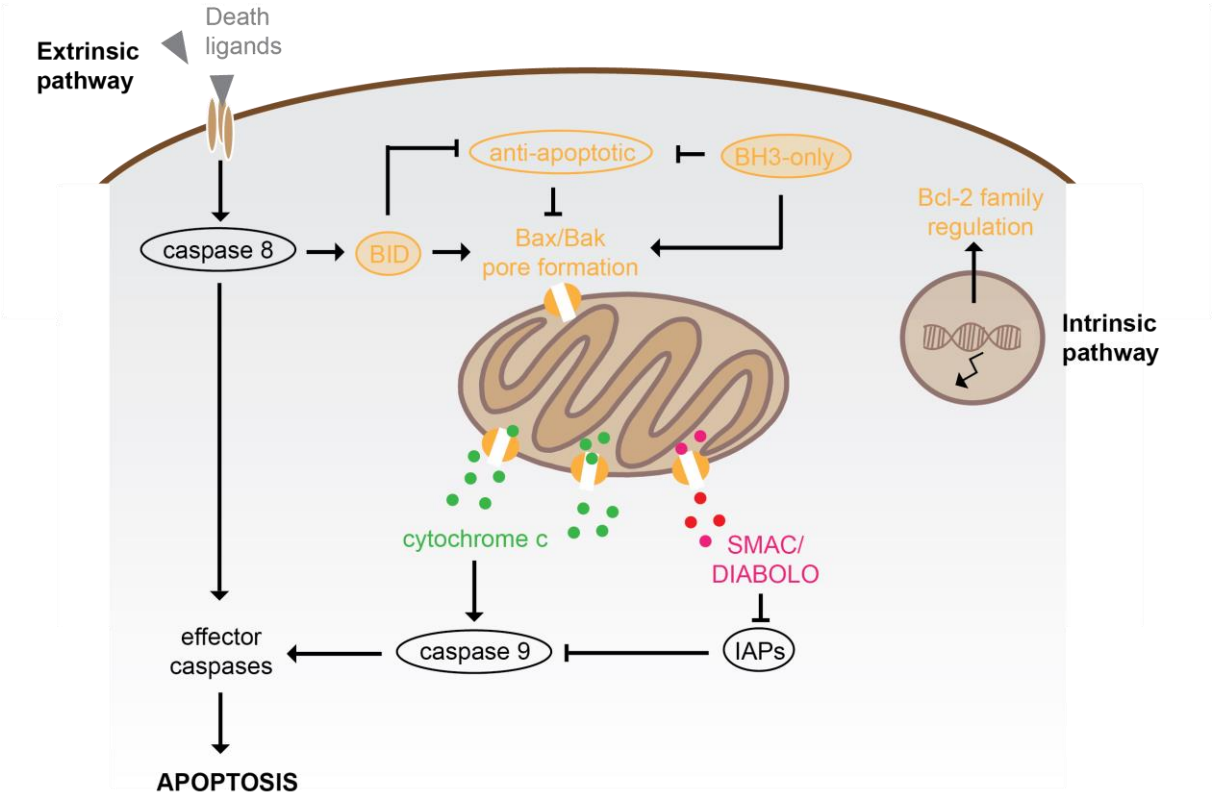

Figure 1.6: The intrinsic and extrinsic pathways of apoptosis. The intrinsic pathway, regulated by the Bcl-2 family (orange), is initiated by cytotoxic stress such as DNA damage, which leads to the upregulation of BH3-only proteins. These inhibit anti-apoptotic Bcl-2 proteins and directly activate the effector proteins Bak and Bax. Upon activation the effector proteins oligomerize and form pores in the OMM, by which cytochrome c and SMAC/DIABOLO (second mitochondria-derived activator of caspases/direct inhibitors of apoptosis protein [IAP]-binding protein with low pI) are released. Caspase 9 is activated directly by cytochrome c and indirectly by the inhibition of IAPs (inhibitor of apoptosis proteins) and activates further effector caspases leading to apoptosis. The extrinsic pathway is initiated by external death ligands, which bind to death receptors in the plasma membrane leading to the activation of caspase 8. Caspase 8 both activates effector caspases leading to apoptosis directly and proteolytically activates the BH3-only protein Bid, which additionally inhibits anti-apoptotic Bcl-2 proteins and activates the effectors leading to pore-formation and downstream apoptosis.

1.3.2 The Bcl-2 protein family

Despite their opposing functions effectors and anti-apoptotic proteins are composed of four BH-domains and have a highly conserved globular structure **(Fig. 1.7)** [82,91,92]. They consist of a helical bundle formed around a central helix α5. Helices α2-α5 form a hydrophobic binding groove, which governs the interface by which the Bcl-2 family proteins interact[82]. The BH3-domain of one family member binds to this BH3-binding groove of another family member[92]. Thereby, the salt bridge formed between a conserved arginine in the BH3 binding groove and an aspartic acid in the BH3 domain has probed crucial for the interaction[93–95]. While, the BH3-only proteins can bind to these binding grooves, they do not contain a binding groove themselves. These mostly intrinsically disordered proteins contain only the BH3 domain that forms into an amphipathic helix, when binding to a partner protein[96]. An exception is the BH3-only protein Bid, which is structured and must be activated by cleavage before its BH3-domain becomes exposed[97]. Most family members are directed to the membrane by a C-terminal transmembrane

helix (TMH)[98]. The interactions take place mostly, but not exclusively on the surface of the OMM, with the soluble domains oriented towards the cytosol[99].

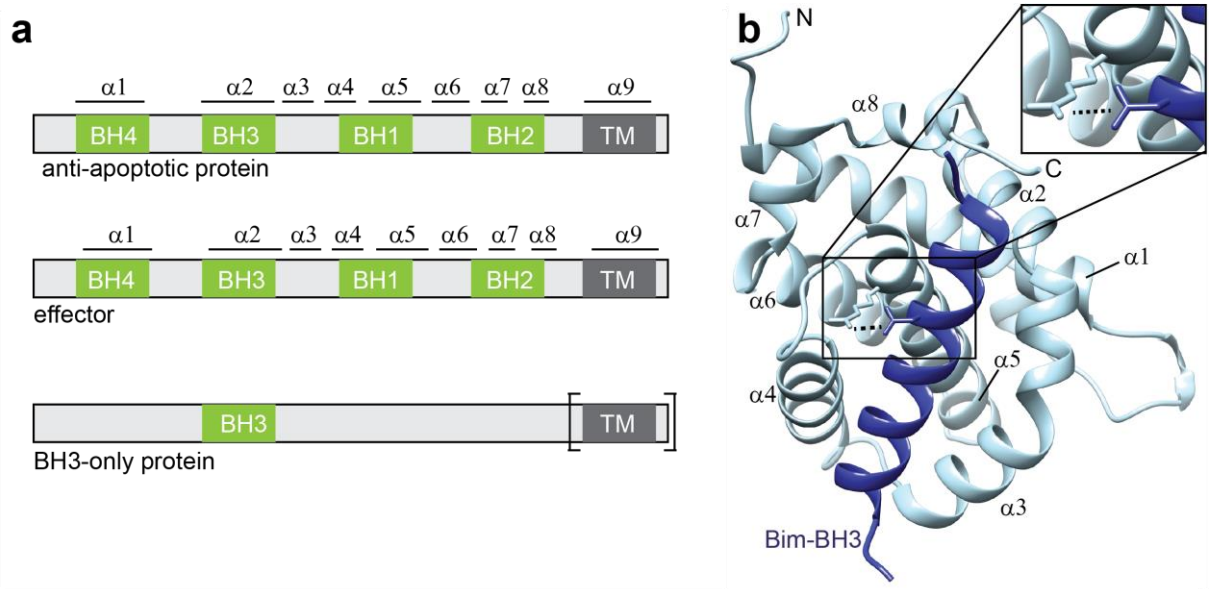

Figure 1.7: Structural analogies in the Bcl-2 protein family. (a) Anti-apoptotic proteins and effectors consist of four Bcl-2 homology (BH) domains, while BH3-only proteins contain only the BH3 domain. Not all BH3-only proteins contain a TMH. The location of helical secondary structure elements is indicated at the top. (b) The highly conserved helical bundle forming around the central helix α5 is presented using the Bak soluble domain (grey) bound to the Bim-BH3 domain (blue) (PDB: 2VX0)[100]. The BH3 binding groove is formed by helices 2-5. The inset shows the interaction highly conserved among Bcl-2 proteins between an arginine in the binding groove and an aspartic acid in the interacting BH3-domain. Here it is formed by Bak R127 and Bim D157.

The subgroup of BH3-only proteins consists of sensitizers, e.g. Bad and Noxa, which competitively bind anti-apoptotic members, leading to the displacement of pro-apoptotic Bax or Bak and activators, e.g. Bid, Bim and Puma, which additionally can directly activate the effectors[101–103]. This led to the development of different models on how the Bcl-2 protein family members control apoptosis[85,104,105]. The unified model combines different pathways and most likely describes the interactions most accurately[106]. It suggests that anti-apoptotic proteins prevent pore-formation by first interacting with the BH3-only proteins (mode 1), so that they are not free to interact with and activate the effectors. At higher concentrations the anti-apoptotic proteins also bind to the effectors directly, which inhibits their activation (mode 2). Despite the structural homology between effectors and anti-apoptotic proteins, predominantly the effectors undergo distinct structural transformations upon the activation of pore formation[107,108]. However, also for anti-apoptotic proteins a pro-apoptotic function has been described, as seen for BclxL after the N-terminus is cleaved[109]. In the light of the structural analogies, this suggests that small structural features regulate the pro- and antiapoptotic functions of the individual Bcl-2 family members.

1.3.3 The effectors Bak and Bax

The two effectors differ in their localization in healthy cells[90]. While Bak is bound to the membrane surface by its C-terminal TMH, Bax is mainly soluble with its TMH bound to its hydrophobic groove. It has been shown that the membrane affinity is governed by the TMH, which is more hydrophobic in Bak[110,111]. Consequently, when chimeric proteins are produced, in which the TMHs are interchanged, the membrane location is switched for the two players. Additionally, Bak can be turned into a soluble protein by mutating the TMH making it less hydrophobic[112]. Many Bcl-2 proteins have been shown to translocate between a membrane-bound and a soluble form[108,110]. For most Bcl-2 proteins the equilibrium is shifted strongly towards the membrane-bound form, while it favors the soluble form in Bax. The formation of a complex with anti-apoptotic proteins like BclxL has been proposed to enforce the retrotranslocation of Bax back to the soluble form[113].

When BH3-only proteins are upregulated to induce apoptosis, the equilibrium for Bax shifts strongly to the membrane bound form and both proteins oligomerize and permeate the OMM, where they form pores[82]. This requires a large conformational change. The structure then transforms from the inactive monomer[114–117], which is very similar to the structure of the anti-apoptotic proteins[92,118], to an oligomer, whose structure is still under debate. As shown in **Fig. 1.7**, BH3-proteins or the respective BH3-peptide can activate Bak and Bax by binding to their hydrophobic groove[103,119]. A "hit-and-run" model has been proposed for this interaction[120,121], as the affinity of BH3-only proteins to the effectors is in the µM-range and, thus, quite low[122]. Consequently, early studies at low concentrations could not detect complexes of effectors and BH3-proteins[121]. For Bax, a second binding site has been proposed at the rear end, which could be essential to drive Bax to the membrane bound state, because its binding groove is occupied by its TMH in the soluble state[123]. However, site-directed mutagenesis could not confirm that this interaction site is relevant for activation[124–126].

Several studies have contributed structural information on the active state. High resolution structures of possible dimeric intermediate states of Bak and Bax induced by BH3-only proteins in detergents, show that the core (α-helices 2-5) and latch domain (α-helices 6-8) separate during the activation process **(Fig. 1.8)**[119,127]. Additionally, antibody epitope binding assays revealed that helix 1 becomes solvent exposed after activation[128,129]. This process was determined as a key step for the downstream conformational transition [130]. During these structural rearrangements hydrophobic regions become exposed, which then interact with the membrane. The core stays mostly folded, but exposes the BH3 region, which is buried in the inactive, monomeric state, enabling dimerization by interaction of one BH3 domain with the hydrophobic groove of another monomer[131,132]. These symmetric homodimers and perhaps sometimes Bak/Bax-heterodimers form the starting point for larger assemblies that lead to pore formation[119].

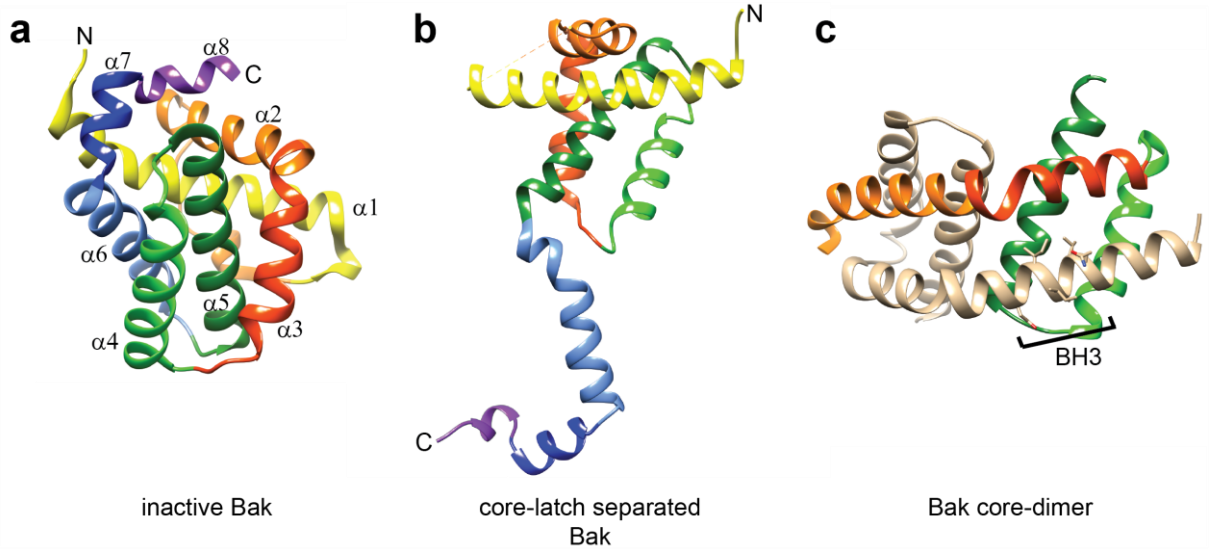

Figure 1.8: High-resolution crystal structures of different Bak conformations. (a) The soluble domain of inactive Bak (PDB: 2IMT)[114]. The color coding of secondary structure elements is used in all structures. (b) Upon activation by a BH3 peptide in the presence of the detergent CHAPS, Bak separates into a core and latch domain (PDB: 4U2U)[127]. (c) The cores then form dimers with the BH3 domain of one monomer binding to the BH3-groove of the other (PDB: 4U2V)[127].

Cross-linking experiments could tether the α6 helices, suggesting the homodimers form larger oligomers with these helices parallel to each other[129,133]. However, further studies could also cross-link many other regions and these inter-dimer crosslinks did not saturate, implying that they might not describe defined protein-protein interfaces[134–137]. Images of the Bax pore recorded by various microscopical methods have shown that Bax forms a growing pore[138,139], which can even get large enough to release mtDNA[140]. Thereby, linear and arc-shaped Bax assemblies were found, which could either originate from different projection angles or show different stages of pore formation. Membrane pores formed by proteins can either be proteinaceous, which means they are completely lined by proteins or lipidic, where the pore lumen is formed by both proteins and lipids. It has long been discussed that both Bak and Bax most likely form lipidic pores [81,139,141–144]. Recently, Cowan *et al.* showed that Bak core dimers can be bridged by lipids[145]. By studying the distances and accessibility of specifically labeled residues on Bak and Bax in a membrane environment, the different helices could be localized with respect to each other and the membrane surface [137,141,146]. They show that the core domains form a symmetric dimer, in which helices α2 and α3 are water accessible and helices α4 and α5 are in peripheral membrane contact. Additionally, the latch is also in peripheral membrane contact and helix α9 remains a TMH. Compiling all data, two models on how the dimers could be lining the pore lumen have withstood[141,147,148]. In both models the core domain has a crescent shape with a hydrophobic surface formed by the helices α4 and α5, which fits well to the toroidal pore. The adjacent lipids are stabilized by the amphipathic helix α6 and the whole arrangement is anchored to the membrane by the TMH. In the clamp model the two helices α6 clamp the membrane on opposite sides, while in a second model the core dimers are on the same side with both helices α6 stabilizing the pore rim on the opposite side[141]. Consequently, the TMHs are either antiparallel

(clamp model) or parallel (Mandal model). While all of these studies reveal essential aspects, a higher-resolution structural picture of Bak or Bax activation is still missing.

1.4 The inner mitochondrial membrane protein MPV17

After MPV17 was first suggested to be a peroxisomal protein involved in glomerulosclerosis[149–151], this was later confuted[152]. It is now commonly accepted that MPV17 is a membrane protein located in the inner mitochondrial membrane and that its dysfunction is linked to a severe hepatocerebral disease[152–155].

1.4.1 Clinical background

So far, approximately 50 different mutations including missense and nonsense variants in the gene encoding for MPV17 were reported in about 100 patients located around the globe with an about even distribution between genders **(Fig. 1.9)**[155]. With a prevalence of 1 in 1600 births it is more common in the Navajo population of the southwestern United States of America[156,157]. In those examples, the associated disease, termed Navajo neurohepatopathy, was found to be caused by the mutation R50Q in MPV17[157].

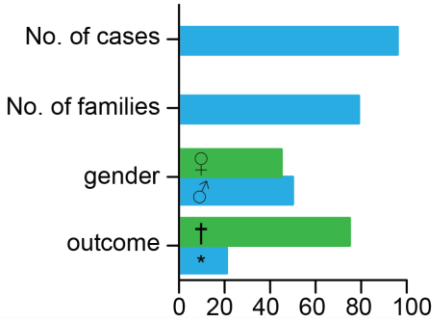

Figure 1.9: Clinically described cases of pathological MPV17 variants in patients. 96 patients from 79 families have been diagnosed with diseases connected to mutated MPV17. The distribution between male and female is about equal and the outcome deadly in most cases.

The most cases describe a hepatocerebral mitochondrial DNA depletion syndrome, which describes a reduced copy number of mtDNA, while the mitochondrial genome itself remains intact[158]. This disease, often starting at an early infant age with a poor prognosis, leads to childhood death in the majority of the patients[152,155,156]. The clinical features encompass hepatological manifestations with liver dysfunction leading to liver failure in most patients, neurological manifestations, predominantly developmental delay and metabolic manifestations such as lactic acidosis and hypoglycemia[153,155,159]. In a few cases MPV17 variants led to a later-onset neuromyopathic disease with a better prognosis[157,160,161]. Additionally, several cases of multiple mtDNA deletion in liver and muscle tissues have been described in patients with mutated MPV17[162,163]. The reported cases show that the clinical outcome correlates with the location of mutations in the MPV17 gene. A better survival was seen for biallelic missense pathogenic variants over nonsense variants. Especially patients with the mutations R41Q, R50Q and P98L showed a better outcome, suggesting that these mutations result in an at least partially functional protein[155,160]. As MPV17 deficiency has led to both mtDNA depletion and deletion, it has been proposed to be classified as a human mtDNA maintenance defect (MDMD)[164,165]. So far, MDMDs have been

described for mutations in 20 different genes, all encoded by the nucleus and involved in either the synthesis of mtDNA, maintenance of the deoxyribonucleotide supply or in mitochondrial fusion[165]. However, for MPV17 the exact function and underlying pathomechanism is unresolved and the therapy remains merely symptomatic. The protein is known to be crucial for the mtDNA maintenance by conserving a balanced mitochondrial nucleotide pool and has been suggested to act as a transporter for dNTP precursors[155,166]. Consequently, MPV17 deficiency leads to a reduction of dNTPs and DNA in mitochondria, while its overexpression increases the production of reactive oxygen species[152,155,167]. This is further supported by a study showing that an adeno-associated viral vector expressing human MPV17 was able to restore the mitochondrial DNA copy number and to prevent liver degeneration in mice[154].

1.4.2 Biochemical background

The MPV17 gene is found on chromosome 2p23-21 and is formed by eight exons[151]. It encodes a protein of 176 amino acids predicted to form four or five transmembrane helices located at TM1: AA18-38, TM2: ~53-73, TM3: ~94-114, TM4: ~131-151 and TM5: 155-172 **(Fig. 1.10)**[159,168]. The C-terminal helix TM5 was only predicted by Antonenkov *et al.*[168]. According to these predictions disease-related mutation sites are found within the membrane and in loop regions located both in the matrix and the intermembrane space[155].

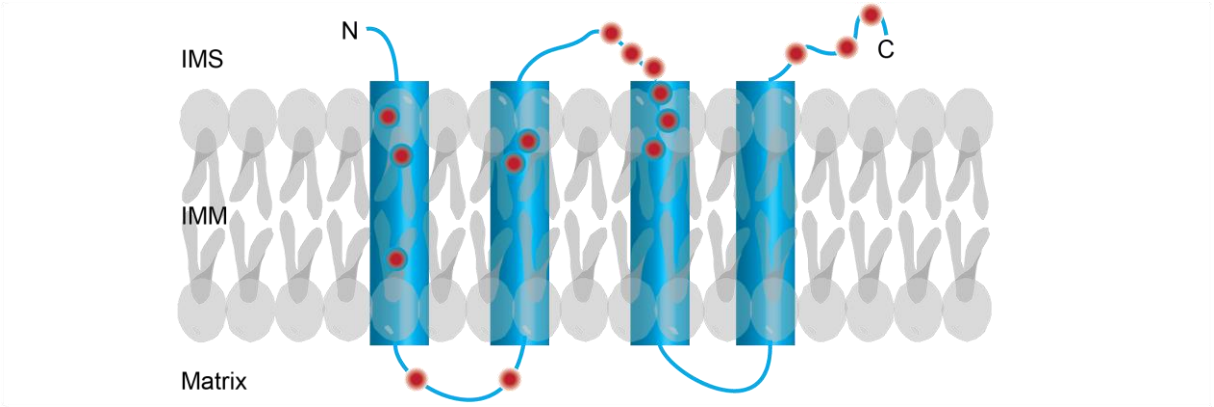

Figure 1.10: Secondary structure prediction of MPV17. Most predictions published show that MPV17 is likely to form four transmembrane helices. In red the disease related mutation sites are marked. IMS = inter membrane space, IMM = inner mitochondrial membrane.

Several MPV17 homologues have been identified in the mitochondria of other organisms, including MPV17 in mice, rats and zebrafish, as well as Sym1 in yeast[169–171]. As these homologues could rescue the MPV17 function in knockout cells they can be used as valuable model systems to investigate the molecular function of MPV17[149,170,172]. In line with this notion, not only the predicted helical geometry correlates for the different variants, but also both MPV17 and Sym1 were shown to be transported into mitochondria by the protonmotive force dependent TOM-TIM import machinery in a presequence independent manner[152,171]. A recognition site at the C-terminus of the yeast homologue Sym1 could be detected only after the OMM was removed, indicating that the C-terminus is located in the

intermembrane space[171]. Furthermore, MPV17 was shown to form a non-selective channel with gating properties[153]. In electrophysiological experiments, the conductance of MPV17 was sensitive to changes in the mitochondrial membrane potential, redox state, pH and phosphorylation with a maximal calculated pore size of ~1.8 nm. The channel was found to be closed at a high membrane potential, a high ATP/ADP ratio that favors protein phosphorylation and a reducing environment[168]. These conditions associated with functional mitochondria, explain how a channel can exist in the inner mitochondrial membrane alongside a high membrane potential. A pore that probed closed at physiological membrane potentials was also detected for Sym1[171]. A very similar maximal pore size of ~1.6 nm further underlines the analogies, between the homologues. By extracting Sym1 from mitochondria using digitonin, this study also revealed that the final membrane channel of Sym1 consists of a homo-hexamer or dodecamer[171]. Further studies propose that MPV17 might be a subunit of larger protein complexes (> 600 kDa), suggesting that other membrane proteins are required for pore formation in the IMM [154,169].

Despite initial studies on MPV17 function and secondary structure content[168], no higher-resolution structural information is available for this essential membrane protein. To obtain a deeper understanding of the structural and functional relationships in MPV17 and the mechanisms behind disease-causing mutations, production and *in vitro* handling of this membrane protein is required for an in-depth biophysical analysis and structural investigations. So far recombinant protein was only produced in yeast cells[168], which makes isotope labeling more challenging despite recent advances in the field[173]. For future NMR studies, an expression in bacterial production hosts would be advantageous for state-of-the-art isotope labeling enabling high-resolution NMR studies. The handling of recombinant protein before inserting it into planar bilayers for conductivity measurements has been done either in DPC-micelles in the case of human MPV17[168] or by denaturing it in SDS-micelles and refolding it into Triton X-100 in the case of Sym1[171]. These studies suggest, that MPV17 tolerates harsh detergents and even unfolding and refolding and still maintains its functionality in a lipidic environment. This opens a wide set of possibilities for its handling also for future in vitro studies and is the basis of this work.

1.5 Objectives

This thesis aims to address two distinct research objectives on pore-forming membrane proteins located in the mitochondrial membranes.

In the first aim, the pro-apoptotic Bcl-2 family protein Bak is analyzed. After the structure of the dormant inactive soluble domain has been solved and recent studies could show that the core and latch domains separate upon activation and form dimers, this work aimed at solving the structure of the full-length protein in a membrane encompassing the missing N-terminal residues (1-15) and the transmembrane helix with a segmental approach and observing the transitions taking place upon activation in a membrane environment at high-resolution. For the latter observation, a membrane mimetic had to be optimized, that enables the investigation of the structural transitions by combining a close to native environment for Bak and an experimental setup, which is applicable to high-resolution NMR studies as well as other structural methods. Another goal was to compare the structurally converging Bcl-2 proteins Bak and BclxL and determine characteristics explaining their opposing functions and to study the interaction between these two proteins in a membrane environment.

In the second aim, the inner mitochondrial membrane protein MPV17 is investigated. With neither the structure nor the function solved for this disease-related protein, the goal was to first develop a strategy to enable an NMR-characterization of the monomer in a suitable membrane mimetic. For this, a production procedure in *E. coli* had been developed prior to this work. As MPV17 has been shown to form pores, another aim was to screen for a membrane mimetic that can stabilize this pore state and enable future structural studies with cryo-EM. During this process cysteines probed critical for oligomerization. Therefore, the effect of cysteines on structure, stability and the tendency to form oligomers was analyzed. Finally, studying the effect of disease-related mutations on oligomerization aimed at further understanding the functional relationships leading to the severe and often lethal disease developed in patients carrying mutations in the MPV17 gene.

2 Bak

2.1 Results

2.1.1 Structural studies on Bak

Several crystal structures of inactive BakΔTM are available (PDB: 2IMT, 2IMS, 2JCN, 2YV6)[114–116]. All structures were generated using a N-terminally truncated construct starting at A18 or S23. An NMR backbone assignment and structure of the N-terminally truncated BakΔTM construct in complex with a Bid-BH3 peptide has also been published (BMRB: 19045; PDB: 2M5B)[103]. However, the backbone assignment of the apo-form has not been deposited in the Biological Magnetic Resonance Data Bank (BMRB). It was first published with an incomplete assignment by Moldoveanu *et al*[103,114] and recently completed[174]. Interestingly this 2D-[^{1}H, ^{15}N]-HSQC spectrum does not completely converge with the spectrum of inactive BakΔTM containing the full N-terminus, obtained in this work. An approximate overlay generated with a figure found in Moldoveanu *et al.*[114] can be found in **Fig. 2.1**. While some residues, as highlighted in the glycine area (upper box), superimpose quite well, the chemical environment of other backbone NH-groups (lower box) changed strongly making a complete and reliable transfer of the assignments impossible.

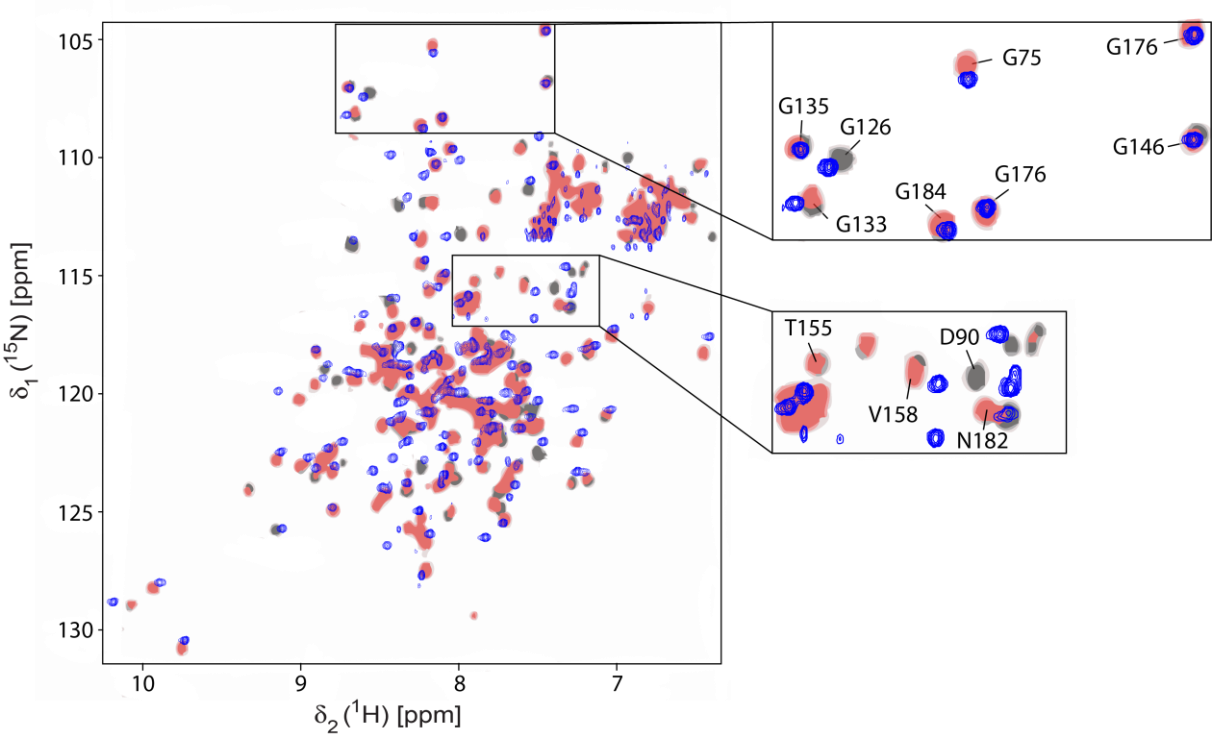

Figure 2.1: Overlay of 2D-[^{1}H, ^{15}N]-HSQC spectra of different BakΔTM constructs. BakΔTM with the full-length N-terminus (blue) is superimposed on an overlay of the truncated BakΔTM without (black) and with 2-fold excess of Bid-BH3 peptide (red). Adapted from Moldoveanu et al[114].

Due to these differences, it was necessary to perform a *de novo* assignment of apo BakΔTM. The obtained NMR resonance assignments enabled a refinement of the crystal structure including the entire N-terminus.

Regarding the C-terminal transmembrane helix (TMH), there is only little information and no structure available. A peptide of the TMH (AA I188-S211) was shown to form an α-helical secondary structure in DMPC-vesicles and to induce carboxyfluorescein leakage from large unilaminar vesicles, but it remains unclear whether the latter effect is linked to the pore-forming activity of full-length Bak[175]. To bring more light onto these unanswered questions, the remaining part of this chapter is dedicated to Bak-TMH. Finally closing with a simulated structural model of the full-length protein in nanodiscs.

2.1.1.1 NMR resonance assignment and structure refinement of BakΔTM harboring an intact N-terminus

For the backbone assignment of BakΔTM 3D-HNCA, HNCO, HNCACB and HNH-NOESY experiments were recorded using a *U*-[^{13}C, ^{15}N]-labeled sample. As shown for the HNCA strips of residues R11 to E16, the quality of the spectra was sufficient to assign 80% of the non-proline residues **(Fig. 2.2).**

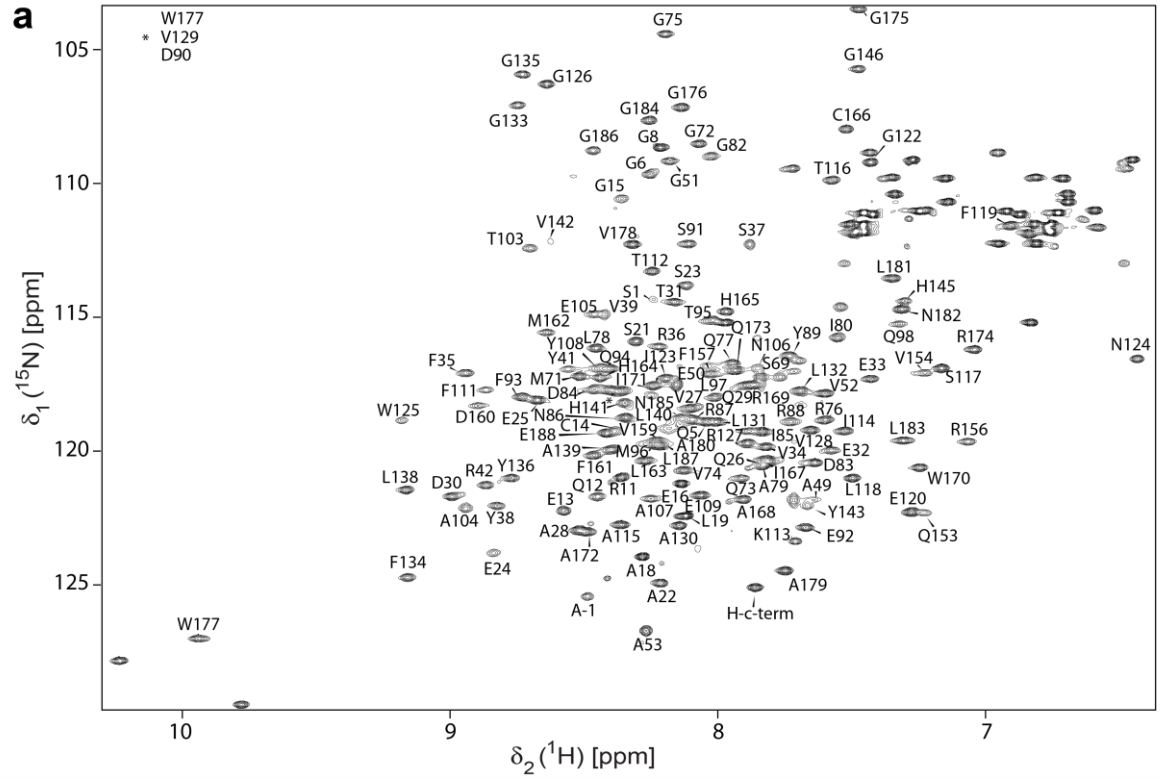

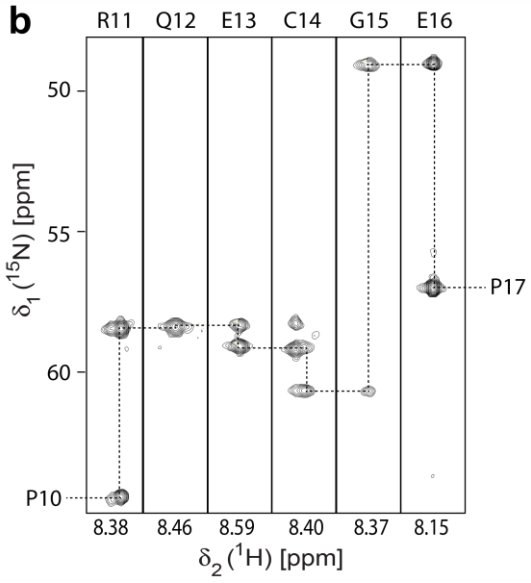

Figure 2.2: Backbone resonance assignment of BakΔTM. (a) 2D-[^{1}H,^{15}N]-HSQC spectrum of BakΔTM with all assigned peaks. (b) 3D-HNCA-strips of residues R11 to E16 visualize the quality of the 3D data. Broken lines indicate the sequential connections. The data was acquired on a 195 µM sample at 950 MHz at 303 K.

Using the Cα, Cβ, CO, N and Hα shifts, the secondary chemical shifts (secCS) were calculated with Talos^{+} **(Figure 2.3a)**[176]. While positive secCSs correspond to α-helical regions, the negative secCSs relate to β-sheets and values close to 0 define unstructured regions. As expected the protein contains mainly α-helical content, which corresponds nicely with the eight α-helices defined in the published structure and indicated at the top of the figure[114]. Additionally, ^{1}H-^{15}N residual dipolar couplings (RDC) were recorded using 10 mg/mL Pf1-phage as an alignment medium and {^{1}H}-^{15}N heteronuclear NOEs (hetNOE) were measured to probe dynamics in the ns-ps time scale. The resulting secCSs and RDC's were used to refine the crystal structure of truncated BakΔTM (PDB: 2IMS)[114] **(Figure 2.3b)**. This led to a good agreement between experimental and back-calculated RDC's (R = 0.95, Q = 0.15) and confirms that this construct is properly folded, as reported for the truncated version. As most of the N-terminal residues missing in the structures reported so far were assigned, the herein obtained data clearly show that this region is unstructured. This was also confirmed by the {^{1}H}-^{15}N hetNOE experiment **(Fig. 2.3a)**. The smaller the value, the more dynamic the corresponding residue, while values close to one indicate very rigid structural conformations. In BakΔTM, the only very dynamic region is the N-terminus up to S21 which explains why this part could not be crystalized and was cleaved off or deleted in former structural studies[114–116]. The rigid regions correlate well with the eight α-helices with more flexible elements between the α-helices, especially for the longer loop region before helix 2 (E50-S69) and the unstructured C-terminus starting at L183.

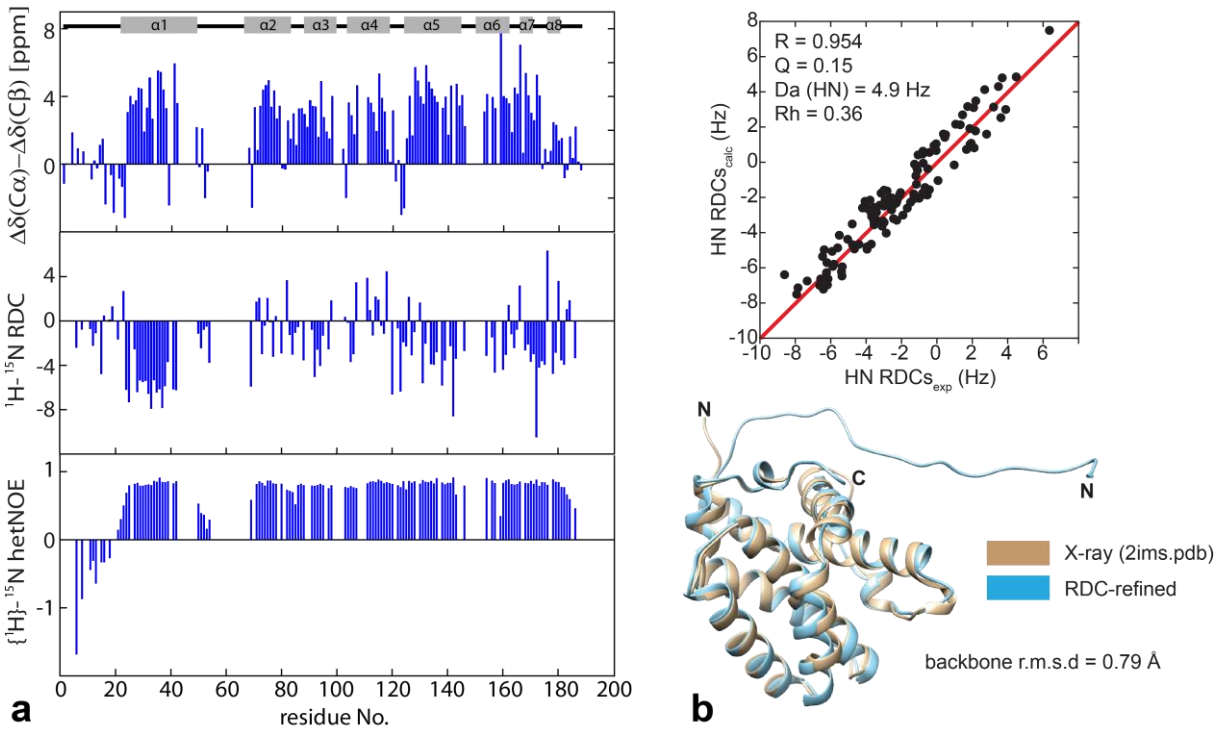

Figure 2.3: Structure refinement of BakΔTM. (a) Secondary chemical shifts (top) and ^{1}H-^{15}N residual dipolar couplings (RDC) (middle), which were used for the structure refinement. At the bottom the {^{1}H}-^{15}N heteronuclear NOE (hetNOE) is shown, reporting on the ns-ps dynamics. The α-helical structure elements are indicated at the top in grey. (b) Overlay of the refined structure of BakΔTM and its initial structure PDB: 2IMS.[114] The correlation between experimental and back-calculated RDCs is shown at the top. The structure refinement was performed by Dr. Franz Hagn.

2.1.1.2 Production and Characterization of Bak-TMH

Earlier studies on the transmembrane helix of Bak used a synthetic peptide (AA I188-S211)[175]. In this work, the Bak TMH was produced as a fusion protein, N-terminally fused to GB1 and cleavable with thrombin **(Fig. 2.4a)**. The construct was designed analog to the BclxL-TMH published by Raltchev *et al.*[177], consisting of the TMH as well as the linker connecting it to the soluble domain (L183-S211). The additional GSGS-linker between the Thrombin cleavage site and the Bak-TMH proved crucial for cleavability. The four residues natively linking the soluble and TM domain in Bak, provided insufficient space for thrombin accessibility. In contrast, for the BclxL-TMH fusion construct an additional linker was not necessary, as the native linker connecting the TMH and the soluble domain is longer. In BclxL, eighteen amino acids connect the two domains (Y195-W213), from which eleven amino acids (E202-W213) were left on the BclxL-TMH-construct.

Next, a sequence analysis of the C-terminal domains in Bak versus BclxL was performed revealing analogies **(Fig. 2.4b)**. Based on the hydrophobicity and basicity the sequential alignment showed that the same positions feature the same type of amino acids with eight residues being identical. However, despite the high sequence similarity, the two TMHs displayed different purification behaviors. While the BclxL-TMH could be produced in higher yields as solemnly a monomer, making a SEC purification

redundant, this step was necessary for the Bak-TMH in order to separate the monomer from the large amounts of oligomeric species **(Fig. 2.4c)**. Both Bak-TMH species were pooled, stored at 4 °C for several weeks and separately resubjected to SEC **(Fig. 2.4d)**. Each species eluted from the column as before suggesting no functional relationship between the two. If the oligomeric species were functionally relevant one would expect an equilibrium forming between the mono- and oligomeric form.

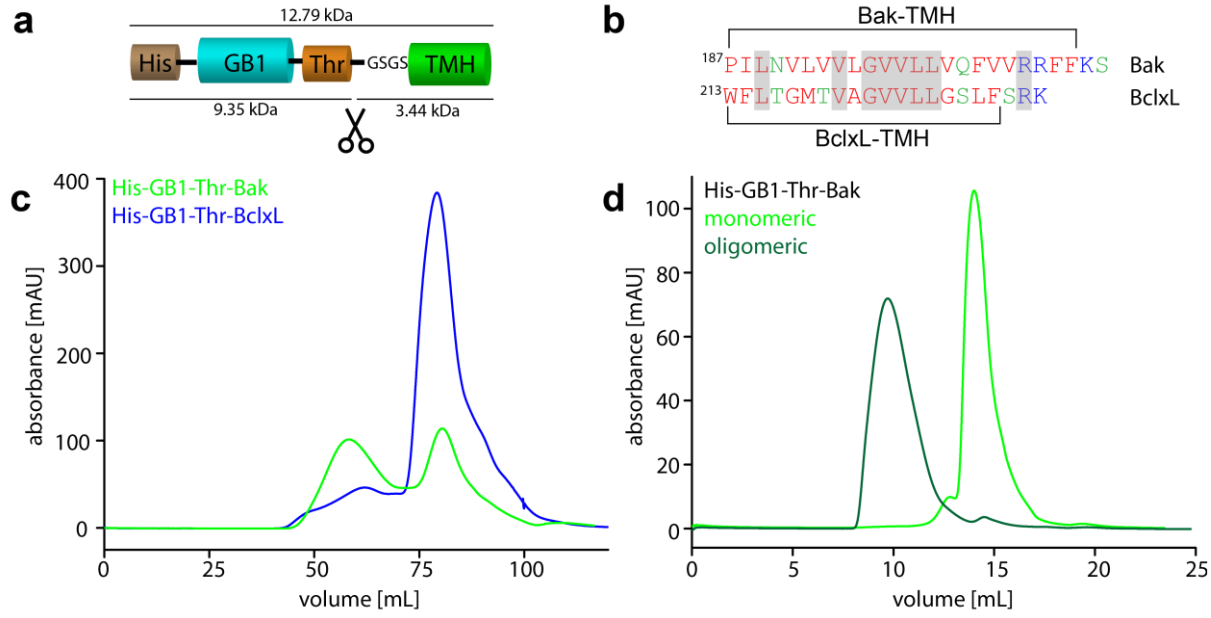

Figure 2.4: Production of His_6-GB1-Bak-TMH. (a) The fusion construct used for the production of the Bak-TMH. The molecular weight of both the fusion construct and the cleavage products are indicated. (His = His_6-tag; Thr = Thrombin cleavage site). (b) Comparison of the Bak- and BclxL-TMH sequences. The polarity of each amino acid is represented by its font color (red = apolar; green = polar; blue = basic). Identical amino acids are highlighted in grey. (c) Overlay of SEC profiles of Bak- and BclxL-TMH 1L purifications in DPC on a preparative Superdex™ 200 column. (d) Overlay of SEC runs of the pooled and concentrated monomeric and oligomeric Bak-TMH re-injected on an analytical Superdex™ 200 column to analyze whether an equilibrium is formed.

These differences in their oligomeric states raised the question whether the TMH might have additional functions besides being the membrane anchor of the functionally relevant soluble domain. The strong oligomerization tendency and an earlier study showing pore-formation suggest that the TMHs could also be involved in Bcl-2 protein functionality[175]. Therefore, the secondary structure content and stability of both TMHs were compared by far-UV CD spectroscopy **(Fig. 2.5)**.

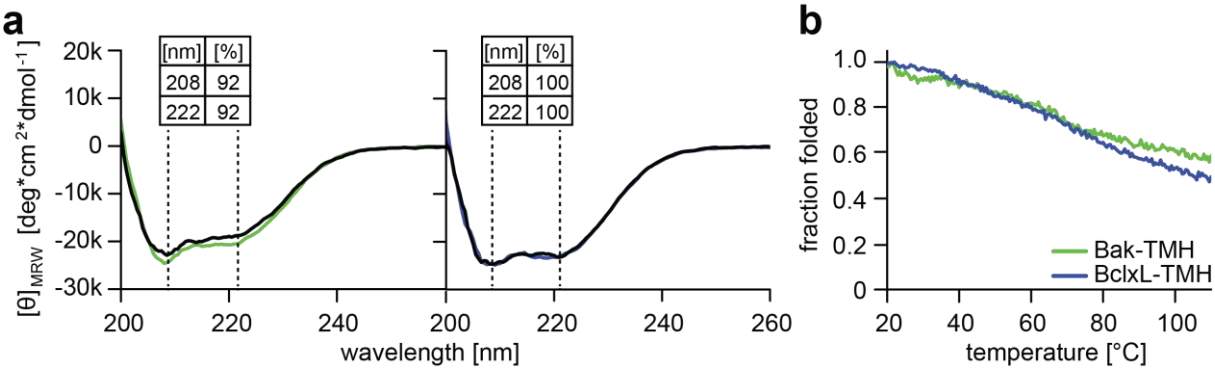

Figure 2.5: Comparison of Bak- and BclxL-TMH in DPC micelles with circular dichroism. (a) Far-UV-CD spectra

of Bak-TMH (green) and BclxL-TMH (blue). The rescans after subjecting the samples to 110°C and returning to the starting temperature are shown in black respectively. The percentile refolding efficiency is indicated in the tables by the characteristic minima in α-helical structures: 208 nm and 222 nm. (b) Temperature scan from 20 °C to 110 °C of Bak-TMH (green) and BclxL-TMH (blue) monitoring the CD-signal at 222 nm.

The far-UV CD spectra are very similar for the Bak- and the BclxL-TMH in DPC micelles **(Fig. 2.5a)**. Both show a similar amount of α-helical secondary structure with little effect from refolding after subjecting to heat. While scan and rescan are identical for the BclxL-TMH, the thermal refolding efficiency is slightly decreased for the Bak-TMH reaching only 92 % of the original α-helical content. This is coherent with the lower yield of monomeric Bak-TMH after refolding during purification. Additionally, neither TMH is completely unfolded when subjecting to heat **(Fig. 2.5b)**. Both display a gradual decrease of the α-helical secondary structure monitored at 222 nm with more than 50 % left at 110 °C.

Next, both TMHs were inserted into lipid nanodiscs, as it is more native to study the TMH in a lipid bilayer membrane. In order to compare the results with those achieved for the BclxL-TMH by Raltchev *et al.*[177], the nanodisc preparation was done accordingly. Therefore, His_6-GB1-Bak-TMH was purified in SDS instead of DPC micelles. The assembly ratio of 1:6 used for the BclxL-TMH in ΔH5-nanodiscs by Raltchev *et al.*[177], was further optimized leading to an optimal assembly ratio of 1:5 resulting in one Bak-TMH per nanodisc. The SEC profiles of the obtained nanodiscs before and after Thrombin cleavage are shown in **Fig. 2.6a**. As expected, the elution volume slightly increases after cleavage, because the extra membranous domain GB1, which increases the hydrodynamic radius, is cleaved off and elutes separately at 18.2 mL. Interestingly, GB1-Bak-TMH runs as a double band and slightly higher than expected at about 15 kDa on SDS PAGE gels **(Fig. 2.6b)**. This double band vanishes after thrombin cleavage and is replaced by a band for GB1 at about 9 kDa, whereas the Bak-TMH is too small to be visible on this gel.

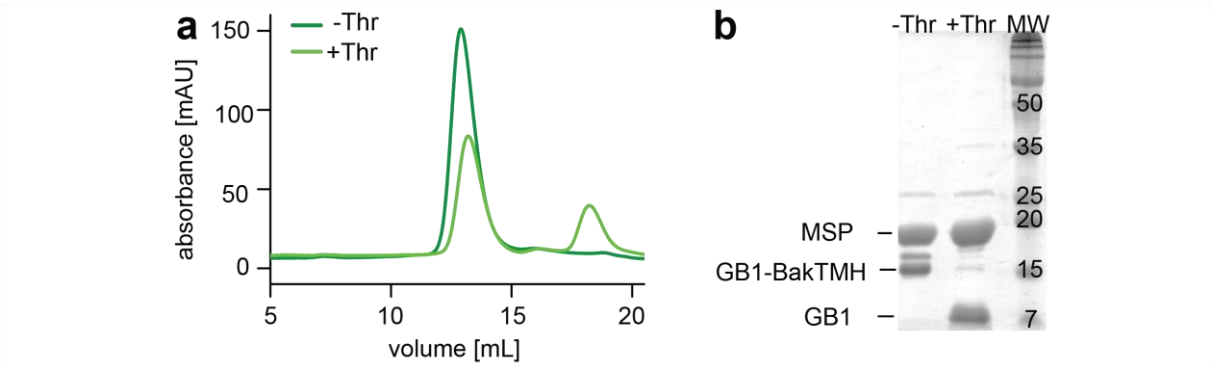

Figure 2.6: Nanodisc assembly of the Bak-TMH in ΔH5-nanodiscs. (a) Size exclusion chromatograms of His_6-GB1-Bak-TMH in ΔH5-nanodiscs before (dark green) and after (light green) the thrombin cleavage run on an analytical Superdex™ 200 column. (b) SDS PAGE analysis of the Thrombin cleavage performed between the two SEC runs. The protein molecular weight standard (MW) in shown on the right. Masses are indicated in kDa.

In order to study the oligomerization behavior of Bak-TMH in nanodiscs a proteolytic assay was applied **(Fig. 2.7a)**[178]. The starting material used in this assay, was the GB1-Bak-TMH fusion construct

stabilized in detergent micelles. Once the fusion protein was inserted into nanodiscs, the Bak-TMH-containing nanodiscs were separated from the empty ones by Ni-NTA affinity purification and SEC. In the next step, the GB1-tag was cleaved off by thrombin. Finally, the cleaved product was separated by a second SEC and the area under both UV-detected peaks was derived. After normalizing these absorption peak integrals by the according extinction coefficient, the amount of TMH (= the amount of GB1) per nanodisc (= two MSP molecules) could be calculated. By using different assembly ratios of GB1-fused Bak-TMH and MSP and varying the length of the MSP construct defining the size of the final nanodisc, the oligomerization tendencies could be assayed **(Fig. 2.7b)**.

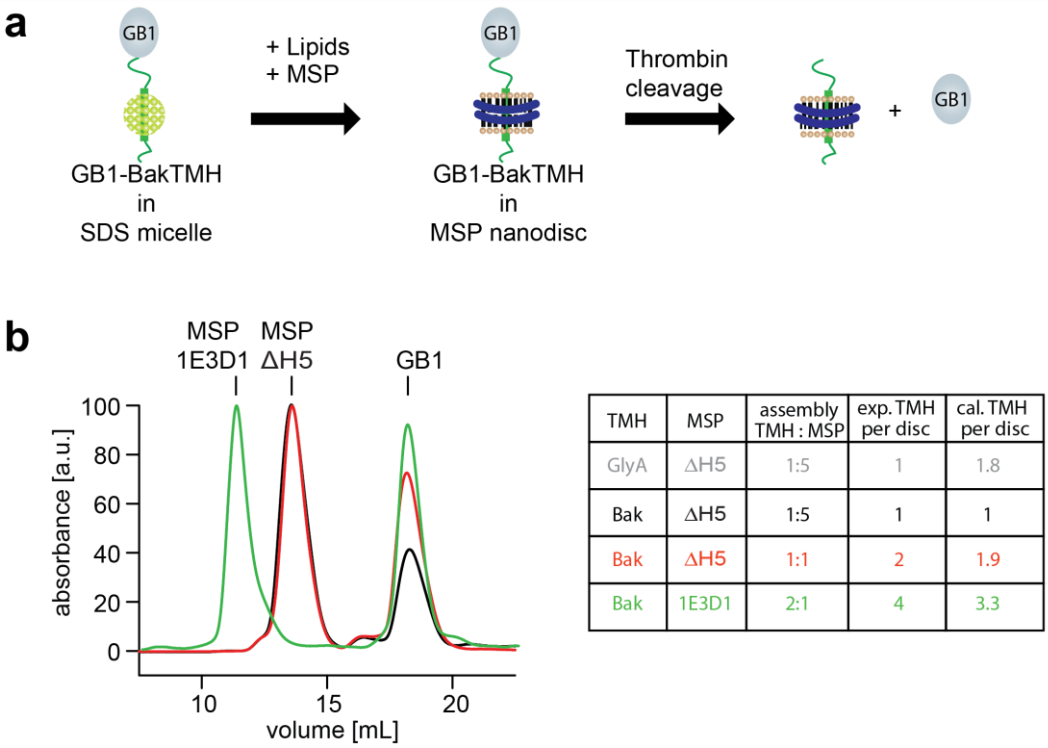

TMH	MSP	assembly TMH : MSP	exp. TMH per disc	cal. TMH per disc
GlyA	ΔH5	1:5	1	1.8
Bak	ΔH5	1:5	1	1
Bak	ΔH5	1:1	2	1.9
Bak	1E3D1	2:1	4	3.3

Figure 2.7: Proteolytic assay to quantify the amount of Bak-TMH per nanodisc. (a) Overview of the nanodisc assembly procedure. The GB1-Bak-TMH fusion construct is assembled into nanodiscs out of SDS micelles. Finally, the GB1 is cleaved off resulting in a 1:1 stoichiometric ratio between GB1 and incorporated Bak-TMH. (b) SEC profiles of different Bak-TMH nanodisc assemblies run on an analytical Superdex™ 200 column after thrombin cleavage were color coded according to the table on the right. The absorption peak integrals were used to calculate the ratio of TMH/nanodisc. The table shows the applied assembly conditions as well as the expected and calculated amount of TMH/nanodisc. For a dimeric protein like the Glycophorin A (GlyA) TMH expected and calculated ratios differ, which is not the case for the Bak TMH.

If no oligomerization takes place, the ratio of protein/nanodisc is close to the theoretically expected value based on the chosen assembly conditions. The herein probed assembly ratios revealed no oligomerization tendencies, as the expected and calculated ratios correlate well. An assembly ratio of 1:5 (Bak-TMH:MSP1D1ΔH5) resulted in the incorporation of one helix per nanodisc. This behavior is quite similar to what has been reported previously for the BclxL-TMH [177] and is in contrast to the dimeric Glycophorin A (GlyA) TMH for which the same assembly conditions resulted in a ratio of almost two helices per nanodisc. Both the assembly conditions and the nanodisc sizes (using MSP1D1ΔH5 (8 nm)[45]

and MSP1E3D1 (12 nm)[44]) were varied but the obtained data indicated no tendency of the Bak-TMH to form oligomers in lipid bilayers.

2.1.1.3 NMR Structure determination of Bak-TMH

The structure of the Bak-TMH was determined both in DPC-micelles and ΔH5-nanodiscs. 2D-[^{1}H, ^{15}N]-TROSY spectra of Bak-TMH were recorded in both membrane mimetic systems leading to the total amount of NMR resonances as indicated in **Fig. 2.8**. The backbone resonance assignments could be obtained by conducting 3D-TROSY-HNCA and HNCO experiments for *U*-[^{2}H, ^{13}C, ^{15}N]-Bak-TMH in DPC-micelles as well as HNH- and NNH-NOESY experiments for *U*-[^{2}H, ^{15}N]-Bak-TMH in both membrane mimetic systems. As the construct used for the triple resonance experiments did not contain the native linker connecting the TMH to the soluble domain, these residues could not be assigned.

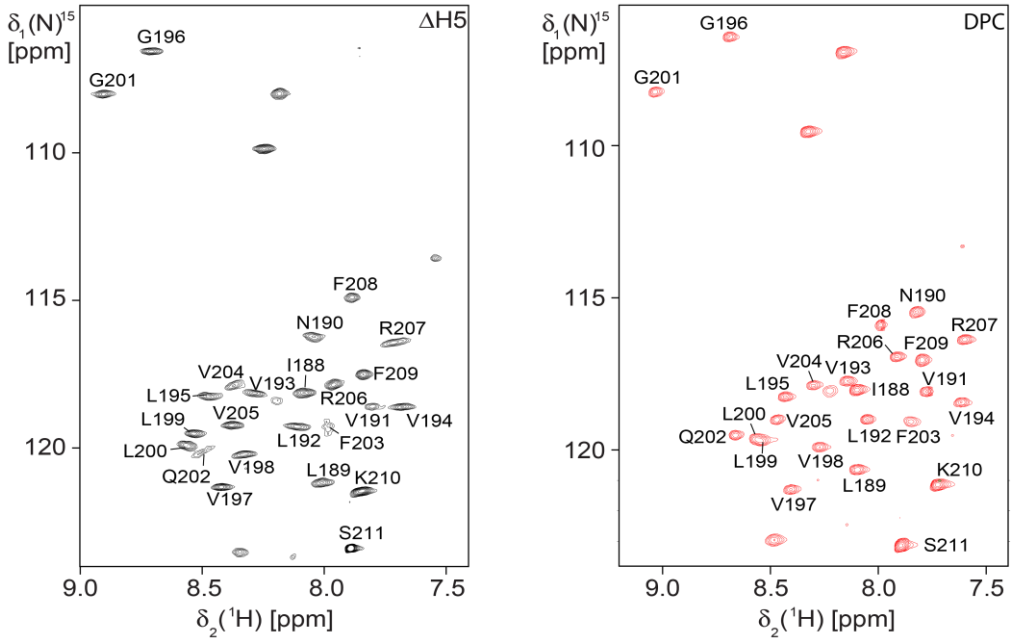

Figure 2.8: Assignment of Bak-TMH. 2D-[^{1}H, ^{15}N]-TROSY spectra of 300 µM *U*-[^{2}H, ^{15}N]-Bak-TMH in ΔH5-nanodiscs (black) measured at 315 K and 600 MHz and in DPC-micelles (red) measured at 310 K and 800 MHz.

The low dispersion is consistent with an α-helical secondary structure and unstructured loop regions at the termini. Comparing both spectra, several peaks shifted due to the distinct chemical environment of DPC micelles and a lipid bilayer. The sample in ΔH5-nanodiscs shows broader lines due to the larger overall size of the system, which leads to slower tumbling and thus faster T_2-relaxation. ΔH5-nanodiscs have a molecular weight of 95 kDa[179], while DPC forms micelles of about 20 kDa[27].

The NOESY-data not only show all sequential connections, but also confirm the transmembrane nature of the helix **(Fig. 2.9)**. While water contacts are visible for the loop regions at both ends of the helix, continuous lipid/detergent contacts are visible for the entire helical part. The most prominent contacts are to the -CH_2 and -CH_3 groups of the fatty acid chains. As expected, these get weaker towards the terminal residues. On the other hand, the latter show contact to the cholate head group. As DPC has the shorter fatty acid chain with only 12 carbons instead of 14 in DMPC, it is expected to form a thinner

hydrophobic membrane region, which perhaps explains the weaker cross peaks to methyl groups in the flanking regions when the Bak-TMH is in DPC-micelles.

The additional peaks originate from side chain contacts, e.g. the Hβ's in N190 (~2.8 ppm), F208, F209 (~3 ppm), S211 (~3.8 ppm). These are visible because the sample was prepared using protonated ^{12}C-glucose leading to the fractional protonation of side chains.

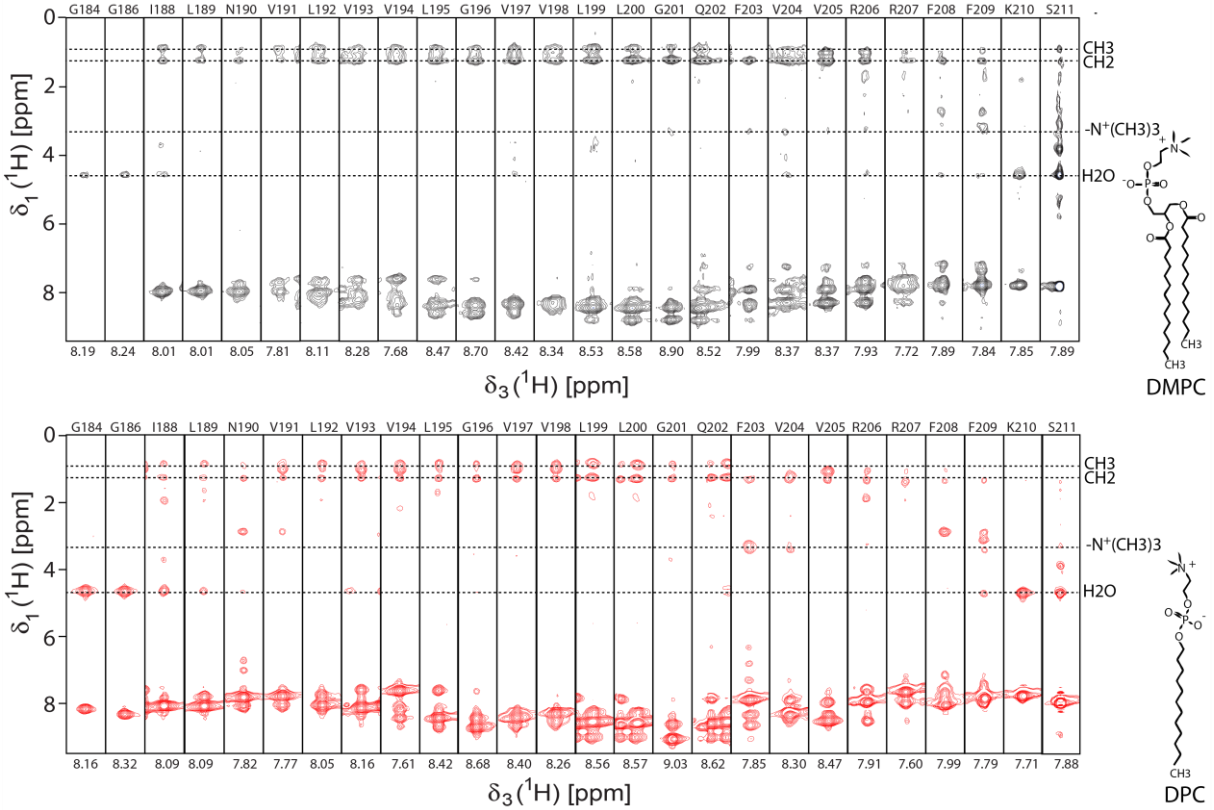

Figure 2.9: ^{15}N-edited [^{1}H, ^{1}H]-NOESY-TROSY strips of 300 µM [^{2}H, ^{15}N]-Bak-TMH. The upper figure depicts Bak-TMH in ΔH5-nanodiscs (75 % DMPC/ 25 % DMPG) (black). It was recorded at 315 K and 600 MHz. The lower figure shows Bak-TMH in DPC-micelles (red). It was recorded at 310 K and 800 MHz. Lipid/detergent contacts are indicated by dotted lines. The lipid DMPC and detergent DPC are illustrated on the right for comparison.

The α-helical structure could further be confirmed by the TALOS^{+} results[176] and a SecCS analysis **(Fig. 2.10a+b)**. Both were calculated only for Bak-TMH in DPC-micelles, as carbon chemical shifts were only recorded for that sample. The TALOS^{+} secondary structure prediction probabilities were plotted as positive values for predicted α-helices and negative values for predicted β-sheets. The Cα chemical shifts result in the same representation with values close to zero corresponding to unstructured loop regions. Both prediction tools suggest that the transmembrane helix is formed by residues L189 to R206. It must be taken into account, however, that these values are not completely reliable, as no Cβ-shifts were recorded and thus were not included in the calculations. Comparing these results to the internal dynamics of the Bak-TMH in DPC-micelles **(Fig. 2.10c-e)**, reveals that the rigid helical structure most likely is longer. Both the longitudinal T_1- and the transverse T_2-relaxation was recorded and the respective relaxation rates were derived ($R_x=1/T_x$). As relaxation is sensitive to the motion of a nuclei in the ns to

ps time scale, these measurements enable the study of dynamics for individual residues within the molecule. In both cases I188 to F209 were found to be rigid in the ns to ps time scale, while the flanking regions are dynamic. This is also represented by the correlation time τ_c derived from the T_1 and T_2 values in **Fig. 2.10e**. τ_c describes the average time it takes for a residue to change its orientation by one radian. The larger a protein is, thus the slower it tumbles, the shorter the correlation time is. Therefore, smaller τ_c values refer to more dynamic motions.

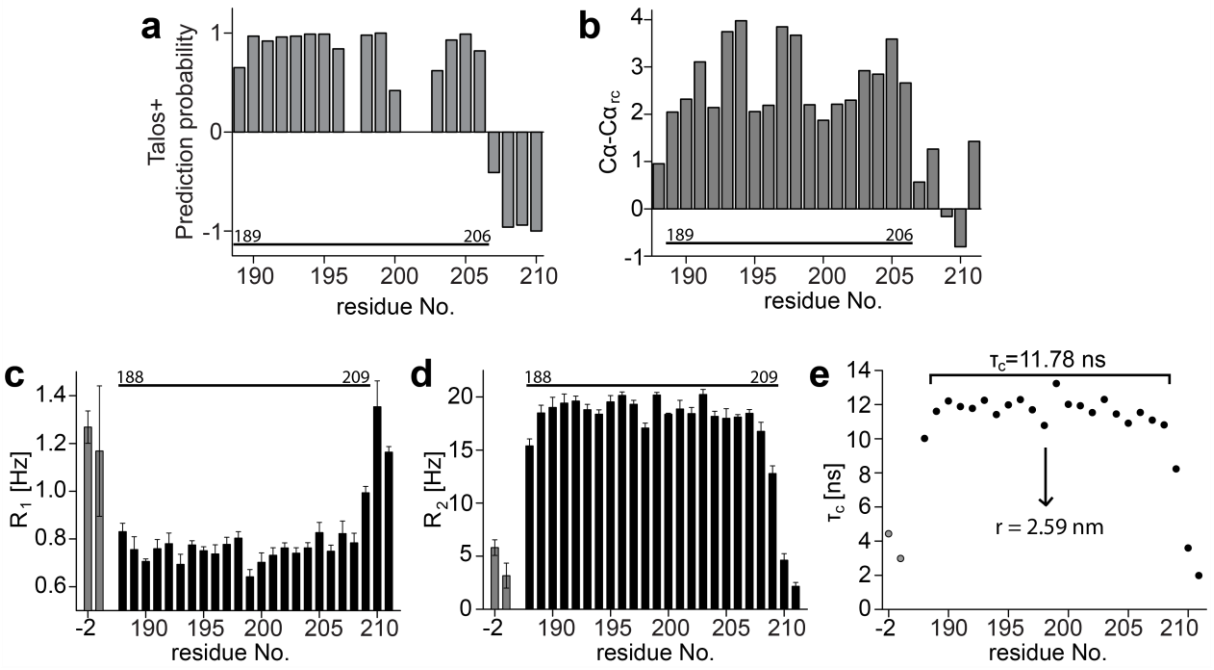

Figure 2.10: Secondary structure prediction and dynamics of Bak-TMH in DPC-micelles measured at 310 K and a DPC-concentration of 288 mM. The derived helical conformation is indicated at the top by a line. (a) TALOS$^+$ secondary structure prediction probabilities. Positive values predict α-helices and negative values predict β-sheets. (b) Secondary chemical shifts based on Cα. (c+d) R_1 (=1/T_1)- and R_2 (=1/T_2) relaxation rates plotted against the sequence. (e) The correlation time τ_c in nanoseconds derived from the T_1 and T_2 relaxation time constants. τ_c was averaged using the rigid parts as indicated at the top to calculate the hydrodynamic radius r. The residues -1 and -2 correspond to the N-terminal GSGS-linker and are colored in grey. The native sequence of the construct used for all these measurements was P187-S211.

The hydrodynamic radius r of 2.59 nm was derived from the average correlation time for the rigid helix, as this is the part tumbling with the size-defining DPC micelle. It correlates well with published data of DPC-micelles with and without a peptide, also measured at 310 K[180]. The reported hydrodynamic radius of 1.87 nm for an empty DPC-micelle increases to 2.1-2.3 nm in presence of a 17-residue peptide. As the Bak-TMH has 30 residues a further increase in size appears reasonable.

Combining all this information and data, the structures were calculated both in DPC-micelles and ΔH5-nanodiscs **(Fig. 2.11)**. Both structures were calculated based on the NOESY-data, as well as H-bonds, defined by missing water exchange peaks, and additionally the TALOS$^+$ data in the case of DPC-micelles. The C-terminal Bak-TMH forms a rigid membrane helix from P187 to F209 with only the termini, which are located outside the membrane, displaying flexibility.

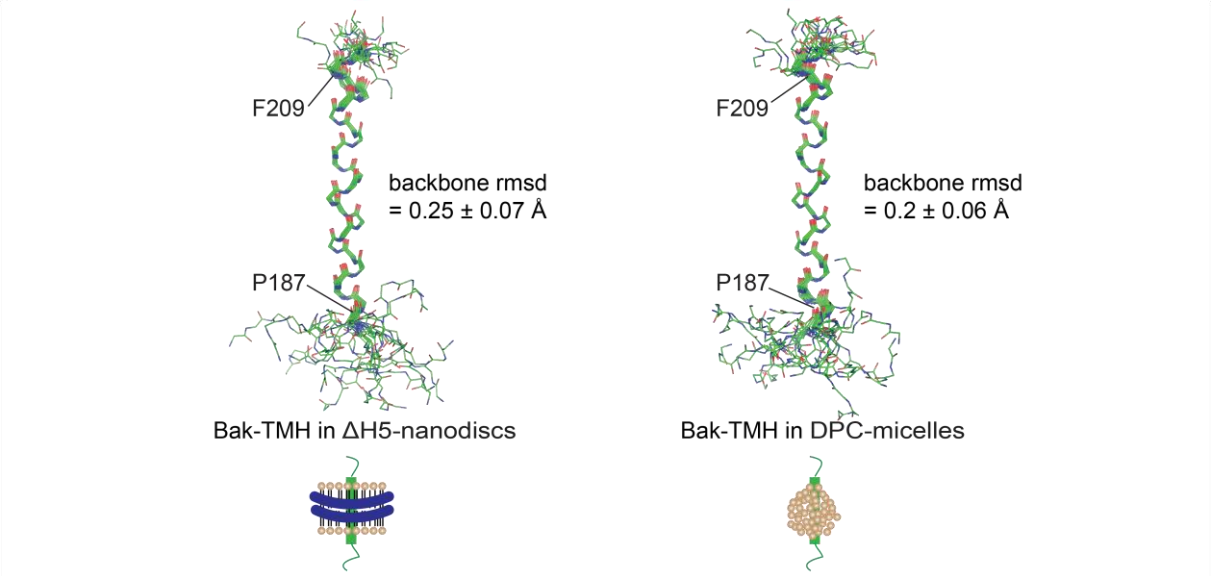

Figure 2.11: NMR-structures of the Bak-TMH. On the left, the Bak-TMH is show in ΔH5 nanodiscs. On the right, the Bak-TMHis depicted in DPC-micelles. In both cases, an overlay of the 20 lowest energy structures is displayed. The backbone root-mean square distance (rmsd) is indicated for the ordered region (P187-F209).

Despite the high sequence identity shared with the BclxL-TMH **(Fig. 2.4)**, the Bak-TMH forms a longer helical stretch. As the membrane thickness is limited, this most likely results in a more tilted orientation within the membrane. Taken together with the higher hydrophobicity, this suggests a stronger membrane anchorage due to a stronger interaction with the hydrophobic membrane.

A table with the structural statistics of the 20 lowest energy structures and the data accession codes can be found in the appendix.

2.1.1.4 Sortase A-mediated ligation of full-length Bak

In an attempt to work with the full-length Bak protein, a calcium dependent Sortase A pentamutant was used to ligate the soluble domain and the TMH in ΔH5-nanodiscs **(Fig. 2.12)** [181]. In analogy to the protocol published for the Sortase A-mediated ligation of BclxL[177], the Sortase-motif (LPXTG) was introduced before the His_6-tag at the C-terminus of the soluble domain (BakΔTM-Sor).

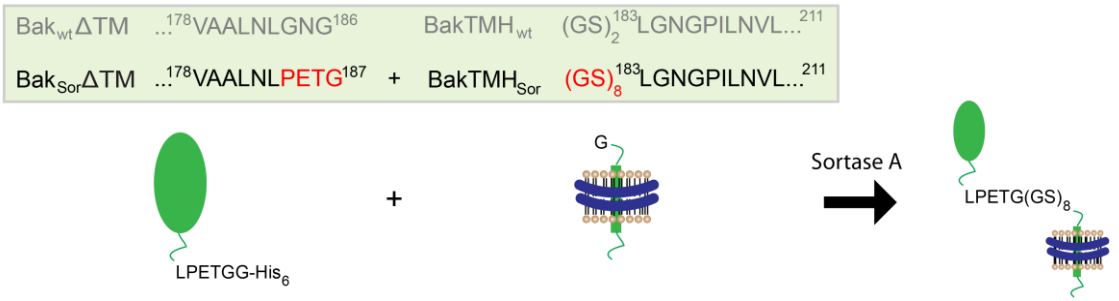

Figure 2.12: Overview over the constructs used for Sortase A-mediated ligation of Bak. The wild-type (wt) construct sequences are shown in grey for comparison.

However, ligation probed more difficult for this Bcl-2 protein with very low yields. In order to rule out systematic errors, BakΔTM-Sor was simultaneously ligated to the Bak- and BclxL-TMH **(Fig. 2.13,**

left). The SDS-PAGE gel showed a ligated Bak-BclxL product forming with the BclxL-TMH after 90 and 120 minutes, while no product formed with the Bak-TMH. In both cases, a band for the side product of BakΔTM ligated to the MSP (Bak-MSP) emerged as regular MSPΔH5 was used instead of the version lacking an N-terminal glycine (MSPΔH5-ΔnG). This explains the low yield also for the BclxL-TMH. The assembly was optimized by using MSPΔH5-ΔnG for the nanodisc assembly and extending the N-terminal linker of the Bak-TMH to match the length in the BclxL-TMH construct, thus, making it more accessible for the Sortase A ligation. This resulted in the formation of a small amount of Bak-full-length (Bak-FL), while no Bak-MSP side product was formed anymore. However, the achieved yield was too low for subsequent analysis, and far from yields necessary for NMR. As working with the full-length structure was not essential for this work, the Sortase A-mediated ligation was not further pursued due to the encountered issues.

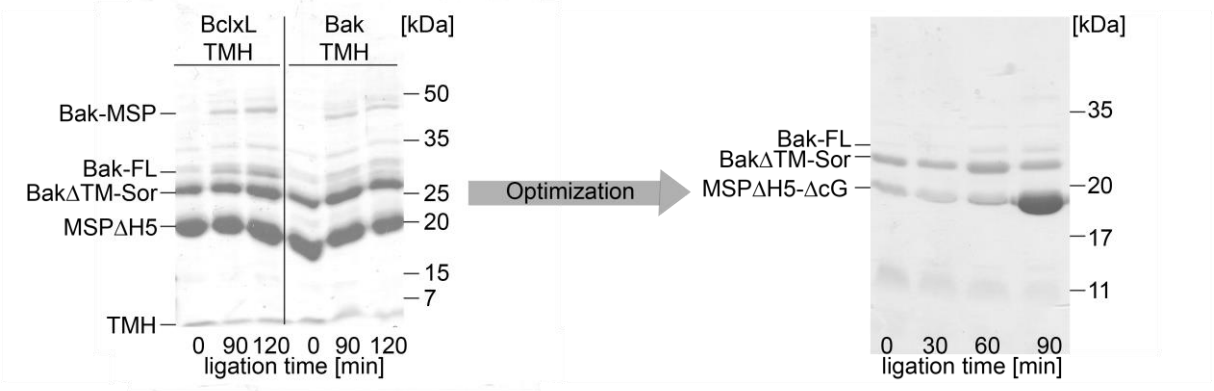

Figure 2.13: Sortase A-mediated ligation of Bak. SDS-gels of samples taken at the indicated time points during Sortase A-mediated ligation. On the right, BakΔTM-Sor was coupled to the BclxL- or Bak-TMH as indicated. As MSPΔH5 with a terminal glycine was used, an undesired side product formed between BakΔTM-Sor and MSPΔH5 (Bak-MSP). Bak-FL refers to the respective full-length product. On the left, MSPΔH5 lacking its N-terminal glycine (MSPΔH5-ΔnG) and a Bak-TMH construct with a longer N-terminal linker were used. The reactions were performed using 30 µM of the respective helix and a final ratio of TMH:BakΔTM-Sor:SorA of 1:3:0.16.

2.1.1.5 Simulation of the full-length structure in nanodiscs

In order to assess the orientation of Bak's soluble domain towards the membrane, HDX-MS measurements were conducted with and without the addition of [Ni^{2+}]-doped ΔH5-nanodiscs. Subtracting the data highlights the differences in accessibility **(Fig. 2.14)**. Positive values/red coloring indicate less accessibility in the membrane-bound state. Thus, helices 7 and 8 show the greatest effect, while the loop region between helices 4 and 5, oriented in the same direction, is also affected. This strongly suggests that this side of BakΔTM is oriented towards the membrane in the inactive state. The corresponding HDX-MS coverage maps, exemplary HDX graphs for single peptides and heat maps of the raw data can be found in the appendix.

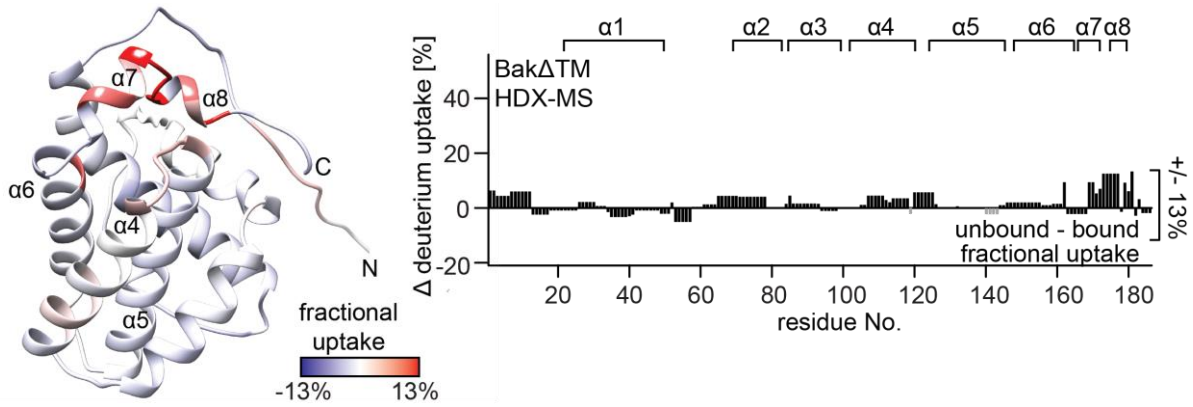

Figure 2.14: HDX-MS derived effects of membrane-binding on BakΔTM. The HDX values after 120 min of BakΔTM bound to ΔH5 nanodiscs are subtracted from the values with soluble BakΔTM and color-coded on the BakΔTM structure (left) or plotted against the amino acid sequence (right). In the structure, higher fractional uptake in the unbound state is colored in red, while less uptake is colored in blue. The α-helical secondary structure is indicated above the plot. HDX-MS measurements were performed by Florian Rührnößl (AG Buchner, TUM).

The structures of both the Bak-TMH in ΔH5-nanodiscs and the soluble domain were computationally ligated and embedded into a DMPC:DMPG membrane for a subsequent molecular dynamics (MD) simulation of 200 ms duration. The resulting full-length structure reveals a tilted transmembrane helix, which is expected due to the membrane thickness. The soluble domain is oriented towards the membrane with helices 7 and 8 and the loop region between helices 4 and 5. This correlates well with the HDX-MS results shown above. In **Fig. 2.15** the MD-simulated structure is visualized in a native mitochondrial environment.

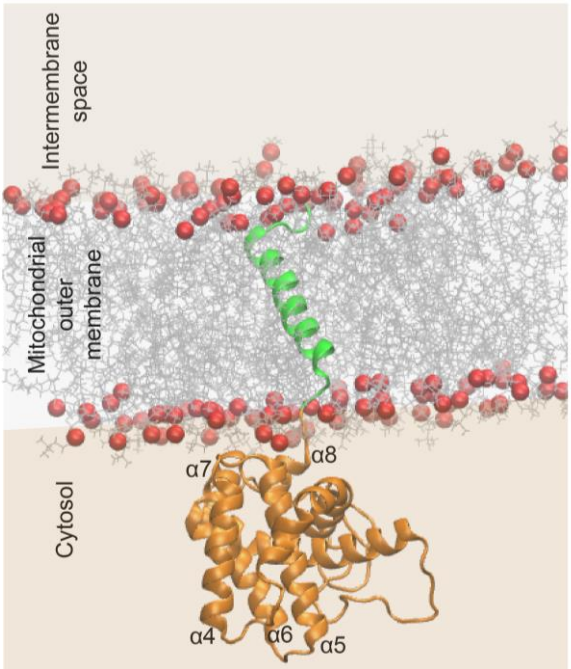

Figure 2.15: MD-based full-length structure of Bak. All structural information from NMR and HDX-MS was combined in this structural model of Bak in a DMPC:DMPG membrane. The MD-simulation was performed by Dr. Franz Hagn.

Not depicted in this MD visualization is the flexibility between the TMH and the extramembranous domain enabled by the short linker between the two domains. Thus, to visualize the relative motions between the TMH and the soluble domain, the distance between the centers of mass (COMs) of both domains were analyzed for all frames of the 200 ns simulation. The quite large fluctuations (~10 Å) in the calculated distances, which were obtained **(Fig. 2.16**), support the notion that both domains are quite flexible in their relative orientation.

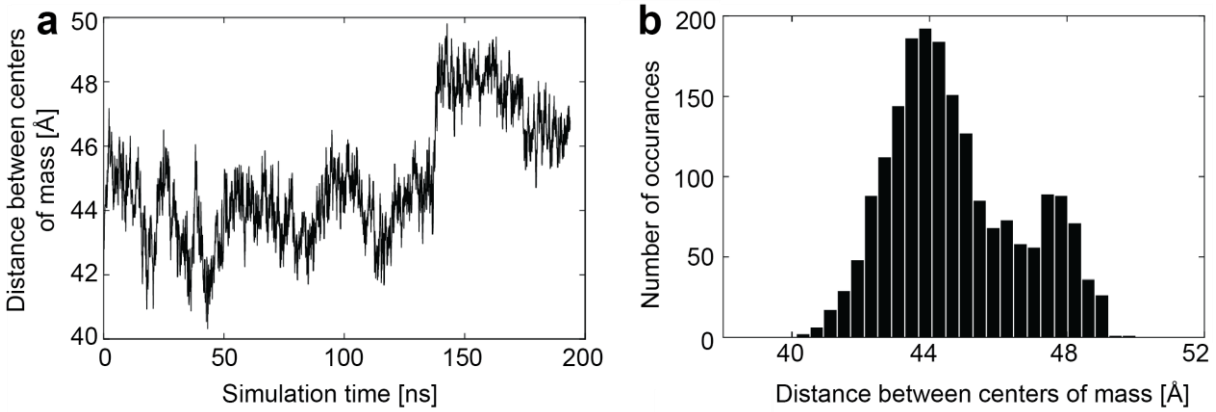

Figure 2.16: Analysis of the molecular dynamics simulation of full-length Bak anchored at a lipid bilayer membrane. (a) Distance between the centers of mass of the Bak TMH (residues 190 to 209) and the soluble domain (residues 26 to 184) plotted against the simulation time. (b) Histogram plot of the observed distances in (a) shows a broad distribution indicative of extensive relative motions between the two structural elements. This analysis was performed by Dr. Franz Hagn.

2.1.2 Comparative studies on BakΔTM and BclxLΔTM

As the Bak-TMH showed no functional relevance other than anchoring the soluble domain to the membrane in the performed biophysical experiments, further efforts were directed towards the soluble domain. In this chapter pro-apoptotic BakΔTM is compared to anti-apoptotic BclxLΔTM to pinpoint structural features determining their functionality. Interestingly, pro- and anti-apoptotic Bcl-2 proteins share a high structural analogy despite their opposing functions[92,98] **(Fig. 2.17)**. While their helical bundles are structurally confined, the unstructured regions exhibit marked differences. Besides the longer linker connecting the soluble and transmembrane domain, BclxL also has an extensive linker between its helices α1 and α2 (G21-A84) which is much shorter in Bak (G51-S69). In contrast, Bak has a long unstructured N-terminus (M1-S23), which is much shorter in BclxL (M1-R6) and a longer helix α1.

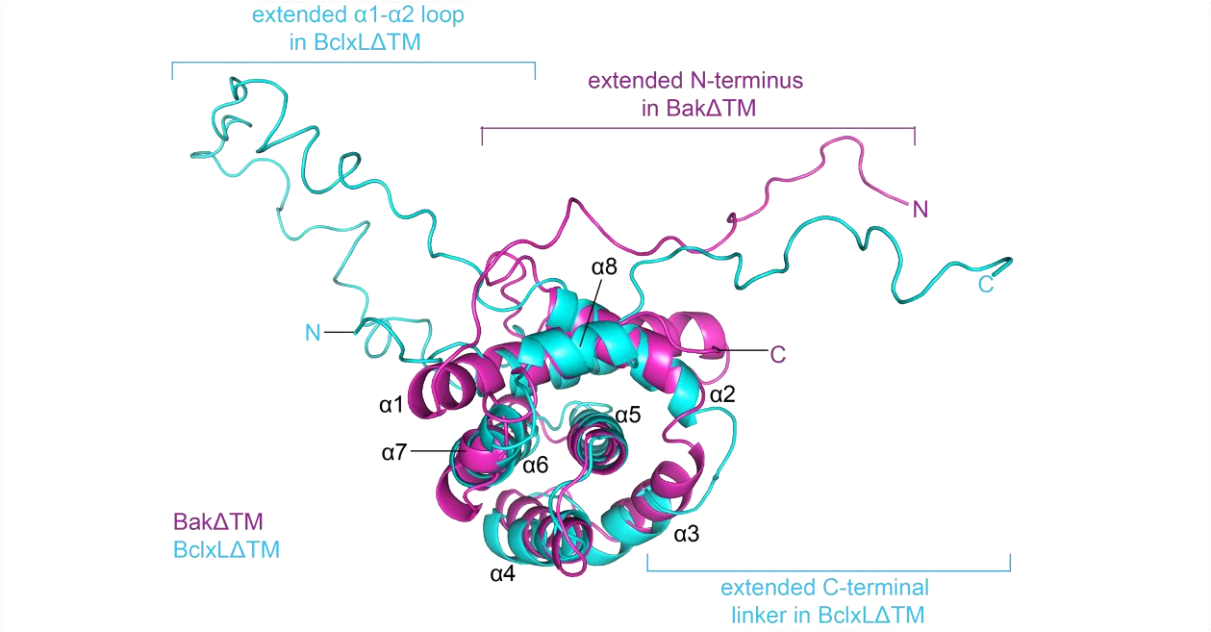

Figure 2.17: An overlay of the NMR-refined Bak soluble domain and the BclxL soluble domain (PDB: 1LXL[118]) confirm a high structural similarity for the helical bundles of the two functionally opposing Bcl-2 proteins. The most pronounced differences are found in the unstructured regions, as indicated.

First, the functionality of the utilized ΔTM-constructs was probed as a prerequisite for detecting functional differences. Then, different strategies were applied to determine structural and functional relationships. On the one hand, chimeric constructs were developed interchanging the distinct unstructured loop regions in Bak and BclxL and their activity was monitored. On the other hand, a variety of biophysical methods was applied to the inactive soluble domains in solution, which highlight striking differences for the two apoptotic players.

2.1.2.1 Expression and Purification

BakΔTM was produced similar to BclxLΔTM[177]. However, the expression was induced with only 0.2 mM IPTG and an MEAS-header was added to increase the expression yields[114]. Despite this optimization, a markedly reduced production level was yielded for Bak compared to BclxL, suggesting toxic effects of Bak even in *E. coli* cells. Furthermore, while BclxLΔTM forms a very pure monomer at high yields with some dimer only forming at high concentrations, BakΔTM results in far less protein showing an additional large peak at void volume consisting of impurities, as assessed by size exclusion chromatography **(Fig. 2.18)**. In order to characterize this behavior in more detail, a more quantitative investigation of the stability of both proteins in solution was conducted, after first confirming their functionality.

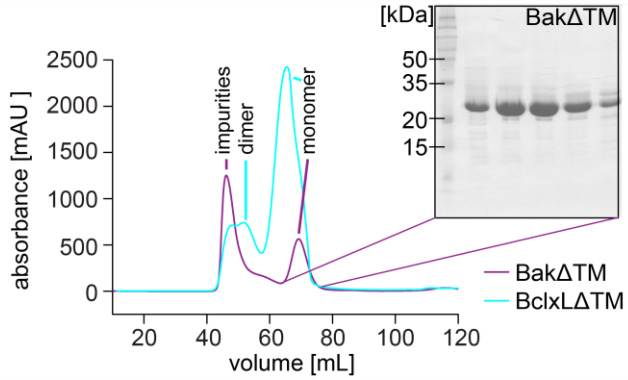

Figure 2.18: The SEC profiles, run on a preparative Superdex™ 75 column, display the production levels of BakΔTM (magenta) and BclxLΔTM (cyan). The SDS-PAGE shows the peak fractions of BakΔTM. The corresponding molecular weight is indicated on the left.

2.1.2.2 Functionality assay

The functionality of BakΔTM and BclxLΔTM was validated by applying an established liposome permeabilization assay in which the pore-forming activity of Bcl2 proteins is monitored based on fluorescence quenching[58,182]. The liposomes were formed using an OMM-like lipid mixture resembling the composition of the OMM quite closely[58], thus, ensuring conditions similar to those encountered by the Bcl-2 proteins in their native environment. A stable membrane binding was mimicked by replacing the missing transmembrane helix by Ni^{2+}-caged lipids in the liposomes, which direct Bak- and BclxLΔTM to the membrane surface via their C-terminal His_6-tags. This setup leads to a native-like attachment, which was also described in an earlier study[183]. In line with this work, BakΔTM showed no pore forming activity when Ni-lipids were omitted, even if the activator cBid was added **(Fig. 2.19)**. In contrast, when BakΔTM was C-terminally bound to the membrane via Ni-lipids, BakΔTM selectively permeabilized the liposomes when activated by cBid. High amounts of Ni-lipids led to BakΔTM autoactivation, indicating that a high local density of Bak at the membrane surface facilitates its oligomerization that is required for pore formation.

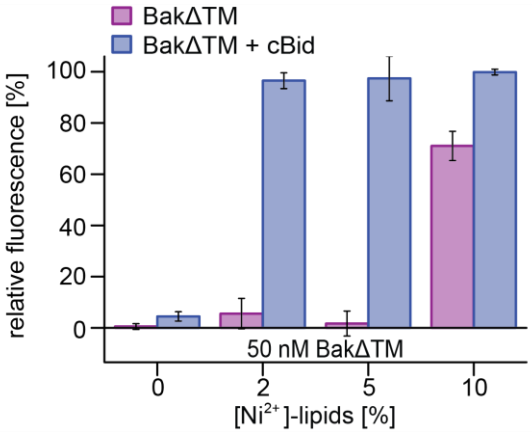

Figure 2.19: Liposome permeabilization assay – influence of Ni^{2+}-caged lipids on BakΔTM activity. Liposomes were formed with OMM-like lipids and subjected to 50 nM BakΔTM +/- 20 nM cBid. The data is averaged for the time frame of 9000-10000 s and the standard deviation calculated from three measurements, respectively.

In order to resemble the native situation, where Bak is not autoactive under normal cellular conditions, the presence of 2% (w/w) Ni-lipids was found to be optimal and was used in further assays unless indicated otherwise. In this setup, BakΔTM showed the expected activation profile, where pore formation was activated by cBid and inhibited by BclxLΔTM **(Fig. 2.20a)**. Addition of the BH3-only activator cBid in concentrations higher than BclxLΔTM reestablished pore-formation **(Fig. 2.20b)**. This implies that BclxLΔTM binds directly to BakΔTM and inhibits its pore-forming activity, in line with the displacement model of Bcl2 proteins[85]. When an activator like cBid is present, the activator mainly binds to BclxL, for which it has a higher affinity[120,184], thereby hindering the interaction between the pro- and anti-apoptotic players. Once the concentration of activator exceeds the concentration of BclxL, BakΔTM is released from its complex with BclxL and is activated by the excess of this activator.

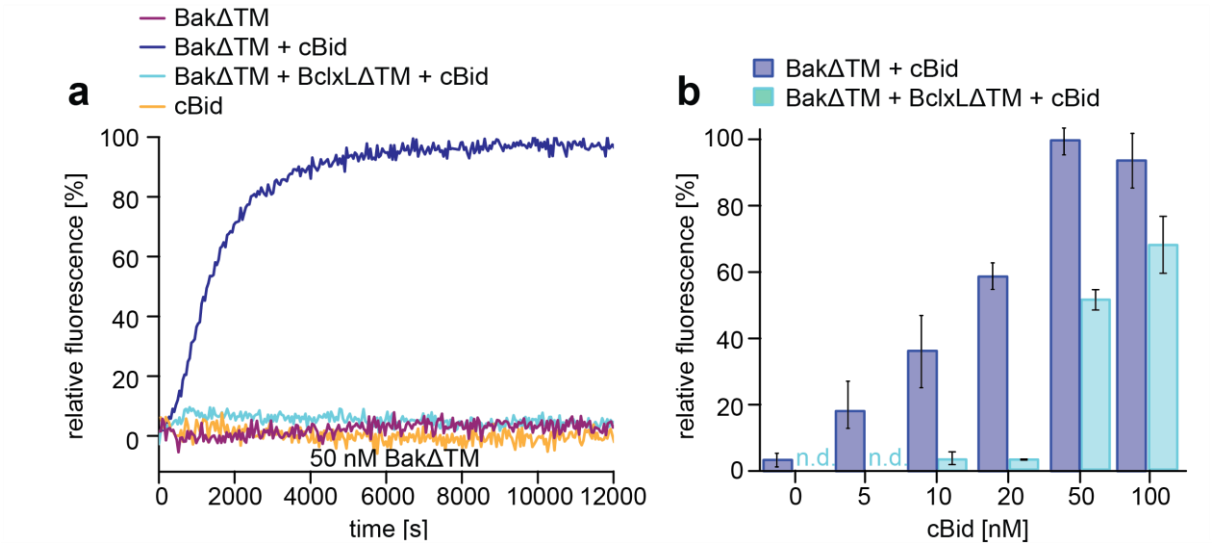

Figure 2.20: Liposome permeabilization assay – functionality at low BakΔTM concentrations. (a) Pore formation of 50 nM BakΔTM (magenta) is activated by 20 nM cBid (blue). 20 nM cBid alone (orange) shows no liposome permeabilization. Addition of 25 nM BclxLΔTM (cyan) inhibits pore-formation. (b) Increasing amounts of cBid are titrated to 50 nM BakΔTM in the absence (blue) and presence (cyan) of 25 nM BclxLΔTM. The data is averaged for the time frame of 9000-10000 s and the standard deviation calculated from three measurements, respectively.

Interestingly, as already seen in the Ni-lipid titration, when BakΔTM was added at higher concentrations, it formed pores autonomously **(Fig. 2.21)**. This behavior may be a relevant feature also in the cell[185] but turned out to be important for subsequent structural studies which require high protein concentrations.

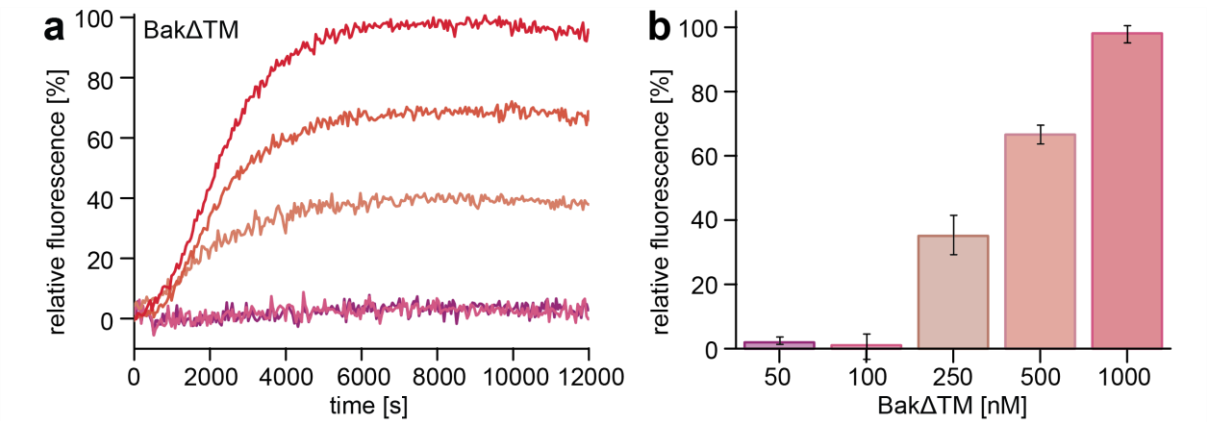

Figure 2.21: Liposome permeabilization assay – BakΔTM becomes autoactive at increasing concentrations. (a) The averaged kinetics for increasing BakΔTM concentrations color coded as indicated in (b). (b) The bar diagrams represent data from the kinetic experiments shown in (a) averaged between 9000 -10000 s. The standard deviation was calculated from three measurements.

To obtain further insights on the impact of lipids on Bak pore formation in this setup, the OMM-like lipid mixture was compared to an *E. coli* polar lipid extract. The *E. coli* extract contains slightly more cardiolipin, a lipid widely discussed to be important for Bcl-2 pore formation[186–188], and has a higher overall content of negatively charged lipids. When comparing the concentration dependence of BakΔTM pore formation in both lipid systems, the *E. coli* lipid extract slightly favored autoactivation, perhaps due to the higher content in negative charges and the membrane curvature induced by cardiolipin **(Fig. 2.22)**.

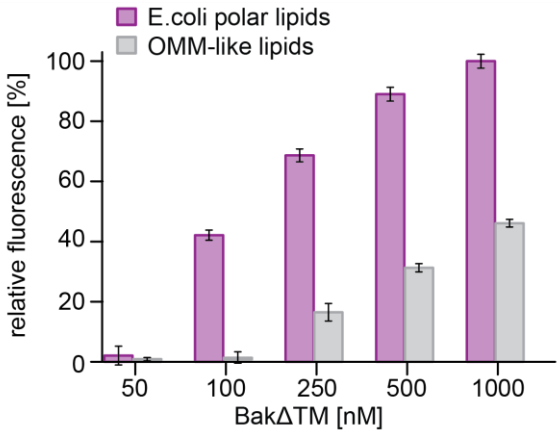

Figure 2.22: Liposome permeabilization assay – influence of the indicated lipid compositions on BakΔTM autoactivity. The data is averaged for the time frame of 9000-10000 s and the standard deviation calculated from three measurements, respectively.

At high protein concentrations, the addition of an activator BH3-only protein, such as cBid, further accelerated the pore forming kinetics **(Fig. 2.23)**. As shown for the time point of 420 s, BakΔTM alone reached 50% of its final signal amplitude. Adding increasing amounts of cBid raised the signal amplitude from 50% to 75% at this time point. This suggests that BakΔTM is sufficient to form pores even without the addition of an activator. However, an activator still can increase the pore forming rates. The Puma-BH3 peptide is even more potent at activating BakΔTM. This corresponds to the dissociation constants

reported in the literature[122], which is lower for Bak and Puma (260 nM[189]) than for Bak and cBid (800 nM[120]). In contrast, the anti-apoptotic protein BclxLΔTM inhibits Bak pore-formation, when an activator is present or absent.

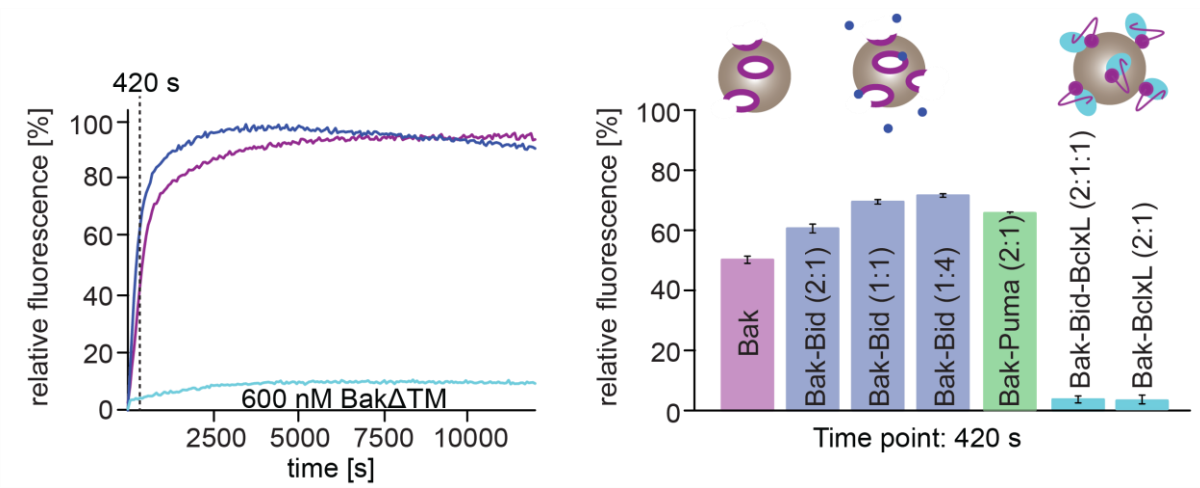

Figure 2.23: Liposome permeabilization assay – high BakΔTM concentrations. 600 nM BakΔTM is highly active with (blue) and without (magenta) the activator cBid. Adding BclxL inhibits pore formation (cyan). Left: The relative fluorescence is monitored for 12000 s. The blue curve refers to Bak-cBid (2:1). The cyan curve depicts Bak-cBid-BclxL (2:1:1). Right: The state of pore opening is shown for BakΔTM alone or with different ratios of cBid, Puma and BclxLΔTM at the time point 420 s. At the top, a cartoon visualization shows Bak in red, cBid as blue spheres and BclxL in cyan.

However, when BclxLΔTM is added without a His_6-tag, thus, is not C-terminally directed to the membrane, the functionality is strongly decreased **(Fig. 2.24)**. This is in line with **Fig. 2.19**, showing that also Bak is inactive when not C-terminally directed to the membrane[183] and underlines the importance of a membrane anchorage achieved by the TMH in the full-length protein.

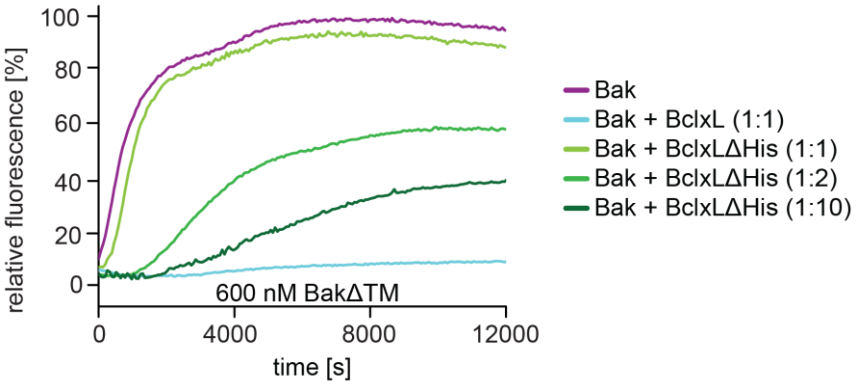

Figure 2.24: Liposome permeabilization assay – titration of BclxLΔTMΔHis_6 to BakΔTM. This underlines the importance of the C-terminal membrane anchorage also for the functionality of BclxL. Not even 10x excess of BclxLΔTMΔHis_6 can restore the Bak inhibition which is achieved with 1x BclxLΔTM.

Taken together, these data allow the conclusion that the utilized protein samples show the expected functional properties and thus, are suitable for a more detailed investigation of the associated structural transformations.

2.1.2.3 Functional relevance of the extended linkers in BclxL

In order to assess the functional relevance for the extended linkers in BclxL, two mutated constructs were studied. On the one hand, BclxLΔTM was used without its loop between helices α1 and α2 (BclxLΔTMΔL12). This construct has been widely applied for structural studies on BclxL and it has been shown, not to reduce the anti-apoptotic activity. As expected, BclxLΔTMΔL12 showed the same anti-apoptotic behavior as BclxLΔTM in the pore-forming assay **(Fig. 2.25)**.

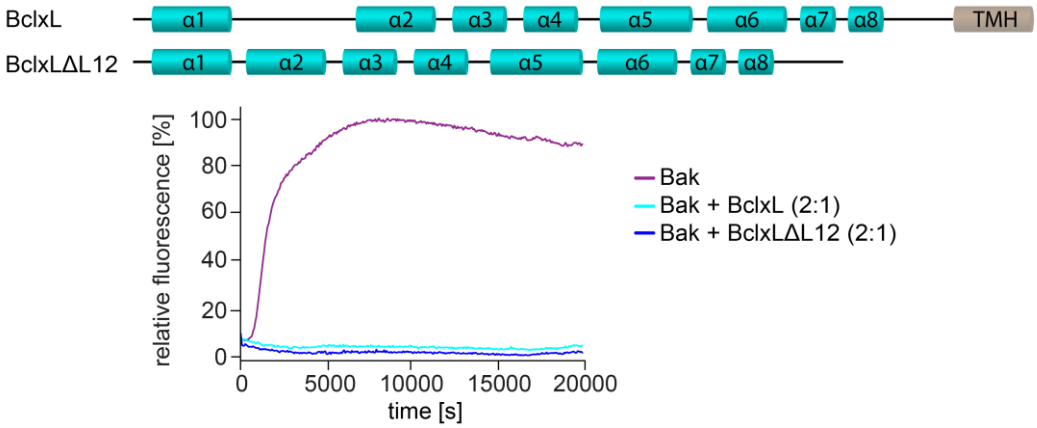

Figure 2.25: Liposome permeabilization assay – with BclxLΔTMΔL12. 600 nM Bak (magenta) is equally inhibited by 300 nM BclxLΔTM (cyan) and the mutant BclxLΔTMΔL12 (blue). The secondary structure elements of BclxL and the mutant BclxLΔTMΔL12 lacking the linker between helices α1 and α 2 are visualized at the top.

On the other hand, the linker connecting helices α8 and α9 in BclxL was cloned into Bak (BakΔTM-xL-link). This construct showed a reduced autoactivity **(Fig. 2.26)**. The maxima of the averaged data from three independent measurements in triplicates were normalized by setting the maximum of BakΔTM to 100 %. BakΔTM-xL-link very reproducibly showed an autonomous pore-forming capability of 93.8 % (± 0,0055 %). Thus, varying the linker connecting the TMH and the soluble domain has influence on the functionality. However, most likely this variation does not modulate the functional domain, but simply changes the distance between the soluble domain and the membrane surface. Therefore, Bak which must interact with the membrane surface for its activation has a shorter linker. When the extended linker in BclxL is introduced into Bak, it is slightly less prone to interact with the membrane, leading to a reduced autonomous pore-formation.

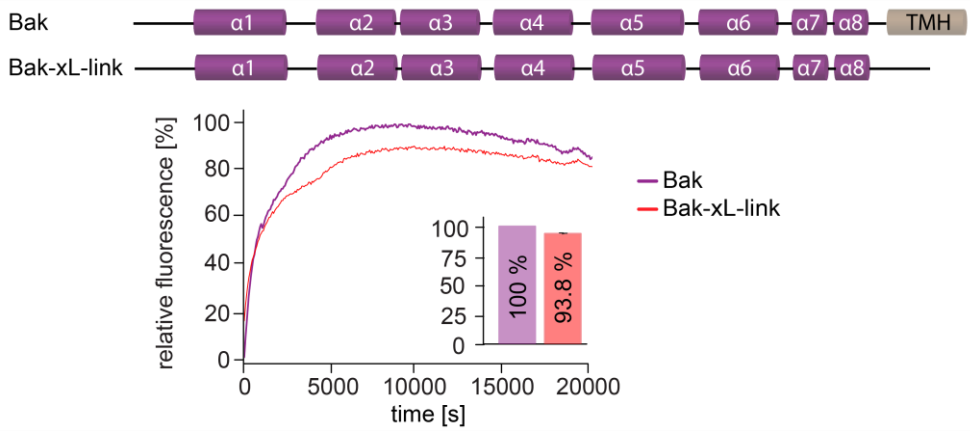

Figure 2.26: Liposome permeabilization assay – with BakΔTM-xL-link. 600 nM BakΔTM (magenta) and BakΔTM-xL-link (red) are both autoactive on liposomes. However, BakΔTM-xL-link reaches only 93.8% ± 0,0055 % of the maximal pore formation achieved by BakΔTM, as depicted in the inset. The pore-forming efficiency was calculated using the averaged data from three separate measurements in triplicates, respectively.

2.1.2.4 Biophysical characterization of the soluble domains

Different biophysical methods were applied to the soluble domains of Bak and BclxL to detect alterations in their stability facilitating the conformational change taking place in Bak upon activation. In agreement with previous reports, BclxLΔTM has a thermal stability of approximately 78 °C[190]. Both the far-UV-circular dichroism (CD) and the differential scanning calorimetry (DSC) measurements consistently show a single unfolding transition at 78.1 °C **(Fig. 2.27)**. In contrast, BakΔTM shows a fundamentally different behavior in these experiments. Monitored by far-UV-CD, a gradual decrease in secondary structure with 50% of the secondary structure remaining at ~ 90 °C was detected which finally melted in a distinct transition at 97.3 °C. The DSC measurement confirmed the high melting point of BakΔTM. Additionally, an earlier heat-absorbing event at 76.4 °C was identified. This event does not seem to be linked to changes in the secondary structure. As Bak oligomers have been reported to assemble already at 43 °C[191], this could represent the dissociation event of the oligomer.

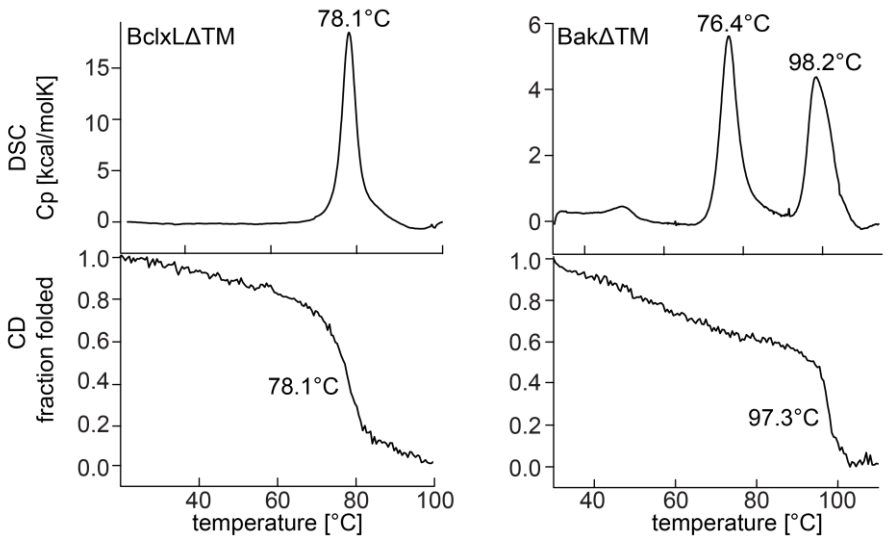

Figure 2.27: Melting temperatures of BclxLΔTM (left) and BakΔTM (right). On the top, the heat absorbing events were detected by DSC. Below, the melting temperature was measured using far-UV CD spectroscopy.

Subsequent dynamic light scattering (DLS) measurements confirm that BakΔTM forms larger assemblies when subjected to moderate heat (43°C), while BclxLΔTM consistently stays in a monomeric state **(Fig. 2.28)**. Both proteins have a hydrodynamic diameter of 5.6 nm at 25 °C. This parameter is unaltered for BclxLΔTM after prolonged incubation at 43 °C. However, for BakΔTM, a gradual increase in diameter up to 30 nm is detected, presumably representing an oligomeric state.

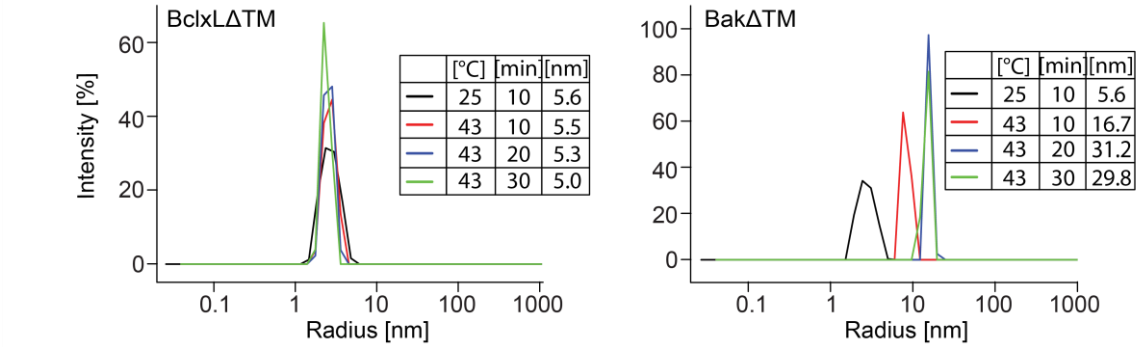

Figure 2.28: DLS measurements. BclxLΔTM (left) and BakΔTM (right) were subjected to varying temperatures and incubation times, as indicated in the insets respectively. The tables on the right state the hydrodynamic diameter in [nm], which is calculated from the measured hydrodynamic radii.

The very high melting point detected for Bak is unusual, but has also been reported for the other pro-apoptotic Bcl2 family member Bax.[182,192] In addition, this very high thermal stability is in agreement with NMR peak intensity patterns observed in a 2D-[^{1}H,^{15}N]-HSQC experiment with deuterated *versus* protonated BakΔTM **(Fig. 2.29a-b)**. Upon deuteration, several HSQC resonance signals in the protein core are absent, indicating that these residues are protected from the solvent. As indicated in **Fig. 2.29c**, both, the center of helix 5, located in the protein core, and the periphery of helices 1, 2, 6 and 8, which are oriented toward helix 5, are affected. This suggests a very stable protein core that does not permit hydrogen back-exchange. On the contrary, for BclxLΔTM both protonated and deuterated HSQC spectra proved nearly identical **(Fig. 2.29a-b)**.

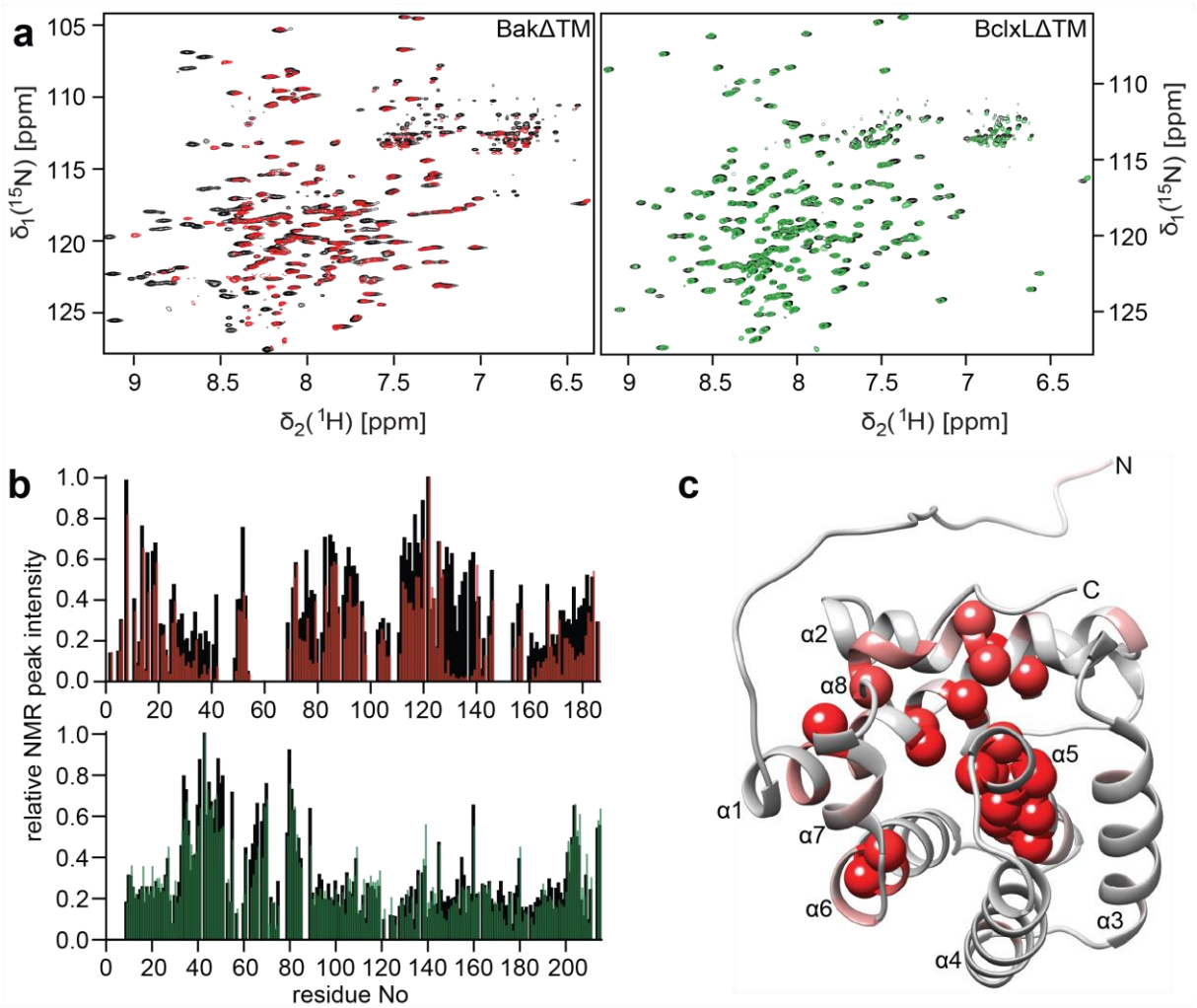

Figure 2.29: Deuteration effect on BakΔTM and BclxLΔTM. (a) 2D-[^{15}N, ^{1}H]-HSQC spectra of deuterated BakΔTM (red) and BclxLΔTM (green) are overlayed with the spectra of the respective protonated samples (black). (b) The peak intensities of the spectra shown in (a) are plotted against the sequence. (c) The NMR peak height ratio of the deuterated *vs.* protonated BakΔTM spectra was used to identify inaccessible amino acids, shown as red spheres on BakΔTM.

As Puma is known to inhibit the anti-apoptotic effect of BclxL and support the activation of pro-apoptotic Bcl-2 proteins[189,193], the Puma-BH3 peptide was added to both BclxLΔTM and BakΔTM, respectively, and the changes in stability were monitored by far-UV-CD spectroscopy **(Fig. 2.30)**. While the Puma-BH3 peptide stabilized BclxLΔTM, increasing the melting temperature by ~7 °C, it had no significant effect on the stabilization of BakΔTM in solution. These effects correlate well with the corresponding protein functions, as BclxL is stabilized in its inactive conformation by Puma, while the transient low-affinity binding to Bak is assumed to activate the protein in a hit-and-run manner and only in the presence of a membrane.

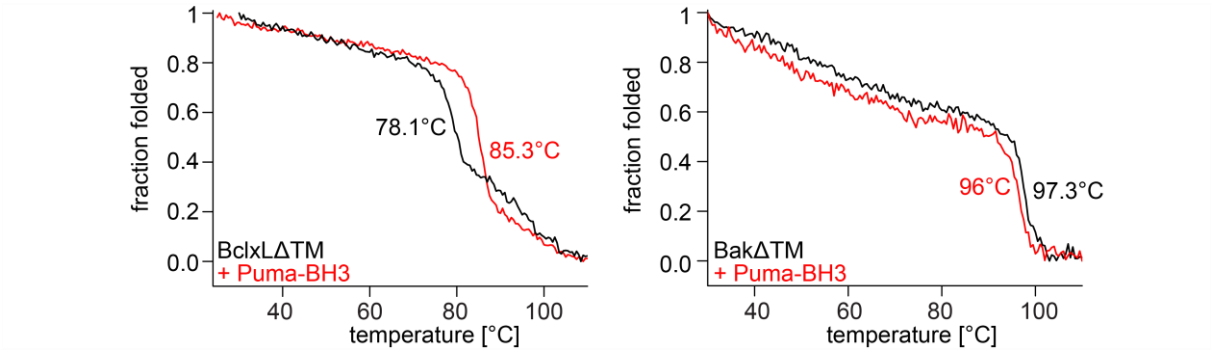

Figure 2.30: Far-UV CD-detected thermal unfolding of the soluble domains of BclxL (left) and Bak (right) in the presence (red) and absence (black) of the activator Puma-BH3 peptide.

Chemical unfolding experiments were conducted, in order to gain more detailed information on the molecular basis of the differences in oligomeric assembly of both Bcl2 proteins. Unfolding of the secondary structure was detected by far-UV CD spectroscopy, while unfolding of the tertiary structure was monitored with the fluorescence signal emitted by the tryptophan residues in the protein. While secondary and tertiary structure of BclxLΔTM unfold at a GuHCl concentration of 4.2 M in a one step process, BakΔTM shows a distinctly different behavior **(Fig. 2.31)**. In this case, an equilibrium folding intermediate is populated, leading to a two-step unfolding process. The midpoint of the first unfolding transition from the native to the intermediate state was detected by CD and fluorescence spectroscopy at 2.7 M GuHCl concentration, while the final unfolding step occurs at 4.6 M GuHCl.

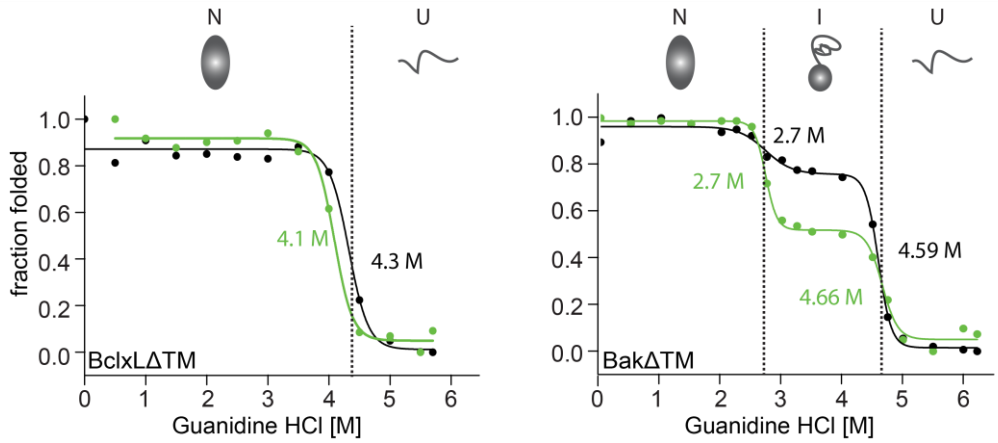

Fig. 2.31: GuHCl-induced chemical unfolding of BclxLΔTM (left) and BakΔTM (right). The unfolding of the secondary structure, monitored by far-UV-CD at 222 nm, is shown in black, while changes in the tertiary structure, monitored by Trp-fluorescence, are depicted in green. The native (N), intermediate (I) and unfolded (U) states are indicated at the top

The different populated states become apparent when monitoring the tryptophan fluorescence **(Fig. 2.32)**. Tryptophans that are buried inside the hydrophobic protein core typically show a blue-shifted emission maximum between 309 nm and 335 nm, the latter occurs in a partially buried hydrophobic environment. For a solvent exposed tryptophan, the emission maximum shifts to 355 nm.[194] For BclxLΔTM the fluorescence spectra clearly indicate that the tryptophan side chains are present in two distinct environments. The folded state shows a broad distribution of the six tryptophans at wavelengths of 320-340 nm in both GuHCl and urea, correlating well with their localization in the structure. While

W57 in the α1-α2 loop is solvent exposed, the other five tryptophans are partially buried. At 4 M GuHCl the maximum slightly red shifts, indicating the beginning of protein unfolding. Finally, a more defined maximum at 355 nm is reached, demonstrating the unfolded species with completely solvent exposed tryptophans. In urea no red shift is detected, indicating that BclxL is stable up to the 7.8M urea measured. In contrast BakΔTM shows three distinct environments during unfolding. In the folded state, the tryptophans are mainly buried in the hydrophobic core in both GuHCl and urea, giving rise to an emission maximum at 315 nm. At 2.5 M GuHCl concentration, the environment starts to change towards a partially buried conformation with a maximum at 335 nm. At 4.5 M GuHCl concentration, the protein begins to unfold completely and the tryptophan fluorescence undergoes a red shift to an emission maximum at 355 nm. Also, BakΔTM is more stable in urea, not reaching the unfolded state. However, the partially buried intermediate state with a fluorescence maximum of 335 nm is formed at 7 M urea.

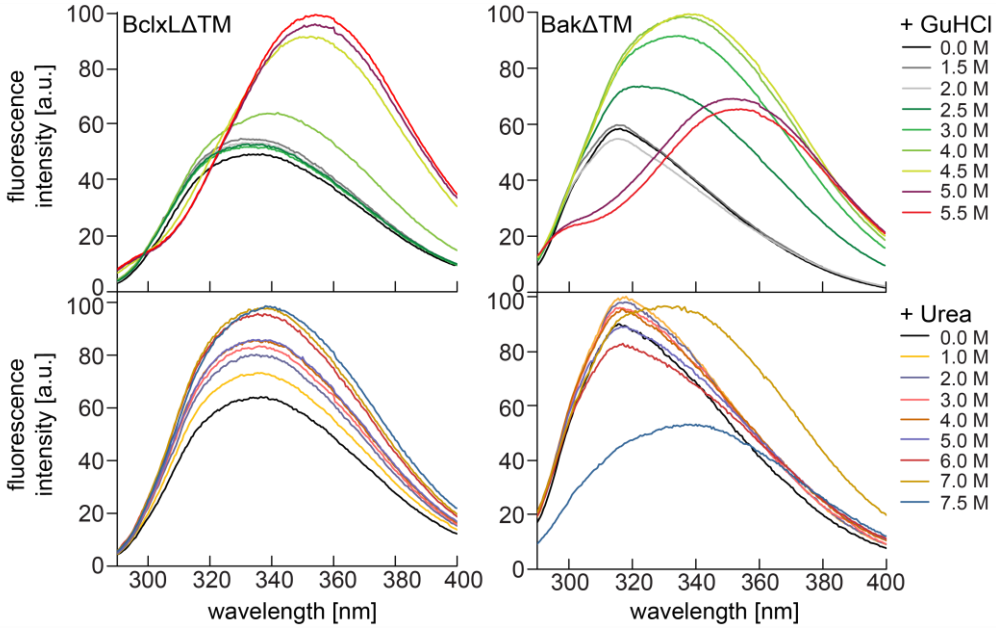

Fig. 2.32: Tryptophan fluorescence emission spectra of BclxLΔTM (left) and BakΔTM (right) at different GuHCl concentrations (top) and urea concentrations (bottom) upon excitation at 280 nm.

The detected red shift in tryptophan fluorescence indicates that these hydrophobic side chains get more solvent exposed in the intermediate state. This was confirmed by the binding of SYPRO Orange, a fluorescent dye which only fluoresces strongly after binding to regions with a low dielectric constant such as exposed hydrophobic protein patches that are confined to a protein core in the folded state[195]. An increased exposure of hydrophobic protein parts during the first step of GuHCl-induced unfolding could be detected **(Fig. 2.33)**. Together with the persistence of an almost native-like secondary structure content **(Fig. 2.31)**, this state can therefore be defined as a molten globule[196].

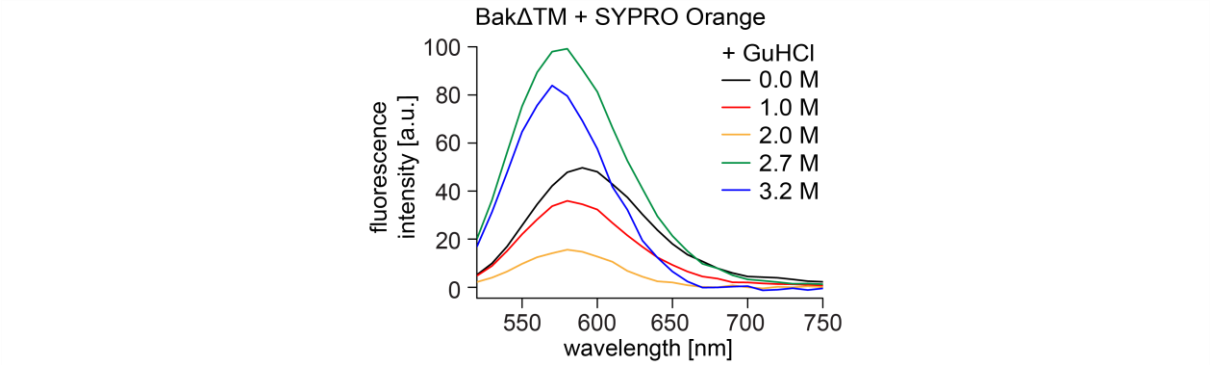

Fig. 2.33: Fluorescence emission spectra of SYPRO Orange binding to BakΔTM at varying GuHCl concentrations.

The loss in tertiary structure in the intermediate is also evident from 2D-TROSY-NMR experiments where a low chemical shift dispersion was detected **(Fig. 2.34a)**. While the peaks are shifted with 1.5 M GuHCl, the overall spectrum still represents a folded protein. At 2.5 M GuHCl, thus approximately the point of inflection in the transition to the intermediate state, BakΔTM has lost its tertiary structure. Monitoring the peak shifts up to a GuHCl concentration of 1.5 M reveals that three regions, namely helix 1, 3 and the BH3 domain are most strongly affected by the chaotropic agent **(Fig. 2.34b)**. A systematic chemical shift perturbation is observed due to the increased amount of salt.

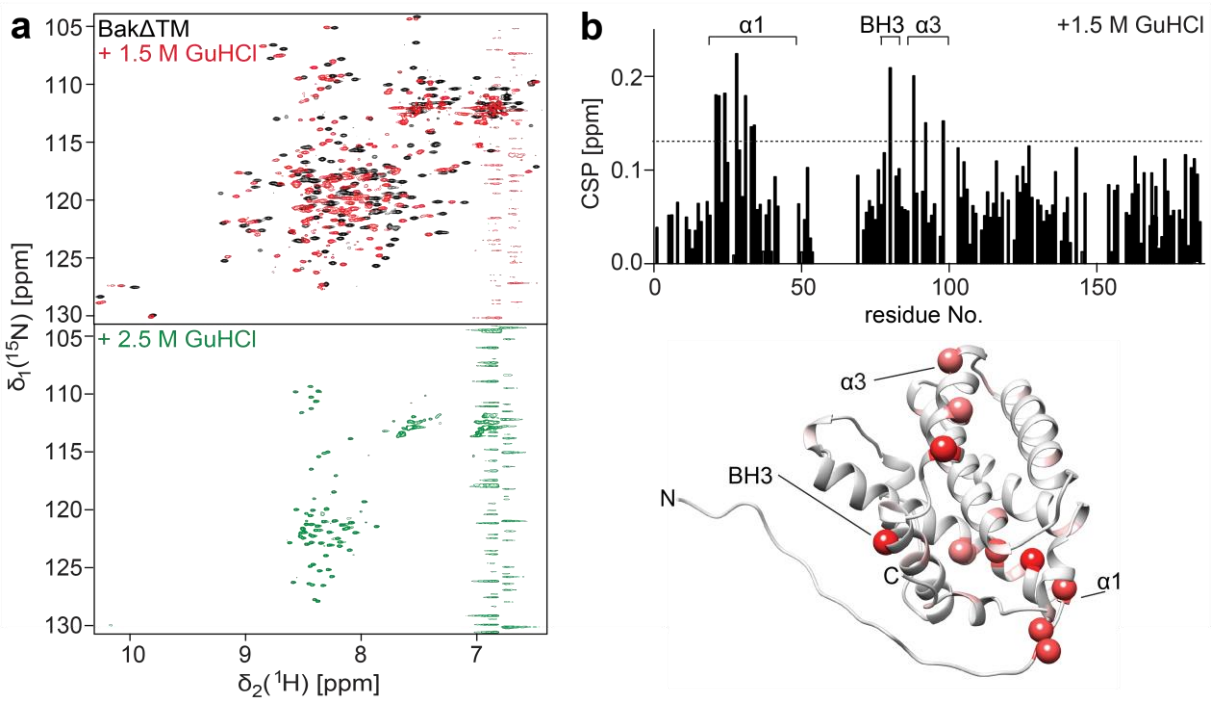

Fig. 2.34: NMR measurements of BakΔTM with GuHCl. (a) 2D-[^{1}H, ^{15}N]-HSQC spectra of BakΔTM in the absence (black) and presence of 1.5 M GuHCl (red) and 2.5 M GuHCl (green). (b) Chemical shift perturbation (CSP) plot of the 2D-[^{1}H-^{15}N] HSQC spectra of BakΔTM ± 1.5 M GuHCl. The most significant shifts (above the dotted line) are presented as red spheres on the structure.

In contast, for BclxLΔTM the native-like folded state is still detectable up to 4.5 M GuHCl, suggesting that a 2-state equilibrium between the folded and unfolded state is formed as the protein unfolds **(Fig.**

2.35a). Also, when comparing the chemical shifts in the presence and absence of 1.5 M GuHCl, the overall effect is smaller for BclxLΔTM and not specific for helix 1 **(Fig. 2.35b)**.

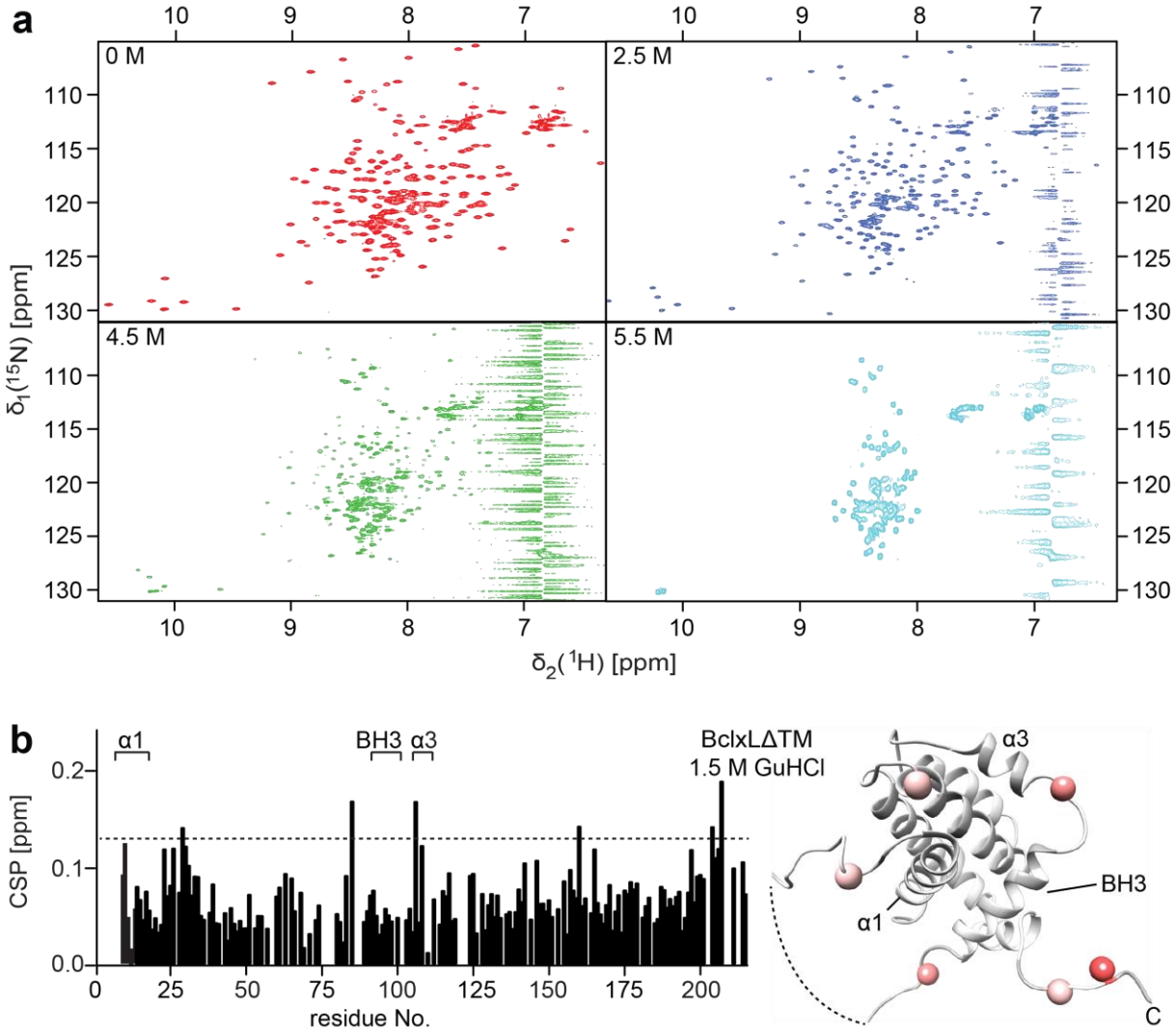

Fig. 2.35: NMR measurements of BclxLΔTM with GuHCl. (a) 2D-[^{1}H, ^{15}N]-HSQC spectra of BclxLΔTM with increasing concentrations of GuHCl. (b) Chemical shift perturbation (CSP) plot of the 2D-[^{1}H, ^{15}N] HSQC spectra of BclxLΔTM ± 1.5 M GuHCl. The most significant shifts (above the dotted line) are presented as red spheres on the structure.

These data highlight striking differences between pro-and anti-apoptotic Bcl2 proteins in their protein folding profiles and suggest a functional role of the reported Bak folding intermediate in the pore-forming process at the membrane. The following chapter elucidates whether a Bak folding intermediate can also be present in a lipid bilayer environment and has any relevance for the activation process taking place during Bak-mediated apoptosis.

2.1.3 Characterization of Bak's active state

Bak's pore forming state, thus the active conformation has been a key research goal for decades. Previous studies presented crystal structures of possible dimeric intermediate states of both, Bak and Bax, during pore formation induced by BH3-only proteins in detergents, showing that the core (α-helices 2-5) and latch domain (α-helices 6-8) separate during the activation process [119,127]. While the N-terminal residues up to helix 2 are not visible in these structures, specific antibody binding assays could show that helix 1 becomes solvent exposed after activation [128,129]. This process was determined as a key step for the further conformational transition [130]. In addition, it has long been discussed that both Bak and Bax most likely form lipidic rather than proteinaceous pores [81,141,142]. A recent study could show that lipids are bound between dimeric Bak core domain interfaces [145]. While all these studies reveal essential aspects by studying different Bak constructs, a detailed structural picture of the conformational transitions of full-length Bak in a native lipid environment is still elusive. After the pore forming assay revealed autoactivation of BakΔTM bound to liposomes at the concentrations used for biophysical studies **(Fig. 2.21)**, this system was used to study the active state in a membrane like environment. In order to analyze the active state with NMR, a more homogenous and smaller system had to be developed. For this, a nanodisc system was established, which additionally enabled the selective study of both the active and inactive states in a lipid membrane environment.

2.1.3.1 Characterization of Bak's active state by CD spectroscopy

After Bak probed to spontaneously form pores at concentrations higher than 100 nM when bound to liposomes **(Fig. 2.22)**, this system was used to characterize the active state with CD spectroscopy. As differences were seen for the applied lipid mixtures (*E.coli* polar/OMM-like lipids), BakΔTM was studied in both. First, the secondary structure content of active and inactive BakΔTM was compared **(Fig. 2.36a+b)** by recording the far-UV CD spectra of BakΔTM with and without liposomes as well as with liposomes and an activator (cBid or the Puma-BH3 peptide). The determined content of α-helical secondary structure was comparable in all cases. However, the measured thermal stabilities of these samples showed that the stability of Bak is heavily decreased upon binding to a membrane surface and is not altered by the additional binding of a BH3 peptide, corroborating the notion that Bak is able to undergo activation even without the influence of activator BH3 proteins **(Fig. 2.36c+d)**. In *E. coli* lipids, bearing a higher content of negative charges, the melting temperature of the active pore state is decreased by ~10 °C, potentially reflecting its higher autoactivation potency. The melting temperatures for all conditions can be found in **Tab. 2.1**. A Puma-BH3 peptide was used instead of the cBid protein to minimize its contribution to the detected CD-signal, while monitoring its thermal unfolding in presence of an activator.

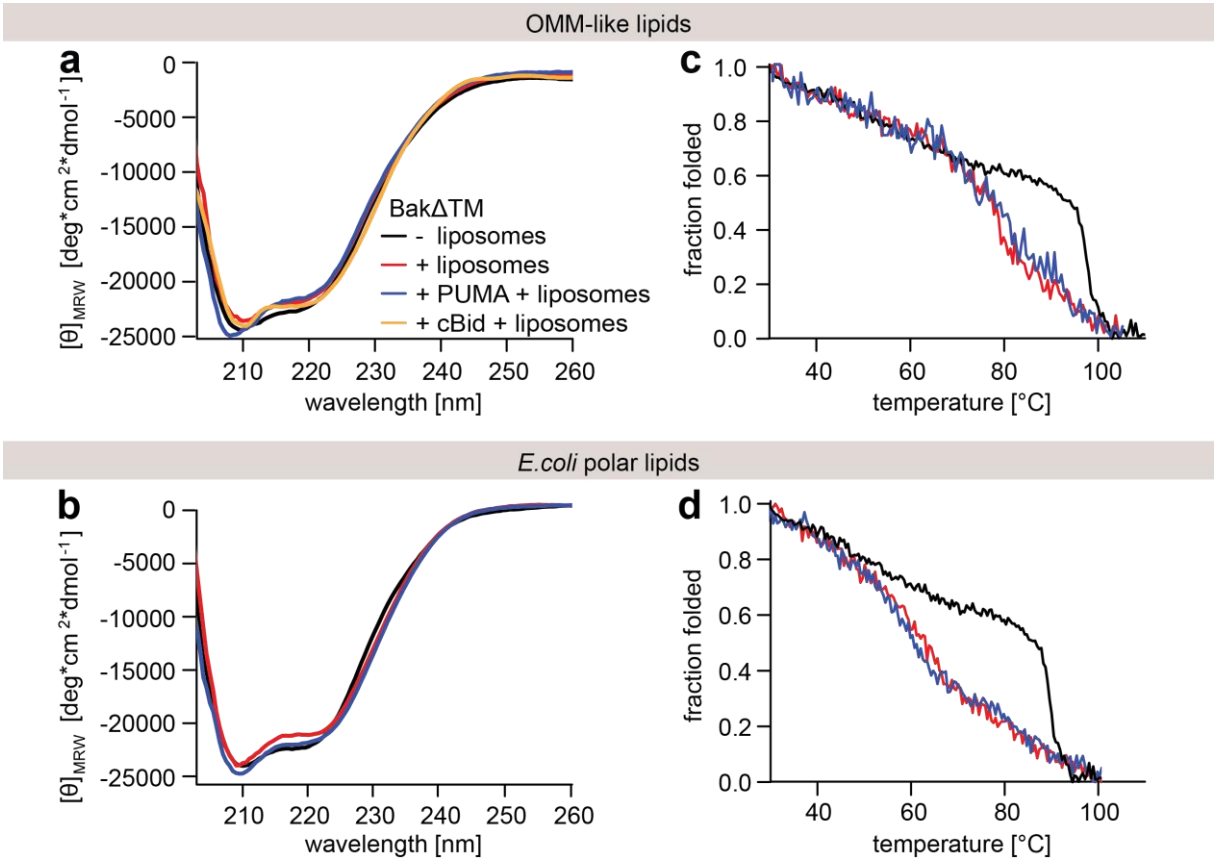

Figure 2.36: Far-UV-CD spectra of BakΔTM (black) with liposomes (red) and Puma-BH3 (blue) or cBid (orange) revealing a notable change in the secondary structure content.

Table 2.1: CD derived melting temperatures of BakΔTM.

BakΔTM	97.3 ± 1.0 °C
+ liposomes[a] (OMM-like lipids)	78.7 ± 0.8°C
+ liposomes[a] + Puma[b] (OMM-like lipids)	78.4 ± 0.7°C
+ liposomes[a] (*E. coli* polar lipid extract)	68.4 ± 0.4°C
+ liposomes[a] + Puma[b] (*E. coli* polar lipid extract)	69.2 ± 0.6°C

[a] Liposomes were formed with the stated lipids + 5% Ni^{2+}-caged lipids.
[b] The Puma-BH3 peptide was added in a 4-fold excess where indicated.
[c] The mean values and standard errors were derived from three independent experiments.

2.1.3.2 BakΔTM bound to nanodiscs

To establish a more defined and homogenous environment for subsequent NMR measurements BakΔTM was attached to lipid nanodiscs. As the active form was the primary conformation of interest, the nanodiscs were formed with *E. coli* polar lipids. Analogue to the liposomes, they were doped with lipids bearing Ni^{2+}-NTA-modified headgroups. To ensure that only bound BakΔTM was present in the nanodisc preparations, a SEC was run and only the fractions containing both the membrane scaffold

protein (MSP) and BakΔTM were pooled **(Fig. 2.37).** Due to the stable attachment of soluble Bak to the nanodisc surface, the nanodisc peak eluted earlier from the column, consistent with a larger hydrodynamic radius.

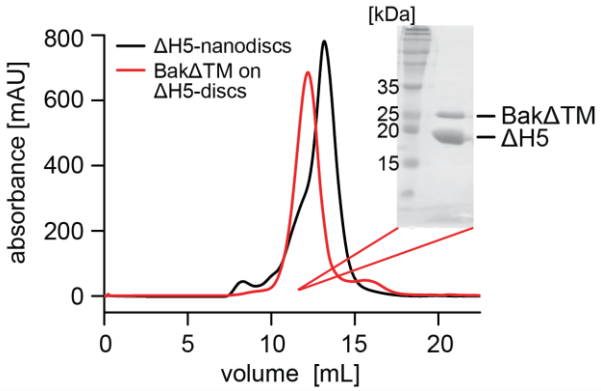

Figure 2.37: Size exclusion chromatogram of empty ΔH5-nanodiscs (black) and BakΔTM bound to ΔH5-nanodiscs via its C-terminal His-tag (red). The nanodiscs were equipped with 4 [Ni^{2+}]-caged lipids per disc in both cases. The SDS-gel shows the main peak fraction of the loaded nanodiscs. The relevant marker bands are indicated on the left.

The effect of this environment on BakΔTM stability was studied by CD-detected thermal melting experiments. While the MSP1D1ΔH5-Ni^{2+}-discs unfold at ~80 °C, an additional melting transition appears when BakΔTM is bound to nanodiscs **(Fig. 2.38).** This melting point at 68.4 °C, is comparable to the melting point of BakΔTM in liposomes, suggesting that BakΔTM converges to its active state also in nanodiscs **(Fig. 2.36d)**. In contrast, the very high melting point of inactive BakΔTM in solution could not be detected in nanodiscs (**Fig. 2.27**).

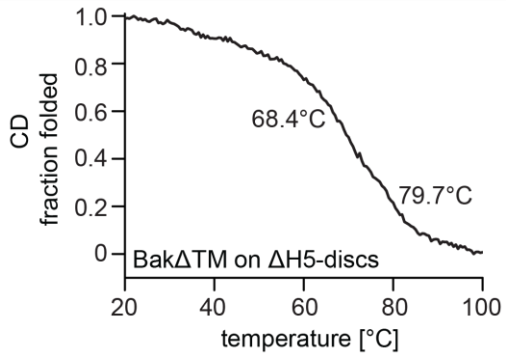

Fig. 2.38: Far-UV CD thermal melting curve of BakΔTM bound to ΔH5-nanodiscs. The detected melting points are indicated.

2.1.3.3 NMR studies on BakΔTM bound to nanodiscs

First a 2D-[^{1}H, ^{15}N]-TROSY spectrum of BakΔTM bound to MSP1D1ΔH5-Ni^{2+}-nanodiscs was recorded. A comparison with the spectrum of BakΔTM in solution identifies no large effects caused by the membrane surface **(Fig. 2.39)**. The spectra overlay completely, which suggests a very similar structure. However, additional peaks arise in the random coil region. This implies that a large part of the protein remains in the inactive state, but part of the protein changes its conformation upon binding to

the nanodisc surface. This contrasts with the CD melting point suggesting that Bak is present in the active state in ΔH5 nanodiscs. However, it must be kept in mind that heat has been found to induce Bak activation[191]. Therefore, it is likely that Bak stays mainly inactive when bound to ΔH5 nanodiscs at moderate temperatures but is activated when subjected to higher temperatures. After adding the activator Bid-BH3 peptide, the signals corresponding to the inactive state vanish from the NMR spectrum, while the additional peaks become more prominent, suggesting that these signals refer to the active state. This active state is characterized by a spectrum indicative of an unfolded protein with a reduced amount of signals. In contrast, in solution, when no membrane mimetic is present, addition of the activator Bid-BH3 peptide leads to CSP's but not an unfolding of the protein[103]. This suggests an important role for the membrane environment in the activation process.

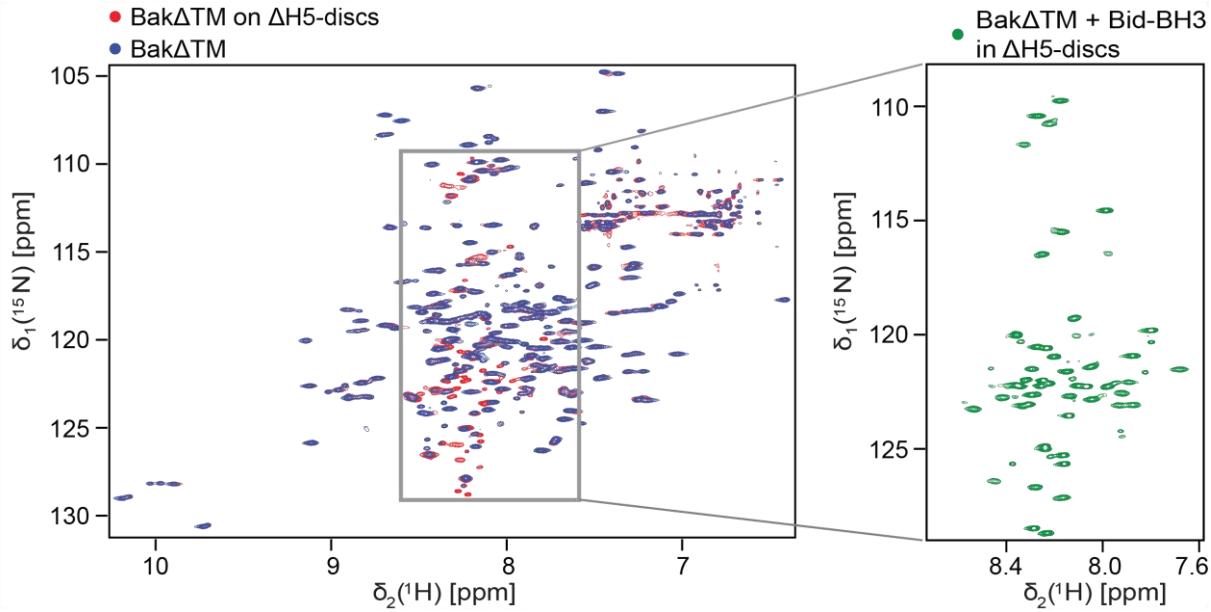

Figure 2.39: Left: Overlay of 2D-[^{1}H, ^{15}N]-TROSY spectra of BakΔTM (blue) and BakΔTM bound to ΔH5-nanodiscs (red). Right: 2D-[^{1}H, ^{15}N]-TROSY spectrum of BakΔTM bound to ΔH5-nanodiscs after adding the activator Bid-BH3 peptide in 8-fold excess. The shown spectral window was reduced to the minimal size needed to contain all signals (except the side chains).

Since Bak activation has to be accompanied by oligomerization to ultimately form a pore structure, cysteine-dependent crosslinking experiments were performed with Bak bound to nanodiscs with and without the addition of Bid-BH3. It could be shown that the inactive form is mainly monomeric, while dimers, trimers and even higher oligomeric species can be detected for the activated form **(Fig. 2.40)**. The faint dimeric band detectable for the inactive state most likely originates from the minor population of active Bak. Furthermore, the SEC analysis shows that BakΔTM forms larger species upon activation, presumably leading to a disruption of the nanodisc structure.

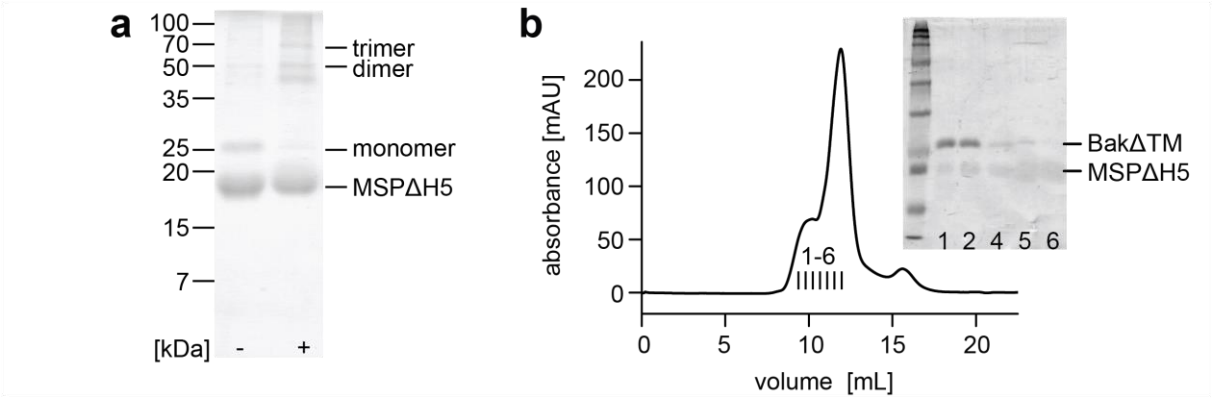

Figure 2.40: Cu/phen crosslinking of BakΔTM bound to ΔH5-nanodiscs ± Bid-BH3 peptide. (a) SDS-PAGE gel of BakΔTM bound to ΔH5-nanodiscs ± Bid-BH3 peptide after Cu/phen crosslinking. (b) Size exclusion chromatogram of BakΔTM bound to nanodiscs after activation by Bid-BH3. Inset: The SDS-PAGE gel shows that activated BakΔTM elutes before the main nanodisc peak. The MSP band is very faint due to increased destaining which is typical for MSP.

An NMR backbone resonance assignment was conducted to clarify which part of the protein unfolds and thus remains visible after activation **(Fig. 2.41)**. Only the N-terminal region up to amino acid Q66 was observed by NMR. This includes the unstructured N-terminal tail (M1-A22), the first helix (α1, S23-Q45) and the loop region connecting the first two helices (E46-S68). Both the low chemical shift perturbation and the sharp line shape of the NMR resonances suggest a highly flexible structural state that most likely is located outside the membrane. In contrast, the remaining parts of Bak are probably located in the membrane or engaged in a higher oligomeric state and therefore invisible due to line-broadening resulting from the slower tumbling time of the larger assemblies as well as possible sample inhomogeneities and intrinsic structural dynamics in the ms-µs time scale.

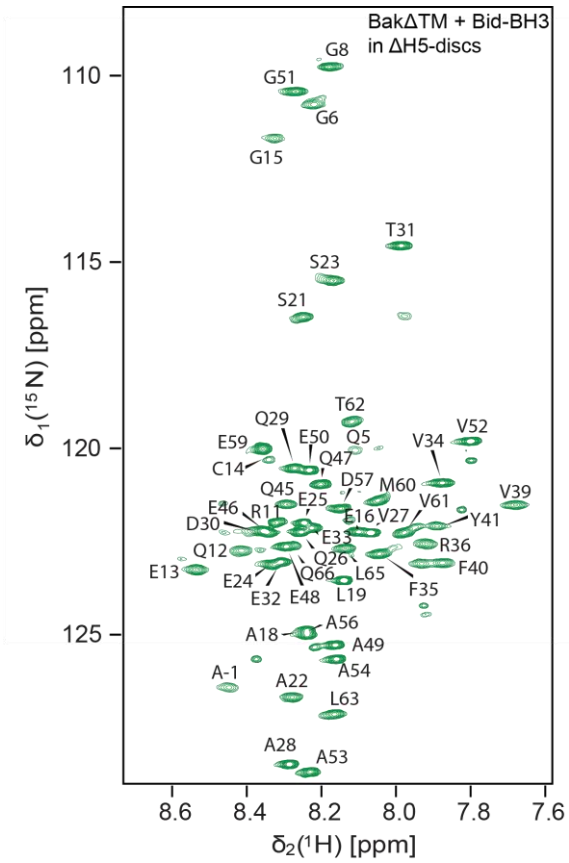

Figure 2.41: NMR backbone assignment of BakΔTM in ΔH5 nanodiscs after activation with 8-fold excess of Bid-BH3 peptide. A full list of assignments can be found in the appendix. The NMR experiments leading to this assignment were performed on a 160 µM sample at 950 MHz and 303 K.

In order to exclude any unspecific effect caused by the presence of lipid nanodiscs, the experiment was repeated using liposomes. As BakΔTM was shown to autonomously form pores without the necessity for further activation at high concentrations in liposomes **(Fig. 2.22)**, this setup was expected to result in the active state without the addition of an activator. The liposome system was optimized for solution-state NMR by reducing the liposome diameter to the smallest size achievable with the available techniques. This resulted in 30 nm liposomes, which proved to still endorse Bak pore-forming activity **(Fig. 2.42a)**. In line with the lipid composition used in nanodiscs, liposomes were formed using *E. coli* polar lipids with 10 % ($\frac{w}{w}$) [Ni^{2+}]-caged lipids. The 2D-[^{1}H, ^{15}N]-TROSY spectrum of BakΔTM bound to [Ni^{2+}]-caged-liposomes overlays well with the Bid-BH3 activated spectrum in ΔH5-nanodiscs, confirming that this conformation in nanodiscs is identical with the pore-forming state in liposomes **(Fig. 2.42b)**. All peaks visible in liposomes overlay with assigned peaks in the spectrum of BakΔTM activated by Bid-BH3 in nanodiscs. The bar diagram shows the backbone amide NMR resonance peak heights of Bid-BH3 activated BakΔTM, normalized by its most intense peak (V27) **(Fig. 2.42c)**. On the bottom, the visible peaks of BakΔTM in liposomes are marked by an orange line. As expected, the peaks with a high intensity in nanodiscs are also visible in liposomes, while peaks that already showed pronounced line-broadening in nanodiscs are not or only barely visible in liposomes. This confirms that the state of BakΔTM induced in ΔH5-nanodiscs upon activation corresponds to the pore-forming state in liposomes at least for the N-terminal region, as this is the only region detectable with NMR.

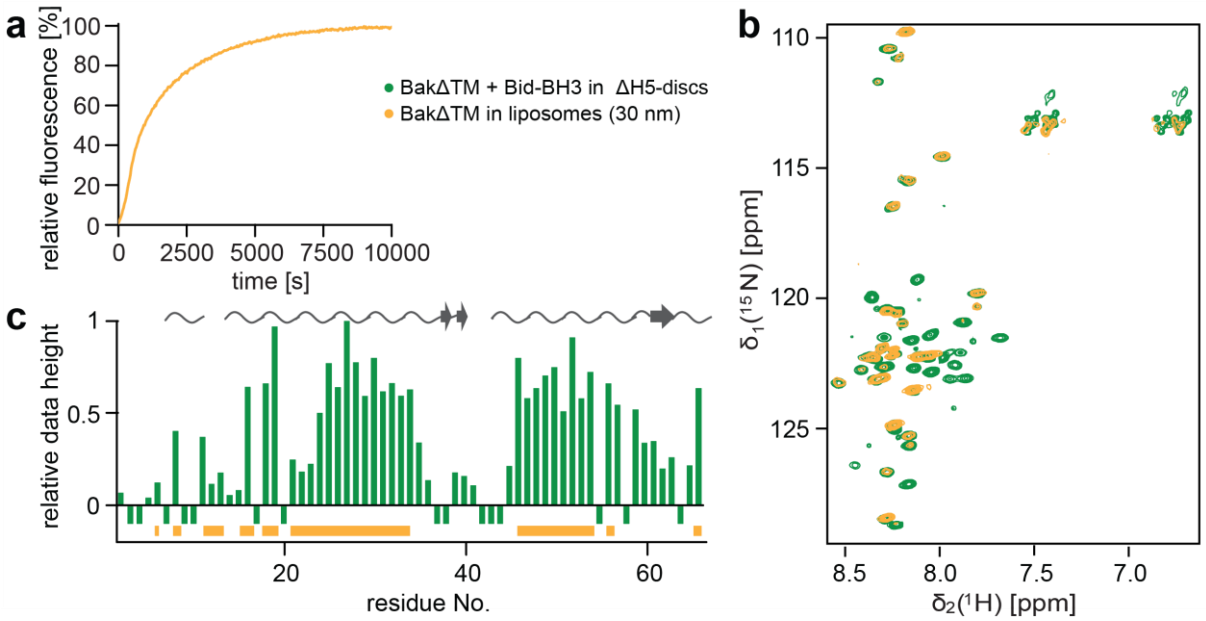

Figure 2.42: NMR studies on BakΔTM in liposomes. [Ni^{2+}]-caged liposomes with a diameter of 30 nm were used for the data acquisition. (a) Liposome permeabilization assay: 600 nM BakΔTM is autoactive also in liposomes with a diameter of 30 nm. (b) Overlay of 2D-[^{1}H, ^{15}N]-TROSY spectra of BakΔTM in ΔH5 nanodiscs activated by 8-fold excess of Bid-BH3 (green) and BakΔTM in 30 nm liposomes (orange). (c) Plot of the relative data heights of Bid-BH3 activated BakΔTM in nanodiscs. Peaks that are also visible in liposomes are indicated in orange at the bottom, while the chemical shift-derived secondary structure is indicated at the top.

In order to compare the dynamic nature in the ns-ps time scale of BakΔTM in its inactive conformation in solution and its active state embedded in a membrane, {^{1}H}-^{15}N-heteronuclear NOE (hetNOE) experiments were conducted **(Fig. 2.43)**. While high hetNOE values (~ 0.8) describe rigid structures, low or negative values refer to flexible parts of the protein. In coherence with the low chemical shift dispersion, the N-terminal region (aa 1-20) proves highly dynamic in both conformations. In the inactive state, BakΔTM has a compact fold and is therefore less dynamic in the examined time scale. Only the loop regions between helices α1 and α2 and helices α2 and α3 show reduced hetNOE values and thus are more flexible than the rigid main fold of the protein. In contrast, the active state probes highly dynamic for the amino acids visible in the spectrum. A less dynamic region is visible between E32 and E48, however. Together with the fact that this amino acid stretch consists of several positively charged residues, this suggests that this part of active BakΔTM is in contact with the membrane surface. Additionally, this is supported by the missing assignment of some amino acids in that area. Most likely they are not visible due to line-broadening effects originating from the association/dissociation dynamics at the membrane surface.

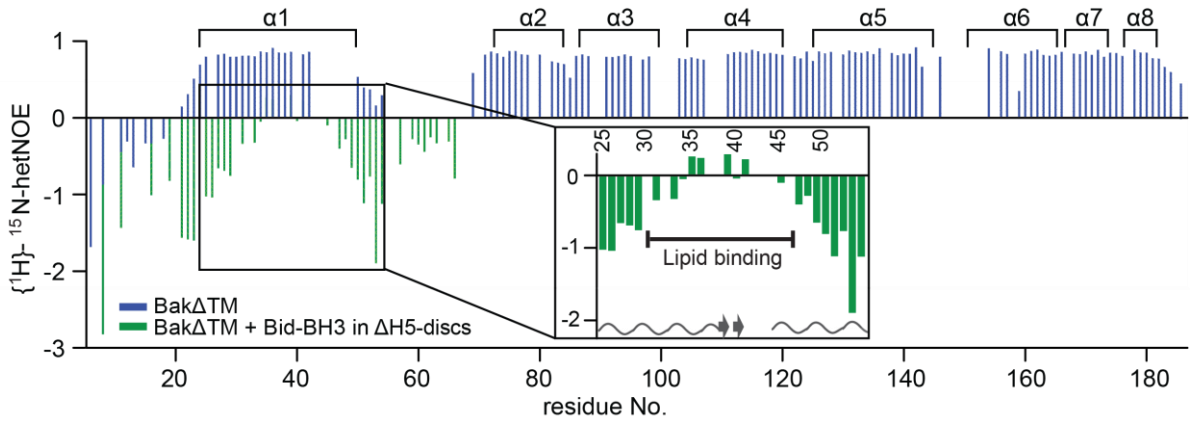

Figure 2.43: {^{1}H}-^{15}N-heteronuclear NOE data of BakΔTM in the inactive state in solution (blue) and the active state in ΔH5-nanodiscs after Bid-BH3 activation (green). At the top, the α-helical structural elements of the inactive state are indicated. For the active state, residues 25-54 are enlarged showing a less dynamic stretch between residues 30 and 46 – a potential lipid binding site. At the bottom of this inset, the chemical shift-derived secondary structure elements are displayed. Wavy lines represent random coil, while arrows refer to β-sheet secondary structure.

Taken together, the nanodisc system not only enables studying the active state with NMR due to its homologues sample properties but also permits selective analysis of both the active and the inactive state in a membrane environment. This permits an investigation of the interaction between Bak and its interaction partners using the complete soluble domains instead of peptides, as described for the Bak-BH3-peptide[93]. A detailed study of this interaction can be found in **chapter 2.1.4**.

2.1.3.4 HDX-MS studies on BakΔTM bound to nanodiscs

As the helices 2-8 of active membrane-inserted BakΔTM were not detectable using NMR, hydrogen-deuterium exchange mass spectrometry (HDX-MS) was applied to investigate the entire protein in its active conformation. This method is used to study the solvent accessibility of each residue by following the exchange rate of hydrogen to deuterium with mass spectrometry. The derived data provide information on protein structure and dynamics. In the inactive membrane-bound state, BakΔTM displays a tight protein core with very low amide proton exchange rates after 10 seconds for both the core part of helix 5 and the neighboring helices, in particular helices α1 and α4 **(Fig. 2.44)**. After 120 minutes, significantly more exchange can be detected for all the neighboring helices indicating that these become accessible with time. Helix 5, however, remains inaccessible, corroborating the absent amide exchange seen in the NMR measurements described above **(Fig. 2.29)**. In contrast, in the active state the protein core consisting of the helices 4-7 stays solvent inaccessible even after 120 min, while helix 1 displays rapid deuterium uptake. Similar to the inactive state, helices α2 and α3 become more accessible after 120 min. This supports the NMR-data showing a soluble unfolded N-terminus located in the cytosol, while the remaining protein is partially or fully embedded in the membrane.

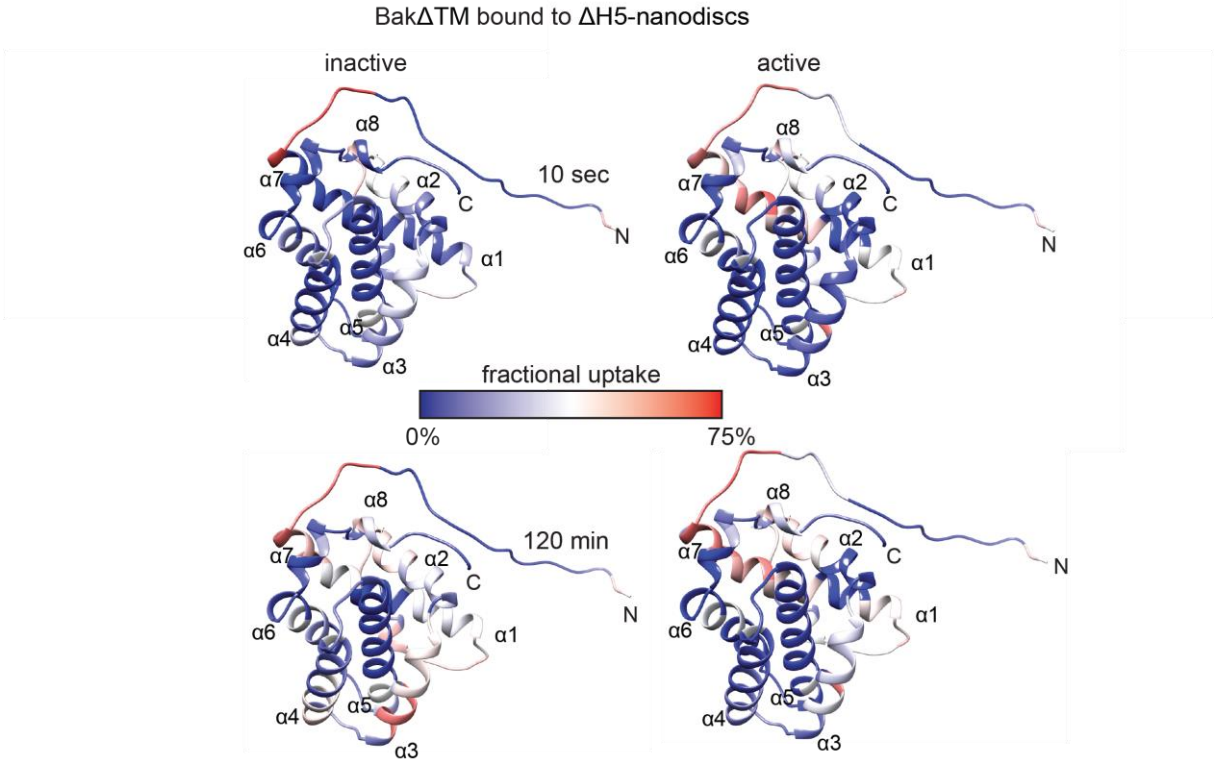

Figure 2.44: HDX-MS experiments of BakΔTM bound to ΔH5-nanodiscs in the inactive state and after Bid-BH3-induced activation. The HDX was plotted on the inactive BakΔTM structure and colored according to the measured exchange rates after 10 sec and 120 min as indicated. The blue coloration refers to low (less accessible) and the red coloration to high (more accessible) fractional uptakes of deuterium. HDX-MS measurements were performed by Florian Rührnößl (AG Buchner, TUM).

Comparing the two states after an exchange time of 10 s reveals that Bak activation enables 56 % more deuterium uptake for the core part of helix 1 **(Fig. 2.45)**. In contrast, the C-terminal end of helix 2, the sides of helices α3 and α4 oriented towards the solvent and the loop between helices α4 and α5 become less accessible indicating that these elements either integrate into the membrane or are shielded by protein-protein interactions within the pore. Most likely this is also the case for helices 5-7. Here, the comparison shows no difference, as these already were inaccessible in the inactive state.

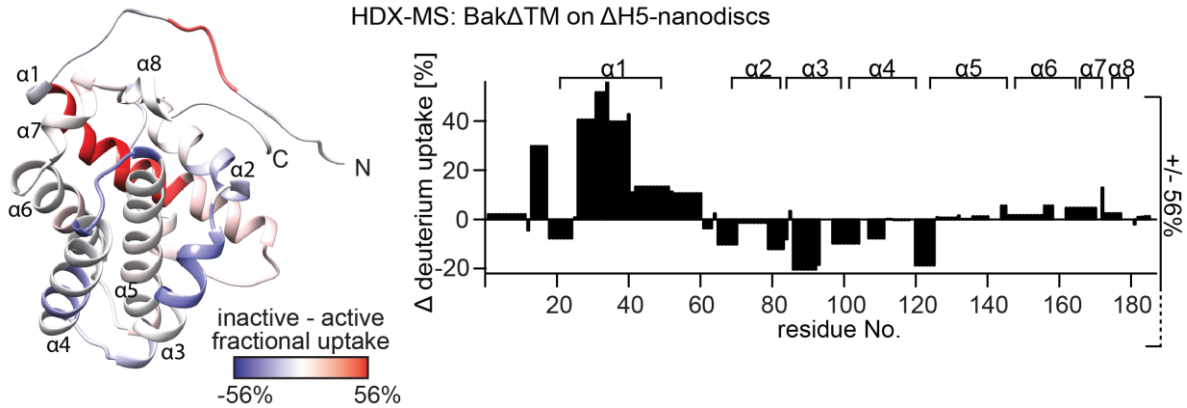

Figure 2.45: Comparison of the HDX-MS experiments of BakΔTM bound to ΔH5-nanodiscs in the inactive state and after Bid-BH3-induced activation. The HDX rates of the active state were subtracted from the inactive state using the data measured after 10 s, respectively. Left: The resulting values were color-coded on the BakΔTM structure. Red coloration refers to a higher fractional uptake after activation, while blue coloration indicates less

uptake. Right: The resulting values were plotted against the sequence with the secondary structure elements indicated at the top. HDX-MS measurements were performed by Florian Rührnößl (AG Buchner, TUM).

The corresponding HDX-MS coverage maps, exemplary HDX graphs for single peptides and heat maps of the raw data can be found in the appendix.

2.1.3.5 Mutagenesis of BakΔTM

After the unfolding studies using GuHCl suggested that the dissociation of helix 1 from the rest of the protein plays a key role in initiating Bak activation, this unfolding of helix 1was now also confirmed as part of the activation process by both NMR and HDX-MS methods. Therefore, it can be concluded that the dissociation and unfolding of helix 1 is the triggering point for the subsequent conformational changes necessary for activation. The GuHCl-induced unfolding studies show that this region is sensitive to salt **(Fig. 2.34)**, implying that electrostatic interactions could be involved in this process. The anti-apoptotic protein BclxLΔTM did not show this behavior **(Fig. 2.35)** even though it shares a similar overall fold with BakΔTM **(Fig. 2.17).** Therefore, the structures of BakΔTM and BclxLΔTM were compared, revealing differences in the charge distribution in proximity to helix 1. These findings suggest that a stabilization of helix 1 by adding counter charges to unbalanced charges and/or eliminating them could reduce the first step of activation and subsequent pore-formation. Based on these stabilizing factors, two variants were developed. Variant 1 (BakΔTM_1) stabilizes the interaction between helix 1 and the latch domain by substituting the uncoupled charge at R156 for Q **(Fig. 2.46)**. This stabilizes the hydrophobic patch found in this region in BclxL thereby enforcing a salt bridge between E32 and R36, similar to the one between E7 and D11 in the helix 1 of BclxL.

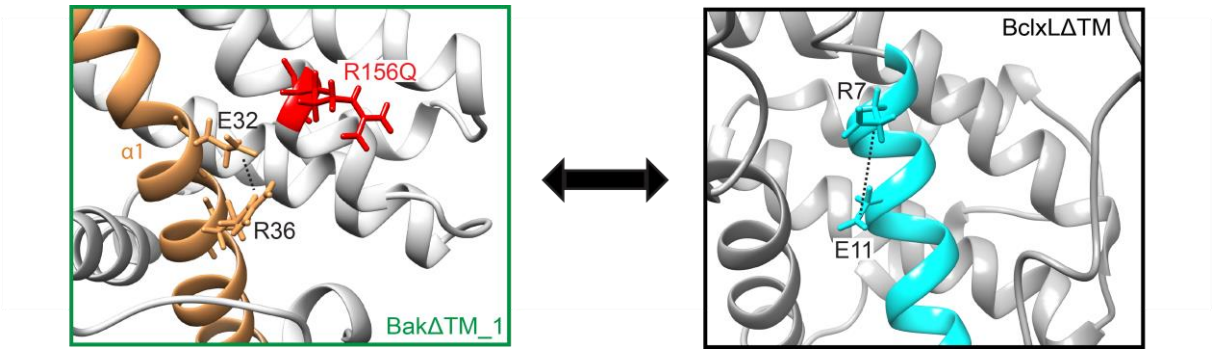

Figure 2.46: Enlarged view of the mutation site in BakΔTM_1. In the left picture, the mutation site R156Q is shown. The salt bridge, which is expected to form between E32 and R36 in helix 1 is indicated with a dashed line. For comparison, the corresponding region of BclxLΔTM is displayed in the right panel. Helix 1 is highlighted in beige for BakΔTM and in cyan for BclxLΔTM.

Variant 2 (BakΔTM_2) additionally stabilizes the interaction between helix 1 and the BH3 domain. I80E and N86E, located in the BH3 domain, were introduced as countercharges for R76 and R45, respectively **(Fig. 2.47)**.

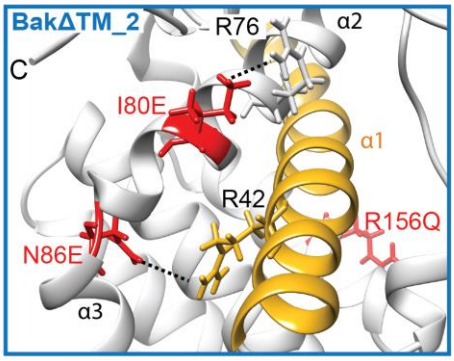

Figure 2.47: Enlarged view of the mutation sites in BakΔTM_2. The salt bridges expected to be formed by the mutants I80E and N86E are indicate by the doted lines, respectively. Helix 1 is highlighted in gold.

A third variant (BakΔTM_3) was designed using a different approach. After the mere contact with a lipid bilayer probed capable of activating Bak, it can be concluded that the interaction with lipids can trigger the unfolding of helix 1. Therefore, the charged lipid surface could be another key factor in activation. Several arginines are located in the Bak surface area oriented towards the lipid bilayer. Therefore, in variant 3 these arginines were mutated to R11Q, R169A and R174N **(Fig. 2.48)**.

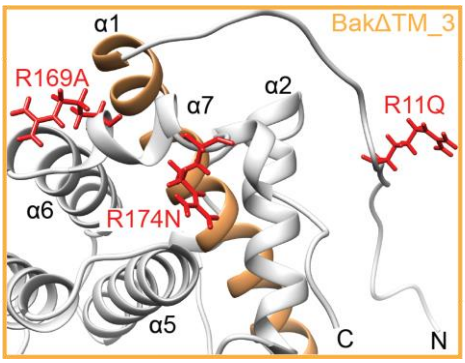

Figure 2.48: Enlarged view of the mutation site in BakΔTM_3. The arginines located on the surface area of BakΔTM oriented towards the membrane surface, namely in helix 7 and the unfolded N-terminus, were mutated leading to a less charged surface area in proximity to the lipid bilayer. Helix 1 is highlighted in sand.

After successful cloning of the three variants, the production, secondary structure and stability were found to be analog to BakΔTM for all constructs suggesting that the introduced mutations do not interfere with a compact native protein fold **(Fig. 2.49)**.

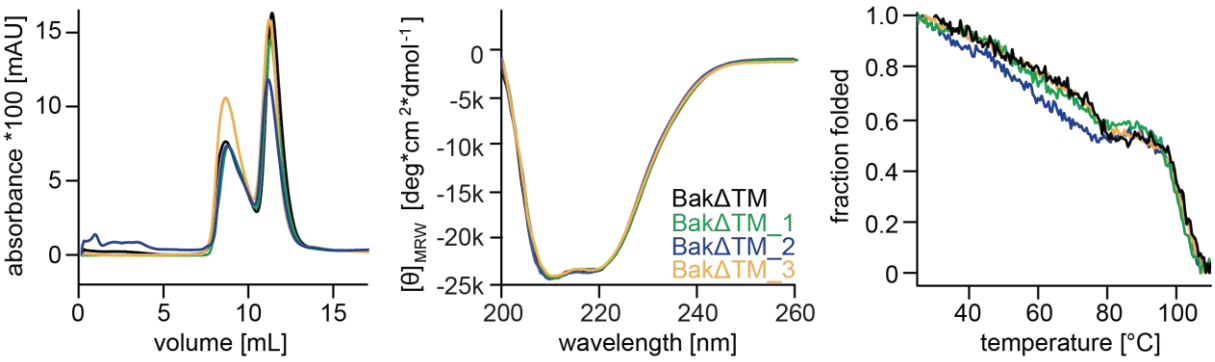

Figure 2.49: Size and secondary structure of the BakΔTM variants. Left: The size exclusion profiles of the variants

are very similar to that of the wild type. The SEC was performed on a Superdex 75 Increase 10/300 GL column. Middle: The far-UV-CD spectra superimpose well. Right: Also, the far-UV-CD detected unfolding at 222 nm is very similar for the wild type and mutant constructs.

The established liposomes permeabilization assay was first applied to monitor the ability of the Bak variant to autonomously form pores in liposomes. As anticipated, the variants show a different behavior than the wild type BakΔTM **(Fig. 2.50)**. On the one hand, both the variants, that were designed based on the strategy of stabilizing helix 1 analogue to the charge distribution found in BclxLΔTM, display reduced pore forming abilities. A small reduction of autoactivation is seen already when only the latch domain (BakΔTM_1) is stabilized in respect to helix 1. This effect is enhanced when mutations stabilizing the interactions between helix 1 and the core domains are added (BakΔTM _2). This further suggests that helix 1 stability could be an important factor in triggering activation. On the other hand, BakΔTM_3 created to reduce the surface charge in the lipid binding area leads to a comparable amount of efflux, indicating similar autoactive pore forming abilities as the wild type. Thus, the mutated arginines do not seem to be important for autoactivation and no further studies were pursued with this variant.

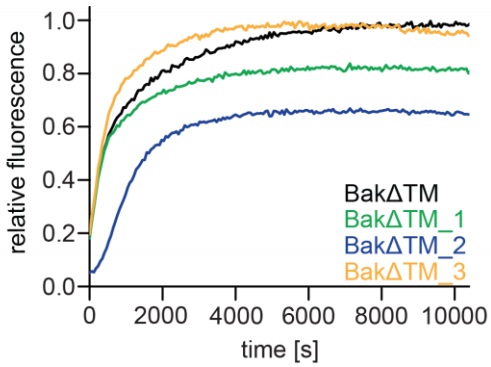

Fig. 2.50: Liposome permeabilization assay – the autoactivity of BakΔTM variants. 600 nM of the respective BakΔTM variant was added to *E. coli* polar liposomes.

Next, the liposome permeabilization assay was performed under cell-like conditions, using OMM-like lipids and concentrations of Bak, that do not enforce autoactivity. This setup also resulted in the reduction of activity characterized by a delayed onset of activation, while the functional relationship to cBid and BclxL remained **(Fig. 2.51)**.

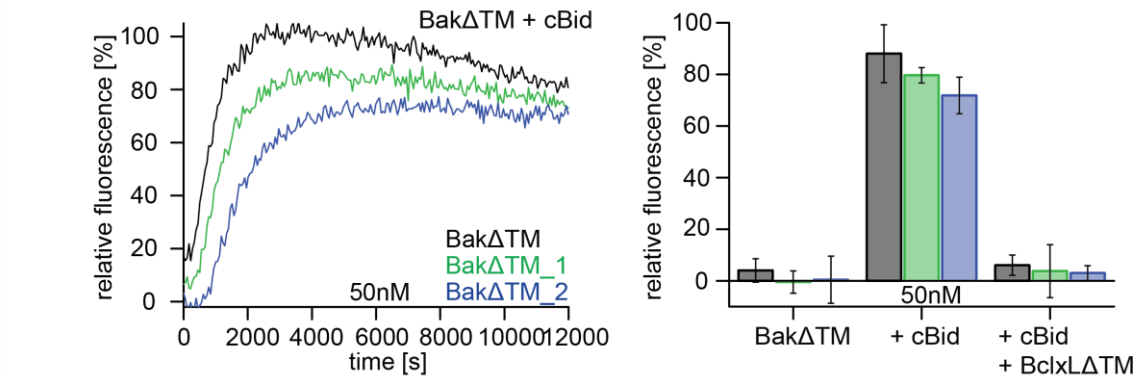

Figure 2.51: Liposome-permeabilization assay – functionality of BakΔTM mutants at low concentrations. 50 nM of the respective BakΔTM variant was used.

Taken together, these studies on active BakΔTM in a membrane environment reveal that helix α1 not only detaches from the rest of the protein but indeed unravels during this process and remains unfolded in the active state. As a short stretch of this unfolded helix 1 presented reduced dynamics, this state is perhaps stabilized by binding to the membrane surface. The developed setup, in which BakΔTM is activated on a nanodisc further enables studies with interaction partners using the full-length soluble domains, as will be discussed in the following chapter.

2.1.4 Interaction of BakΔTM and BclxLΔTM on a membrane surface

The Bcl-2 protein family interacts in a very conserved manner. Binding has been found to always be mediated by one protein inserting its BH3 domain into the BH3 groove of its partner protein. This was also shown for the interaction of Bak and BclxL [93]. A 16-residue Bak peptide containing the Bak-BH3 domain (AA 77-83) binds to the BclxL binding groove located between helices α2, α4, α5 and α7 **(Fig. 2.52)**. However, in the structure of inactive BakΔTM the hydrophobic side chains of the amphipathic BH3 domain are buried. Thus, a structural rearrangement of Bak must occur before BclxL can bind and unfold its anti-apoptotic potency. As the structural rearrangement accompanying activation only takes place in a membrane environment, this interaction could not be studied in a full-length context so far.

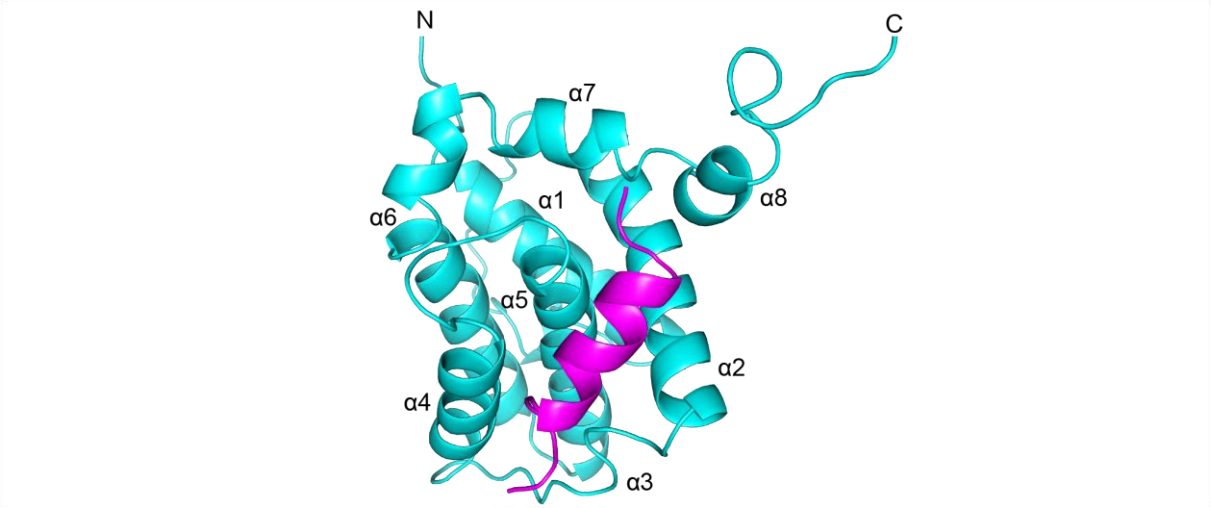

Figure 2.52: Structure of the Bak-BH3 peptide bound to BclxLΔLΔTM (PDB: 1BXL)[93]. BclxLΔLΔTM is colored in cyan while the Bak-BH3 peptide (AA 72-87) is colored in magenta.

The setup described in **Chapter 2.1.3** offers the opportunity to study the soluble domains of both Bak and BclxL bound to a membrane and thus, very natively mimics the scenario in the cell. This will be analyzed in the following chapters.

2.1.4.1 Structural characterization of the interaction using the full soluble domains

In order to study the interaction of BakΔTM and BclxLΔTM in a nanodisc environment, ^{15}N-labeled BakΔTM was mixed with BclxLΔTM and the mixture was added to ΔH5-nanodiscs doped with 5 [Ni^{2+}]/disc. The amount of [Ni^{2+}]/disc was increased to raise chances for both being bound to the same nanodisc. The quality of the 2D-[^{1}H, ^{15}N]-TROSY spectrum seemed reduced already before activation with very faint peaks referring to the inactive species **(Fig. 2.53)**. The inactive species overlayed well with BakΔTM bound to ΔH5-nanodiscs, but no influence of BclxLΔTM was seen on this species. It was assumed that the amount of nanodisc-bound ^{15}N-BakΔTM was too low for decent spectra, due to the high amount of bound BclxLΔTM, which had been added in 2-fold excess.

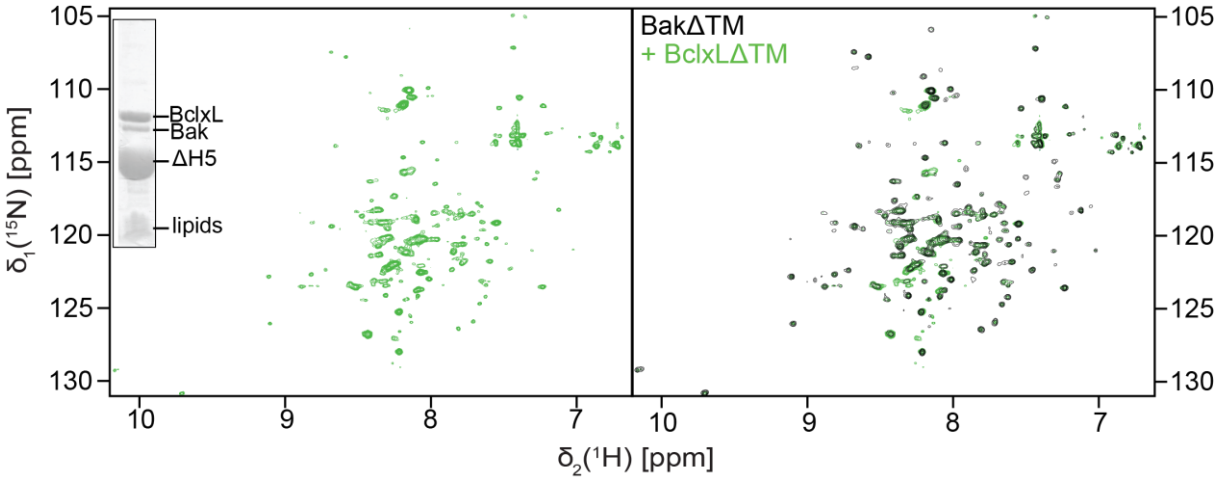

Figure 2.53: 2D-[^{1}H, ^{15}N]-TROSY spectrum of ^{15}N-labeled BakΔTM and unlabeled BclxLΔTM bound to ΔH5-nanodiscs containing [Ni^{2+}]-caged lipids (green). The inset on the left depicts an SDS-PAGE of the NMR sample,

showing that the sample contains more BclxL than Bak. On the right the spectrum is superimposed on a spectrum without BclxLΔTM (black). The spectra were recorded at 303 K and 600 MHz.

Despite the unclear outcome of this setup, the Bid-BH3 peptide was added, leading to a full conversion to the activated state **(Fig. 2.54)**. Surprisingly, local differences could be seen in both signal intensity and chemical shifts by the presence of BclxLΔTM, suggesting that BclxL not only interacts with the BH3-domain, not visible in the active species, but also has an influence on the N-terminal region. The intensity of the very N-terminal residues A2-G6 strongly increased in the presence of BclxLΔTM and F35-Y41 displayed marked chemical shift perturbations, with F35 and R36 moving too far to be assigned without further experiments. Moreover, additional peaks appeared, for example in the glycine region.

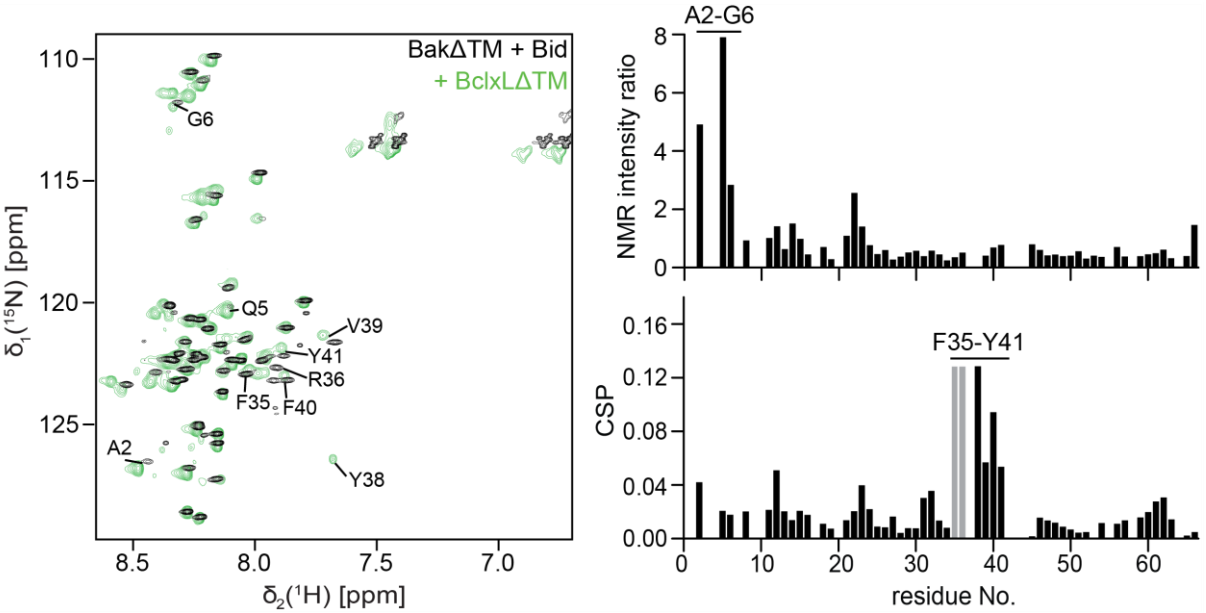

Figure 2.54: Left: 2D-[^{1}H, ^{15}N]-TROSY spectra of the samples shown in Figure 2.53 after Bid-BH3 peptide induced activation. Right: At the top, the intensity ratios show that the presence of BclxLΔTM leads to an increase of peak intensities at the very N-terminus. At the bottom, the CSP-plot implies an interaction site at F35-Y41. F35-R36 shifted too strongly to be assigned and are depicted in grey. The spectra were recorded at 303 K and 600 MHz.

As BH3-only proteins also interact with the anti-apoptotic player, which is unfavorable in this case, an activation procedure was sought for Bak that does not affect the interaction between the two Bcl-2 proteins. As the affinity of Bid is higher for BclxL than Bak[120,184], adding Bid theoretically does not lead to Bak activation until most of BclxL is inhibited. In order to circumvent this difficulty, different possible activation strategies were considered. As autoactivation is strongly reduced in nanodiscs compared to liposomes, the differences between these preparations were examined as well as the effect of moderate heat as both the CD-data and previous reports suggest an activating effect of heat on Bak[191].

Three major differences between the applied liposome and nanodisc systems were apparent. In liposomes the lipid bilayer surface area is significantly larger and displays a curvature absent in the flat nanodisc structure. Additionally, 2-10% (w/w) of [Ni^{2+}]-caged lipids were used in liposomes, while the maximal amount was lower in nanodiscs. As a curvature could not be realized in nanodiscs, this point was not approached. However, both the nanodisc size and the amount of [Ni^{2+}]-caged lipids were varied

and the amount of activated species in the 2D-[^{15}N, ^{1}H]-TROSY spectra was compared to the spectrum of fully activated BakΔTM after Bid-induced activation **(Fig. 2.55)**. For this, the peak heights were normalized using the peak intensity of G8, a non-overlapping peak which is identical in the active and inactive state, thus, should represent 100 %. Neither of the strategies led to a defined trend. All the examined setups resulted in 7-13% of activated species, except when using 1 [Ni^{2+}]/disc in ΔH5-nanodiscs, where the amount of activated species was reduced to only 1%. Increasing the lipid bilayer surface area had no activating effect in the applied range (diameters of 8-12 nm). In order to keep the system as small as possible a further increase is not desired for NMR measurements. As the amount of [Ni^{2+}] in nanodiscs was defined by the number of [Ni^{2+}] per nanodisc, as shown in the figure, the total percentage of [Ni^{2+}] in the lipid mixture decreased with increasing nanodisc diameters. Assuming both the Ni amount and the size had an effect, these effects might have been compensated resulting in the missing increase of activated species with growing nanodisc size. The applied 3 [Ni^{2+}]/disc correspond to 7 % (w/w) of total lipids in ΔH5-nanodiscs with a diameter d of 8 nm, 4.7 % (w/w) in 1D1-nanodiscs (d = 10 nm) and 2.6 % (w/w) in 1E3D1-nanodiscs (d = 12 nm). When taking into account that in liposomes approximately half the [Ni^{2+}]-ions are located on the inside of the liposome, thus, not accessible for BakΔTM, this setup displays only about 5 % (w/w) [Ni^{2+}]-ions. This amount was almost reached in 1D1-nanodiscs and even exceeded in ΔH5-nanodiscs without leading to full activation. Even if there is a small effect by increasing the lipid patch size and/or the amount of [Ni^{2+}]-ions, this is far from the desired full activation. Therefore, these approaches were not further pursued.

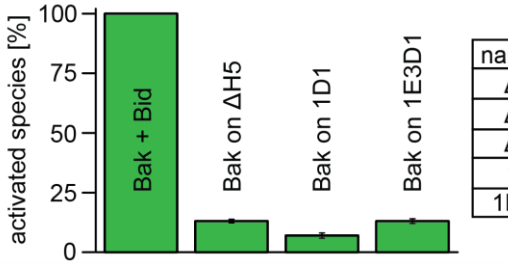

nanodisc	Ni/disc	Ni [%]
ΔH5	1	2.3
ΔH5	3	7
ΔH5	4	8
1D1	3	4.7
1E3D1	3	2.6

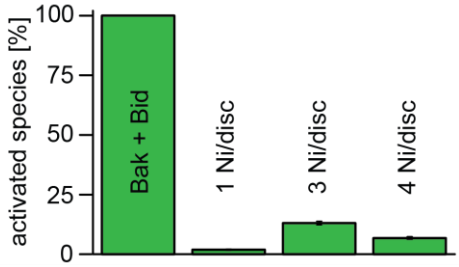

Figure 2.55: Via its C-terminal His_6-tag, BakΔTM was attached to nanodiscs differing in size or the amount of [Ni^{2+}]-lipids per disc. The 2D-[^{1}H, ^{15}N]-TROSY spectra were compared for the amount of spontaneously activated species. The percentage of activated species is depicted in comparison to the completely activated form after Bid-BH3 induced activation. Left: Differently sized nanodiscs each equipped with 3 [Ni^{2+}]-lipids per disc were utilized. Right: ΔH5-nanodiscs with varying amount of [Ni^{2+}]-lipids per disc were applied. The percentile activation was calculated by comparing the peak heights of the active peaks for S21, A28, T31, G51, V52, A53 to those in fully activated Bak after normalizing them by the highest peak G8. Error bars refer to the standard deviation. The table compiles the different setups, with the left column displaying the (w/w) percentage of [Ni^{2+}] in the total lipid composition to make it comparable to the 10 % (w/w) used in liposomes.

Thus, the heat induced activation was investigated as a next step. 2D-[^{1}H, ^{15}N]-TROSY spectra of BakΔTM bound to ΔH5-nanodiscs were recorded at increasing temperatures. **Fig. 2.56** shows that raising the temperature leads to more pronounced peaks in the random coil area (around 8 ppm), where the active species is detected, while the signals referring to the inactive species fade. Finally, after holding the sample at 50°C for 6h and decreasing the temperature to 30 °C, BakΔTM could be fully activated.

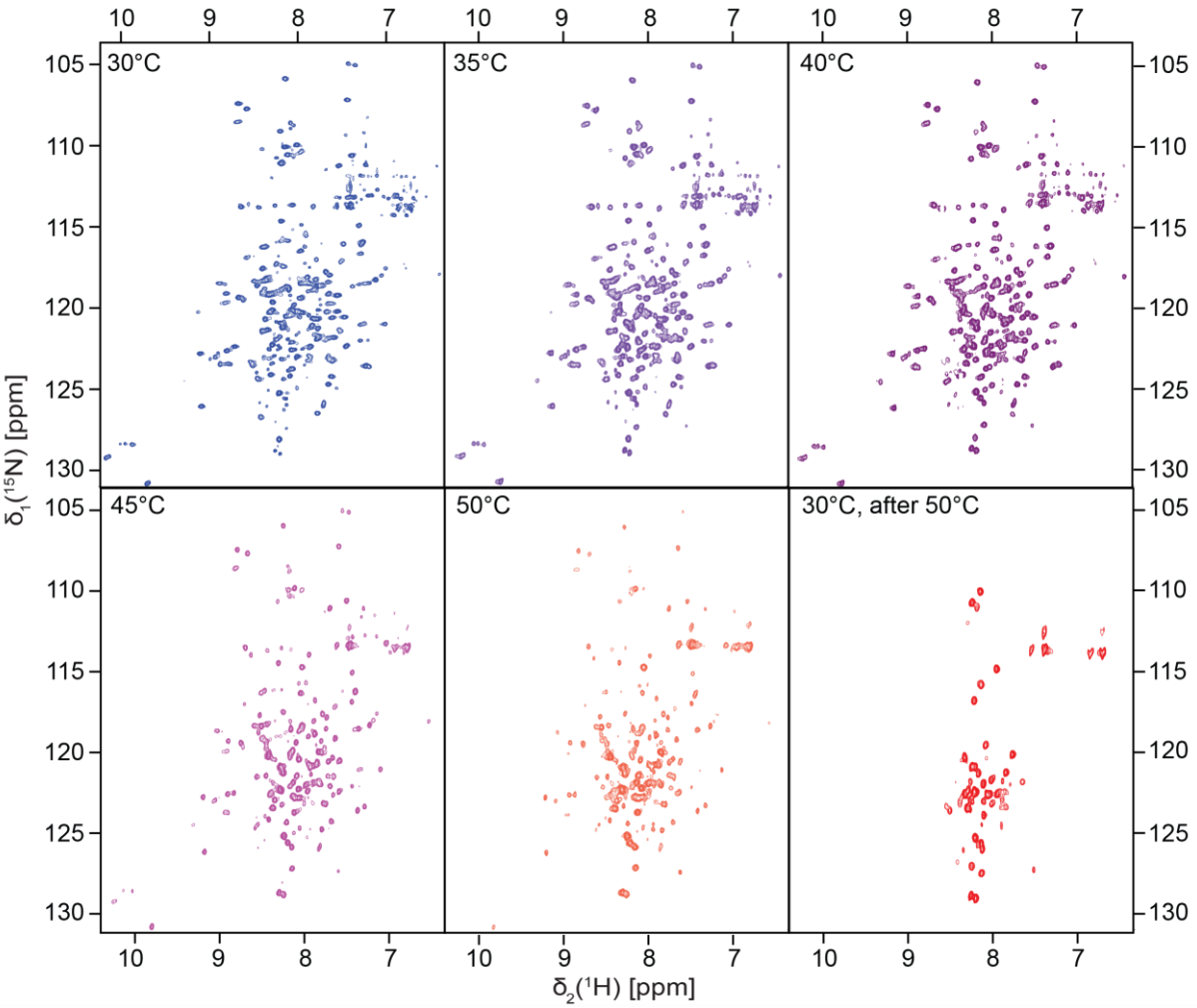

Figure 2.56: The 2D-[^{1}H, ^{15}N]-TROSY spectra of 250 µM BakΔTM bound to ΔH5-nanodiscs were compared for the amount of spontaneously activated species. The temperature was raised to the indicated temperature 30 minutes before the measurement was started. Each temperature was held for 6 h. The spectra were recorded at 600 MHz.

The temperature scan was repeated in the presence of BclxLΔTMΔHis. This BclxL-variant was utilized even though it showed a lower functionality in the liposome permeabilization assay, because the overall amount of bound BakΔTM is reduced when both proteins are added with a His-tag, leading to reduced spectral quality as seen in **Fig. 2.53**. At the 1000-fold higher concentrations used in NMR, the reduced activity can most likely be compensated. Comparing the BakΔTM spectra with BclxLΔTM **(Fig. 2.57)** to those without **(Fig. 2.56)** implies that BclxLΔTM leads to a higher amount of active Bak species. In the presence of BclxLΔTM, BakΔTM is fully activated already at 40°C, suggesting that BclxL stabilizes the active species, by pulling it out of the equilibrium.

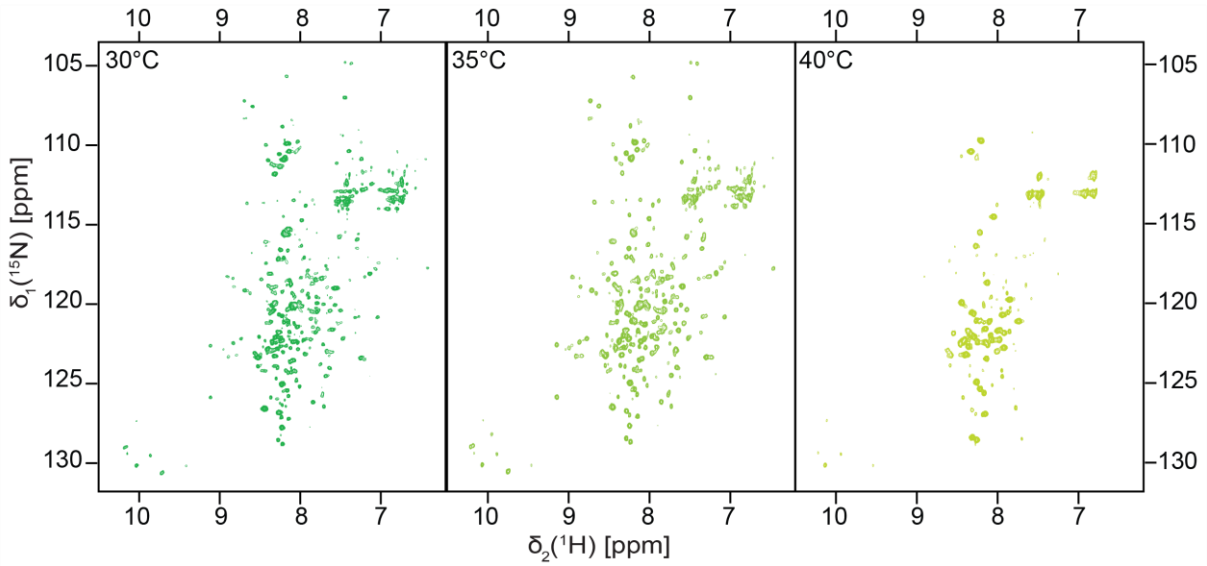

Figure 2.57: The 2D-[^{1}H, ^{15}N]-TROSY spectra of BakΔTM bound to ΔH5-nanodiscs in the presence of 10-fold BclxLΔTMΔHis were compared for the amount of spontaneously activated species. The temperature was raised to the indicated temperature 30 minutes before the measurement was started. Each temperature was held for 6 h. The 2 mM of unlabeled BclxLΔTMΔHis used in this sample is slightly visible due to the natural abundance of ^{15}N (~0.36 %)[197]. These spectra were recorded at 800 MHz

When the heat activated species are compared **(Fig. 2.58)**, the same effects are evident as seen after Bid-induced activation **(Fig. 2.54)**. Again, the peak intensities at the very N-terminus increase in the presence of BclxLΔTMΔHis and while the chemical environment of most amino acid backbone groups remains unchanged, there is a large effect in the region between F35 and Y41, which indicates binding. Interestingly, when comparing this binding site to the hetNOE data in **Figure 2.43** and the peak heights in **Figure 2.42c**, this is also the are in the N-terminal region that shows the least dynamics and has the lowest peak height, suggesting binding to the membrane surface.

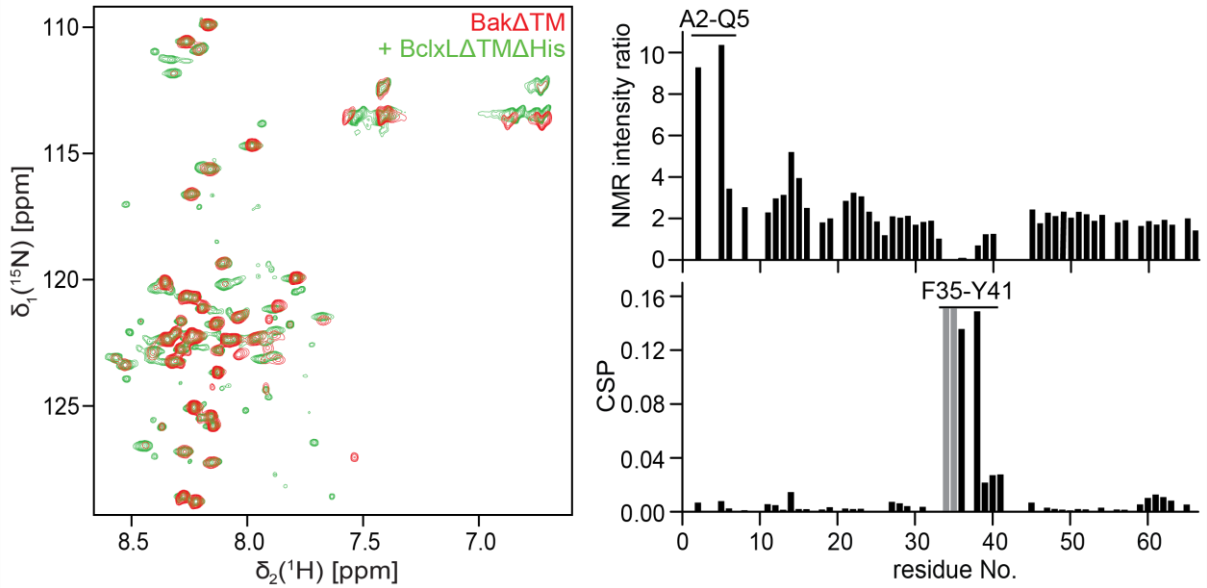

Figure 2.58: Left: 2D-[^{1}H,^{15}N]-TROSY spectra of BakΔTM bound to ΔH5-nanodiscs in the presence (green) and absence (red) of 10-fold excess of BclxLΔTMΔHis after heat induced activation. Right: At the top, the intensity ratios show that the presence of BclxLΔTMΔHis leads to an increase of peak intensities at the very N-terminus. At the bottom, the CSP-plot implies an interaction site at F35-Y41. F35-R36 shifted too strongly to be assigned

and are depicted in grey. The 2 mM of unlabeled BclxLΔTMΔHis used in this sample is slightly visible due to the natural abundance of ^{15}N (~0.36 %)[197].

Reversing this setup to binding ^{2}H-^{15}N-labeled BclxLΔTM and an excess of unlabeled BakΔTM to the ΔH5-nanodiscs did not show any chemical shift perturbation in the BclxLΔTM spectrum after heat-induced activation **(Fig. 2.59)**. This most likely is due to the fact, that the His_6-tag in BclxLΔTM is more accessible due to the longer C-terminal linker. Thus, higher amounts of BclxLΔTM were bound to the [Ni^{2+}]-containing nanodiscs even though slightly more BakΔTM (1.1-fold excess) was added to the sample. Consequently, the amount of complexed BclxLΔTM was too low to induce chemical shift perturbations.

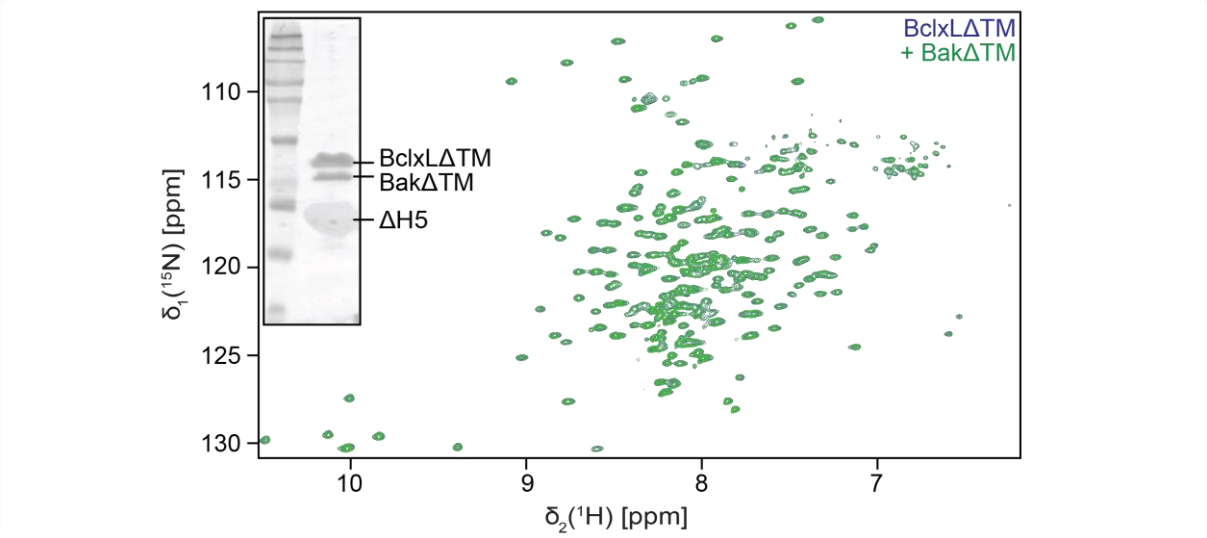

Figure 2.59: 2D-[^{15}N, ^{1}H]-TROSY spectra of *U*-[^{2}H, ^{15}N]-BclxLΔTM bound to ΔH5-nanodiscs in the presence (green) and absence (blue) of BakΔTM after heat induced activation. No difference is detected most likely because more DN-BclxLΔTM bound to the nanodiscs equipped with [Ni^{2+}]-caged lipids even though BakΔTM was added in 1.1-fold excess.

In the next step, HDX-MS was performed on BakΔTM or both Bak- and BclxLΔTM bound to liposomes. This setup was chosen because size is not limiting for HDX-MS and the liposome permeabilization assay showed that BakΔTM is autonomously activated and inhibited by BclxLΔTM in a liposomal environment **(Fig. 2.23)**, obviating the need for additional activation procedures. Comparing the deuterium uptake for both samples shows that the accessibility of residues 26-40 is reduced by up to 44% when BclxLΔTM is present, corroborating the NMR-data in suggesting a binding site for BclxLΔTM in the activated Bak helix α1 **(Fig. 2.60)**. Interestingly, while residues 26-34 show a gradual increase in deuterium uptake over time, residues 35-40 remain inaccessible. As no HDX-MS data could be obtained for residue Y41, this again is in line with the NMR-data displaying increased CSPs for residues 35-41. Also interesting are the findings on the subsequent residues 42-60. In the presence of BclxLΔTM their accessibility is reduced by ~ 10% at early time points but is even increased compared to the sample lacking BclxLΔTM after 2 hours. As the residues flanking the proposed binding site F35-Y41 on both sides show reduced accessibility after 10 s, which gradually increases with time, they are

most likely shielded by the binding BclxLΔTM but do not directly interact, enabling solvent exchange over time. Surprisingly, no pronounced differences were detected for the Bak-BH3 domain (residues 77-83), which is known to bind to BclxL. Most likely because, the BH3 domain is inaccessible in both states. In the active pore-forming state it is bound to the Bak BH3-binding groove of a second Bak protein, while it is bound to the BclxL BH3-binding groove when inhibited by BclxL.

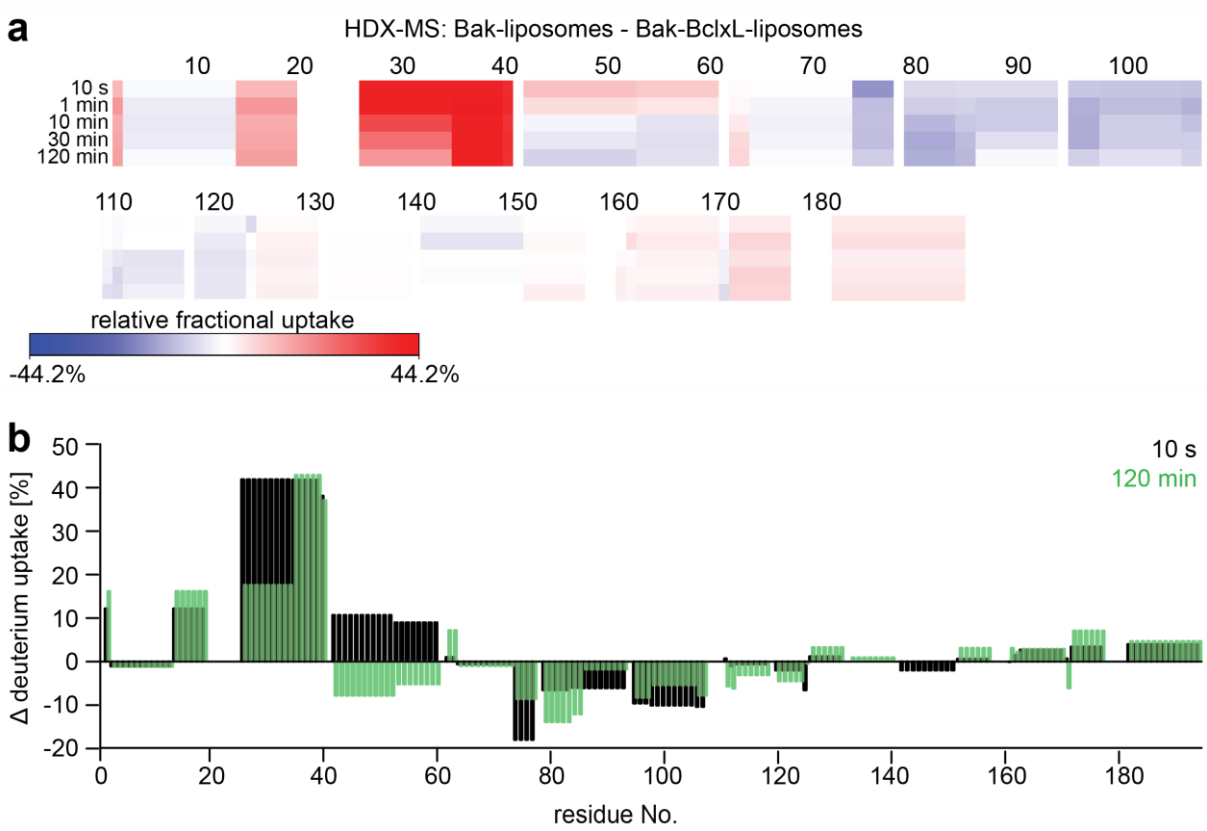

Figure 2.60: HDX-MS on BakΔTM and BclxLΔTM bound to liposomes. (a) Heat map of the subtracted HDX rates of BakΔTM and both Bak- and BclxLΔTM bound to liposomes are displayed for all measured time points. Higher fractional uptake for the BakΔTM-liposome sample is colored in red, while less uptake is colored in blue. The data was analyzed only for the BakΔTM sequence, while the BclxLΔTM sequence was not taken into account. (b) The data shown in (a) is plotted against the sequence for the extreme time points 10 s (black) and 120 min (green). The HDX-MS measurements were performed by Florian Rührnößl and Annika Strauch (AG Buchner, TUM).

As these experiments were performed in liposomes, a direct comparison to the data achieved in nanodiscs was possible **(Fig. 2.61)**. The HDX exchange rates were very similar for both the autoactivated species in liposomes and the BH3-activated species in nanodiscs presenting an identical profile with only slight differences in the absolute deuterium uptake. Furthermore, the gradual changes upon time behaved very similar, showing an almost identical pattern also after two hours. This further strengthens the assumption that the activated species in nanodiscs and liposomes are identical, and results obtained from either can be directly compared.

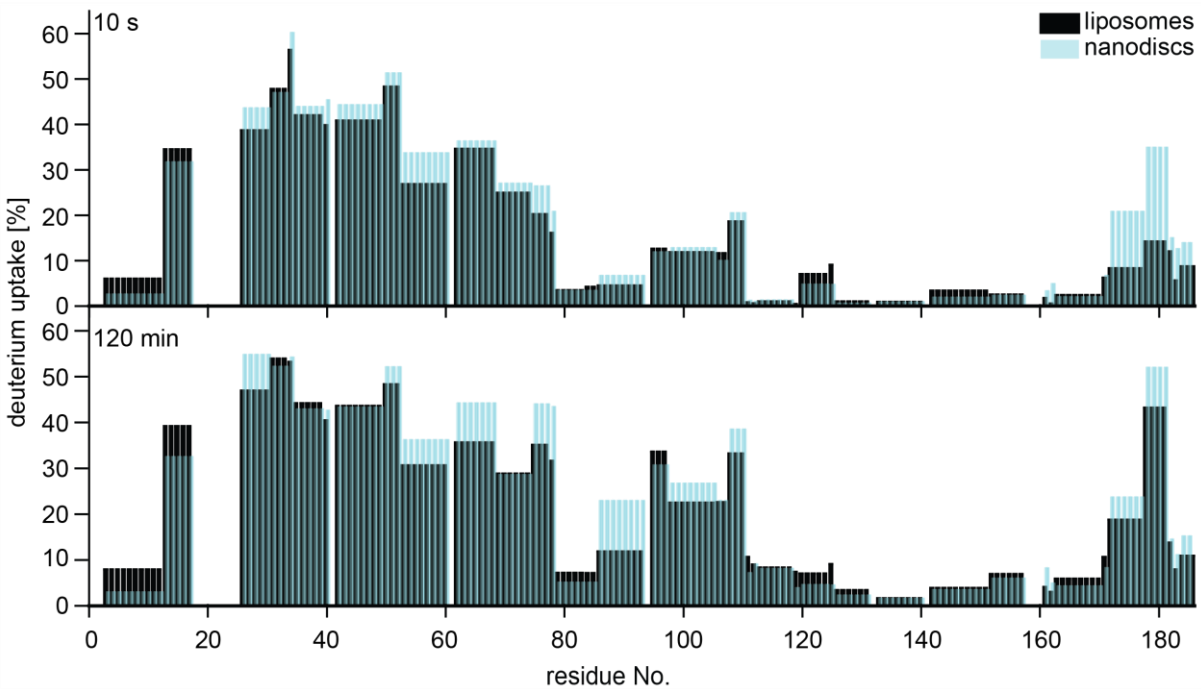

Figure 2.61: Comparison of the deuterium uptake of the active Bak species in liposomes (black) and ΔH5-nanodiscs. The HDX-MS detected deuterium uptake is compared after 10 seconds at the top and after 2 hours at the bottom. The HDX-MS measurements were performed by Florian Rührnößl (AG Buchner, TUM).

2.1.4.2 Structural characterization of the interaction using a peptide approach

In order to study the interaction site also in BclxLΔTM the Bak helix α1 was C-terminally fused to BclxLΔTM and produced as described for BclxLΔTM. Both the size exclusion chromatogram and stability probed similar to wild type BclxLΔTM **(Fig. 2.62)**. The SEC retention volume of the monomer was almost identical even though the construct contains 26 additional residues. As the Bak helix supposedly binds the BH3 binding site in BclxL, the additional helix has little influence on the overall hydrodynamic radius. Also to note is, that the dimer formed by BclxLΔTM eluting slightly after the impurities coming at void volume (46 mL) is absent in the chromatogram of BclxLΔTM-BakH1, suggesting that the helix blocks the dimerization site. However, it cannot be excluded that BakH1 facilitates the formation of larger oligomers which run at void volume, by interacting with the binding groove of a second BclxL-BakH1 monomer.

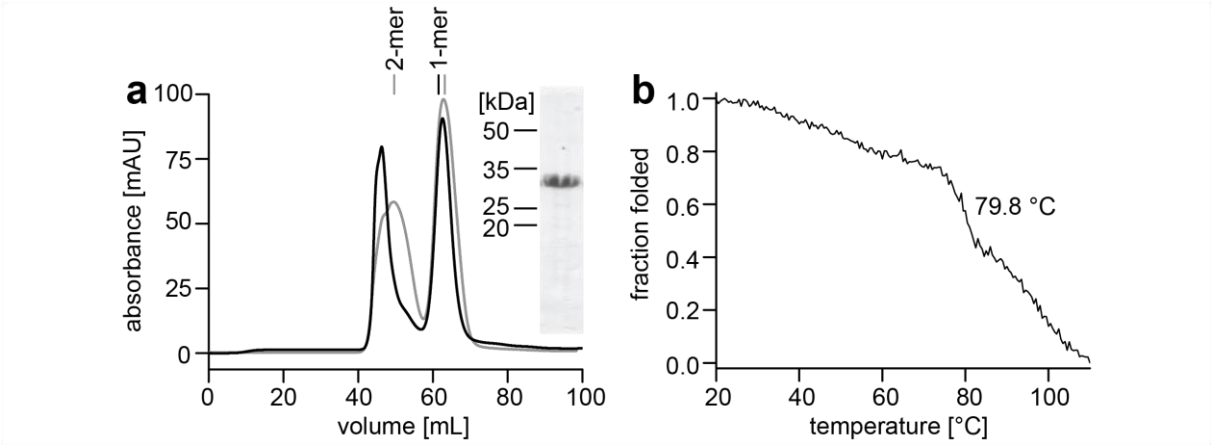

Figure 2.62: Size and stability of the BclxLΔTM-BakH1 fusion construct. (a) SEC of BclxLΔTM-BakH1 (black) superimposed on BclxLΔTM (grey). Only BclxLΔTM tends to form a dimer at high concentrations. The SEC was run on a preparative Superdex 75 column. The SDS-PAGE on the right shows very pure BclxLΔTM-BakH1. (b) Far-UV CD derived thermal stability of BclxLΔTM-BakH1.

For the backbone resonance assignment, a *U*-[^{2}H, ^{13}C, ^{15}N]-labeled BclxLΔTM-BakH1 sample was prepared to record a set of 3D TROSY-based triple resonance experiments, consisting of HNCO, HN(CA)CO, HNCA, HN(CO)CA, HNCACB, ^{15}N-edited-[^{1}H,^{1}H]-NOESY and a ^{15}N-edited-[^{1}H,^{15}N]-NOESY experiment. The quality of these 3D NMR spectra was sufficient to assign 72 % of the backbone amide resonances in the protein, while parts of the BclxL binding groove and the second half of BakH1 could not be assigned **(Fig. 2.63)**.

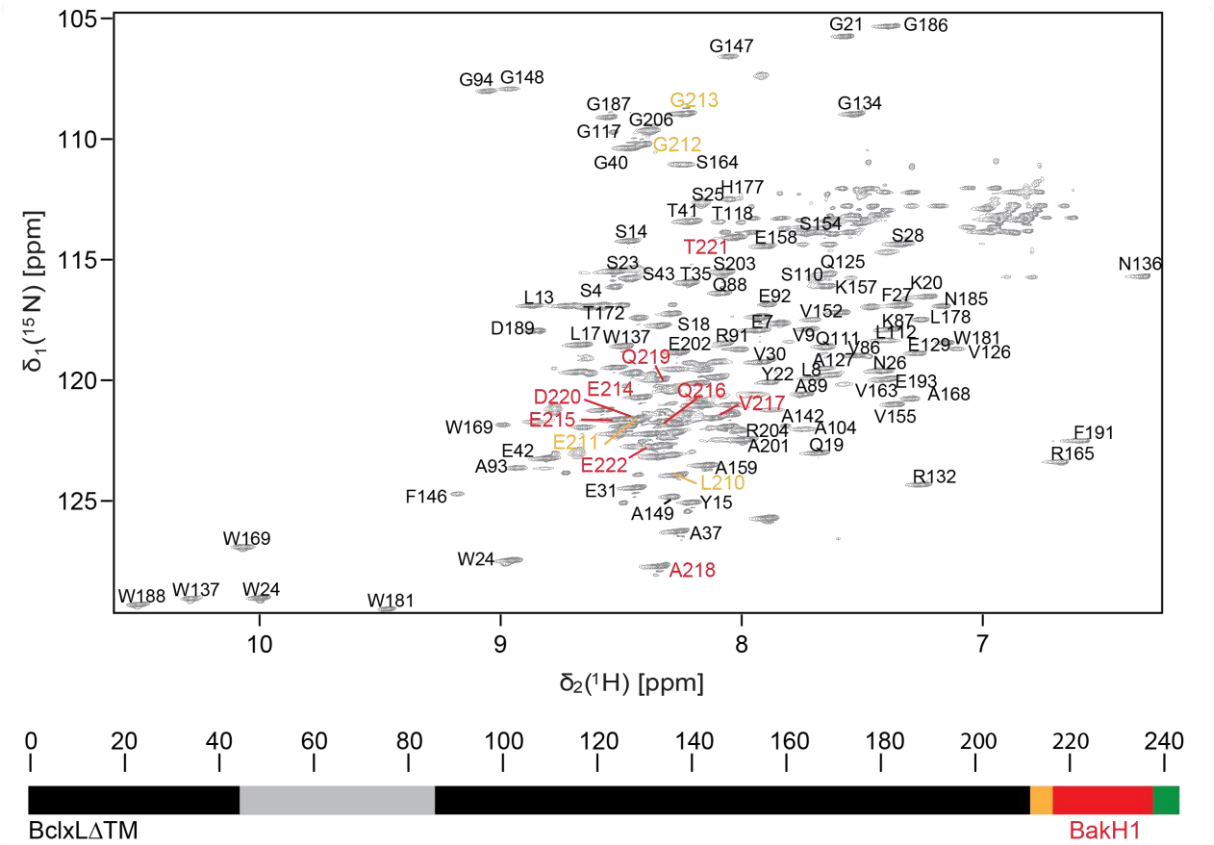

Figure 2.63 Backbone resonance assignment of the 2D-[^{1}H, ^{15}N]-TROSY using 1.5 mM *U*-[^{2}H, ^{13}C, ^{15}N]-BclxLΔLΔTM-BakH1 at 303 K and 800 MHz. In the strongly overlapping regions only the peaks corresponding

to the linker (orange) and the Bak α-helix 1 (red) are labeled. The complete assignment can be found in the appendix. Bellow a scheme of the fusion protein construct is shown. The construct used for the assignment did not contain the loop connecting the BclxL helices α1 and α2 (grey). The C-terminal His-tag is indicated in green.

A detailed NMR-analysis of the assigned residues was performed to further characterize the interaction of BakH1 and BclxL **(Fig. 2.64).** Comparing the peak intensities and the chemical shift perturbations of BclxLΔLΔTM-BakH1 and BclxLΔLΔTM suggests that the BakH1 binds to the BclxL binding groove located between helices α2, α4, α5 and α7[93]. Additionally, α3 is strongly affected, which is in line with the binding effects seen for the interaction of the Bak-BH3 domain with BclxL, shown in **Fig. 2.52**. There, the BclxL helix α3 has shifted and is not a clearly defined α-helix anymore, which has also been described for the interaction of the Puma-BH3 peptide and BclxL[93,198]. The strong effect on helix α3 is also supported by the high R_2-relaxation rates (> 30 Hz) of the few signals that remain visible in helix 3. These high values indicate chemical exchange, which is supported by the low peak intensities and the undetectable neighboring regions, which most likely have been broadened beyond detection by the binding event. When concentrating on the BakH1, C-terminally fused to BclxLΔTM, both the R_2-relaxation rates and the $\{^1H\}$-^{15}N heteronuclear NOE of the backbone amide groups indicate binding for the invisible residues as both values increase, indicating reduced dynamics in the ns to ps timescale, before the signals are no longer detectable.

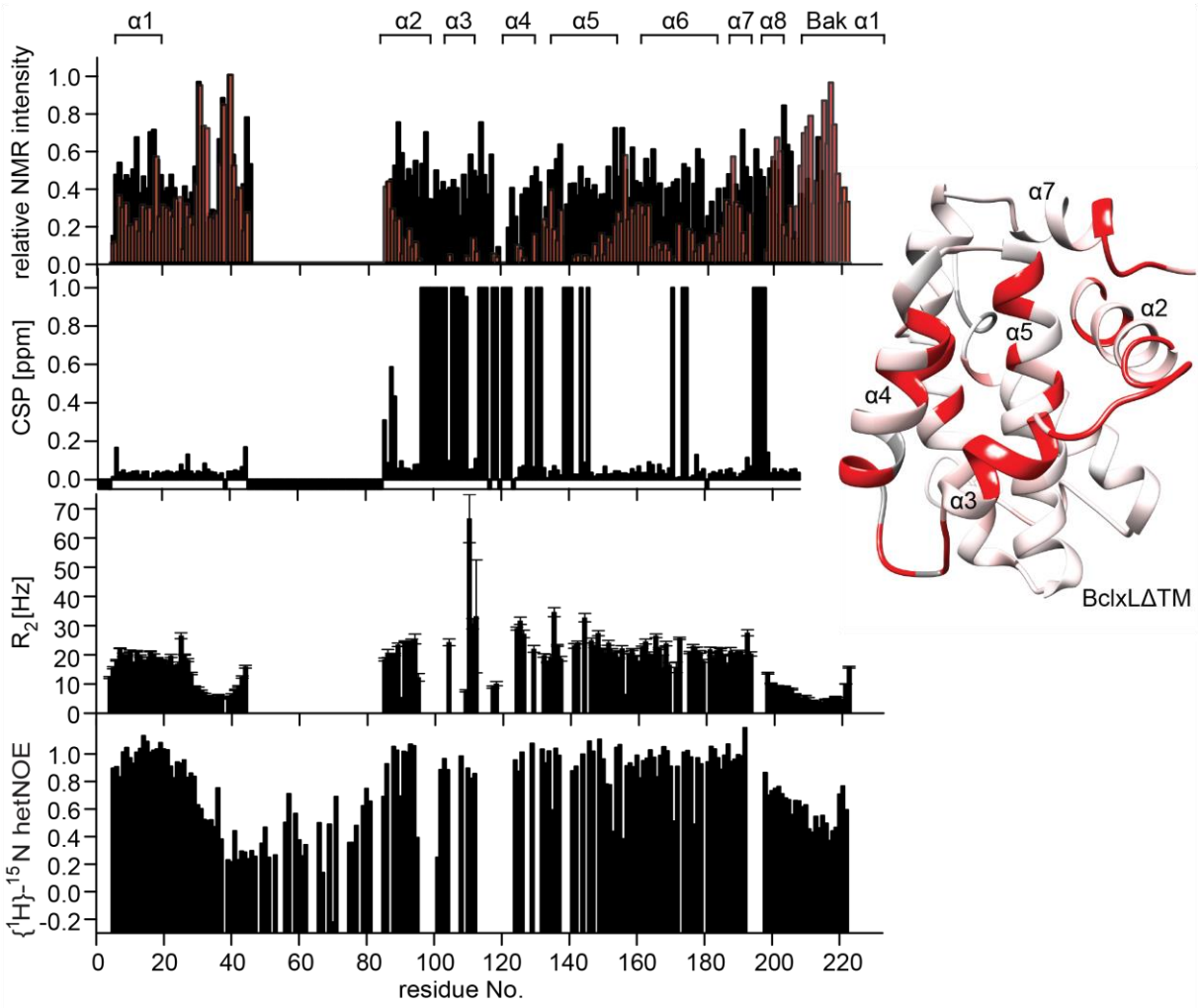

Figure 2.64: NMR-characterization of BlcxLΔTM-BakH1. At the top, the relative NMR intensities of [^{2}H, ^{15}N]-BclxLΔLΔTM (black) and [^{2}H, ^{13}C, ^{15}N]-BclxLΔLΔTM-BakH1 (red) are overlayed. Beneath, the chemical shift perturbations are shown. The CSP of the signals completely vanishing, when BakH1 is present, were set to 1.0, to indicate the strong change. On the right, these CSPs are mapped on the BclxLΔTM structure in red (PDB: 1lxl)[118]. Bellow, the R_2-relaxation rate is shown for [^{2}H, ^{13}C, ^{15}N]-BclxLΔLΔTM-BakH1. At the bottom the {^{1}H}-^{15}N heteronuclear NOE (hetNOE) of [^{15}N]-BclxLΔTM-BakH1 is shown, reporting on the ns-ps dynamics. The α-helical structure elements are indicated at the top.

To further support the binding of BakH1 to the BclxL binding groove, ITC was performed by titrating the Puma-BH3 peptide, which is known to bind to BclxL's binding groove[198], to both BclxLΔTM and BclxLΔTM-BakH1 **(Fig. 2.65)**. In both cases the K_D and the stoichiometry were unaffected by the presence of BakH1. However, the differential power was reduced by about half in the presence of the BakH1. Analyzing the thermodynamics further revealed, that not only the enthalpy (ΔH), but also the entropy (ΔS), were strongly affected while the free energy was not affected **(Fig. 2.65c)**.

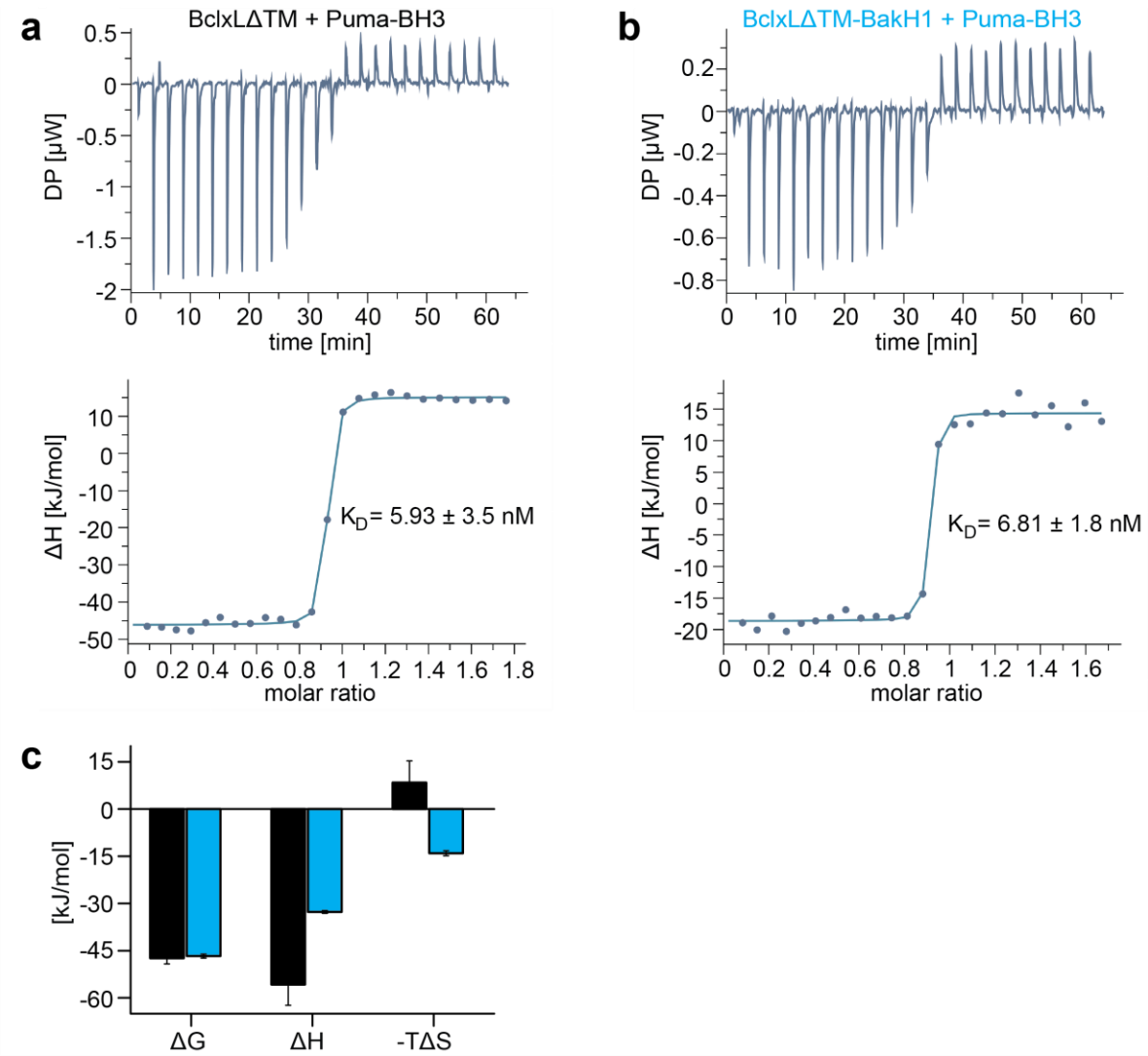

Figure 2.65: ITC-titration of the Puma-BH3 peptide to BclxLΔTM (black) and BclxLΔTM-BakH1 (blue). (a) and (b) show the respective titration results and the derived K_D value for both constructs. The only difference is seen in the total differential power, which is lower for BclxLΔTM-BakH1 when applying the same concentrations. In (c) the derived thermodynamic properties are compared. The standard deviations were calculated from three separate titrations. DP: differential power, ΔH: enthalpy, ΔG: free energy, ΔS: entropy.

A direct approach using the Bak helix 1 peptide (Bak-H1) was not successful, due to solubility issues. The peptide was only soluble in DMSO and formed a gel when titrated to aqueous solutions, e.g. for NMR measurements. Due to the amphipathic nature of this helix no solubility issues were expected.

These first structural results obtained for the interaction of BakΔTM and BclxLΔTM on a membrane strongly suggest, that these two functionally opposing Bcl-2 like proteins not only interact via the Bak-BH3 domain but also at Bak helix α1. However, it remains elusive what the role of these two interaction sites is. This will be discussed in more detail in the following chapter.

2.2 Discussion

In this work, the pore forming Bcl2 protein Bak was studied, which is permanently located at the mitochondrial outer membrane in healthy cells[128]. In contrast, the second effector Bax is mainly located in the cytosol with its TMH bound to its hydrophobic groove prior to activation. For the latter effector, binding of BH3-only proteins has two simultaneous effects: (i) detachment of the TMH for a stable membrane interaction and (ii) activation of the conformational changes required for pore formation[117]. Thus, using Bak enables the selective investigation of the structural changes along the pore forming trajectory at the membrane.

In order to achieve a more complete picture of the initial inactive state, a segmental approach was applied similar to the one published for BclxL[177]. Here, the Bak soluble domain was used harboring an intact N-terminus. This enabled investigations also on the first ~20 AA, which had been neglected in earlier work[103,114,127]. A restrained or partially structured state has been proposed for this N-terminal part after C14 was crosslinked to C166 in the inactive but not the active state[129]. In this work, the backbone resonances were assigned for the construct containing its complete N-terminus enabling further NMR studies, which showed that these residues are flexible and unstructured **(Chapter 2.1.1)**. Additionally, the high-resolution NMR structure of the transmembrane helix was determined in both ΔH5-nanodiscs and DPC-micelles revealing that the Bak TMH is longer than the TMH of BclxL[177]. NMR relaxation measurements supported this by confirming the length of the helical region, as nuclei in rigid structured regions are less dynamic in the ns-ps timescale than in the adjacent unstructured regions outside the membrane. With these data a structural model of the full-length, membrane-anchored protein could be constructed. It shows a tilted Bak TMH, as expected for a TMH of this length to match the membrane thickness. Additionally, the model suggests that the soluble domain is oriented towards the membrane with its helices 7 and 8 and the loop between helices 4 and 5. This is in line with the HDX-MS data of the soluble domain in solution and C-terminally bound to [Ni^{2+}]-caged lipids in ΔH5-nanodiscs. Furthermore, the short linker connecting the TMH to the soluble domain is shown to be flexible, enabling degrees of freedom for the two domains to move with respect to each other. However, a sortase A-mediated ligation to compile the full-length construct proved challenging. Only after the linker was extended to the length of the linker connecting the two domains in BclxL, low yields of ligated protein were achieved also for Bak. Thus, the region is less accessible in Bak, suggesting that the soluble domain in BclxL is more mobile. This makes sense, when considering that BclxL must “catch” the exposed BH3-domain in Bak with its hydrophobic binding groove to inhibit apoptosis.

According to the current understanding, oligomerization is a key factor for the functional role of Bak in pore formation.[108,199,200] Consequently, after an oligomeric Bak TMH was detected by size exclusion chromatography beside the monomeric species, it was investigated whether the Bak TMH shows tendencies for oligomerization suggesting a functional role also for this domain during pore formation. However, the performed proteolytic assay detected no tendency towards oligomerization. Additionally,

it was shown that no equilibrium forms between both species ruling against a functional relationship between them. Taken together, these data suggest that the TMH of Bak is not actively driving oligomerization but instead serves as a stable membrane anchor, similar to the TMH of anti-apoptotic BclxL in a lipid environment[177]. However, based on these experiments, a role of the TMH in the final membrane pore cannot be excluded.

Consequently, the soluble domain must be determining a Bcl-2 proteins function. Therefore, further studies were focused on this domain. At first, the influence of various sample parameters, such as protein concentration, lipid composition, membrane location and the interaction with pro-survival BclxL, on the pore-forming activity of Bak in liposomes was investigated systematically **(Chapter 2.1.2)**. In these experiments, mimicking the transmembrane helix by a C-terminal hexahistidine tag and Ni-NTA-modified lipids [183] for stable membrane attachment proved essential for pore formation. Consistent with earlier studies [85,87,88,106], Bak formed pores only after activation by an activator BH3 protein such as cBid or Puma-BH3 at low Bak concentrations (< 100 nM), and its pore formation was efficiently inhibited by membrane-attached anti-apoptotic BclxLΔTM. If cBid was added, the inhibitory effect of BclxL was neutralized. However, Bak activation still required an excess of BH3-only proteins over BclxL. Furthermore, maximal BH3-dependent activation of Bak pore formation was observed if cBid was present at least at an equimolar stoichiometry to Bak, suggesting that at low protein concentrations Bak activation is exclusively dependent on its interaction with activator BH3 proteins. These findings support existing models of Bcl2 protein pore formation that have been combined in the unified model described in **Chapter 1.3.2**[106]. This model suggests that pro-survival Bcl2 proteins are able to bind to both, BH3-only and effector Bcl2 proteins, and the relative protein levels determine the apoptotic outcome. In contrast, when Bak is present at a higher concentration, a scenario that is encountered in most structural studies, it forms membrane pores in an autoactive manner, i.e. without the need for BH3-mediated activation[107,185]. Such a concentration-dependent activation pathway is consistent with earlier studies where knockout of BH3 activators in mice did not abrogate apoptosis[85] and where Bax/Bak expression in full Bcl2 protein knockout cells was sufficient to induce apoptosis[107] even without BH3 activators, arguing for the existence of Bak/Bax autoactivation *in vivo*.

Further efforts were directed towards determining the features governing pro- and anti-apoptotic functionality despite their highly conserved fold[95]. Thus, the soluble domain of Bak and BclxL were compared using various methods. The distinct unstructured loop regions showed no functional relevance. Instead, protein folding studies revealed clear differences in the folding pathway of pro- and anti-apoptotic Bcl2 proteins. Interestingly, BakΔTM probed more resistant to heat than BclxLΔTM even though Bak undergoes major conformational changes upon activation. This is in line with previous studies, reporting a high melting temperature also for the other effector Bax[182,192]. The very stable protein core is also supported by the reduced accessibility of the core residues around helix 5 in Bak. Additionally, a distinct behavior was detected during chemical unfolding, where only BakΔTM, but not

BclxLΔTM formed a molten globule intermediate. While the formation of this intermediate characterized by half-buried tryptophane side chains probed quite resistant to the chaotropic agent urea, it formed at low concentrations when subjected to the chaotropic salt GuHCl, suggesting that the breakage of electrostatic interactions play a role. Further analysis revealed that helix 1 in Bak is especially sensitive to GuHCl, while no defined trend could be detected for BclxL. These data indicate that, despite a high structural similarity, the distinct functional features of Bcl-2 proteins are encoded in the stability and interaction pattern of individual secondary structure elements. The ability of effector Bcl2 proteins to undergo large conformational changes has been previously termed as "metastable"[78], further highlighting specific features in their intrinsic folding landscape.

In order to study the activation process taking place in a membrane environment, the pre-pore state of BakΔTM was stabilized on lipid nanodiscs. While the high protein concentrations required for structural investigations are expected to lead to autoactivation, this was not seen in lipid nanodiscs. Compared to liposomes this membrane mimetic is smaller and constrained in size by the surrounding membrane scaffold protein[35,179]. Bak proved mainly monomeric when attached to the lipid surface of nanodiscs, and the concentration-induced autoactivation was efficiently suppressed **(Chapter 2.1.3)**. At the same time, BakΔTM was still able to form oligomers upon BH3-dependent activation, as probed by cysteine-mediated crosslinking and size exclusion chromatography. Most likely, the high stability of the formed Bak oligomers disrupts the nanodiscs providing enough space to stabilize these larger structures. Thus, by applying this nanodisc setup, the membrane insertion of Bak could specifically be triggered by the addition of activator BH3 peptides and the investigation of the stabilized associated structural states was enabled. This analysis revealed that the N-terminal region of Bak (residues 1-66, encompassing helix 1 (α1) and the loop region to α2) adopts a flexible random-coil conformation, confirming earlier studies at lower resolution obtained by epitope mapping and EPR spectroscopy[91,128,130,131,135,183]. The excellent agreement with these previous studies obtained at lower protein concentrations indicates that the higher concentration used for NMR does not alter the activation pathway of Bak. This could also be shown by the very similar hydrogen/deuterium exchange profiles generated for autoactivated Bak in liposomes and Bid-BH3-activated Bak in nanodiscs. Moreover, the NMR experiments provide novel insights on the interaction between a central part of α1 and the membrane surface, which most likely stabilizes this dynamic partially unfolded conformation. The remaining parts of BakΔTM are probably located inside the membrane and are therefore invisible in NMR due to line-broadening effects resulting from the slower tumbling time of the membrane mimetic as well as possible sample inhomogeneities and intrinsic structural dynamics in the ms-μs time scale. In order to obtain a more global structural picture of Bak, HDX-MS was applied to probe the structural state of the membrane incorporated parts of Bak.

The herein presented data contribute to a better structural and mechanistic understanding of the pore forming process of Bak, which is depicted in **Fig. 2.66** and is consistent with current structural models of pore formation by Bcl2 proteins [141,148]. Prior to membrane insertion (stage 1), Bak is present in a

membrane-attached state via its C-terminal TMH. The latch helices α6-8 are in contact with the membrane surface, as indicated by reduced HDX in this area if bound to lipid nanodiscs. This resting state is compactly folded and does not insert into the membrane. However, the proximity to the membrane destabilizes the soluble domain of Bak, as probed by the reduced thermal stability of BakΔTM in liposomes. The main trigger to induce pore formation is the engagement of the Bak soluble domain with an activator BH3 protein, such as Bid or Puma (stage 2) [101–103]. Upon interaction with a BH3-only protein, α3 and α4 in Bak form the canonical binding groove [100,103], which eventually leads to a shift in the location of α2 and α3 with respect to α1. The latter effect implies changes in the interaction between α2 and α1, possibly facilitating the dissociation of α1 from the helical bundle. As probed by NMR experiments, a central part of the unfolded α1 then interacts with the surface of the membrane most likely contributing to the stabilization of its core-detached conformation. Once α1 is detached (stage 3), the core helices α2 - α5 become exposed and can form stable dimers (stage 4), a step that is considered to be essential for pore formation[127,145]. As evident from the crystal structures of Bak core dimers[127,145], α2 of one Bak monomer needs to insert itself between α3 and α4 of the second monomer[131]. Thus, widening of the cleft between α3 and α4 by transient binding of activator BH3 proteins might contribute to an enhanced Bak homo-dimerization activity and ultimately pore formation. The participation of the Bak core helices in a final compact structural assembly, presumably a pore-like structure, could be confirmed by the strong solvent protection in HDX-MS experiments, while solvent exchange rates of the latch helices (α6-α8) slightly increase, indicating a more exposed position. However, due to the occurrence of multiple structural states, the HDX data can only provide ensemble-averaged information. Nonetheless, the tendencies seen in these data provide insights on the global changes in solvent protection of BakΔTM upon activation.

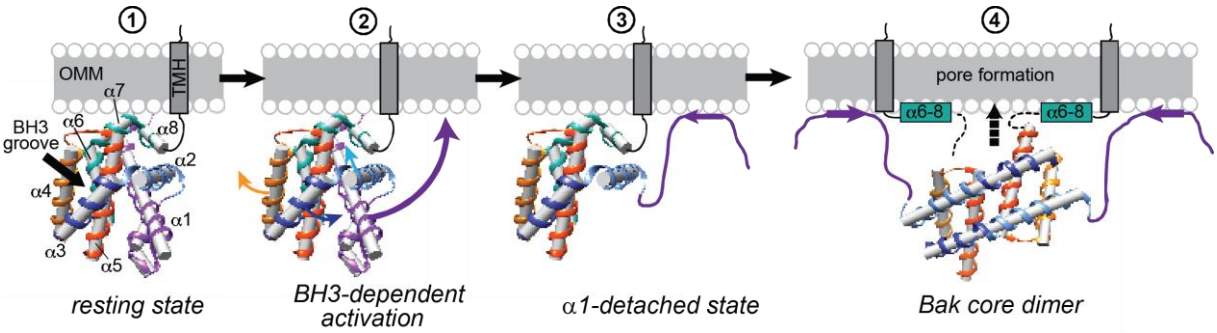

Figure 2.66: Model of the structural changes in Bak upon activation. (1) The resting state of Bak on the outer mitochondrial membrane is characterized by a compact soluble domain fixed to the membrane by the C-terminal transmembrane helix, to which it is linked by a short flexible loop. The color coding indicated here is maintained throughout the figure. (2) Once a BH3-only protein binds to the BH3-binding groove helices 3 and 4 are pushed apart, which probably weakens the interaction of helices 2 and 3 with helix 1 facilitating the detachment of helix 1, which then interacts with the membrane (3). This induces the detachment of the core and latch domains, homodimerization and pore formation (4). Perhaps the detachment of helix 1 and the separation of the core and latch domain are not separable and occur simultaneously. As no structural information on the pore is available the core dimer is depicted here.

At the same time, BakΔTM activation can be induced by higher BakΔTM concentrations on the membrane surface without the participation of activator BH3 proteins [185]. Since Bak is stably attached to the membrane at any protein concentration, the only concentration-dependent process during Bak activation is its homo-dimerization or oligomerization. This could be explained if a conformational equilibrium between the compactly folded state (stage 1) and the α1-detached state (stage 2) is formed, which is strongly in favor of stage 1 when no activator is present. At high protein concentrations, the occurrence of spontaneously detached α1 is more likely, enabling its unfolding and membrane binding (stage 3). This process leads to the exposure of the Bak BH3 domain, which subsequently can activate further Bak molecules[201] in an autocatalytic manner. Pore forming activity is further enhanced by the presence of negatively charged lipid headgroups, which might strengthen the interaction of the positively charged residues in α1 and the membrane surface. However, it is likely that not only the positive charge but further aspects of the membrane mainly linked to the presence of cardiolipin play a role, as the presence of cardiolipin has been reported to be essential for Bak and Bax activation[186,202]. In contrast, when no membrane is present, not even a BH3-only activator can induce the large conformational changes leading to activation, as seen for the Bak soluble domain in complex with Bid-BH3[103]. Thus, the stabilization of the detached conformation of α1 by a membrane surface might strongly facilitate the necessary global structural changes in Bak. In a cellular context, the exposed Bak BH3 domain is readily neutralized by anti-apoptotic Bcl2 proteins, leading to low levels of complexes of activated Bak or Bax with pro-survival Bcl2 proteins [203]. The herein described activation pathways of Bak are in very good agreement with the unified model of Bcl2 proteins where both, direct activation of Bak/Bax as well as activation of Bak/Bax in complex with anti-apoptotic Bcl2 proteins by BH3 proteins are considered to take place in parallel [106].

Interestingly, in contrast to the data presented here, a previous study with full-length Bak containing a mutated, amphipathic TMH, did not see autoactivation at higher concentrations[112]. Due to the amphipathic nature of the TMH, this mutant has reduced membrane binding properties [88,111] most likely caused by the interaction of the mutated TMH with its BH3 binding groove, as seen for the other pore forming member Bax[117]. This explanation is in line with a previous study showing that mutations in the Bax TMH that reduce membrane residence also reduce its pore-forming activity[204]. Furthermore, that tendency is also evident from the Bak pore forming assays without Ni-lipids, lacking stable membrane binding.

The relevance of α1 dissociation for pro-apoptotic functionality is further corroborated by previous studies showing that the deletion of the N-terminal BH4 domain (containing α1) leads to a reversal of Bcl2 proteins from anti-apoptotic to pro-apoptotic functionality[109] or increases the pore-forming activity of pro-apoptotic effector proteins[205]. This implicates that pore-formation is intrinsically inhibited by the interaction between α1 and the remaining protein. In line with this notion, the mutagenesis experiments aiming at altering the α1 interaction within Bak led to reduced pore-formation, consistent with an

abolished pore-forming activity of Bak if α1 is covalently tethered to the surrounding α-helices [130]. A comparison of the mutation sites applied in this work (I80, N86, R156) to a databank listing pathological phenotypes (https://www.oncomx.org/)[206–208] reveals that two of the herein chosen positions in Bak, N86 and R156, occur in various cancers, presumably due to their lower apoptotic potency. Even though the measured effects are very likely caused by altered interactions involving α1, an impact on the downstream pore assembly process cannot be completely excluded from the herein presented data. Since no structure of a full Bak or Bax pore has been reported, future systematic rationally designed mutagenesis studies exploring the modulation of Bak functionality will be required to provide a more detailed understanding of the key residues that define pro- or anti-apoptotic Bcl2 proteins. However, the information provided here will be beneficial for a better mechanistic understanding of the initial steps of Bak activation that might be relevant for novel therapeutic approaches aiming at selective activation or inhibition of apoptosis.

The structural relevance of the Bak species generated by activation in lipid nanodiscs was further strenthend by interaction studies with BclxL. Not only could specific binding effects be detected by NMR spectroscopy, but these experiments using the full soluble domains revealed a novel binding site within the unfolded helix 1 of Bak **(Chapter 2.1.4)**. Furthermore, this binding site could be confirmed by HDX-MS in a liposome environment. The discovered binding site in helix 1 is in line with a previous publication on Bax, proposing that the interaction with an antiapoptotic protein extends or at least affects the N-terminal region of Bax after they found that the epitope for binding the monoclonal antibody 6A7 located at the N-terminal part of helix 1 in Bax (residues 13-19) was not accessible upon binding antiapoptotic proteins[106]. In contrast, another study using the antibody Bak Ab-1 specifically targeting the N-terminus and helix 1 (residues 1-52) in Bak still bound, when Bak was bound to BclxL[209]. Both antibodies were initially used to distinguish the active from the inactive state, as they only bound to Bak or Bax in the respective active state. The differences seen for both could originate from the distinct epitopes targeted respectively.

Considering that Bcl-2 proteins usually interact via a BH3 domain and a hydrophobic groove, which has also been shown for the interaction of Bak and BclxL[93], it could be difficult to distinguish between the Bak binding sites when trying to define where BakH1 binds in BclxL. Additionally, as the BH3 domain is the central binding partner in the Bcl-2 protein family, the BakH1 binding site most likely binds with lower affinity. Therefore, a peptide approach was chosen. However, the peptide of helix 1 was insoluble in aqueous solutions rendering interaction studies with BclxL difficult. With the fusion-construct developed instead, binding of the BakH1 to the BclxL binding groove could be shown both with NMR-measurements and by competitive ITC-titrations using the Puma-BH3 peptide, which is known to bind to the hydrophobic groove in BclxL with nM affinity[198]. Many signals in the potential interaction sites were invisible in the NMR experiments, most likely due to binding kinetics in the µs-ms timescale rendering a structure determination by NMR difficult. However, the data compiled shows clear evidence

that the BakH1 is indeed binding to the hydrophobic groove in BclxL with its C-terminal region, which therefore is invisible together with many residues located at the BH3 binding groove of BclxL. Reduced dynamics in the ns-ps timescale indicative of binding can be extrapolated for these invisible regions, as both the T_1/T_2-rates and the $\{^1H\}$-^{15}N hetNOE indicate increasing rigidity for the flanking visible residues. Furthermore, the competitive ITC-titration indicates a second heat absorbing process taking place when the BakH1 is present resulting in a reduced overall enthalpy ΔH and an increased entropy ΔS. As the binding constant K_D is not altered, the resulting free energy ΔG, which only describes the initial and final state[210], remains unchanged by the presence of the BakH1. However, the processes taking place between these two states are distinct. This is evident from the different enthalpic and entropic contributions when the BakH1 is present. In general, the individual processes adding up to the apparent ΔH and ΔS are the sum of several contributions by the solvent and the involved protein and ligands and cannot be related in detail from this data[210]. But the direct comparison shows that part of the enthalpy produced by the binding of the Puma-BH3 peptide to BclxL is compensated when BakH1 is present, indicating a second endothermic process, which can be explained by the release of the BakH1 from the binding groove and the accompanying disruption of non-covalent interactions. Moreover, this is supported by the reduced entropic term ($-T\Delta S$), corresponding to a positive entropy or measure of the degree of disorder. When a ligand binds, this leads to reduced disorder but is compensated when a second ligand is freed by the process. As the K_D for the PUMA-BH3 peptide is not altered by the presence of BakH1, the affinity of this helix most likely is much lower than that of the PUMA-BH3 domain and possibly also as the Bak BH3 domain. Consequently, the BH3 domain in Bak probably is the main interaction site for BclxL, as known from the literature[93]. At this point, the role of the additional binding site can only be speculated, considering that the detachment and unfolding of helix 1 occurs as an early step during activation, this could be the initial trigger for BclxL binding to Bak. Once the Bak BH3 domain is exposed, it binds to the BclxL binding groove more readily due to its higher affinity leading to an inhibition of the oligomerization and downstream pore-formation. If anti-apoptotic proteins like BclxL are summoned to the structurally converging Bak monomer by the early stage exposure of its Helix 1, this also explains how antiapoptotic proteins can so efficiently inhibit pore-formation even though the exposed Bak BH3 domain is prone to also interact in homodimers leading to down-stream apoptosis.

All in all, the data presented here, not only offer novel structural insights on the inactive and the activated Bak species but also provide new information on the mechanisms of Bak activation and its inhibition by anti-apoptotic proteins, which will be of interest to the broad scientific and medical community.

3 MPV17

3.1 Results

3.1.1 Prior studies

Prior to this work, a production procedure was developed for MPV17, which facilitated NMR structural studies. As the *E. coli* expression system enables the most simple and cost efficient isotope labeling, the gene was cloned into a pET vector. However, expression was possible only after MPV17 was fused to the solubility and expression helper GB1 **(Fig. 3.1)**[211]. The fusion protein construct was produced into inclusion bodies, dissolved in GuHCl and purified using Ni-affinity chromatography. After careful refolding by adding the unfolded protein dropwise to DPC micelles, GB1 was cleaved utilizing a Thrombin cleavage site. For a nearly complete cleavage the insertion of an additional GGSS spacer between MPV17 and the protease site was necessary. Additionally, a cysteine-free mutant, MPV17ΔCys, was produced by exchanging the four cysteine residues for alanines. This variant could be expressed and purified analogue to the wild type protein.

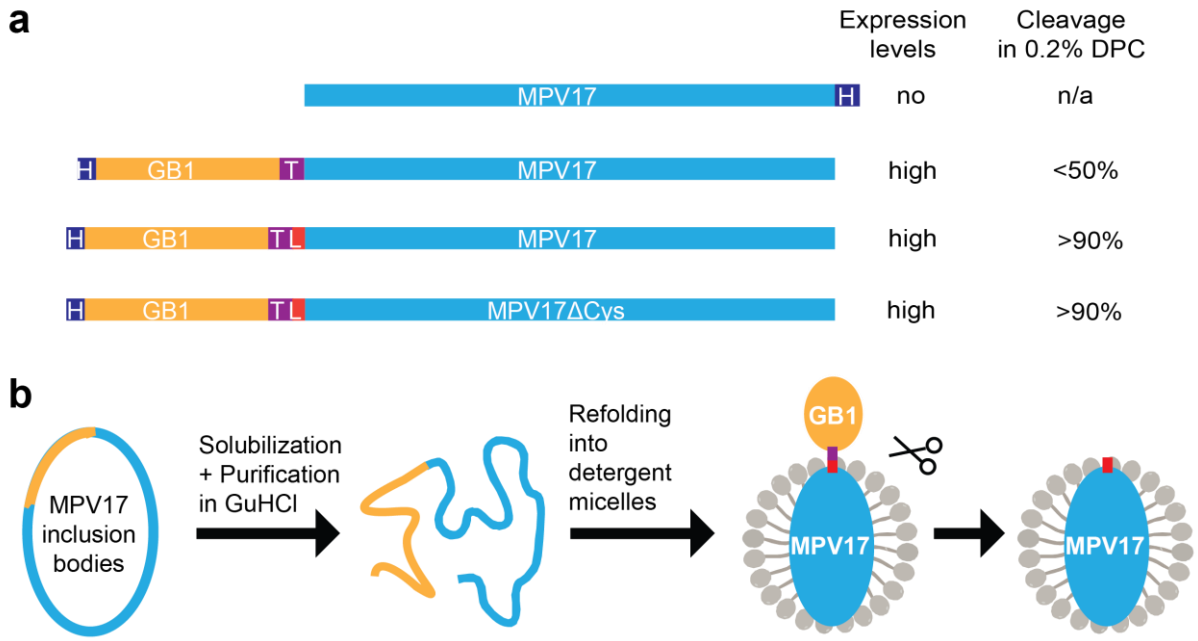

Figure 3.1: (a) Overview of different pET MPV17 gene constructs and the resulting expression and thrombin cleavage yields. MPV17ΔCys refers to a mutant in which all cysteines are replaced by alanines. (H = His_6-tag, T = thrombin cleavage site, L = GGSS-linker) (b) Illustration of the purification protocol developed for MPV17. It is expressed in inclusion bodies, solubilized and purified in GuHCl, refolded into detergent micelles before the expression helper GB1 is finally cleaved by thrombin.

In this work, the effect of various detergents and other membrane mimetics was tested on the stability of MPV17, in order to find the most suitable candidate for structural studies. Lacking a functionality assay, the protein folding was monitored to ensure that a correctly folded protein was obtained. This

enabled initial structural studies using NMR. Additionally, the protein was studied in amphipoles, nanodiscs and liposomes.

3.1.2 Purification and Characterization of recombinant MPV17 in detergent micelles

First, the purification protocol developed previously was applied, resulting in a homogenous protein preparation **(Fig. 3.2)**. As probed by SDS-PAGE, the size difference between MPV17 in DPC-micelles and the cleaved soluble GB1 was sufficient for separation on a size exclusion column. The yielded protein was very pure, showing only a slight dimeric band but no impurities or residual cleaved GB1.

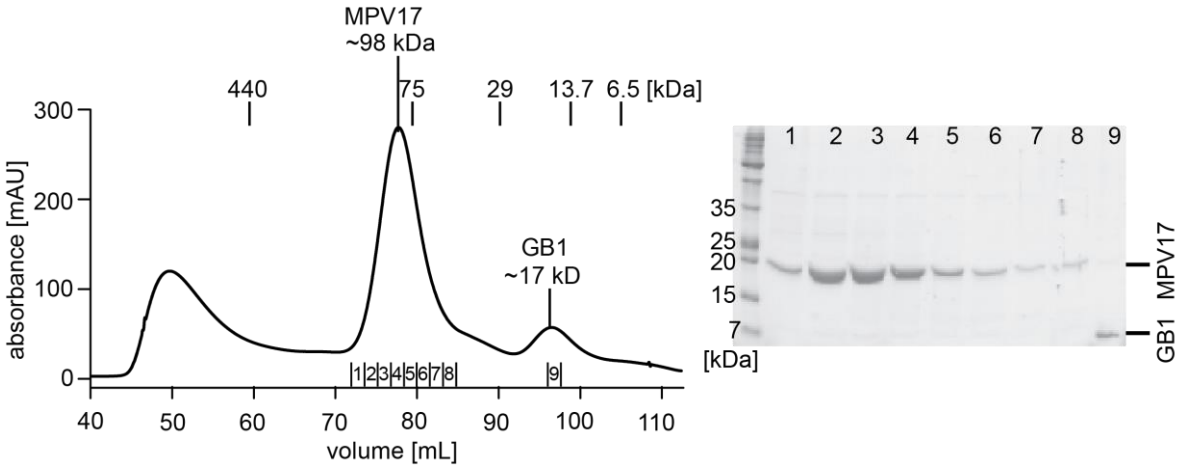

Figure 3.2: The size exclusion chromatogram of MPV17wt in DPC-micelles after thrombin-cleavage. The molecular weight calibration is indicated at the top and the fractions, which were applied to SDS-PAGE are indicated at the bottom. On the right the corresponding SDS-PAGE of the fractions is shown.

The zwitterionic detergent DPC, has controversially been discussed to induce α-helical secondary structure[212,213], underlining the importance to verify the structural conformation also in other membrane mimetics. Therefore, MPV17 was also refolded into milder non-ionic detergents and the biophysical properties were compared to those in DPC. As no functional assay is available for MPV17, the protein folding was studied to monitor the integrity of the refolded MPV17 protein preparations.

Table 3-1: Overview of detergents used for MPV17 purification.

Detergent	CMC	Conc. (refolding)	Conc. (SEC)	Precipitation
C12E8	0.0048	0.5	0.02	purification
CYMAL-7	0.0099	0.5	0.05	purification
DDM	0.0087	0.5	0.02	purification

DPC	0.047	0.5	0.1	-
LMNG	0.001	0.5	-	refolding
OG	0.53	3	-	refolding
OGNG	0.053	0.5	-	refolding

As displayed in **table 3-1**, not all detergents were capable of stabilizing refolded MPV17. In octyl glucoside (OG) and the neopentyl glycols (LMNG and OGNG) MPV17 precipitated during refolding. As the amount of folded protein was too low for a subsequent SEC, only the remaining detergents C12E8 and the maltosides (Cymal-7 and DDM) were compared to DPC in further studies. The size exclusion chromatograms displayed homogenous MPV17 samples in all four detergents **(Fig. 3.3)**. The slightly varying elution volumes can be explained by the differing micelle sizes of the utilized detergents. As CYMAL-7 has been reported to form the largest micelles of ~78 kDa, MPV17 elutes from the column earlier than in the other detergents. Interestingly, while the refolded protein in DPC always contained a large species eluting from the column at void volume, which most likely consists of a misfolded aggregated species, the milder detergents lacked this second species. Considering the precipitation taking place in these mild detergents during different steps of purification, predominantly dialysis and thrombin cleavage, the yielded amounts of homogenous protein suggest that it is mainly the misfolded species which is lost to precipitation and therefore not visible in the size exclusion chromatogram.

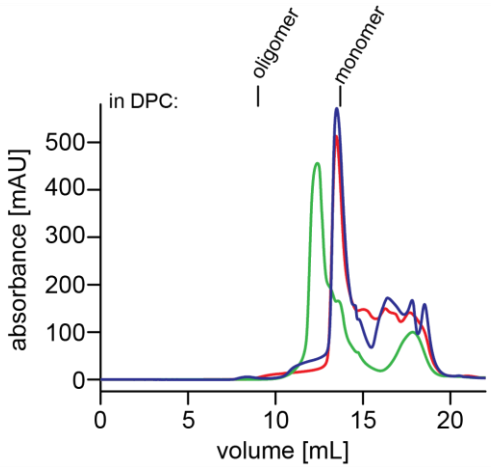

Figure 3.3: Size exclusion chromatograms of MPV17wt in C12E8 (red), DDM (blue) and CYMAL-7 (green). The retention volume of the monomeric and oligomeric species stabilized in DPC is indicated at the top for comparison.

Probed by far-UV CD spectroscopy, MPV17 displayed the characteristic minima for an α-helical secondary structure at 208 nm and 222 nm. As estimated with the $[\theta]_{MRW}$ value at 222 nm, the α-helical content was ~ 60 % for all detergents tested **(Fig. 3.4)**. Additionally, the thermal unfolding traces of MPV17 were measured by heating the sample while monitoring the CD signal at 222 nm. In these

experiments the apparent stability of MPV17 was lowest in C12E8 (42°C), followed by an almost identical behavior in both maltoside detergents (53 °C) and highest in DPC (73 °C).

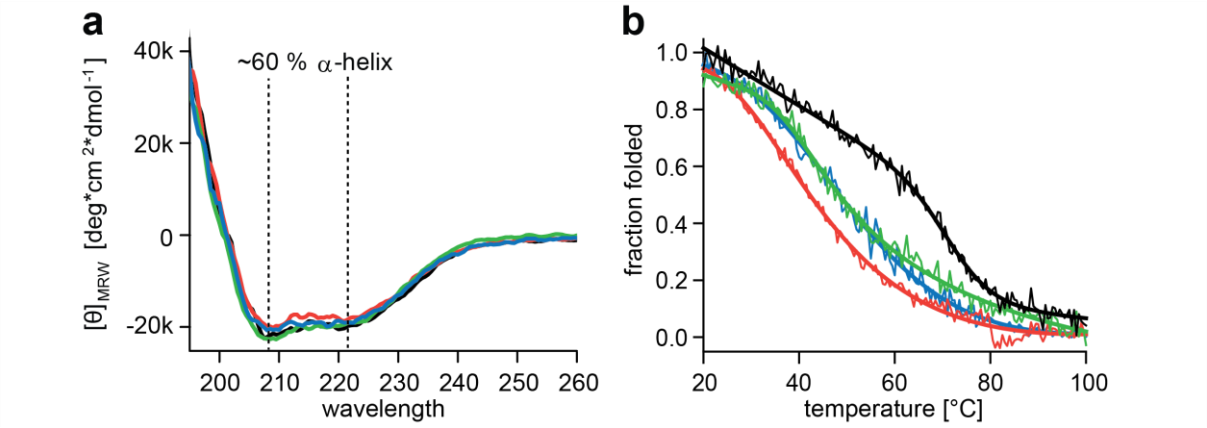

Figure 3.4: CD measurements of MPV17 in various detergents. (a) Far-UV CD spectra of MPV17 in detergent micelles. DPC (black), DDM (blue), CYMAL-7 (green), C12E8 (red). The minima at 208 and 222 nm show ~ 60% α-helical secondary structure for all conditions tested. (b) Unfolding traces of MPV17 in detergent micelles color coded in (a) monitored by far-UV CD spectroscopy.

The cooperative unfolding event seen for MPV17 in all detergents suggests that the protein is compactly folded in all preparations.

Next, 2D-[^{15}N,^{1}H]-TROSY NMR spectra of deuterated *U*-[^{2}H, ^{15}N]-MPV17 were recorded in the different detergents **(Fig. 3.5)**. All samples resulted in decent spectra with a similar NMR signal dispersion, which further supports the CD-data in suggesting that the structure of MPV17 is not strongly influenced by the chosen detergent. In order to evaluate, which detergent to proceed with for subsequent multidimensional NMR measurements, several criteria were compared. In an adequate spectrum, signal intensities are expected to be homogenous throughout the spectrum and the number of signals should roughly correspond to the 174 non-proline residues present in MPV17. As some regions are prone to signal overlay in 2D-spectra, it can be more reliable to compare the amount of well separated signals. This is the case for the tryptophan ε NH signals, which are separated from the backbone amide resonances (shown as an inset in the left lower corner) and the glycine backbone amide region located at the high-field edge of the ^{15}N dimension (105-110 ppm). While six out of seven tryptophan side chains were detectable in both DPC and C12E8, only 3-4 were distinguishable in the maltoside detergents. The sixteen glycines were visible only in DPC, while signals were missing when MPV17 was stabilized in the milder detergents. Furthermore, the signal intensities were homogenous only in DPC and the number of overall signals was clearly reduced in C12E8 and even more so in DDM and CYMAL-7. These differences can be explained by the reduced stability of MPV17 in the mild detergents, as probed by Far-UV CD spectroscopy. Consistent with their low melting temperatures, MPV17 partially precipitated during the NMR experiment measured at 37 °C, leading to a loss in protein concentration of up to 50%. This was not the case in DPC micelles, which is very beneficial for multidimensional NMR measurements requiring a sample to be stable for hours and days at elevated temperatures. Therefore, a more detailed NMR structural characterization of MPV17 was performed in DPC micelles.

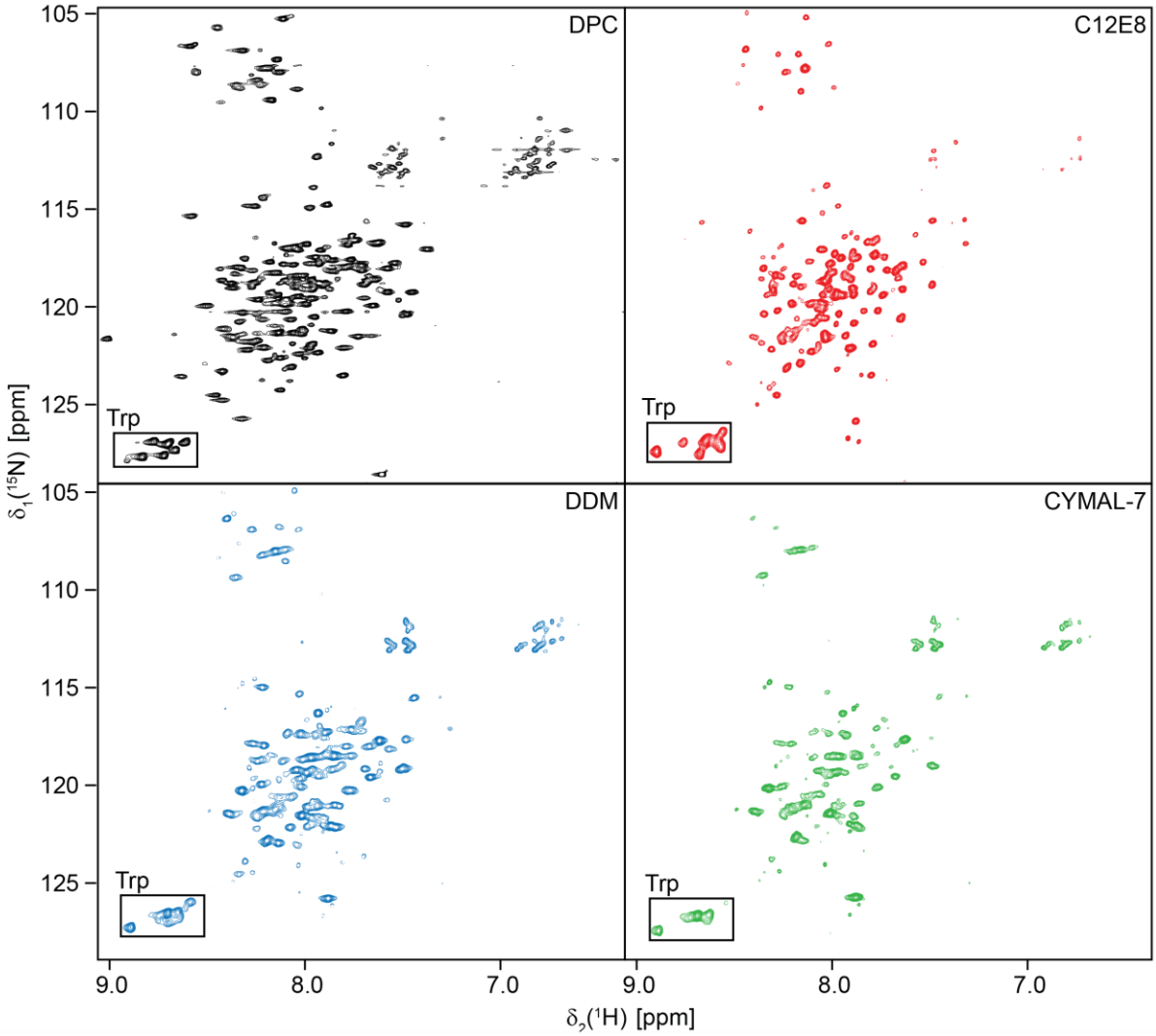

Figure 3.5: 2D-[^{1}H, ^{15}N]-TROSY spectra of MPV17 in different detergent micelles recorded at 310 K and 950 MHz. The samples were concentrated as follows: DPC – 140 µM, C12E8 – 72 µM, DDM – 77 µM, CYMAL-7 – 88µM. The respective insets show the tryptophan ε NH signals.

3.1.3 High-resolution NMR studies on MPV17 in DPC micelles

For the backbone resonance assignment, a *U*-[^{2}H, ^{13}C, ^{15}N]-labeled MPV17 sample in DPC micelles was used to record a set of 3D TROSY-based triple resonance experiments, consisting of HNCO, HN(CA)CO, HNCA, HN(CO)CA, HNCACB and a 3D-^{15}N-edited-[^{1}H,^{1}H]-NOESY experiment. The quality of these 3D NMR spectra was sufficient to assign 89% of the backbone amide resonances in the protein (**Fig. 3.6**).

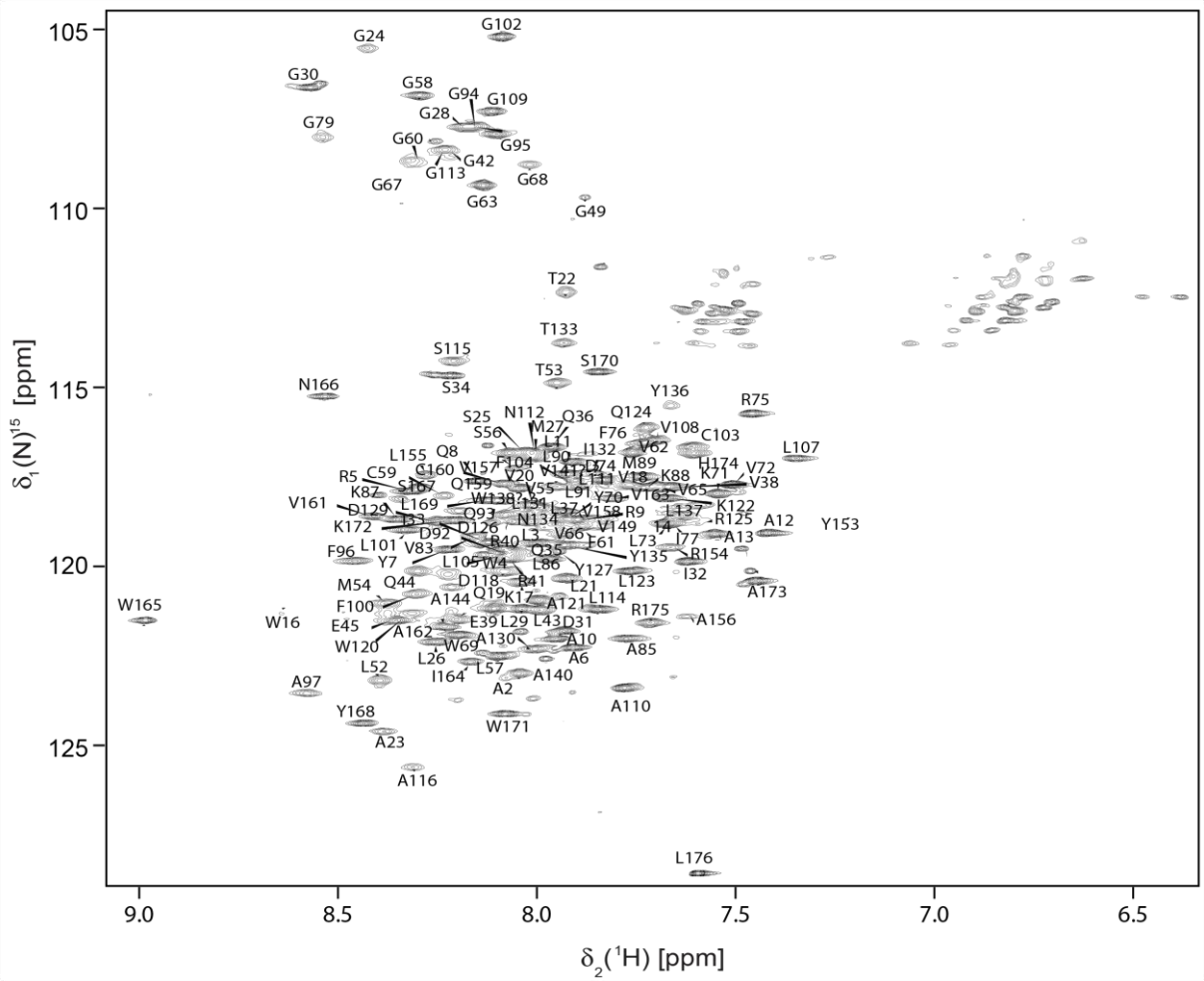

Figure 3.6: NMR backbone assignment of 500 µM MPV17 in DPC micelles recorded at 310 K on a 900 MHz NMR spectrometer.

The ^{13}C secondary chemical shift information enabled an almost complete estimation of the secondary structure content **(Fig. 3.7)**. The Cα and Cβ shifts suggest that MPV17 forms six α-helices, adding up to an α-helical content of ~ 65%, which confirms the CD data.

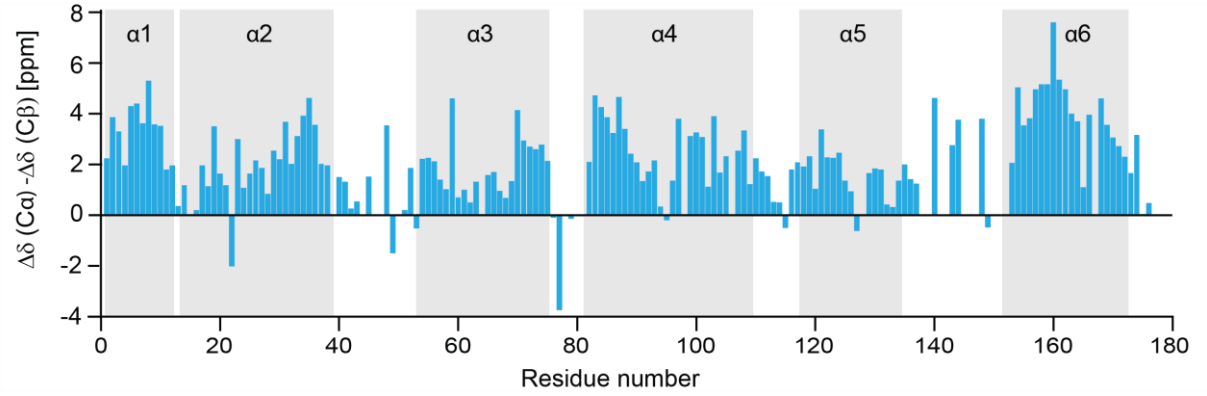

Figure 3.7: Secondary chemical shift data of MPV17 in DPC-micelles indicate a mainly α-helical secondary structure. The derived helical secondary structure elements are highlighted in gray. This measurement was performed by Dr. Franz Hagn.

Additionally, a {^{1}H}-^{15}N heteronuclear NOE experiment was recorded, to obtain information on the dynamics of MPV17 in the ns to ps time scale **(Fig. 3.8)**. As high hetNOE values (~ 0.8) describe rigid

structures, while low or negative values refer to flexible parts of the protein, the obtained pattern correlates well with the location of the experimentally determined α-helical secondary structure elements. The detected flexible residues correspond mainly to the assigned loop regions. This is supported by the calculated order parameter profile based on chemical shift information, which agrees well with the ^{15}N-hetNOE results.

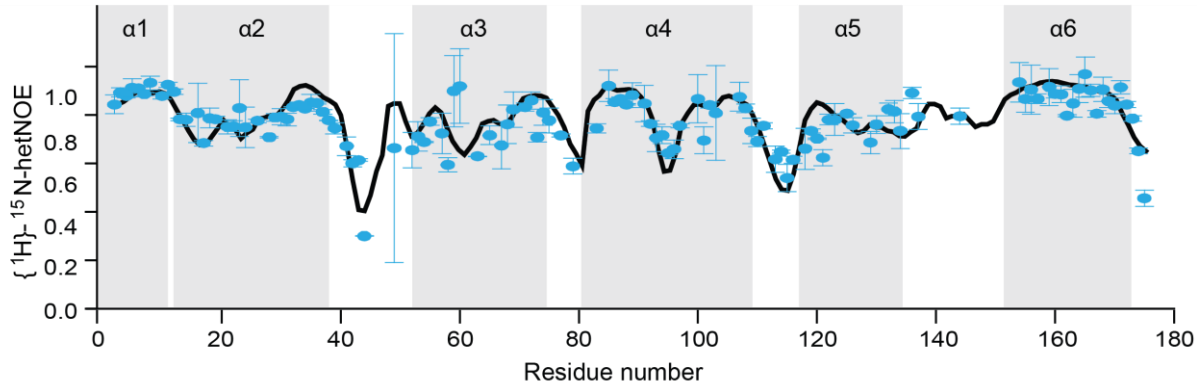

Figure 3.8: {^{1}H}-^{15}N-heteronuclear NOE data of MPV17 in DPC micelles support the secondary structure elements (highlighted in gray) determined by the secondary chemical shift data. High values indicate rigid regions and low values imply dynamical regions in the ns to ps time scale. The black line shows the predicted order parameter pattern calculated from the chemical shift data for comparison. This measurement was performed by Dr. Franz Hagn.

Furthermore, NMR paramagnetic relaxation enhancement experiments were used to probe the membrane localization of the secondary structure elements of MPV17 in the DPC micelle. The NMR peak intensities of the backbone amides were compared to the ones obtained after the respective paramagnetic agent was added **(Fig. 3.9)**. The paramagnetic properties of Gd^{3+}-chelated DOTA affect only those residues located outside the membrane, because the reagent is soluble in aqueous solution. In contrast, the spin-labeled fatty acid 16-doxyl-stearic acid (16-DSA) is hydrophobic and integrates into the DPC micelles. Thus, the residues of MPV17 located in the membrane region show reduced intensities. The intensity plot obtained with Gd^{3+}-chelated DOTA (green), shows the largest effects on signals that correspond to residues in MPV17 loop regions located outside of the determined secondary structure elements. Additionally, helix 5 seems to be in contact with the solvent, as it displays stronger effects than the other helices. In contrast, 16-DSA (blue) reduces the intensities predominantly in helical secondary structure elements. Supporting the data obtained with DOTA, helix 5 is less affected by 16-DSA.

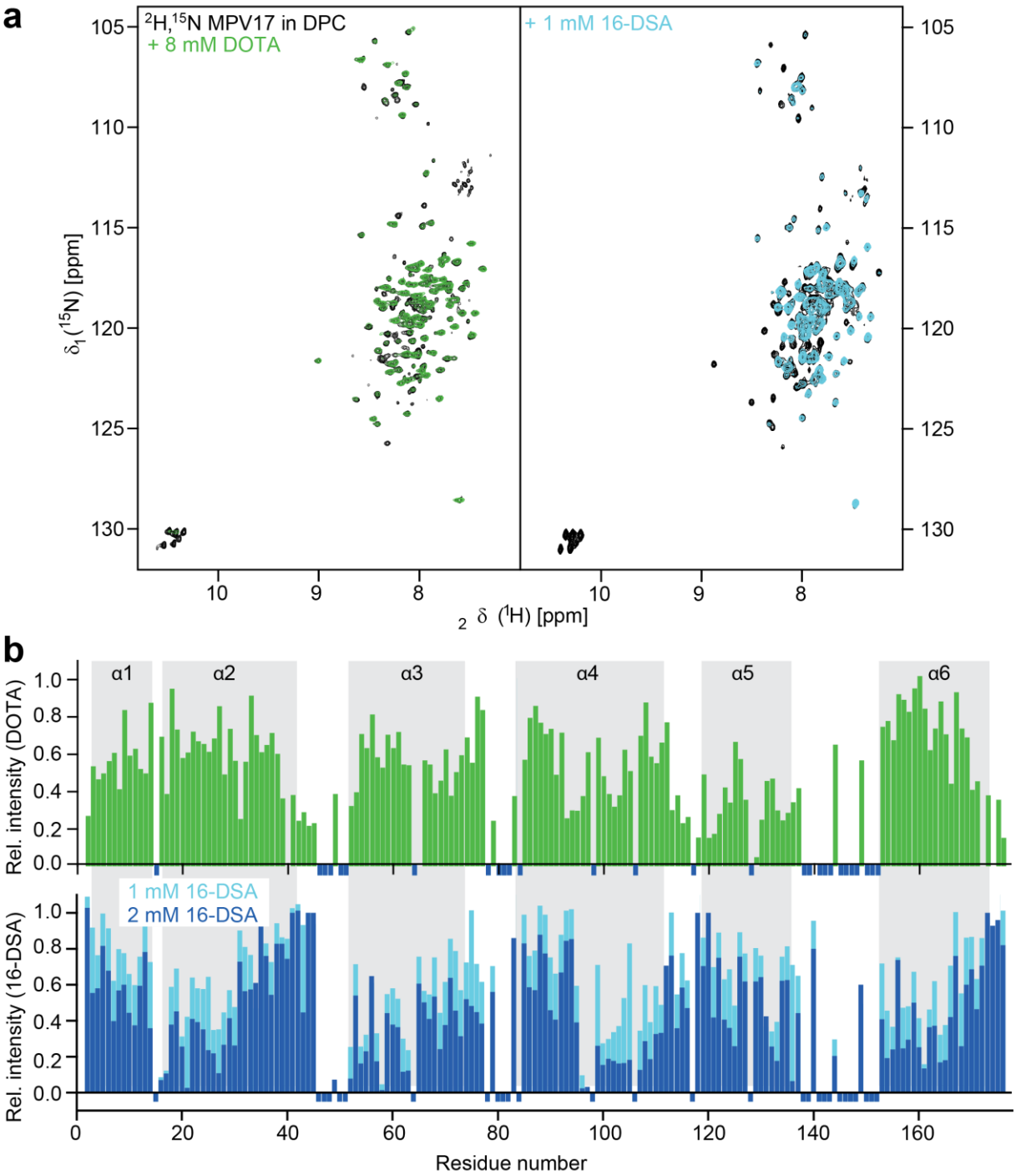

Figure 3.9: Membrane localization of MPV17 in DPC-micelles probed by paramagnetic relaxation enhancement. (a) 2D-[^{1}H, ^{15}N]-TROSY spectra of MPV17wt (black) overlayed with the spectra after 8 mM Gd^{3+}-chelated DOTA (green) or 1 mM 16-doxyl stearic acid (DSA) (blue) were added. (b) The relative NMR intensities of the spectra in (a) were plotted against the sequence. Water soluble DOTA leads to signal reduction of the solvent exposed residues, while the spin-labeled fatty acid DSA leads to signal reduction of the residues located within the DPC-micelle. Negative bars indicate unassigned residues. The secondary structure elements are highlighted in gray. These measurements were performed by Dr. Franz Hagn.

In order to determine the tertiary structure of MPV17 in DPC micelles, an ILVAFYM-labeled sample was produced and stabilized in deuterated DPC (d_{38}-DPC). HNH-, HCH-, CCH- and CNH-NOESY-experiments were recorded for assigning the 2D-[^{13}C-^{1}H]-HMQC spectrum and deriving distance restraints for structure calculations **(Fig. 3.10)**. However, the methyl signals displayed a very low

chemical shift dispersion rendering an NMR-based structure determination very difficult. The only residues with some dispersion are those influenced by nearby side chains with ring-currents, as seen for L169 in the low-field region of the spectrum which shows a cross peak for the W165 side chain in the HCH-NOESY (not shown). For these measurements, the alanines were uniformly protonated with a ^{13}C-label at the C_β-position. Therefore, no alanine NH-backbone signals were visible in the TROSY and their methyl groups showed peak splitting due to coupling to the neighboring nuclei. As seen in the NOESY-strips of A110 and L111, no long-range contacts were visible. The only cross-peak not referring to the own or neighboring side chain is the cross-peak to water at ~4.7 ppm. Due to this lack of long-range contacts and many residues not being assignable because of the severe signal overlap for monomeric MPV17 in DPC-micelles, this approach was not further pursued.

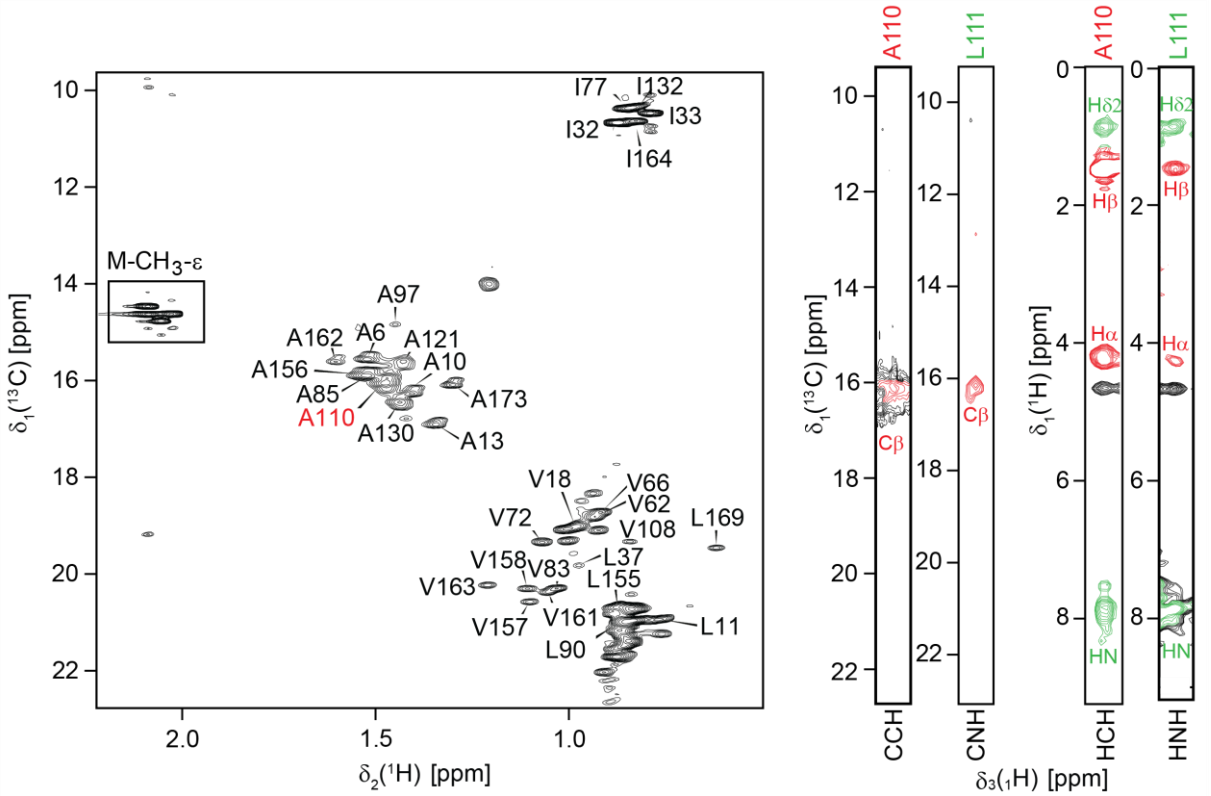

Figure 3.10: Methyl group assignment of ILVAFYM-MPV17 in *d*$_{38}$-DPC. Left: The 2D-[^1H, ^{13}C]-HMQC spectrum with the assigned alanine-C_β, isoleucine-$C_{\delta2}$, leucine-$C_{\delta2}$ and valine-$C_{\gamma2}$ methyl groups. The four methionine-C_ε methyl groups are visible but could not be assigned due to a lack of NOE contacts. The NOESY-strips leading to the assignment of A110 are depicted on the right. The assigned peaks are color coded for A110 (red) and L111 (green). The respective NOESY experiment is indicated at the bottom. The measurements were conducted on a 290 µM sample at 310 K and 950 MHz.

3.1.4 Stabilizing MPV17 in native-like membrane mimetics

After it turned out that an NMR-based structure calculation with MPV17 in DPC micelles is difficult, a more native membrane mimetic was sought to stabilize this membrane protein. Therefore, MPV17 was transferred to amphipoles, phospholipid nanodiscs and liposomes, using MPV17 in DPC micelles as a starting material in all cases.

3.1.4.1 Stabilizing MPV17 in amphipoles

Amphipoles are amphipathic polymers that are short and flexible. They bind to the hydrophobic transmembrane parts of a membrane protein with a very small K_D[40]. Therefore, they do not dissociate from the protein and can be diluted unlike detergents, which must be present above the CMC in order to prevent precipitation of the membrane protein. Compared to detergents, amphipoles have been found to stabilize membrane proteins forming particles similarly homogenous as detergents, which is an important requisite for NMR studies. A8-35, the amphipol used in this study, forms 40 kDa large hydrated particles in solution[214], which makes it larger than DPC micelles, but still in a range which can be used for solution-state NMR.

In the first step, MPV17 was transferred to amphipoles in the presence of a reducing agent. The SEC showed a homogenous peak at an elution volume corresponding to a molecular weight of ~ 150 kDa **(Fig. 3.11)**. The thermal unfolding profile further revealed a higher stability than in detergent micelles. This has been described for amphipoles before and facilitates NMR studies at the high temperatures necessary for good spectra of large proteins[40].

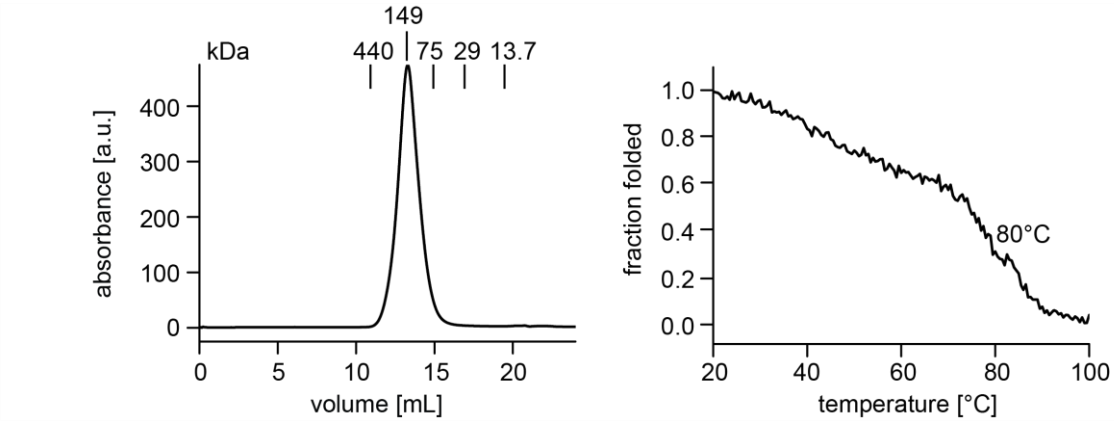

Figure 3.11: Left: SEC of MPV17 in amphipoles in the presence of 5 mM DTT. Right: Far-UV detected thermal unfolding at 222 nm in amphipoles.

Therefore, a 2D-[^{15}N,^{1}H]-TROSY spectrum was recorded of ^{2}H,^{15}N-labeled MPV17 in amphipoles **(Fig. 3.12)**. While the overall dispersion of the backbone signals is similar to the spectra in DPC micelles, the sample homogeneity appears strongly decreased with severe line broadening reducing the quality of the spectrum.

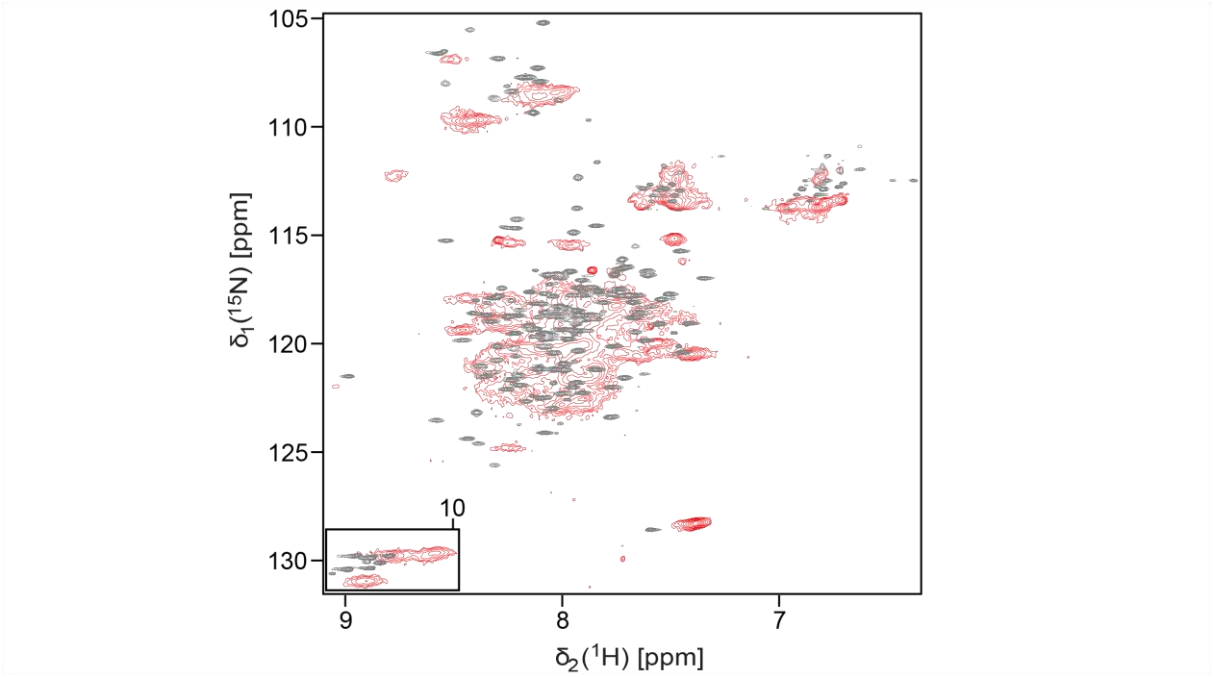

Figure 3.12: 2D-[^{1}H, ^{15}N]-TROSY spectrum of MPV17 in amphipoles (red) superimposed with the MPV17 spectrum in DPC micelles (gray). Both spectra were measured at 600 MHz and 310 K.

One explanation for the severe line broadening observed during NMR measurements could be the size of the MPV17 particles. According to the SEC, MPV17 is unlikely to be a monomeric protein in amphipoles. To capture a picture of this presumably oligomeric protein assembly, negative stain EM images were recorded **(Fig. 3.13)**. Initial images stained with uranyl acetate **(a)** revealed small protein particles of 10 – 20 nm. As MPV17 is expected to form a pore, the sample was next stained with uranyl formate **(b)**. Due to its smaller grain size, this stain has been shown to penetrate small pores, resulting in a black dot in the middle of the protein[215]. For MPV17, this stain also showed protein-like particles sized at 10-20 nm consistent with the earlier results, but so far no pore could be observed in the middle.

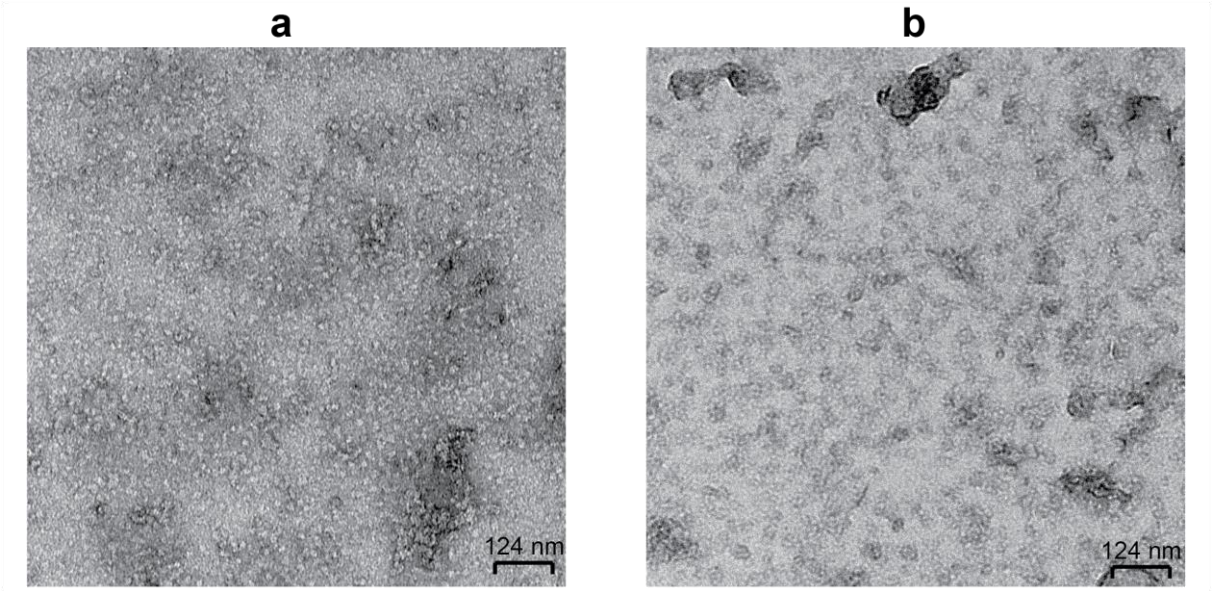

Figure 3.13: Negative stain EM images of MPV17 in amphipoles stained with uranyl acetate (a) and uranyl formate (b). The negative stain EM measurements were conducted by Dr. Tilak Gupta (MPI of Biochemistry, Martinsried).

In order to evaluate whether a disulfide-linked oligomer was stabilized in amphipoles, the cysteine free version of MPV17 and the wild type MPV17 without reducing agent were transferred to amphipoles and the size was characterized by SEC **(Fig. 3.14)**. There, no cysteine-dependent size changes could be observed.

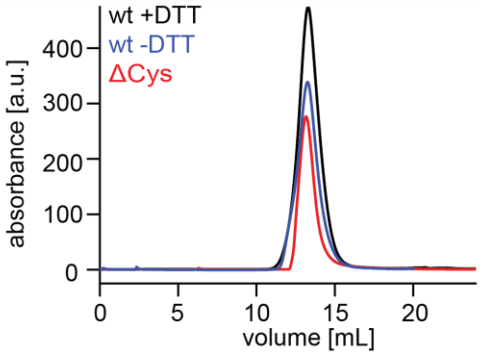

Figure 3.14: Overlay of SEC profiles of MPV17 in amphipoles with 5 mM DTT (black), no DTT (blue) or MPV17ΔCys (red).

3.1.4.2 Stabilizing MPV17 in phospholipid nanodiscs

Furthermore, an assembly into phospholipid nanodiscs was attempted. Unfortunately, MPV17 could not be stabilized in ΔH5 (8 nm[45]), 1D1 (10 nm) or 1E3D1 (12 nm) nanodiscs, suggesting that it forms larger oligomeric species in lipids, which are not compatible with the up to 12 nm large nanodiscs utilized for this purpose. After increasing the concentration of the reducing agent DTT to 10 mM, finally a small amount of GB1-MPV17 filled nanodiscs could be purified **(Fig. 3.15)**. However, even 50 mM DTT could not increase the yield to amounts enabling further studies. At least, a comparison of the size exclusion chromatograms before and after Thrombin cleavage shows the expected delayed elution indicating a lower apparent weight for the cleaved protein. These data suggest that MPV17 can be inserted in phospholipid nanodiscs, but the strong and at least partial cysteine-mediated oligomerization in a lipidic environment leads to low yields.

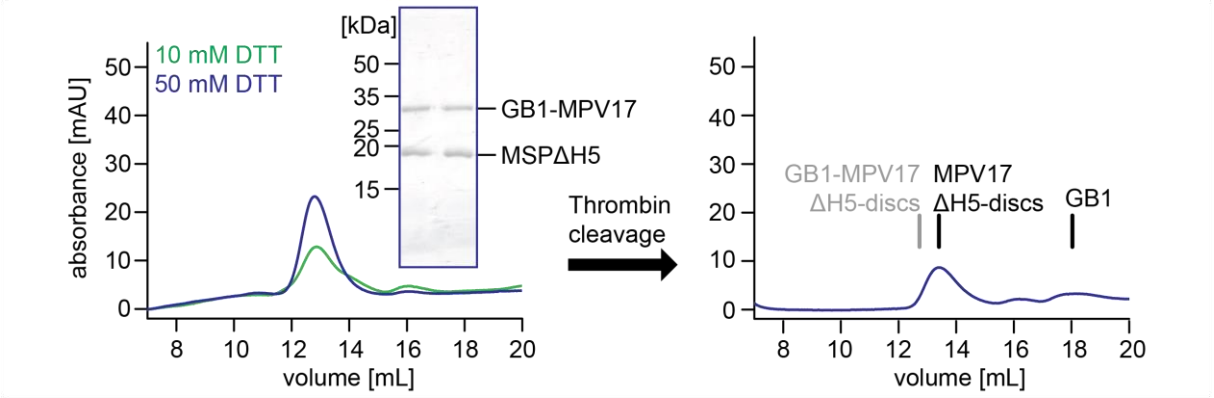

Figure 3.15: SEC of nanodisc assemblies with MPV17 in ΔH5-nanodiscs with 10 mM DTT (green) and 50 mM DTT (blue) resulted in small yields of GB1-MPV17 filled nanodiscs. The inset shows the SDS-PAGE of the peak fractions after SEC for the assembly in 50 mM DTT with the molecular weight marker indicated on the right. After thrombin cleavage and the second SEC the yields of MPV17 in ΔH5-nanodiscs were too low for further characterization. As indicated, the elution volume of the filled nanodiscs shifted too lower molecular weights after

GB1 was cleaved and a second peak eluting GB1 appeared. The elution volume of uncleaved GB1-MPV17 in ΔH5-nanodiscs is shown in gray for comparison.

In the next step, the cysteines in MPV17 were blocked by Methyl-methanethiosulfonate (MMTS), which methylates the sulfhydryl groups of cysteine side chains (met-MPV17). In this setup, the formation of disulfide bonds is prevented, which presumably destabilizes the larger oligomers forming in a lipid environment. Indeed, when the nanodisc assembly was repeated under the conditions used for the unmodified wild type MPV17, yields strongly increased **(Fig. 3.16)**. The same effect could also be achieved by using the cysteine-free variant, MPV17ΔCys. Thus, when cysteines are replaced or blocked, MPV17 can be stabilized in phospholipid nanodiscs, presumably due to reduced oligomerization.

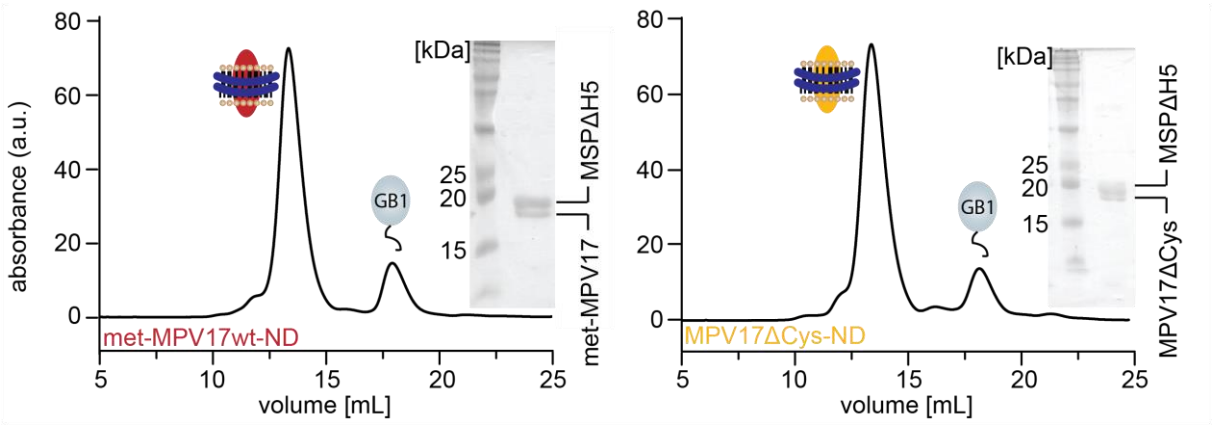

Figure 3.16: SEC profiles of methylated MPV17 (left) and MPV17ΔCys (right) in ΔH5-nanodiscs after GB1 cleavage. As indicated by the cartoons, the larger peaks contain the filled nanodiscs, while the smaller peak detects the GB1. The SDS-PAGE shows the respective peak fraction of the nanodisc peak.

To quantify the average amount of the respective MPV17 variant per nanodisc, the GB1 proteolysis assay, described in **Chapter 2.1.1.2 Production and Characterization of Bak-TMH**, was applied [178]. As the first two lines in **Table 3.2** show, the average number of the MPV17 variant per ΔH5-nanodisc was almost identical for both met-MPV17 and MPV17ΔCys. More than 1.4 MPV17 molecules assembled into nanodiscs even at lipid nanodisc assembly conditions that would favor the incorporation of a monomer, suggesting that MPV17 also tends to oligomerize, when no disulfide bonds are formed. When larger nanodiscs and MPV17-to-MSP ratios facilitating the incorporation of more than one MPV17 were used, on average almost three MPV17 monomers were incorporated. Additionally, these experiments indicate that the lipid composition might have an influence on the oligomerization of MPV17. The assemblies into ΔH5-nanodiscs show that the negatively charged and dimeric lipid cardiolipin (CL), which is highly abundant in the inner mitochondrial membrane seems to impede the incorporation of an oligomer. In contrast, about double the amount of MPV17 is incorporated into nanodiscs, when cardiolipin was substituted for the negatively charged monomeric lipid DMPG.

Table 3.2: Overview of the different MPV17 nanodisc assemblies. The assembly ratios, lipids and MSP constructs were varied, resulting in similar amounts of MPV17 per disc for both MPV17 samples. (PC/PG = 75 % DMPC + 25 % DMPG; PC/CL = 80 % DMPC + 20 % Cardiolipin)

Ratio assembly	MPV17 construct	MSP construct	Lipid mix	MPV17 per disc
1:2	ΔCys	ΔH5	PC/CL	1.45
1:2	met	ΔH5	PC/CL	1.42
1:4	ΔCys	1E3D1	PC/CL	1.44
1:2	ΔCys	1E3D1	PC/CL	1.69
1:1	ΔCys	1E3D1	PC/CL	2.68
1:2	met	1E3D1	PC/CL	1.58
1:2	ΔCys	ΔH5	PC/PG	3
1:4	ΔCys	ΔH5	PC/PG	2

Next, CD-detected thermal unfolding experiments were performed with MPV17 in nanodiscs, to assay the MPV17 folding state (**Fig. 3.17)**. The two-step unfolding showed a thermal stability of both MPV17 species of about 60 °C followed by the unfolding transition of the MSP ΔH5 at > 70 °C.

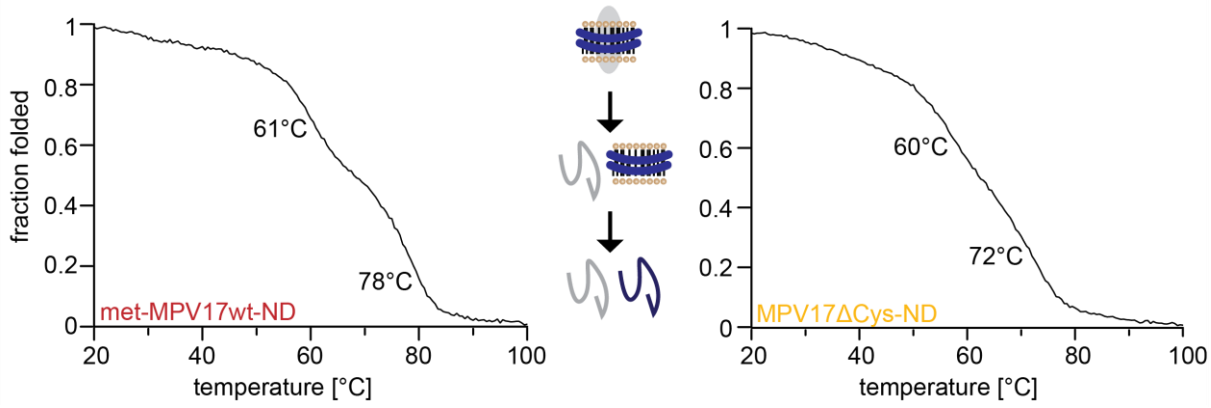

Figure. 3.17: Far-UV detected thermal unfolding of met-MPV17wt (left) or MPV17ΔCys (right) in ΔH5-nanodiscs shows the unfolding of the membrane protein at ~ 60 °C and of MSP ΔH5 at >70 °C.

In addition to the CD-spectroscopic analysis, $^{2}H,^{15}N$-labeled MPV17ΔCys was inserted into MSP1ΔH5 nanodiscs to record a 2D-[$^{15}N,^{1}H$]-TROSY spectrum (**Fig. 3.18**). The obtained spectrum (orange contour lines) showed a very similar backbone amide signal dispersion as in DPC micelles (grey contour lines), indicating that the overall structure of the MPV17 monomer is not heavily altered by the chosen membrane mimetic. The line broadening effects could be caused by the not purely monomeric MPV17

nanodisc preparation, which adds additional heterogeneity. Furthermore, taking into account the proposed oligomeric functional form of MPV17, it seems likely that monomeric MPV17 trapped in small lipid nanodiscs would show an enhanced level of exchange dynamics in the intermediate regime as compared to a more stable oligomer, further leading to line broadening effects. Thus, the monomeric form of MPV17 is likely to represent the inactive species that, upon stimulation, needs to assemble into more stable membrane pores.

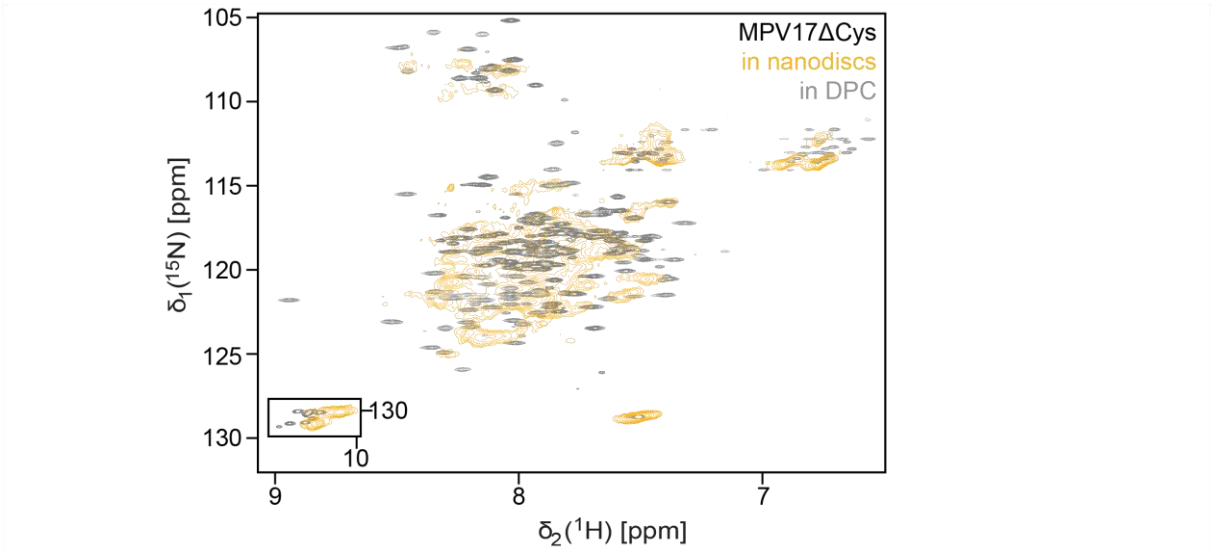

Figure 3.18: 2D-[^{1}H, ^{15}N]-TROSY spectrum of MPV17ΔCys in ΔH5-nanodiscs assembled with DMPC/DMPG-lipids measured at 306K (orange) superimposed with the MPV17ΔCys spectrum in DPC micelles measured at 310 K (gray). The spectrum of MPV17ΔCys in DPC-micelles was measured by Dr. Franz Hagn.

3.1.4.3 Stabilizing MPV17 in liposomes

Finally, MPV17 was stabilized in liposomes. As the lipidic double layer formed by this membrane mimetic is the most native, MPV17 should be the least restrained and chances for it forming an oligomeric structure could be the greatest. For a stable insertion into liposomes, MPV17 required a slow transition from DPC-micelles to POPC/CL (80/20) liposomes. Thus, when the detergent was removed quickly by Biobeads™, it precipitated. The protein could only be transferred to liposomes by dialysis. Far-UV CD measurements show an α –helical secondary structure content and melting temperature **(Fig. 3.19)** similar to what was also seen in micelles **(Fig. 3.4)**, suggesting that the secondary structure determined by NMR in DPC micelles could be native even if the helical elements do not tightly fold into a tertiary structure in a micellar environment. Furthermore, the thermal melting temperature in liposomes matches the one seen for the modified MPV17 in nanodiscs **(Fig. 3.17)**.

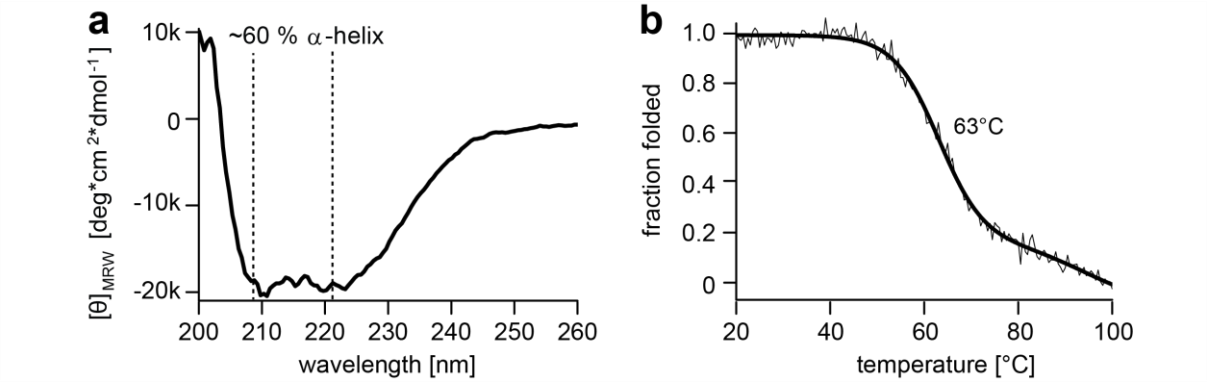

Figure 3.19: Far-UV CD spectroscopy on MPV17 in liposomes (POPC/CL – 80/20). The CD spectrum indicates an α-helical secondary structure (a) that unfolds at ~63°C (b).

3.1.5 Probing the effect of cysteines on the MPV17 structure and oligomeric state

Since the nanodisc assemblies suggested an impact of cysteines on the oligomeric state of MPV17, their effect on the protein structure and oligomerization was studied in more detail. For this, both the wild type protein and the cysteine-free version were compared in DPC-micelles, as the most structural data could be gained in this membrane mimetic. Compared to the SEC of MPV17 in **Fig. 3.2**, MPV17ΔCys behaves very similarly **(Fig. 3.20a)**. It yields a homogenous peak, a high purity as probed by SDS-PAGE and the SEC-derived molecular weight of ~ 98 kDa is identical for both constructs. They only differ in the first peak at ~ 50 mL, which is absent in the chromatogram of MPV17ΔCys, suggesting that less oligomerization/agglomeration takes place without cysteines.

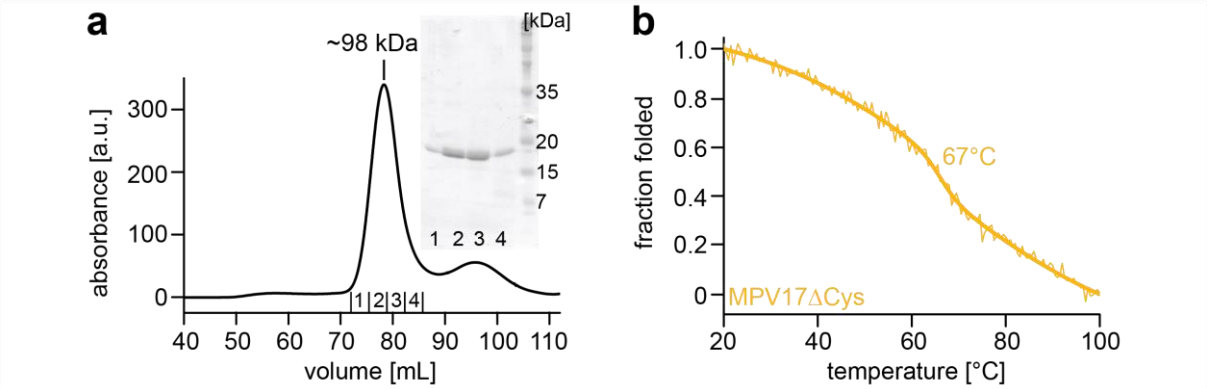

Figure 3.20: SEC (a) and far-UV CD detected thermal unfolding (b) of MPV17ΔCys in DPC-micelles.

Comparing the Far-UV CD melting curves for both protein constructs, reveals an only slightly increased stability for MPV17wt at 73 °C **(Fig. 3.4)** as compared to MPV17ΔCys at 67 °C **(Fig. 3.20b)**. Taken together, these initial data on MPV17ΔCys in DPC-micelles suggest that the cysteine residues do not play a critical role for the folding and the stability of the MPV17 monomer.

When considering the location of the four cysteine residues (C59, C99, C103, C160) in respect to **Figures 3.7 and 3.9**, it becomes evident that all four cysteines are located within α-helical structures and do not show enhanced dynamics in the ns to ps time scale (high ^{15}N-hetNOE values). Furthermore, all cysteine residues are heavily affected by 16-DSA indicating a location inside the hydrophobic membrane area. The α-helical geometry also suggests that C99 and C103 are pointing toward the same side in α-helix 4, which could be relevant for the formation of inter- or intra-monomer disulfide bridges most likely in the membrane.

Thus, the question arises whether all four cysteines are accessible for blockage by the MMTS label and potentially contributing to the assumed intermolecular disulfide bonds inhibiting nanodisc assemblies with the wild type protein. For this, the cysteines in MPV17 were methylated by ^{13}C-labelled MMTS and a 2D-[^{13}C-^{1}H]-HMQC was recorded to detect the number of methyl groups **(Fig. 3.21)**. Four methyl groups appeared in contrast to the buffer reference sample, indicating that all four cysteines are labelled by MMTS. Thus, all four cysteines potentially could be contributing to the formation of higher oligomers.

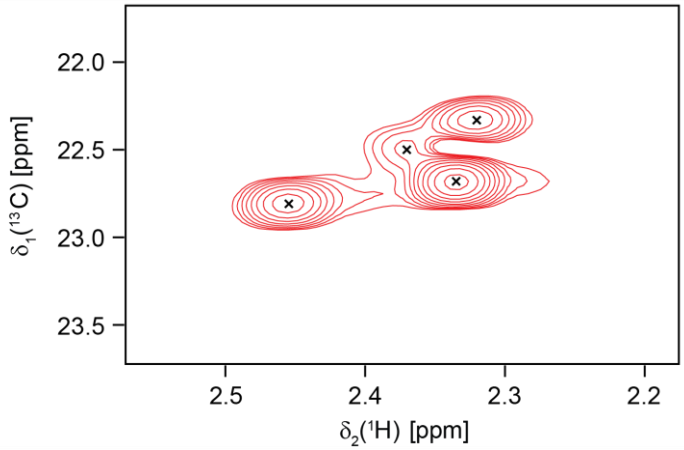

Figure 3.21: 2D-[^{1}H, ^{13}C]-HMQC spectrum of MPV17 labelled with ^{13}C-MMTS shows that all four cysteines are accessible to labelling.

In order to obtain a better understanding of the role, the cysteine residues have on the MPV17 structure, a sequence specific NMR backbone resonance assignment was performed for both the methylated MPV17wt (met-MPV17wt) and MPV17ΔCys in DPC micelles (**Fig. 3.22**). These backbone amide signal positions were compared to MPV17wt in a 2D-[^{15}N,^{1}H]-TROSY experiment using chemical shift perturbation (CSP) plots. In met-MPV17wt the CSP effects are more broadly distributed around the modified cysteine residues than for MPV17ΔCys, for which the CSP pattern is sharply clustered around the mutated cysteine residues. This verifies the insights gained in **Fig. 3.21**, suggesting that all four cysteines are labelled by the MMTS label. Apparently, the incorporation of the additional -SCH_3 moiety instead of the substitution of cysteines by the smaller alanine, leads to minor steric clashes as well as to changes in the electronic properties of the cysteine residues, which more heavily affects neighboring regions. All in all, the overall peak distribution is not greatly varied and the cysteine variations do not

seem to affect the overall protein fold. This supports the CD-findings suggesting that the overall fold is not changed by the removal of cysteines.

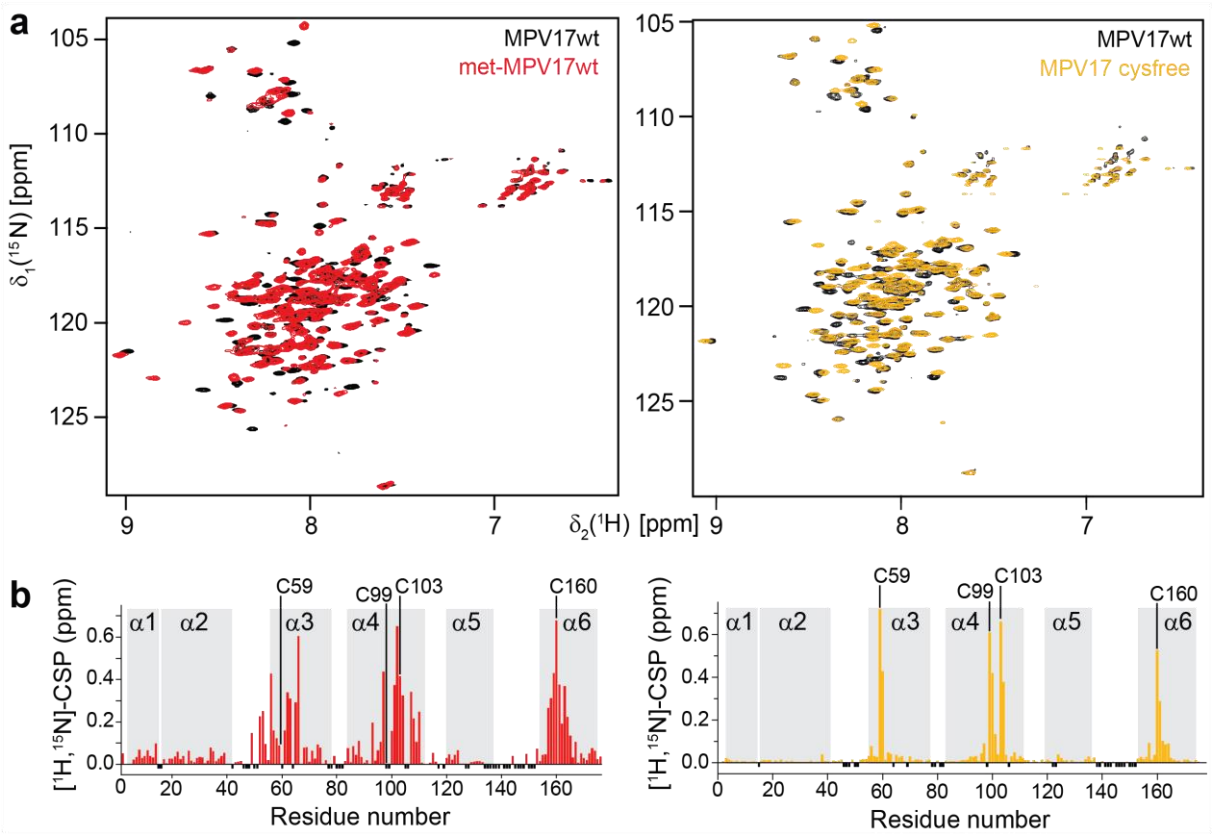

Figure 3.22: NMR analysis of cysteine-modified and cysteine-free MPV17 in DPC-micelles. (a) Overlay of 2D-[^{1}H, ^{15}N]-TROSY spectra of MPV17-wt (black) and cysteine-methylated MPV17-wt (red) or cysteine-free MPV17 (yellow). (b) NMR chemical shift perturbation plots of met-MPV17-wt (red) and MPV17-cysfree (yellow) using MPV17wt as a reference. The location of α-helical secondary structure elements is highlighted in gray and the positions of the four cysteines are marked accordingly.

Next, the effect of the cysteine residues on MPV17 oligomerization was probed by studying the impact of the reducing agent DTT. First, NMR experiments were performed at reducing and non-reducing conditions using *U*-[^{2}H, ^{15}N]-MPV17 in DPC micelles. As shown in **Fig. 3.6**, MPV17 shows a well resolved spectrum under reducing conditions (**Fig. 3.23a**). However, the absence of a reducing agent resulted in marked line broadening and signal disappearance. Comparing both spectra in an NMR signal intensity plot revealed that residues located near cysteines were the most affected. These pronounced effects suggest the formation of dimers or even larger oligomers even in DPC-micelles, when the cysteines can form disulfide bridges.

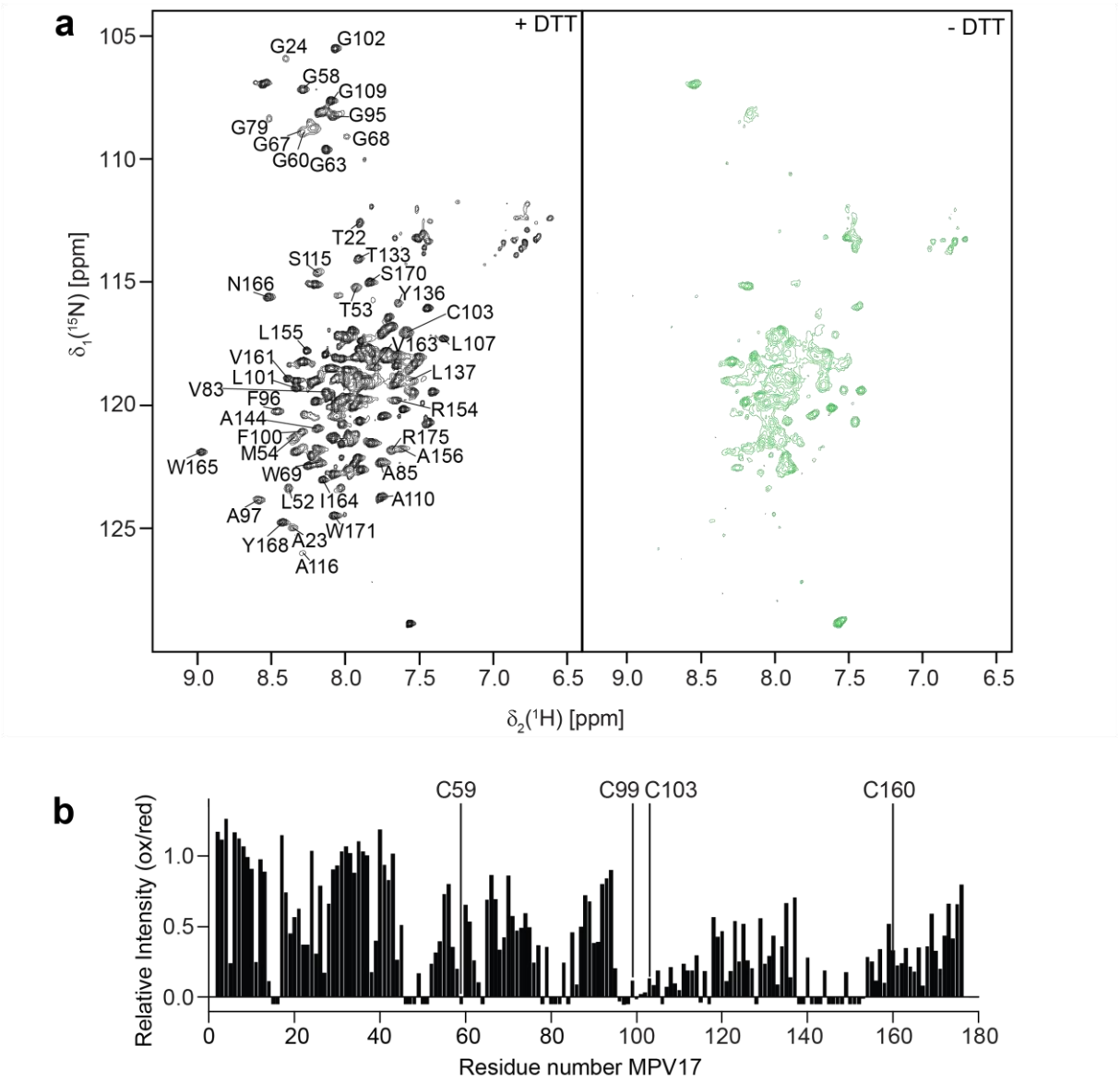

Figure 3.23: (a) 2D-[^{1}H, ^{15}N]-TROSY spectra of 170 µM MPV17 in the presence of 5 mM DTT (black) and after DTT was removed by dialysis (green). Spectra were measured at 310 K. The assigned peaks refer to the signals disappearing in the absence of a reducing agent. (b) NMR signal intensity plot of the spectra shown in (a). Negative bars indicate missing signals or resonance assignments.

These results were further supported by the size exclusion chromatograms performed after the NMR measurements **(Fig. 3.24)**. While the reduced sample showed an unchanged SEC profile after the measurement, the oxidized sample displayed an only small monomeric peak with most of the protein eluting earlier indicative of a higher oligomeric condition.

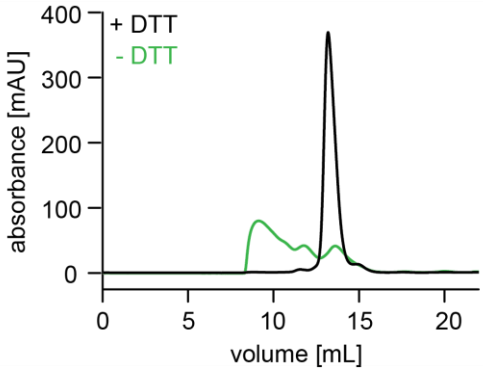

Figure 3.24: Size exclusion chromatograms of DN-MPV17 in DPC-micelles after the NMR measurements shown in Figure 3.23.

To study these oligomerization tendencies in more detail, crosslinking assays were performed in both DPC-micelles and the more native liposomes. First, the oxidizing agent Cu^{2+}-phenanthroline (Cu/phen) was used to monitor the cysteine-dependent crosslinking of MPV17wt in DPC micelles and POPC:CL liposomes (**Fig. 3.25**)[216]. These experiments, performed in the absence of reducing agents, showed a monomeric and dimeric band for MPV17 in DPC micelles, but surprisingly no higher oligomers, independent of the presence of Cu/phen. This difference to the NMR measurements and subsequent SEC suggesting higher oligomers can most likely be explained by the 10-fold lower concentration and lower temperature (293 K instead of 310 K) used in the crosslinking experiments. In liposomes mainly monomeric MPV17 was present before the oxidizing agent was added, probably due to a shorter storage time before the crosslinking was performed. However, once Cu/phen was added, the formation of dimers and of higher oligomeric species could be detected in liposomes. These data again show that the cysteines in MPV17 are prone to form disulfide-bonds, suggesting that oxidative stress could induce oligomerization.

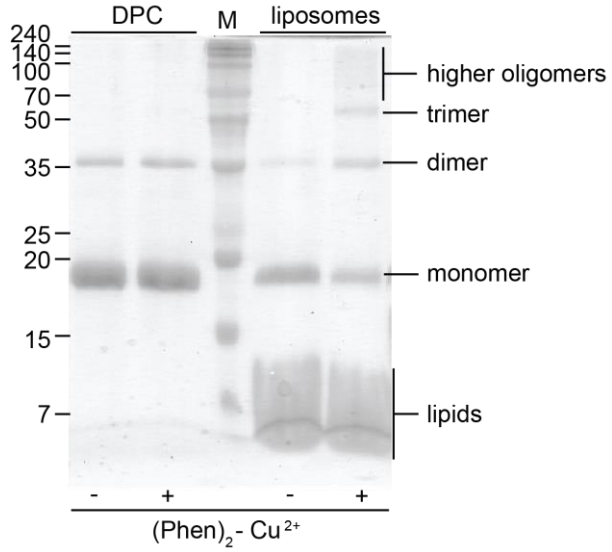

Figure 3.25: SDS-PAGE after Cu/phen mediated crosslinking of MPV17 in DPC-micelles and POPC:CL liposomes after eliminating the reducing agent. The molecular weight marker (M) in the middle is labelled on the left in [kDa], while the visible bands are explained on the right.

To verify these results, crosslinking experiments were also performed with the amino-selective crosslinker BS^3. This enabled the investigation of oligomeric tendencies in the presence and absence of DTT (**Fig. 3.26**). Consistent with the NMR spectrum and SEC profile in **Fig. 3.23** and **Fig. 3.24**, predominantly monomeric MPV17 could be detected in DPC micelles, when the cysteines were reduced by DTT. Also in liposomes, the presence of DTT enabled only limited crosslinking, resulting in a faint band of dimeric MPV17 on the SDS-PAGE gel. When no DTT was added, large oligomeric species were crosslinked by BS^3, similar to the results seen for the cysteine-mediated crosslinking experiments. These data further highlight the role of MPV17 as a redox-regulated protein.

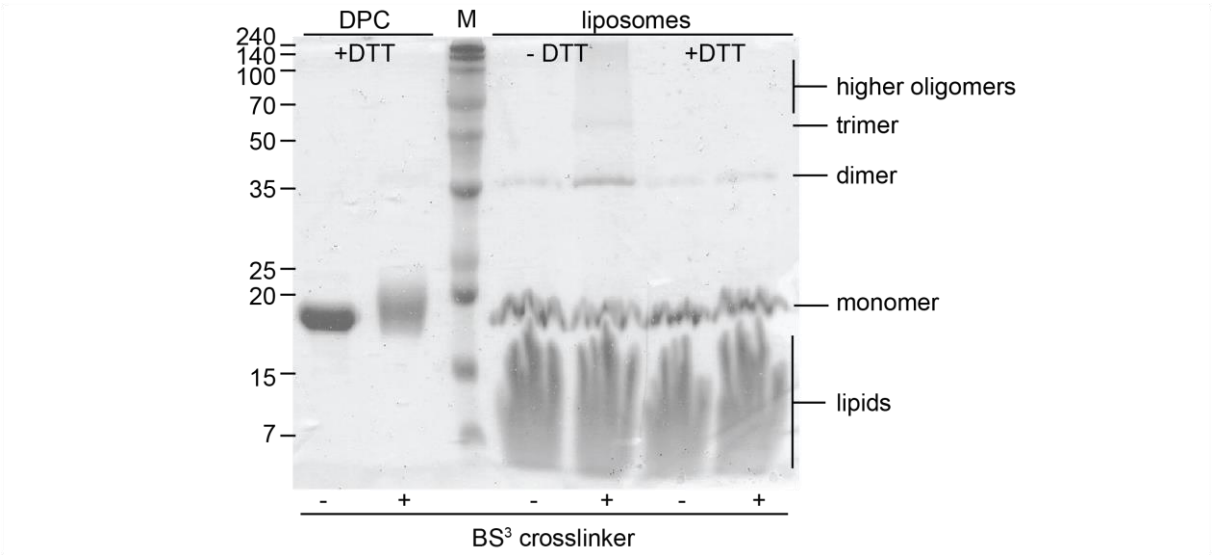

Figure 3.26: SDS-PAGE of amino selective crosslinking of MPV17 in DPC micelles and liposomes with BS^3 in the presence or absence of the reducing agent DTT.

3.1.6 Effect of disease-linked mutations on oligomerization

Several mutations in MPV17 have been linked to diseases such as the hepatocerebral form of the mitochondrial-DNA-depletion syndrome (MDDS)[164,165]. In order to study the differences encountered by disease-related mutations, three prototype variants (R50W, Q93P and N166K[152,217]) were produced. The expression and purification were performed analogue to the wild type protein, resulting in monomeric protein and a larger oligomeric species. The data for the variants and wild type MPV17 were summarized in **Table 3.3**. While the elution volumes and the derived molecular weight was comparable for the homogenous peak in all samples, the overall yields varied strongly. MPV17-R50W expressed most strongly, followed by MPV17-Q93P. For these variants, the void peak was about as high as the monomeric peak, suggesting that higher concentrations result in more oligomerization/agglomeration. The variant MPV17-N166K expressed comparable to the wild type protein. All variants showed identical amounts of α-helical secondary structure **(Fig. 3.27)**, suggesting the folding is not hampered by the mutations.

Table 3.3: SEC profile analysis of MPV17 and its disease related mutants, run on a Superdex 200 Increase 10/300.

MPV17 construct	Elution volume [mL]	Calculated MW [kDa]	Peak height [mAU]	Peak height void [mAU]
wt	14.33	~ 95	820	120
R50W	14.59	~ 85	1205	1195
Q93P	14.46	~ 90	840	705
N166K	14.48	~ 89	695	185

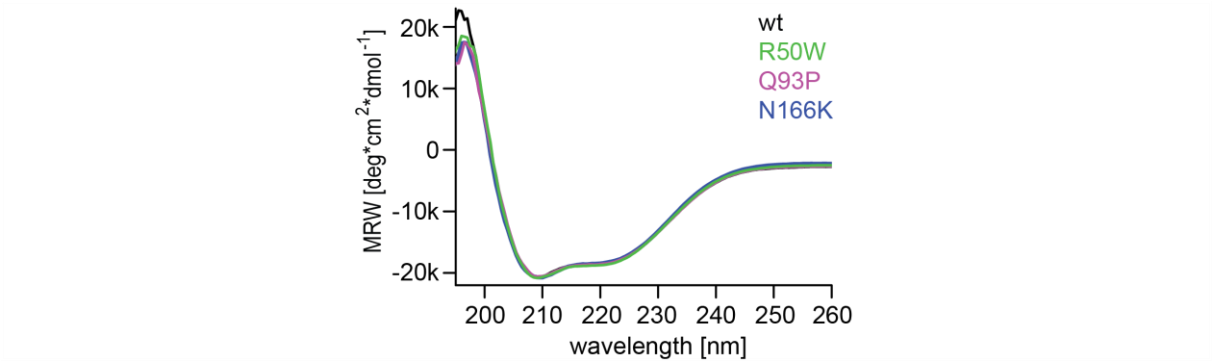

Figure 3.27: The far-UV CD spectra of MPV17wt and its disease related mutants R50W, Q93P and N166K suggest a very similar fold in all variants in DPC micelles.

Assuming that the functionality of MPV17 is strongly linked to its oligomeric state, the mutants' oligomerization tendency was studied by applying the lipid nanodisc assay. In contrast to MPV17wt, which could only be incorporated into MSP1ΔH5 lipid nanodiscs in very small amounts if a high concentration of DTT was added **(Fig. 3.15)**, the variants assembled into nanodiscs with higher yields. **Figure 3.28** compares the assemblies in the presence of 10 mM DTT. Especially the mutants R50W and Q93P yielded high amounts of nanodisc incorporated protein, suggesting that these mutations weaken the oligomerization tendency of MPV17. Interestingly, all tested mutants inserted into nanodiscs with only one MPV17 per nanodisc. This number is lower than the number obtained with MPV17ΔCys or met-MPV17wt **(Table 3.2)**, suggesting that the investigated mutations interfere with the interaction between the individual MPV17 monomers, leading to the expected insertion of one monomer under assembly conditions that strongly favor this stoichiometry. This data further indicates that inter-monomer disulfide-bonds only form if MPV17 is able to initially interact in a non-covalent manner. In line with this notion no mutations of single cysteine residues are among the known disease linked MPV17 variants.

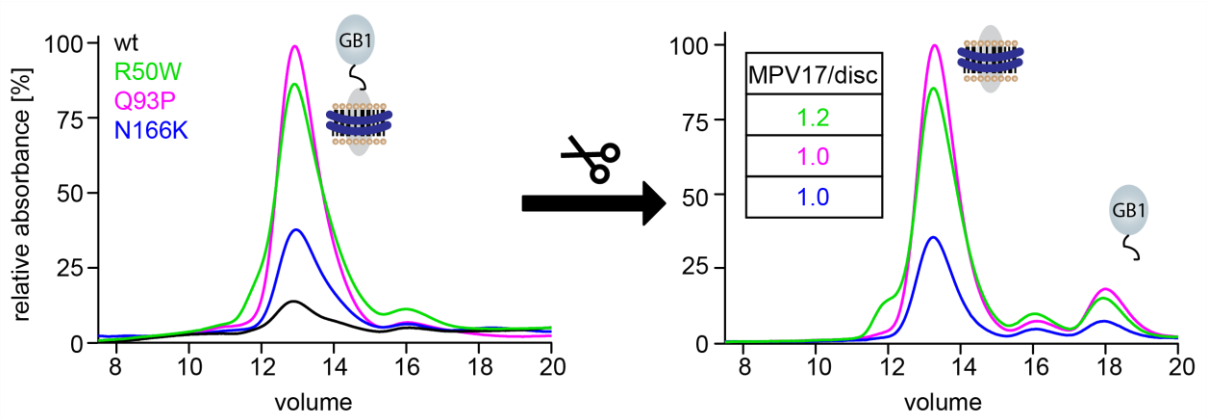

Figure 3.28: Nanodisc assembly with MPV17wt and disease-linked mutants in the presence of 10 mM DTT. The trace for MPV17wt can also be found in Figure 3.15. The MPV17 mutants insert into nanodiscs more readily than the wild type version, suggesting a less pronounced tendency for oligomerization. The GB1-cleavage assay, used to determine the number of MPV17 monomers per nanodisc, results in values close to one, which are lower than for cysteine-free MPV17 (see table 3.2).

3.2 Discussion

This work demonstrates that the human inner mitochondrial membrane protein MPV17 can be produced efficiently in *E. coli* enabling cutting-edge isotope labeling schemes for NMR studies. Additionally, the protocol for purifying MPV17 out of bacterial inclusion bodies described in **Chapter 3.1.1** will facilitate the high-level production of MPV17 for further biochemical, biophysical and structural investigations.

In line with a previous study on the yeast homologue Sym1[171], this work shows that also human MPV17 tolerates denaturation and refolding into detergent micelles. Furthermore, in **Chapter 3.1.2**, a systematic biophysical approach is presented for the identification of optimized detergent conditions that enable high-resolution NMR studies. By comparatively characterizing MPV17 refolded into various detergents using size exclusion chromatography, CD and NMR spectroscopy, DPC was identified as the detergent in which MPV17 behaves most favorably. While the purification of sufficient amounts for NMR studies was also possible in the detergents C12E8, DDM and CYMAL-7, the reduced thermal stability and the accompanied partial precipitation ruled against proceeding with more costly isotopic labeling necessary for 3D-NMR-experiments. Still, the far-UV-CD-derived secondary structure content and the homogenous size distribution probed by SEC suggest a similar fold in all these detergents. The milder detergents not being capable of supplying long term stability to the stabilized monomer, underlines the suggested functional relevance of the oligomer, which will be discussed below. In contrast, the high thermal stability probed for MPV17 in DPC, enabled NMR experiments at 37 °C without precipitation. This was essential for obtaining an almost complete NMR backbone resonance assignment.

Based on this NMR assignment, subsequent NMR measurements provided additional structural insights into the folding state of MPV17 in DPC micelles **(Chapter 3.1.3)**. The mapping of α-helical secondary structure elements on the sequence led to the identification of six α-helical elements. Compared to the secondary structure prediction performed in earlier work[159,168], the location of these experimentally determined α-helices presents differences. While the first three of the four repeatedly predicted α-helices could be confirmed by NMR, the fourth helix was shown to form nearer to the third helix than predicted. The fifth α-helix, which had only been predicted by Antonenkov *et al.*[168], could be confirmed. Additionally, a short α-helix at the N-terminus (AA 2-14) was revealed, giving rise to a total of six α-helices. When taking the paramagnetic relaxation enhancement experiments into account, the α-helices 2-4 and 6 most likely form transmembrane helices, while helix 1, which is also too short to span the membrane and helix 5 probably form extramembranous regions. Assuming that the C-terminus reported to be located in the intermembrane space in Sym1[168], behaves similar in human MPV17, helix 5 would be located in the matrix, while helix 1 and the N-terminus would be located in the intermembrane space **(Fig. 3.29)**. Furthermore, these findings show that all four cysteines are located in the membrane near the matrix. As the sequence conservation is very high among mammalian homologues (> 90 %), the herein detected secondary structure content for human MPV17 most likely is transferable among

species. However, structural information is not available for any other MPV17 homologue. This initial NMR work will serve as a promising starting point for a more detailed NMR or EM structural analysis of MPV17 in detergent micelles or other membrane mimetics, such as lipid nanodiscs of varying sizes in order to incorporate monomeric or oligomeric pore forming species [35,44,45,179].

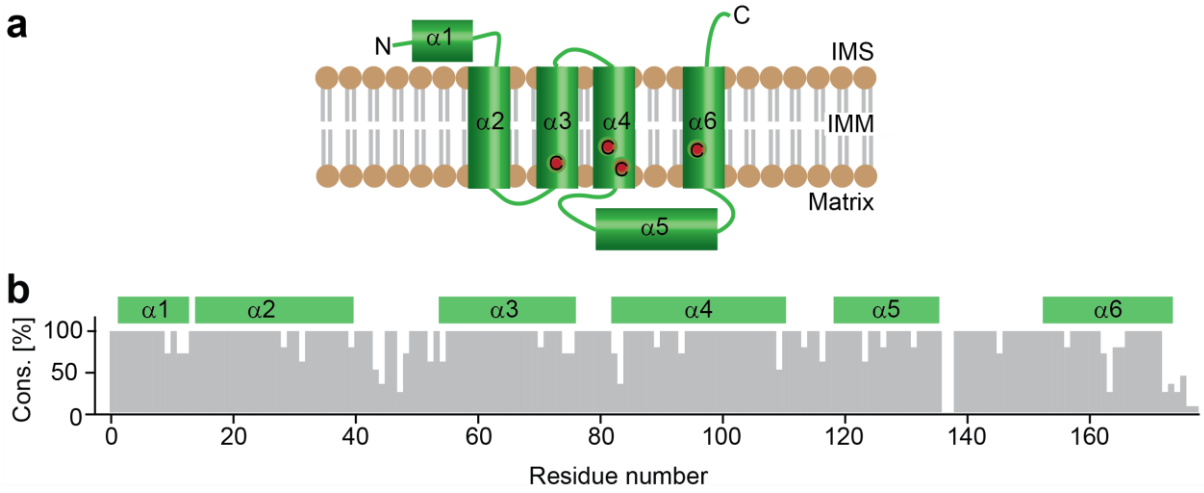

Figure 3.29: (a) Structural model of the secondary structure elements of human MPV17 based on the NMR-characterization in DPC-micelles. The location of cysteines is highlighted in red. IMS = intermembrane space; IMM = inner mitochondrial membrane. (b) The degree of sequence conservation (cons.) is plotted against the sequence for the mammalian MPV17 homologues using human, macaque, bovine, bison, seal, hedgehog, mouse and rat amino acid sequences. The secondary structure elements are indicated in green at the top.

In search of a more native membrane mimetic to stabilize the functional oligomeric pore[168,171], protocols were developed for stabilizing MPV17 in amphipoles, MSP-nanodiscs and liposomes. As shown in **Chapter 3.1.4**, homogenous oligomeric samples could be prepared in all these membrane mimetics after initial purification of the membrane protein in DPC-micelles. The far-UV CD data showed a cooperative unfolding in a similar temperature range as seen in detergent micelles, supporting the notion that MPV17 is properly and similarly folded in all cases. This is in line with a recent study, in which electrophysiological experiments were performed to assess the MPV17 pore functionality using MPV17 produced in the yeast strain *Pichia pastoris*[168]. There, MPV17 could functionally be reconstituted into lipid bilayers after being extracted and purified in DPC micelles clearly supporting the conclusion that MPV17 preparations in DPC micelles are properly folded and capable of forming a channel in a lipid bilayer membrane. In that study five out of the six experimentally determined α-helices were predicted and a very similar size exclusion chromatography profile and far-UV CD spectrum could be obtained.

The NMR-data acquired in amphipoles showed severe line broadening. This could be explained by a high-weight oligomer, suggesting that structural studies should be continued with cryo-EM, as initially intended for the oligomer. However, despite the SEC-profile indicating a species larger than a monomer, it cannot be excluded with certainty that amphipoles might be too harsh to stabilize the oligomer and the line broadening results from a dynamic monomer. Initial negative stain images could not visualize the pore in amphipoles, which could also be closed at the reducing conditions used, as the pore was shown

to be closed under these conditions[168]. The same study showed that the oligomeric pore formed by MPV17 in a lipid bilayer is most likely induced by oxidative stress in the mitochondrial matrix. Consequently, cysteine residues might play a crucial role for MPV17 oligomerization and its pore formation. Human MPV17 contains four cysteine residues at positions 59, 99, 103 and 160. The NMR-acquired localization of secondary structure elements, shows that all cysteines are positioned within α-helices in the protein (see **Fig. 3.29**) and that these regions are located inside the hydrophobic interior of the detergent micelle, indicating that the stable oligomerization of MPV17 is enabled by disulfide bond formation within the membrane. Furthermore, labeling experiments showed that all four cysteines are accessible in the monomer in DPC-micelles and thus, can possibly engage in intermolecular disulfide bonds.

The studies in **Chapter 3.1.5** on the influence of cysteines in MPV17 reveal that MPV17 shows a strong tendency to form oligomers in the absence of reducing agents, which is further enhanced in a lipidic environment. This could be demonstrated with NMR, where the absence of a reducing agent led to severe line broadening even in DPC-micelles and with crosslinking experiments in detergent and liposomes. This oligomeric form might indeed be the functionally active species that forms at oxidative stress conditions. For the yeast homologue Sym1, oligomeric assemblies corresponding to a 6- and 12-mer have been detected by blue-native PAGE [171]. In line with these previous observations, the crosslinking assay in this work detected oligomers up to a hexamer. In addition, while wild-type MPV17 could not be inserted into nanodiscs ranging from 8 to 12.5 nm in size in the established nanodisc insertion assay[178], cysteine-deficient or cysteine-methylated MPV17 could be assembled into nanodiscs. However, even when the cysteine sulfhydryl moieties were not available, MPV17 had a slight tendency to form oligomeric species, as on average more than one MPV17 monomer inserted under nanodisc assembly conditions that strongly favor the insertion of a monomer, i.e., with a large excess of empty nanodiscs in the assembly mixture. In this almost monomeric nanodisc-incorporated state, MPV17 shows a high degree of conformational flexibility, as evident from the strong line-broadening effects in 2D-NMR experiments of MPV17ΔCys in MSP1ΔH5 nanodiscs. The mutation of cysteine residues does not lead to strong NMR spectral changes, indicating that folding of the MPV17 monomer is not dependent on the formation of intra-molecular disulfide bridges. In line with this notion, we found that the thermal stability of MPV17 is only slightly lower if cysteine residues are removed.

Additionally, the assembly of MPV17 into nanodiscs using different lipid mixtures, showed a tendency for higher ratios of MPV17 per nanodisc when a lipid mixture of DMPC/DMPG (75/25) instead of DMPC/CL (80/20) was used. This behavior can be rationalized by tight binding of cardiolipin, which is known to be abundant in the IMM, to MPV17, leading to a preformed protein-lipid assembly that is too large for the 8 nm nanodiscs if higher oligomers are present.

Finally, the impact of disease-linked mutations on the formation of oligomeric states was investigated. As shown in earlier studies, where disease-linked variants still translocated to the inner mitochondrial

membrane[218], the three variants studied in **Chapter 3.1.6** behaved very similar to the wild type during expression, purification and in far-UV-CD detected experiments. The expectation for a disease-causing mutation would be that MPV17 oligomerization and eventually pore formation is markedly reduced. An earlier study revealed that disease-linked mutations in the yeast homologue Sym1 reduce the amount of higher molecular weight complexes, suggesting that the mutations hamper its oligomerization[218]. As shown, a similar behavior was observed with the MPV17 variants R50W, Q93P, N166K. To a varying extent, all of these variants could be inserted into small lipid nanodiscs, which was almost impossible with the wild-type protein. Of note, these variants insert into nanodiscs as a pure monomer, which is in contrast to MPV17 where cysteines have been either removed or blocked. This behavior suggests that MPV17 needs to oligomerize in a non-covalent manner before cysteine residues of neighboring monomers are able to form disulfide bridges.

Furthermore, with the experimentally updated location of α-helical secondary structure elements, the known disease-related mutation sites show a different picture **(Fig. 3.30)**. Unlike earlier assumptions, the mutations are not found in all mitochondrial compartments, but are confined to the intramembrane regions and the loop between helices 1 and 2, which is possibly located in the matrix. As the cysteines are also located in the membrane, this suggests that the oligomerization of MPV17 is mediated by contacts within the membrane, which are hampered by the mutation sites. Thus, the interaction sites are usually shielded from the hydrophobic environment of the membrane, offering an explanation on why the monomer could not be stabilized in nanodiscs and amphipoles, resulting in severe line broadening by oligomerization or internal dynamics when it was forced into a monomeric state. This could also be the reason why no long-range NOE-contacts could be observed for the monomer in DPC-micelles, strongly suggesting that structural studies must be performed on the MPV17 oligomer.

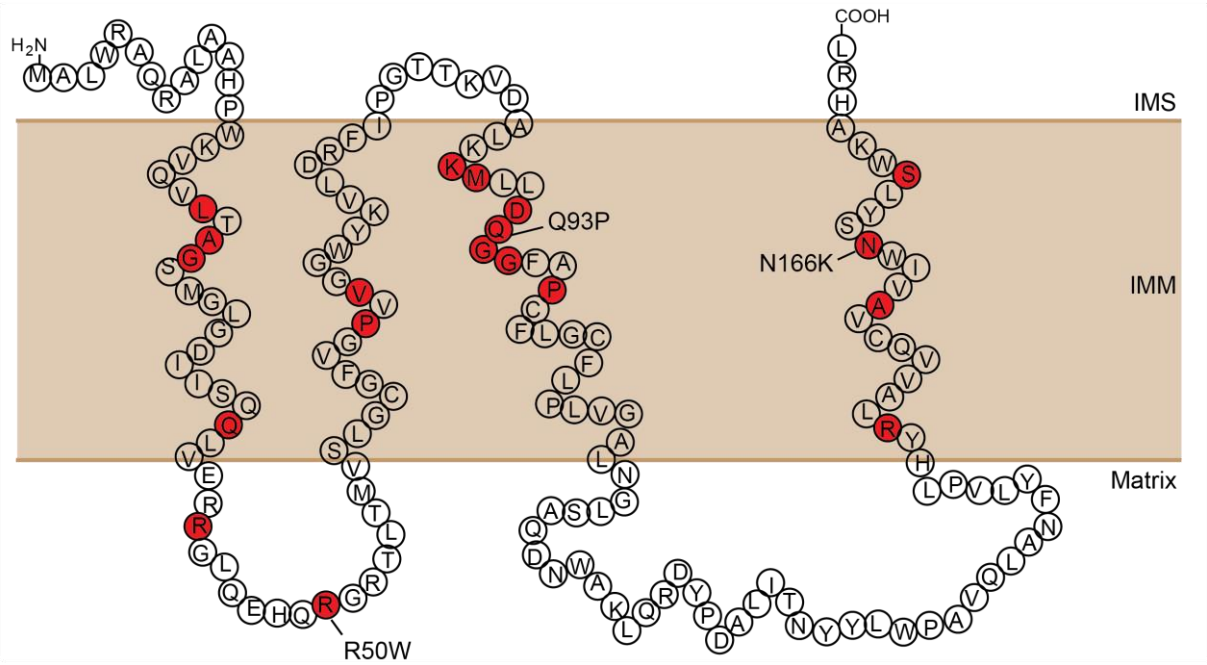

Figure 3.30: Mapping of the disease-related point mutations on the secondary structure of MPV17. The mutation

sites are colored in red, with the mutations investigated in this work indicated. IMS = intermembrane space; IMM = inner mitochondrial membrane.

The herein presented data largely contribute to the understanding of the molecular features of MPV17 and its functional role in the inner mitochondrial membrane. Earlier studies showed that MPV17 forms a membrane pore upon being exposed to oxidative stress [168]. This work shows that oligomerization, which is most likely linked to pore formation, is stabilized by disulfide bonds. Among other possible effects, disease causing mutations can lead to a weakening of MPV17 oligomerization, which would most likely prevent stable pore formation. These insights suggest that the MPV17 pore is important under oxidative stress conditions that can easily occur in the mitochondrial matrix as the site of oxidative phosphorylation, where reactive oxygen species (ROS) are generated. It has been proposed that diseases like the mitochondrial DNA depletion syndrome are linked to ROS stress[152]. A possible explanation for this observation might be that ROS lead to increased mitochondrial DNA damage, increasing the demand for nucleotide precursors to be imported into the mitochondrial matrix **(Fig. 3.31)**. Since MPV17 is located in the inner mitochondrial membrane, it can directly sense buildup of ROS and form a channel that can (selectively) transport the required metabolic precursors. If the MPV17 channel cannot be formed due to a critical mutation in the protein, damaged DNA cannot be repaired or synthesized, leading to its gradual depletion.

In conclusion, this work provided novel structural and functional insights on the disease-linked mitochondrial membrane protein MPV17. Furthermore, the presented production protocols in bacterial hosts will be helpful for a more detailed structural characterization of the MPV17 monomer as well as the final oligomeric pore state at high resolution. Such studies will be essential for obtaining a better mechanistic understanding of the regulation and selectivity of MPV17 under varying cellular stress conditions.

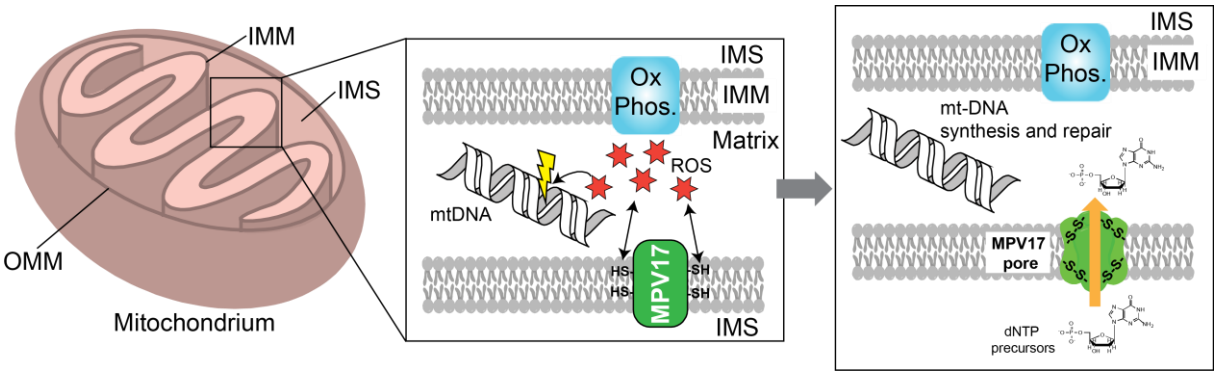

Figure 3.31: Model of MPV17 functionality of redox-dependent oligomeric pore formation. Reactive oxygen species (ROS) are a byproduct of oxidative phosphorylation in the respiratory chain in mitochondria. Enhanced levels of ROS lead to DNA damage and eventually to a lack of protein expression of respiratory chain complexes that are encoded by mitochondrial DNA (mtDNA). MPV17, also located in the inner mitochondrial membrane, is able to sense oxidative stress via its cysteine residues, leading to the formation of a stable oligomeric pore that can serve as an entry channel for nucleotide precursors that are required for mtDNA synthesis and repair. This model can explain the severe effects of MPV17 leading to mitochondrial DNA depletion, mitochondrial misfunction and associated phenotypes such as liver failure in early childhood. OMM: outer mitochondrial membrane, IMM: inner

mitochondrial membrane, IMS: intermembrane space. Ox. Phos.: components of the respiratory chain, esp. complex IV, where electron transfer to O2 takes place.

4 Conclusion and Perspectives

This work focused on two disease-related pore-forming mitochondrial membrane proteins and aimed at providing a deeper understanding of their functionality based on structural insights.

The first part of this work, which was focused on the pro-apoptotic Bcl-2 family protein Bak **(Chapter 2)** not only yielded a structural model for the inactive full-length protein based on NMR structural information generated for all parts of the protein, but also gained structural information on the BH3-induced active state in a lipid environment utilizing phospholipid nanodiscs. It was shown that the helix 1 of Bak not only detaches during the conformational transition[130], but also completely unfolds and partially binds to the lipid membrane surface offering an explanation on how this unstructured region is stabilized during pore formation. Furthermore, the comparative studies on the inactive state of pro-apoptotic Bak and anti-apoptotic BclxL strongly suggest that the intramolecular interaction of individual secondary structure elements is key for defining their functionality. For Bak the interaction of helix 1 with the core protein was shown to be important for its pro-apoptotic functionality as confirmed by site-directed mutagenesis. In addition, by applying an optimized nanodisc setup, the interaction of Bak and BclxL could be studied in a membrane environment, which revealed a novel binding site located at Bak helix 1. As previously shown for the Bak-BH3 domain[93], this binding motif also interacts with the hydrophobic binding groove in BclxL. As helix 1 detaches and unfolds at an early stage during activation, it is very likely that it interacts with BclxL first and facilitates its inhibitory activity. As soon as the BH3 domain becomes exposed, it dissociates the initial complex of BclxL with Bak helix 1 by binding to the BclxL binding site instead and abolishes homo-oligomerization, pore-formation and down-stream apoptosis. To confirm these results structural information on the helix 1 peptide bound to the hydrophobic groove of BclxL would be informative. Due to line-broadening effects NMR-measurements could not resolve the binding site at high resolution. Therefore, a crystal structure determination of the BclxL-Bak-helix 1 fusion construct will be approached next. Additionally, the helix 1 peptide should be optimized to enable studies with the isolated peptide and determine the K_D for the binding to BclxL.

The second part of this work was on structural and functional investigations of the disease-linked inner mitochondrial membrane protein MPV17 associated with mitochondrial DNA maintenance defects **(Chapter 3).** In this work, protocols for the high-level production of MPV17 in *E. coli* were developed and its structural state in various membrane mimetics was analyzed. Additionally, information was obtained on its secondary structure, its membrane location and the role of cysteines during oligomerization. The positions of the cysteine residues and the known disease-related mutations could be located to the membrane or the mitochondrial matrix. Furthermore, it could be shown that disease-related mutations reduce the oligomerization tendency, a process stabilized by cysteines. These insights strongly suggest that MPV17 is a redox-sensitive protein regulating mtDNA maintenance by

transporting metabolic DNA precursors[166]. Future studies will be necessary to gain further high-resolution structural and functional insights.

Taken together, this work provides novel structural und functional insights for both the outer mitochondrial membrane protein Bak and the inner mitochondrial membrane protein MPV17. By utilizing NMR spectroscopy, these dynamical systems could be described in a detail not possible with any other high-resolution structural method[219]. As both play a role in severe diseases, the insights provided in this work could facilitate future development of drugs targeting these essential proteins.

5 Material and Methods

5.1 Material

5.1.1 Instruments

Table 5-1: List of instruments used for the following methods.

Instrument	Manufacturer
ACQUITY UPLC M-class system + automated HDX technology	Waters
ÄKTA™ Pure	GE-Healthcare
with columns: HiLoad 16/600 Superdex 75pg + 200 pg	GE-Healthcare
Superdex 75 + 200 Increase 10/300 GL	GE-Healthcare
Superose 6 Increase 10/300 GL	GE-Healthcare
ÄKTA™ Start	GE-Healthcare
with columns: HiPrep 16/60 Sephacryl S-200 HR	GE-Healthcare
Autoclave VX-150	Systec
Agarose gel caster 1704422	Bio-Rad
CD Spectropolarimeter J-715 (with PTC 348 WI Peltier device)	JASCO
Cell Density Meter WPA CO 8000	Biochrome
Centrifuge HET 1011	Andreas Hettich GmbH
Centrifuge Sorvall LYNX 6000	Thermo Fisher Scientific
Centrifuge Rotor Fiberlite F9-6x1000 LEX	Thermo Fisher Scientific
Centrifuge Rotor T29-8x50	Thermo Fisher Scientific
DynaPro NanoStar Dynamic Light Scattering Instrument	Wyatt
Gel electrophoresis system (Mini-Sub Cell GT Horizontal)	Bio-Rad
Heating block Analog Dry Block Heater	VWR
Hotplate stirrer VMS-C7	VWR

Incubator Heratherm IGS60	Thermo Fisher Scientific
Incubator Shaker Series Innova 40	New Brunswick Scientific
Incubator Shaker Series Innova 44	New Brunswick Scientific
Isothermal titration calorimeter, MicroCal PEAQ-ITC	Malvern
Microcal PEAQ-DSC	Malvern
Microcentrifuge Galaxy MiniStar C1400-RT	VWR
NanoPhotometer® N60	Implen
Nutating Mixer	VWR
Nutating shaker Mini BioMixer 3D	Benchmark Scientific
OmniSEC	Malvern
PCR cycler Mastercycler nexus X2	Eppendorf
Peristaltic Pump P-1	GE Healthcare
pH bench meter FiveEasy FE20-ATC kit	Mettler Toledo
Platform shaker Rotamax 120	Heidolph Instruments
RTS ProteoMaster	Roche
Scale ATILON ATL-84-I	Sartorius AG
Scale Entris 2202-1S	Sartorius AG
Scale Pioneer PA114C Analytical Balance	Ohaus Corporation
Sonifier S-250D	Branson Ultrasonics
Spectra Max ID5	Molecular Devices
Spectrofluorometer FP-8300	JASCO
Stirrer big/small squid	IKA Werke
Table centrifuge Micro Star 17R	VWR
Table centrifuge 5424/5424R	Eppendorf

ThermoMixer C	Eppendorf
Ultrasonic bath Sonorex RK 103 H	BANDELIN
UV Transilluminator Mini Benchtop M-10E	UVP
Vortex Mixer Analog	VWR
Western Blot Pierce Power Blot Cassette	Thermo Fisher Scientific

5.1.2 Chemicals and consumables

The standard laboratory chemicals and consumables were purchased from the following vendors, unless stated otherwise: Anatrace (USA), AppliChem (Germany), Asla biotech (Latvia), Avanti Polar Lipids (USA), Biomatik (USA), Bio-Rad (USA), Carl Roth (Germany), Invitrogen (USA), Merck Millipore (Germany), Roche (Switzerland), Santa Cruz Biotechnology (USA), SERVA (Germany), Sigma-Aldrich (Germany), Thermo Fischer Scientific (USA), VWR (Germany).

5.1.3 Enzymes, Kits and Standards

Table 5-2: List of enzymes, kits and standards

Enzyme	Manufacturer
DNaseI, bovine pancreas	Roche
DpnI	Merck
Lysozyme, chicken egg	Carl Roth
Pfu DNA Polymerase	Promega
TEV protease	Supplied by Dr. Arie Geerlof (Helmholtz Zentrum München)
Thrombine, bovine	Merck Millipore

Kit	Manufacturer
Mix & Go E. coli Transformation Kit	Zymo Research

QuikChange Lightning Site-Directed Mutagenesis Kit	Agilent Technologies
Wizard SV Gel and PCR Clean-Up System	Promega
Wizard Plus SV Minipreps DNA Purification System	Promega

Standard	Manufacturer
DNA 100bp	SERVA
DNA 1kbp	SERVA
Dual Color Protein Standard III	SERVA

5.1.4 Peptides

Table 5-3: List of synthetic peptides used for interaction studies.

Peptide	Sequence	Manufacturer
Bak-H1	^{24}EEQVAQDTEEVFRSYVFYRHQQ^{45}	Biomatik
Bid	^{80}EDIIRNIARHLAQVGDSMDR^{99}	Biomatik
Puma	^{130}EEQWAREIGAQLRRMADDLNAQYER^{154}	Biomatik

5.1.5 Bacterial Strains and Plasmids

Table 5-4: List of bacterial strains used for molecular cloning and recombinant protein expression

Strain	Genotype	Manufacturer
E. coli BL21 (DE3)	fhuA2 [lon] ompT gal (λ DE3) [dcm] ΔhsdS λ DE3 = λ sBamHIo ΔEcoRI-B int::(lacI::PlacUV5::T7 gene1) i21 Δnin5	New England Biolabs

E. coli NEB® 5-alpha	fhuA2 a(argF-lacZ)U169 phoA glnV44 80 (lacZ)M15 gyrA96 recA1 relA1 endA1 thi-1 hsdR17	New England Biolabs
E. coli XL10-Gold®	Tet^rΔ (mcrA)183 Δ(mcrCB-hsdSMRmrr)173 endA1 supE44 thi-1 recA1 gyrA96 relA1 lac Hte [F´ proAB $lacI^qZ$ΔM15 Tn10 (Tet^r) Amy Cam^r]	Agilent

Table 5-5: List of plasmids constructed and/or used for protein expression with the corresponding abbreviation and an explanation. (His = His-tag, TEV = TEV cleavage site, Thr = thrombin cleavage site). The full protein sequences can be found in the appendix.

Plasmid	Abbreviation	Explanation
Bcl2-protein constructs		
pET21a-BakΔTM-His_6	BakΔTM	Soluble Bak domain, with MEAS-header and a C-terminal His-tag (this His-tag is present in all ΔTM constructs)
pET21a-Bak-xL-ΔTM-His_6	BakΔTM-xL-link	BakΔTM with additional C-terminal BclxL-$linker_{195-212}$
pET21a-BakΔTM_x-His_6 (x=1/2/3)	BakΔTM_1/2/3	Mutated BakΔTM (1=R156Q; 2=I80E/N86E/R156Q; 3=R11Q/R169A/R174N)
pET21a-BakΔTM-SorA-His_6	BakΔTM-Sor	BakΔTM with a C-terminal Sortase recognition site
pET21a-BclxLΔTM-His_6	BclxLΔTM	Soluble BclxL
pET21a-BclxLΔLΔTM-His_6	BclxLΔLΔTM	Soluble BclxL lacking the loop between helices 1 and 2
pET21a-BclxL(ΔL)ΔTM-BakH1-His_6	BclxLΔLΔTM-BakH1/ BclxLΔTM-BakH1	Soluble BclxL (± loop) with the BakH1 fused C-terminally
pET21a-Bid- His_6	cBid	Bid with a Thrombin cleavage site replacing the caspase cleavage

pET29-SortaseA-mut- His_6	Sortase A	Sortase A pentamutant[181]
pET15b-His_6-GB1-Thr-BakTMH	Bak-TMH	Bak-TMH with a C-terminal His-tag and an GSGS-header after cleavage
pET15b-His_6-GB1-Thr-BakTMH-Sor	Bak-TMH-Sor	Bak-TMH with a longer linker used with Sortase A
pET15b-His_6-GB1-Thr-BclxLTMH	BclxL-TMH	BclxL-TMH with a C-terminal His-tag[177]
pET15b-His_6-GB1-Thr-GlyATMH	GlyA-TMH	GlyA-TMH with a C-terminal His-tag[178]
MPV17-constructs		
pET15b-His_6-GB1-Thr-MPV17	MPV17wt	MPV17 wild type (with an N-terminal header for all constructs after cleavage: GSGGSS-MPV17)
pET15b-GB1-Thr-MPV17-His_{10}	MPV17-cHis	MPV17wt with a C-terminal His-tag
pET15b-His_6-GB1-Thr-MPV17(noCys)	MPV17-Cysfree	Cysteine free version of MPV17 (C→A)
pET15b-His_6-GB1-Thr-MPV17(mut) (mut=R50W/Q93P/N166K)	MPV17-R50W/-Q93P/-N166K	MPV17 with disease related mutations
MSP-constructs		
pET28a-His_6-TEV-MSPx (x=1D1ΔH5/1D1/1E3D1)	MSP ΔH5/1D1/1E3D1	MSP variants used for the preparation of nanodiscs
pET21a-MSPΔH5-ΔnG-TEV-His_6	MSPΔH5-ΔnG	MSPΔH5 without a N-terminal glycine after TEV-cleavage

5.1.6 Bacterial Growth Media

All media was sterilized before usage. LB-Media was autoclaved at 121 °C for 20 min. M9 minimal media as well as antibiotics were sterile filtrated using a 0.22 µm filter (Millipore) due to heat sensitive components. M9 minimal media was prepared in H_2O for the preparation of protonated NMR-samples or in D_2O for the preparation of deuterated NMR-samples.

Table 5-6: Media used for protein expression. LB-media was used for unlabeled expression, while M9-minimal media was used for isotope labeled expression.

Medium	Recipe	
Luria Bertani (LB)	20 g/L (purchased form SERVA)	
	+ 15 g/L agar agar for plates	
SOC	Peptone	2 % (w/v)
	Yeast extract	0.5 % (w/v)
	Glucose	20 mM
	$MgSO_4$	10 mM
	NaCl	10 mM
	KCl	2.5 mM
M9 minimal medium	Na_2HPO_4	6 g/L
	KH_2PO_4	3 g/L
	NaCl	0.5 g/L
	NH_4Cl	1 g/L
	$MgSO_4$ (1 M)	2 mL/L
	$CaCl_2$ (0.5 M)	0.2 mL/L
	Glucose	2 g/L
	Biotin (1 mg/mL)	1 mL

	Thiamin (1 mg/mL)	1 mL
	Trace elements (1000x)	1 mL
Trace elements (1000x)	EDTA	134 mM
	$FECl_3$	31 mM
	$ZnCl_2$	6.2 mM
	$CuCl_2$	760 µM
	$CoCl_2$	420 µM
	H_3BO_3	1.62 mM
	$MnCl_2$	81 µM

5.1.7 Software, Databases and web-based Tools

Table 5-7: List of Software, Databases and Web-based Tools.

Software	Supplier
Adobe Illustrator CS5	Adobe Systems Incorporated
Dynamics	Wyatt Technology Corp.
Jasco Spectra Manager	JASCO
Mendeley Desktop	Mendeley Ltd.
MicroCal PEAQ-DSC software	Malvern
MicroCal PEAQ-ITC software	Malvern
Microsoft Office 2013	Microsoft
NMR-FAM Sparky 1.413	NMRFAM[220]
OriginPro 9.0G	OriginLab Corp.
ProFit	QuantumSoft
PyMOL 1.8.4.2	Schrödinger

Serial Cloner	Franck Perez
TopSpin	Bruker
UCSF Chimera	University of California
Unicorn 7.1	GE Healthcare
Xplor-NIH	National Institut of Health[221]

Database	Website
BMRB	http://www.bmrb.wisc.edu/
Google Scholar	http://scholar.google.de/
PDB	http://www.rcsb.org/
PubMed	http://www.ncbi.nlm.nih.gov/pubmed
UniProt	http://www.uniprot.org

Web-based Tool	Website
Expasy ProtParam	http://web.expasy.org/protparam/
Expasy Translate	https://web.expasy.org/translate/
MultAlin	http://multalin.toulouse.inra.fr/multalin/[222]
NCBI Blast	http://blast.ncbi.nlm.nih.gov/
OligoAnalyzer	https://eu.idtdna.com/calc/analyzer/
TALOS+	https://spin.niddk.nih.gov/bax/nmrserver/talos/[176]
Tm Calculator	https://www.thermofisher.com/de/de/home/brands/thermo-scientific/molecular-biology/molecular-biology-learning-center/molecular-biology-resource-library/thermo-scientific-web-tools/tm-calculator.html

5.2 Methods

5.2.1 Molecular cloning

Complete genes were inserted into plasmids applying the restriction-free insertion method described by Chen et al.[223] All additional mutations were introduced with the QuickChange Lightning (QCL) kit. The forward and reverse primers were designed and the annealing temperature adjusted with the help of the IDT oligoanalyzer and the Thermo Fisher Tm Calculator.

5.2.1.1 Restriction-free cloning

During the first Polymerase Chain Reaction (PCR) the gene of interest was amplified using primers containing the nucleotide sequence of both the gene and the vector. This resulted in a DNA fragment with overhangs able to anneal to the insertion region of the vector system.

Table 5-8: 1st PCR: Pipetting Scheme.

10x *Pfu* Reaction Buffer	5 µL
dNTPs (10mM)	1 µL
5'-3'-Primer (10 µM)	1.3 µL
3'-5'-Primer (10 µM)	1.3 µL
Template DNA	<0.5 µg
Pfu Polymerase	0.4 µL
ddH_2O	ad 50 µL

Table 5-9: 1st PCR: PCR program.

Initial denaturation	95°C	2 min	
Denaturation	95°C	20 sec	30x
Annealing	55-70°C	20 sec	
Elongation 1	68°C	2 min	
Elongation 2	68°C	5 min	
Storage	10°C	Hold	

After the DNA fragment was isolated (described in **Chapter 5.2.1.2**), a second PCR was performed in order to insert the gene into the vector. The QCL kit was used for this step.

Table 5-10: 2nd PCR: Pipetting Scheme.

10x QCL Buffer	2.5 µL
QCL Solution	0.75 µL
dNTPs (10mM)	0.5 µL
Vector	50 ng
Amplified gene	10x molar excess

Table 5-11: 2nd PCR: PCR program.

Initial denaturation	95°C	2 min	
Denaturation	95°C	30 sec	25x
Annealing	55-70°C	30 sec	
Elongation 1	68°C	5 min	
Elongation 2	68°C	10 min	

QCL Polymerase	0.5 µL	Storage	10°C	Hold
ddH_2O	ad 25 µL			

All PCR's for introducing mutations with the QCL kit were performed as described in **Table 5-10** and **5-11**. In those cases the primers were added in 10x molar excess of the target vector instead of the amplified gene.

After the PCR, 1 µL DpnI was added for 1h at 37°C to digest the residual vector.

5.2.1.2 DNA isolation

The DNA of interest was separated by agarose gel electrophoresis (90 V, 60 min) in TBE buffer. Gels were prepared using 1% (w/v) agarose in TBE buffer and ROTI®GelStain (Carl Roth) to visibilize the DNA under UV light. The Wizard® SV Gel and PCR Clean-Up System was used to purify the DNA.

Table 5-12: Buffers used for agarose gel electrophoresis.

TBE (TRIS/Borate/EDTA) buffer		6x DNA loading buffer	
TRIS pH 8.2	89 mM	TRIS pH 7.6	10 mM
Boric acid	89 mM	EDTA	60 mM
EDTA	2 mM	Glycerol	50%
		Bromophenol blue	0.1%
		Xylene cyanol FF	0.1%

5.2.2 Transformation and DNA amplification

For the transformation, 4 µL of the DpnI digested PCR product was added to 50 µL of NEB®5α competent cells and incubated on ice for 30 min. A heat-shock was performed for 30 sec at 42 °C. After the cells had recovered on ice for 2 min, 200 µL of SOC was added and the cells were incubated at 37 °C for 1 h. Finally the cells were plated on selective agar plates and incubated overnight at 37°C. Single colonies were picked, the DNA purified with the Wizard® Plus SV Minipreps DNA Purification System and sent for sequencing to GATC/eurofins Genomics or GENEWIZ following the protocols stated on the respective website.

5.2.3 Recombinant protein production

Sequenced plasmids were transformed into *E. coli* BL21 (DE3) competent cells for protein expression. After adding the transformed cells, the pre-culture containing LB, 2% glucose and the respective antibiotic was incubated overnight at 37 °C, then added to the main culture (LB + antibiotic) in a 1:40 ratio and grown to an OD of 0.6-0.8. The induction and expression conditions varied for the different protein constructs and are stated in the corresponding protein production protocols.

Both linear[45,179] and circular[46] MSP proteins, as well as Sortase A[224] were produced and purified according to established protocols.

5.2.3.1 Isotopic Labeling

For NMR-measurements proteins must be enriched with detectable isotopes, such as ^{15}N and ^{13}C and large protein systems must be deuterated to improve the sensitivity (see **Chapter 5.2.16**). This is achieved by expressing the protein in isotope labeled M9 minimal media (see **Chapter 5.1.6**). This media contains glucose as the only carbon source and ammonium chloride as the only nitrogen source. By using ^{15}N-NH_4Cl or ^{13}C-glucose, the proteins were expressed in media containing only ^{15}N or ^{13}C as a sole N or C source, respectively. For protonated ^{15}N-labeled samples, a 25 mL preculture was prepared as described above and added to 1 L M9 minimal media for expression. For deuterated proteins, the M9 minimal media was prepared in 99 % D_2O (Sigma Aldrich or Eurisotop) using deuterated glucose (^{2}H, ^{12}C- or ^{2}H, ^{13}C-glucose (Sigma Aldrich or Eurisotop)). For bacteria to grow in D_2O, they must be adapted first. This was achieved by preparing a regular pre-culture as described above. After 24 h 10 mL of the bacteria were spun down at room temperature using 2000 xg and resuspended in 10 mL of the same pre-culture media prepared in D_2O. After another 24 h the bacteria were spun down again and resuspended in 10 mL of M9 minimal media prepared with the desired labeled components in D_2O and an additional 2 % of unlabeled glucose. After 8 h this preculture was added to a larger M9 minimal media preculture (40 mL/L main culture) and was grown over night. This preculture was used to inoculate the main culture and the protein expressed as described above.

For ILVAFYM-labeling, the M9 minimal media was prepared using 99% D_2O, $^{15}NH_4Cl$ and ^{2}H, ^{12}C-glucose. 1 h prior to induction with IPTG, the following components were added 300 mg/L of the LV precursor (ethyl 2-hydroxy 2-^{13}C-methyl 3-oxobutanoate)[225,226], 80 mg/L of the Ile-precursor [$^{13}CH_3$]-Cδ2-α-ketobutyrate[227], 70 mg/L [^{15}N]-Phe, 70 mg/L [^{15}N]-Tyr, 50 mg/L ε-[^{13}C]-Met, 300 mg/L 3-[$^{13}CH_3$]-[^{14}N]-Ala and 2 g/L d_6-succinate in 10 mL D_2O. The LV precursor was back-exchanged in D_2O at pH 12 before it was added to the medium.

5.2.3.2 Buffers

Table 5-13: Buffers used for protein purification.

Buffer A		Buffer B		Buffer C	
TRIS pH 8	20 mM	TRIS pH 8	20 mM	GuHCl	6 M
NaCl	100 mM	NaCl	100 mM	TRIS pH 8	50 mM
EDTA	1 mM	BME	5 mM	BME	5 mM

Dialysis Buffer		Lysis Buffer		MSP Buffer	
TRIS pH 8	10 mM	TRIS pH 8	50 mM	TRIS pH 7.5	20 mM
EDTA	1 mM	NaCl	200 mM	NaCl	100 mM
BME	5 mM	EDTA	1 mM	EDTA	1 mM

Refolding Buffer 1		Refolding Buffer 2		SEC Buffer	
GuHCl	6 M	NaPi pH 7	20 mM	NaPi pH 7	20 mM
TRIS pH 8	50 mM	NaCl	200 mM	NaCl	50 mM
NaCl	100 mM	EDTA	1 mM	EDTA	1 mM
EDTA	5 mM	DTT	5 mM	DTT	1-5 mM
DTT	10 mM	DPC	0.5%		

5.2.3.3 Bcl-2 protein production

<u>BakΔTM/ BclxLΔTM/ Bid</u>

BclxLΔTM and Bid were induced with 1 mM IPTG and expressed for 4 h at 37 °C. For BakΔTM, induction with 0.2 mM IPTG and expression at 20 °C for 16-20 h led to higher yields of the monomer. Cells were spun down (6000 xg, 20 min, 4 °C), washed with Buffer A and frozen at -80 °C.

All purification steps were performed either on ice or at 4 °C. The pellet was resuspended in Lysis Buffer and incubated with lysozym and a tablet of cOmplete™ EDTA-free Protease Inhibitor Cocktail (Roche) for 25 min on a rolling plate. The final cell disruption was performed by sonicating for 10 min (1 sec pulse, 3 sec pause, 30 % amplitude). 10 U of DNase I (Roche)/ 10 mL of cell suspension were added

together with 5 mM $MgSO_4$ and incubated for 25 min on a rolling plate. The cell debris was spun down (50 000 xg, 25 min) and the supernatant applied to a Ni-NTA gravity flow affinity column, equilibrated with Buffer B and incubated on a nutating plate for 1 h. The beads were washed with 5 CV of Buffer B and 5 CV of Buffer B + 10 mM imidazole, followed by elution with 3 CV of Buffer B + 400 mM imidazole. 5 % glycerol was added to Bak/BclxLΔTM before concentrating for size exclusion chromatography (SEC) on a ÄKTA™ Pure system equipped with a HiLoad 16/600 Superdex 75 pg column in SEC Buffer. For NMR measurements, SEC was run in 20 mM NaPi pH 6.8, 1 mM EDTA, 2 mM DTT. When binding to Ni-NTA-lipids followed, the SEC was run without EDTA and DTT was substituted for 5 mM BME.

After the Ni-affinity chromatography, Bid was dialyzed overnight in Buffer A. 20 U thrombin/ 1L cell pellet were added and incubated for 24 h as this construct contains a thrombin cleavage site instead of the caspase-8 cleavage site to mimic the cleavage to cBid. After cleavage was verified by SDS-PAGE, 5 % glycerol were added and the procedure continued as described above for Bak/BclxLΔTM.

This procedure was also applied to all the mutants.

Bak-TMH/ BclxL-TMH/ GlyA-TMH

The transmembrane domains were expressed as GB1-fusion proteins with a Thrombin cleavage site and purified from inclusion bodies as suggested by Raltchev *et al*.[177] The protein pellet was either dissolved in 5 % SDS and purified using a HiPrep 16/60 Sephacryl S-200 HR size exclusion column on a ÄKTA™ Start system at room temperature for subsequent nanodisc assemblies or dissolved in 4 % DPC and purified using a HiLoad 16/600 Superdex 200 pg size exclusion column on a ÄKTA™ Pure system at 4 °C for studies in micelles. The SEC was run in MSP Buffer + 0.5 % SDS or 0.1 % DPC.

Protein prepared in DPC was used to study Bak-TMH in micelles. Thus, thrombin (25U) was added for cleavage, followed by a reverse Ni-NTA gravity flow affinity chromatography step to separate the His-tagged GB1 from the Bak-TMH. Finally, the buffer was exchanged on a NAP™-25 column (GE Healthcare) using SEC-buffer.

5.2.3.4 MPV17 protein production

MPV17 was induced with 0.1 mM IPTG and expressed for 4 h at 37 °C. Cells were spun down (6000 xg, 20 min, 4 °C), washed with Buffer A and frozen at -80 °C.

All purification steps were performed either on ice or at 4 °C. The pellet was resuspended in Lysis Buffer and incubated with lysozym and a tablet of cOmplete™ EDTA-free Protease Inhibitor Cocktail (Roche) for 25 min on a rolling plate. The final cell disruption was performed by sonicating for 10 min (1 sec pulse, 2 sec pause, 30 % amplitude). The lysate was incubated with 10 U of DNase I (Roche)/ 10 mL and 5 mM $MgCl_2$ for 25 min and spun down. The pellet was washed once with Buffer A + 1 % TritonX-100 and twice with only buffer A. The resulting pellet containing inclusion bodies was dissolved in

buffer C + 1 mM $MgCl_2$. The protein solution was applied to a Ni-NTA gravity flow affinity column equilibrated with buffer C and incubated for 1 h on a nutating plate. The beads were washed with 10 CV Buffer B + 10 mM imidazole and eluted with 5 CV Buffer B + 500 mM imidazole. The elution fraction was dialyzed against 5 L of Dialysis Buffer, so that the protein precipitated. The precipitate was dissolved in Refolding Buffer to a maximal protein concentration of 5 mg/mL. It was refolded dropwise into 10-fold excess of Refolding Buffer II and dialyzed overnight in 2 L of Buffer B with 2 mM DTT as reducing agent to remove residual GuHCl. For constructs fused to GB1, thrombin was added to cleave it off, except if the protein was purified for nanodisc assemblies. Then GB1 was left on until after the nanodisc assembly. Finally, MPV17 was purified on a ÄKTA™ Pure system equipped with a HiLoad 16/600 Superdex 200 pg size exclusion column in SEC Buffer + 0.1 % DPC (or other detergent).

This procedure was also applied to all the mutants. For the cysteine-free version the reducing agent was omitted from all buffers.

5.2.4 Membrane mimetics

As described in **Chapter 1.1.5** Membrane proteins must be stabilized in a membrane-like environment in order to obtain their native structure and function[33]. The production of the systems used in this work is explained in the following subchapters starting from the least native after micelles to the most native membrane mimetic[35].

5.2.4.1 Amphipols

Amphipols are polymers with amphipathic properties that can stabilize membrane proteins. Amphipols were prepared as described before[40]. In brief, A8-35 was dissolved in water to form a stock solution of 10% (w/w), and then added to a defined amount of membrane protein in detergent micelles in different ratios (1:3 – 1:5). During the final step, the detergent was removed by incubating with Bio-Beads™ (Bio-Rad).

5.2.4.2 Nanodisc assembly

In this work, the phospholipid nanodiscs were prepared as described previously[179]. A final MSP concentration of 150-200 µM was used in all assemblies. All assemblies were performed at room temperature in 20 mM Tris pH 7.5, 100 mM NaCl, 0.5 mM EDTA (no EDTA was added, when $[Ni^{2+}]$-lipids were used). The nanodiscs for binding BakΔTM were prepared with *E. coli* polar lipids and four 18:1 DGS-NTA (Ni^{2+}) lipids per nanodisc unless indicated otherwise at a MSP:lipid ratio of 1:30. The nanodiscs assembled with Bak-TMH, BclxL-TMH and GlyA-TMH were prepared using 75 % dimyristoyl-phosphocholine (DMPC) and 25 % dimyristoylglycerophosphoglycerol (DMPG). The assemblies were performed at a TMH:MSP:lipid ratio of 0.2:1:38 unless indicated otherwise. Empty nanodiscs were assembled for 1,5 h and the detergent removed with 0.6 g/mL of Bio-Beads-SM2 (Biorad) for 2 h. Nanodiscs containing the GB1-TMH were assembled for 2 h and the detergent removed with 0.6 g/mL of Bio-Beads-SM2 (Biorad) for 3.5 h. MPV17 nanodiscs were assembled with the ratios

of MPV17 to MSP indicated for the individual assemblies. ΔH5-nanodiscs were formed using an MSP to lipid ratio of 1:25. 1E3D1-nanodiscs were formed using an MSP to lipid ratio of 1:85 (80 for the 1:1 ratio of MPV17:MSP). As lipids either DMPC/DMPG (75/25) or DMPC/Cardiolipin (14:1) (80/20) were used. The mixtures were assembled 1.5 h at room temperature with a final MSP concentration of 150 µM. For MPV17wt and the cysteine containing mutations 10 mM DTT were added. 0.6 g/mL of Bio-Beads-SM2 (Biorad) were added and the assembly was shaken for 3.5 h. After the assembly, the nanodiscs containing the respective membrane protein were separated by Ni-NTA affinity chromatography and subjected to SEC. The thrombin cleavage was performed at 37 °C for 4 h, followed by a second SEC to separate the cleaved GB1.

The ratio of membrane protein per nanodisc was calculated by using the fusion protein strategy described by Haeusler *et al.*[178]. Briefly, the membrane protein fused to cleavable GB1 is assembled into nanodiscs and separated from the empty discs by affinity chromatography, in this case Ni-NTA chromatography. Finally, GB1 is cleaved and the sample is directly subjected to size exclusion chromatography on a Superdex™ 200 column, from which the filled nanodiscs and the cleaved GB1 elute separately. Using the integrated peaks and the extinction coefficients ε, the ratio can be calculated using the following formulas[178]:

(1) $n_{GB1} = \frac{Int_{GB1}}{\varepsilon_{GB1}}$ with $n_{MP} = n_{GB1}$

(2) $n_{ND} = \frac{Int_{ND+MP} - (n_{GB1} \cdot \varepsilon_{MP})}{2 \cdot \varepsilon_{MSP}}$

(3) $ratio = \frac{n_{MP}}{n_{ND}}$

Equation 5.1: Formulas to calculate the ratio of membrane protein per nanodisc using a fusion protein strategy. The integrated peaks (Int) and the extinction coefficients ε of GB1, the membrane protein (MP) and the nanodiscs (ND) consisting of two MSP proteins are utilized for the calculations.

5.2.4.3 Production of liposomes

Liposomes are the most native form of membrane mimetic, but they are more inhomogeneous and larger than nanodiscs and thus not applicable for NMR[35]. Liposomes were prepared by dissolving lipids in chloroform and mixing them in the required ratio. Chloroform was dried under a nitrogen gas flow and the ready-to-use dried lipid composition stored at -20 °C. 1-10 mg of lipids were resuspended in 1 mL of the respective buffer, sonicated in a sonication bath for 2 min and subjected to ten freeze and thaw cycles before the suspension was subjected to eleven rounds of extrusion using a 100 nm membrane unless indicated otherwise. For proteoliposomes, MPV17 in DPC was added at a protein to lipid ratio of 1:500. After incubation for 30 min at 4 °C, the liposomes were dialyzed overnight at 4 °C in a 10 kDa MWCO membrane against 1 L of buffer (20 mM NaPi pH 7.0, 50 mM NaCl, 0.5 mM DTT).

The following lipid compositions were used, all presented as mass percentage. OMM lipids were prepared by mixing 46 % L-α-phosphatidylcholine (PC), 25 % L-α-phosphatidylethanolamine (PE), 11

% L-α-phosphatidylinositol (PI), 10% 1,2-dioleyl-*sn*-glycero-3-phospho-L-serine and 7 % 1,1',2,2'-tetra-(9Z-octadecenoyl)cardiolipin. According to the manufacturer, *E. coli* polar lipid extract consists of 67 % phosphatidylethanolamine (PE), 23.2 % phosphatidylglycerol (PG) and 9.8 % cardiolipin (CL). 2-10 % 18:1 DGS-NTA (Ni^{2+}) were added to the lipid mixtures as indicated in the corresponding method sections. For the studies on MPV17 66 % of POPC (palmitoyl-oleoyl-glycero-phosphocholine) and 33 % of cardiolipin (18:1) were used for the liposome preparation. All lipids were obtained from Avanti Polar Lipids.

5.2.5 SDS-PAGE

SDS polyacrylamide gel electrophoresis (SDS -PAGE), developed by Laemmli,[228] was routinely performed after all relevant purification steps. Protein samples were mixed with 2x Laemmli buffer and denaturated at 95°C for 5 min. Gels were casted with a 6 % stacking gel and a 15 % separation gel. The electrophoresis was conducted with 50 mA per gel for 30 min in SDS Buffer.

Afterwards the gel was cooked in water, stained in PageBlue™ Protein Staining Solution (Thermo Fisher Scientific) for 30 min and finally destained in water for several hours.

Table 5-14: Buffer and gel recipes used for SDS-PAGE. Gel recipes make 13 gels.

SDS Buffer

TRIS	3 g/L
SDS	1 g/L
Glycerol	14.4 g/L

2x Laemmli (Protein Loading Dye)

TRIS pH 6.8	65.8 mM
SDS	2.1%
Glycerol	26.3% (w/v)
Bromophenol blue	0.02%
BME	15% (v/v)

Stacking gel (6%)

H_2O	29.3 mL
Acrylamide	7.5 mL
0.5M TRIS, pH 6.8	12.5 mL
10% SDS	0.5 mL

Separation gel (15%)

H_2O	28 mL
Acrylamide	30 mL
1.5M TRIS, pH 8.8	20 mL
10% SDS	0.8 mL

10% APS	0.5 mL	10% APS	0.8 mL
TEMED	0.05 mL	TEMED	0.08 mL

5.2.6 Crosslinking

Crosslinking describes the process of covalently linking two or more molecules by a specific chemical reaction. The crosslinking experiments were performed in order to gain information on the oligomerization status of both BakΔTM in nanodiscs and MPV17 in DPC-micelles and liposomes.

5.2.6.1 Cu/phen Crosslinking

Cysteine-mediated crosslinking was performed using the oxidizing complex Cu^{II}/phenantroline (Cu/phen). Samples were prepared as described above by either performing the final size exclusion without a reducing agent or by dialyzing the samples in a 10 kDa MWCO membrane against 20 mM Tris pH 8.0, 50 mM NaCl for 3 h at RT. A 240 mM Cu/phen stock solution in EtOH:H_2O (1:4) was prepared freshly as described previously[229]. After two steps of 1:10 dilution in H_2O, 30 µM Cu/phen was added to the nanodisc samples (10 or 20 µM) and incubated for 2 h (1 h for MPV17-containing samples) at 25 °C while shaking. The results were analyzed with a non-reducing SDS-PAGE.

5.2.6.2 BS^3-Crosslinking

For BS^3-crosslinking a 25 mM BS^3 (suberic acid bis(3-sulfo-N-hydroxy-succinimide ester) sodium salt) solution was prepared freshly in BS^3 buffer (20 mM NaPi pH 7.0, 50 mM NaCl). The liposome samples were prepared by either dialyzing against BS^3 buffer or adding 20 mM DTT to the liposome buffer. MPV17 in DPC micelles was used directly after the SEC. Samples were diluted to 20 µM in the respective buffer and the BS^3-crosslinker was added at a 1:30 ratio. The reaction was performed at 25 °C for 1 h under shaking. The result was analyzed with SDS-PAGE and Coomassie staining.

5.2.7 UV-Vis spectroscopy

Ultraviolet-visible (UV-Vis) spectroscopy was mainly used to determine concentrations. Light in the UV range contains the energy necessary to excite electrons in both DNA and proteins which leads to their absorbance.[230] As the bases in nucleic acids absorb light at 260 nm, this wavelength is commonly used to determine the concentration of DNA.[231] For DNA the instrument directly calculated the concentration based on the relation of an absorbance $A_{260} = 1$ corresponding to 50 µg/mL double stranded DNA.[231] In proteins the aromatic amino acids, mainly tryptophan and tyrosine, lead to an absorbance at 280 nm.[232] Therefore, the protein concentration is determined by measuring the absorbance at 280 nm and calculating the resulting concentration using the Lambert-Beer law:

$$A_\lambda = \varepsilon \cdot c \cdot d$$

Equation 5.2: Lambert-Beer law. A_λ: absorbance at wavelength λ; ε: molar extinction coefficient [$M^{-1}cm^{-1}$]; c: protein concentration [M]; d: path length [cm]

Both DNA and protein concentrations were measured using a NanoPhotometer®. Molar extinction coefficients as well as the molecular weight, necessary for converting molecular concentrations into mass concentrations, were determined based on the amino acid sequence using the ProtParam Tool. The parameters for the protein constructs used in this work are summarized in the Appendix.

5.2.8 CD spectroscopy

Circular dichroism (CD) spectroscopy was used to determine the secondary structure and its stability. A CD spectrometer irradiates the sample with plane polarized light, formed by a right and left polarized component of equal magnitude and measures the resulting radiation.[233,234] If a sample is optically active it will absorb the two components differently, leading to a resulting radiation with elliptical polarization. This method can be used on proteins as the amino acids contain chiral centers and, thus, are optically active. The elliptical polarization is characteristic for different secondary structure elements.[234]

CD was measured using a CD spectropolarimeter J-715. The temperature was controlled with a Peltier device. All measurements were performed in a 1 mm quartz cuvette with sample concentrations ranging from 5-20 µM. Far-UV spectra were recorded using a wavelength scan from 260 nm to 195 nm with a scanning speed of 100 nm/min and a band width of 1 nm at 20 °C. The resulting ellipticity is the average of 5 scans respectively. The raw data was converted to molar ellipticity with the following formula:[235]

$$\theta_{MRW} = \frac{\theta_{deg} \cdot 10^6}{d \cdot c \cdot N_{AA}}$$

Equation 5.3: Conversion of ellipticity θ_{deg} [mdeg] to the mean residue molar ellipticity θ_{MRW} [$degcm^2dmol^{-1}$]. d: path length [mm]; c: protein concentration [µM], N_{AA}: number of peptide bonds.

The stability of proteins was determined by monitoring the loss of secondary structure upon thermal or chemical unfolding. For thermal transitions the sample was heated with a scanning rate of 60 °C/h using a bandwidth of 2 nm and response and delay times of 1 sec each. The ellipticity was recorded at the determined signal minimum (220-222nm for mainly alpha helical proteins). For chemical transitions samples were prepared with varying amounts of denaturing agents (Urea or GuHCl), incubated over night at 4°C and the ellipticity, again at the determined signal minimum, was measured as a time course measurement with 61 data points generated in 30 sec (bandwidth 1 nm). These data points were averaged

to result in the ellipticity corresponding with each denaturant concentration. All transitions were fitted with the Boltzmann equation.

The helical secondary structure content was calculated using the experimentally determined ellipticity at 222 nm and the ellipticities referring to completely random and completely helical poly-L-lysine in the following formula[236]:

$$\alpha - helical\ content\ [\%] = \frac{\theta_{222}^{exp} - \theta_{222}^{r}}{\theta_{222}^{h} - \theta_{222}^{r}} \cdot 100\%$$

Equation 5.4: Calculation of the α-helical content. θ_{222}^{exp}: experimentally determined mean residue molar ellipticity at 222 nm; $\theta_{222}^{h} = -36000$ degcm^{2}dmol^{-1}; $\theta_{222}^{r} = -3000$ degcm^{2}dmol^{-1}.

5.2.9 Fluorescence spectroscopy

Fluorescence spectroscopy is widely used in protein chemistry as both the intrinsic fluorescence of proteins, for proteins containing aromatic amino acids, as well as fluorescence dyes in variable experimental setups can be used to measure fluorescence and gather information on folding, interaction, kinetics and more[237]. Fluorescence is emitted when an electron returns to the ground state (S_0) after being excited to the first excited state (S_1). During this process it emits light of higher wavelength than the wavelength of its absorption[230].

5.2.9.1 Tryptophan fluorescence

Fluorescence is strongly dependent on the environment of the probe and thus very sensitive to changes in this environment.[194] Therefore a protein's intrinsic fluorescence can be used to monitor its unfolding and assess the compactness of its fold. As tryptophans have the highest sensitivity parameter compared to tyrosines and phenylalanines, their contribution usually dominates the resulting fluorescence. Accordingly it is mainly the tryptophan fluorescence, which is monitored after exciting at 280 nm.[230]

Tryptophan fluorescence was monitored from 290 nm to 400 nm after exciting at 280 nm using a Jasco FP-8300 spectrometer. All measurements were performed on 100 nM samples in a 1 cm quartz cuvette while stirring with 300 rpm at 20 °C. Spectra were measured with a scan speed of 100 nm/min, a bandwidth of 5 nm for both excitation and emission and a response of 0.5 s. Chemical unfolding was detected by monitoring the fluorescence after incubation with varying GuHCl concentrations overnight at 4 °C. Reference spectra were recorded for all measurements and subtracted. The wavelength of the fluorescence maxima was plotted against the GuHCl concentration.

5.2.9.2 Bcl-2 protein liposome assay

The membrane permeabilization assay described by Yethon *et al.*[182] was used to probe pore-forming activity. In brief, 12.5 mM ANTS (8-aminonaphthalene-1,3,6-trisulfonic acid) and 45 mM DPX (*p*-xylene-bis-pyridinium bromide) were added to the lipid resuspension mixture and liposomes were

prepared as explained in **Chapter 5.2.11**. Afterwards the reagents were washed off the outside of the liposomes by performing a NAP™-5 column (GE Healthcare). DPX quenches the fluorescence of ANTS when both are trapped inside the liposomes. Once pores are formed and both reagents are released and dilute, the fluorescence of ANTS increases.

The assay was set up in a 96-well plate (Greiner). 50 nM BakΔTM, 20 nM cBid/Puma-BH3 and 25 nM BclxLΔTM were used for the measurements at low BakΔTM concentrations, while 600 nM BakΔTM and 300 nM cBid/Puma-BH3/BclxLΔTM were used for measurements under autoactive BakΔTM conditions. 10 µL of liposomes with an approximate lipid concentration of 2.5 mg/mL were added directly before measuring. Measurements were performed on a SpectraMax iD5 at 30 °C. The samples were excited at 355 nm (5 nm bandwidth) and the emission recorded at 520 nm (5 nm bandwidth). The samples were measured in triplicates and the data was normalized according to the equation $(F_t-F_0)/(F_{100}-F_0)$ with F_t being the measured fluorescence at time t, F_0 being the initial fluorescence of liposomes without the addition of proteins and F_{100} being the fluorescence measured after completely dissolving the liposomes and releasing all dye by adding 0.2 % Triton X-100. The data is presented as relative fluorescence with 100 % representing the maximum liposome permeabilization seen for the respective conditions compared in the individual figures.

5.2.9.3 SYPRO Orange

SYPRO Orange was used to test for molten globule states. This fluorescent dye only binds to exposed hydrophobic regions, as found in molten globules[238]. While it produces a low fluorescence quantum yield in an aqueous solution, this yield increases after binding to the hydrophobic proteins patches, resulting in fluorescence emission[195]. Samples (100 nM) were pipetted into a 96-well plate and incubated overnight with 0 M – 6 M GuHCl at room temperature. SYPRO Orange was added to the wells in a 1:1000 dilution before the measurement. The fluorescence was detected by a SpectraMax iD5 while exciting at 470 nm and recording the emission spectrum from 520 nm to 750 nm in 10 nm steps. Reference spectra without the protein were recorded for all measurements and subtracted.

5.2.10 Differential Scanning Calorimetry

Differential Scanning Calorimetry (DSC) measures processes induced by changes in temperature, thus, is used to monitor protein folding and measure the melting temperature and thermodynamics. The instrument is equipped with a reference and sample cell, which are heated simultaneously. Heat absorbing processes taking place in the sample cell induce a temperature difference relative to the reference cell. A feedback circuit enables that the sample cell is equipped with the additional heat necessary to maintain equal temperatures between the two cells. This additional heat is proportional to the excess heat capacity of the heat absorbing process. After baseline correction and normalization to

concentration, the melting temperature, enthalpy and heat capacity can be derived from the resulting thermogram.[239]

DSC was performed on a Malvern MicroCal PEAQ-DSC instrument. Samples were dialyzed overnight at 4 °C in the reference buffer (20 mM NaPi pH 7.0, 50 mM NaCl, 1 mM EDTA, 5 mM BME) to ensure buffer matching. A temperature scan was performed on 270 µL of a 30 µM protein sample ranging from 25 to 100 °C or 30 to 115 °C, depending on the melting point of the sample. A heating rate of 60 °C/h was applied. To ensure thermal equilibration and exclude contaminations, sample measurements were only started after three water/water runs followed by buffer/buffer runs resulted in a stable baseline. Each sample measurement was followed by one buffer/buffer run or until a steady baseline was received before the next sample was measured. The data was analyzed using the PEAQ-DSC software.

5.2.11 Isothermal Titration Calorimetry

Isothermal titration calorimetry (ITC) is a biophysical method, which is used to determine binding events between molecules in solution. The method is based on detecting the difference in power required to hold the sample and reference cell at the same temperature while one component, is titrated into the sample cell containing the potential binding partner in solution[240].

The ITC instrument contains two identical cells made of a thermally conducting and chemically inert material. They are mantled by an adiabatic jacket. Both cells are heated to the same temperature by a heater that reacts to temperature differences between the cells by adapting its power supply to the reference cell. Depending on whether the binding reaction is exothermic or endothermic, titrating the potential binding partner to the sample cell leads to a small change in temperature in the sample cell. The heater's feedback system detects the difference in temperature between the two cells and adjusts the power supply heating the sample cell[241]. The power used to hold both cells at the same temperature is plotted against the time in the raw data. For binding events this results in a spike for every aliquot injection. The integral, which equals the total heat exchanged per injection, decreases as saturation nears and ends with a steady state when all binding pockets are filled. Additionally, the exchanged heat is plotted against the molar ratio. This function is sigmoidal for binding events. At the point of inflection, the corresponding molar ratio gives information regarding the stoichiometry (N) while the slope equals the association constant K_a and can be converted to the dissociation constant: $K_d = \frac{1}{K_a}$ [241]. The enthalpy ΔH is received by subtracting the two baselines. These parameters enable the calculation of the change in entropy (ΔS) and Gibbs free energy (ΔG) using the following equation[240,241]:

$$\Delta G = -RT \ln K_a = \Delta H - T \cdot \Delta S$$

Equation 5.5: The Gibbs free energy ΔG can be described as a function of the association constant K_a or by its enthalpic ΔH and entropic ΔS contributions. R is the universal gas constant and T the absolute temperature.

While this measurement technique doesn't allow the determination of the interaction's location, it permits the calculation of all relevant thermodynamic properties of protein-ligand interaction.

The ITC measurements were performed on a MicroCal PEAQ-ITC at 25 °C with 20 titration steps and 1.5 µL per step while stirring at 750 rpm. The reference cell's heating rate was set to 10 µcal/s. 300 µM of a Puma-BH3 peptide was titrated to 30 µM BclxLΔTM-BakH1 in 20 mM NaPi pH 7.0, 50 mM NaCl, 1 mM EDTA, 5 mM BME. Both binding partners were prepared in the identical buffer. The data were analyzed using the MicroCal PEAQ-ITC software.

5.2.12 Dynamic Light Scattering

Dynamic light scattering (DLS) was used to determine the particle size of proteins in solution. This method makes use of light being scattered when meeting particles in solution. The scattering intensity is recorded and relates the measured motion to the diffusion coefficient from which the hydrodynamic radius can be obtained.[242]

DLS measurements were performed on a DynaPro NanoStar instrument. 60 µL of a 10-20 µM sample were measured at 25 °C and 43 °C and at increasing incubation times. In order to sediment any oligomeric particles samples were centrifuged (20,000 g, 20 min, 4 °C) before the experiment. The data was analyzed using the DYNAMICS software package.

5.2.13 Sortase A ligation

The sortase A mediated ligation was performed using a modified Sortase A construct (P94R, D160N, D165A, K190E, K196T), which was found to be more active but calcium dependent[181].

30 µM of the respective TMH in ΔH5-nanodiscs was mixed with BakΔTM C-terminally harboring the Sortase motif (BakΔTM-Sor) and the modified Sortase A construct at a ratio of 1:1:0.08 in sortase buffer (50 mM Tris pH 8, 150 mM NaCl, 20 mM $CaCl_2$, 10 mM BME). The ligation mixture was dialyzed in sortase buffer at room temperature, using a 10 kDa-Slide-A-Lyzer MINI dialysis device (ThermoFischer Scientific). After 30 min, the amount of BakΔTM-Sor and Sortase A was doubled, leading to a ratio of 1:2:0.16. After another 30 min, the same amount of BakΔTM was added again, resulting in a final ratio of 1:3:0.16. After a total of 90 or 120 min, the reaction was stopped by quenching the $CaCl_2$ with 20 mM EDTA.

In the optimized setup, the nanodiscs were formed using MSPΔH5 without the N-terminal glycine (MSPΔH5-ΔnG), to eliminate the side reaction of BakΔTM-Sor and MSPΔH5 and the N-terminal linker of the Bak-TMH was extended to $(GS)_8$ for better accessibility of the terminal glycine.

5.2.14 Hydrogen/Deuterium Exchange Mass Spectrometry

Hydrogen/deuterium exchange (HDX) mass spectrometry (MS) utilizes the lability of backbone amid protons in proteins to gather information on the structure and conformational dynamics of their secondary structure elements. Due to their NH-acidity these protons exchange with solvent protons when they are not shielded or forming a hydrogen bond, as found in α-helices and β-sheets.[243] This technique detects the changes in mass linked to the isotope exchange between the protonated protein and the deuterated solvent. As the hydrogen/deuterium exchange rate is dependent on the accessibility of the individual amid proton, information on the protein folding and dynamics as well as interaction sites can be derived from the exchange kinetics at a per-residue resolution[243,244]. As HDX-MS can be applied to large proteins (>100 kDa) also in complex sample matrices requiring only low concentrations (< µM), it can also be performed on membrane proteins[245,246].

The HDX-MS experiments were performed by Florian Rührnößl and Annika Strauch (Prof. Buchner, TUM) on an ACQUITY UPLC M-class system equipped with automated HDX technology (Waters, Milford, MA, USA). The HDX kinetics were measured after 0, 10, 60, 600, 1800 and 7200 s in technical triplicates and biological duplicates at 20°C. The respective protein sample (approximately 30 µM) was diluted by 1:20 into the corresponding buffer (20 mM sodium phosphate, pH 6.8) containing 99.9 % D_2O or H_2O in the reference sample. The reaction was quenched by adding 1:1 200 mM KH_2PO_4, 200 mM Na_2HPO_4, pH 2.3, containing 4 M guanidine hydrochloride and 200 mM TCEP at 1 °C. A Waters Enzymate BEH pepsin column 2.1 × 30 mm was used for the on-column peptic digest at 20 °C. Subsequent reverse phase chromatography using a Waters Acquity UPLC C18 1.7 µm Vangard 2.1 × 5 mm trapping-column and a Waters Aquity UPLC BEH C18 1.7 µm 1 × 100 mm separation column separated the peptides at 0°C using a gradient. The acetonitrile concentration was increased stepwise from 5–35% in 6 min, from 35–40 % in 1 min and from 40–95 % in 1 min. Following their elution, the peptides were characterized using an in-line Synapt G2-S QTOF HDMS mass spectrometer (Waters, Milford, MA, USA) collecting MS data over an m/z range of 100–2000. The system was calibrated with Glu-fibrino peptide B (Waters, Milford, MA, USA). The peptides were identified by MS^E (Waters, Milford, MA, USA) while automatically raising the collision energy from 20–50 V. The results are presented as relative deuterium levels, a correction for back exchange was not performed, because the automated system measures all samples at identical conditions[247]. The PLGS 3.0.3 and DynamX 3.0 software packages (Waters, Milford, MA, USA) were used for data analysis.

5.2.15 MD Simulations

A molecular dynamics (MD) simulation analyzes the physical movement of atoms and macromolecules, e.g. proteins by allowing them to interact for a defined period of time and calculating the spatial position of each atom as a function of time using Newton's equation of motion[248]. It is increasingly being used in combination with structural biology techniques to both interpret and guide the experimental work[249,250].

The MD simulations were performed by Dr. Franz Hagn (TUM) using the CHARMM-GUI web server (http:/www.charmm-gui.org) [251] to form a template. The NMR-based structure of the Bak-TMH was inserted into a hexagonal box of a DMPC/DMPG (3:1) lipid bilayer in presence of 0.15 M KCl. The system was equilibrated at 310 K in two phases using 3 cycles each. In each cycle, the force constants securing the positions of both protein and membrane were gradually decreased. During the first phase, a time step of 1 fs and a simulation time of 50 ps were applied in each cycle, while this was increased to a time step of 2 fs and a simulation time of 200 ps in the second phase. The total equilibration time was 750 ps. The final MD simulation was performed with NAMD[252] for 129 ns using the isothermal-isobaric ensembles at 310 K in the absence of a transmembrane potential. The particle-mesh Ewald method[253] was applied to define long-range electrostatic interactions. The short-range electrostatic interactions were truncated by a smoothing function. The obtained trajectory was analyzed and visualized using VMD [254].

5.2.16 NMR Spectroscopy

Nuclear magnetic resonance (NMR) spectroscopy is a non-destructive method, which is used to study the 3-dimensional structure and the dynamics of molecules at high resolution[255]. As in any spectroscopic method, it is based on energy states and the population distribution. However, in NMR these states are quantized. As it is the primary method used for the high-resolution structural studies in this work it is described in more detail in the following subchapters.

5.2.16.1 Basics of NMR

Nuclei consist of protons and neutrons. Both have an intrinsic angular moment, also called "spin" because they act as if they were spinning. Together they form the spin I of a nucleus. Pairs of protons ($I = \frac{1}{2}$) or neutrons ($I = \frac{1}{2}$) cancel each other out, so that a nucleus containing an even number of protons and an even number of neutrons has a spin quantum number of $I = 0$. For all other nuclei their spin will produce $2I + 1$ spin states ranging from ($-I$ to $+I$) and induce a rotation about the magnetic field B_0 oriented in the z-direction, when interacting with the external magnetic field B_0. The magnetic moment μ of a nucleus depends on the spin I and the gyromagnetic ratio γ, a constant characteristic for every nucleus[255].

$$\mu = \gamma\hbar\sqrt{I(I+I)}$$

Equation 5.6: The magnetic moment μ of a given nucleus is proportional to its gyromagnetic ratio γ, its spin I and the Planck constant ħ.

The properties of the nuclei used for protein NMR and utilized in this work are summarized in T**able 5-15**.

Table 5-15: Characteristics of the nuclei used in protein NMR[256]:

Isotope	Ground-state spin	Natural abundance [%]	Gyromagnetic ratio γ $[10^6\,T^{-1}\,s^{-1}]$
^{1}H	1/2	~100	267.522
^{2}H	1	0.015	41.066
^{13}C	1/2	1.1	67.283
^{15}N	1/2	0.37	-27.126

Each spin state, that a nucleus can possess, correlates to an energy resonance condition. When energy equal to the difference in energy states (ΔE) is applied, this induces a change in population. This energy difference depends on the magnetic field B_0. For the simplest case of $I = \frac{1}{2}$ allowing only a single-quantum transition between the two states, it is described as follows[255]:

$$\Delta E = \hbar\gamma B_0 = \hbar\omega$$

Equation 5.7: The energy difference ΔE for a single quantum transition depends on the magnetic field B_0, the gyromagnetic ratio γ of the respective nucleus and the Planck constant ħ. ω is the angular frequency of the electromagnetic radiation necessary for the transition in [rad s^{-1}].

The angular frequency ω is the frequency necessary to induce a transition between energy states. This Larmor frequency is directly proportional to the applied field strength and can also be described as an ordinary frequency ν in [Hz][255]:

$$\nu = \frac{\omega}{2\pi} = \frac{\gamma B_0}{2\pi}$$

Equation 5.8: Relationship between the Larmor frequency described as frequency ν in [Hz] and an angular frequency ω in [rad s^{-1}].

The intensity of an NMR signal depends on the population difference of the spin states. Only this difference in population can be observed by NMR. It results in the macroscopic magnetization M_z of the sample and is given by the Boltzmann equation[255]:

$$\frac{n_\beta}{n_\alpha} = e^{\frac{-\Delta E}{kT}} = e^{\frac{-\hbar\gamma B_0}{kT}} = e^{\frac{-\hbar\omega}{kT}}$$

Equation 5.9: Boltzmann equation. n_α and n_β are the population of the α and β states. T is the absolute temperature in [K] and k is the Boltzmann constant.

Consequently, the NMR signal is proportional to the gyromagnetic ratio γ of the observed nucleus, the magnetic field strength B_0 and indirectly proportional to the temperature T. As the energy difference between the two possible states is very small, the population difference is close to zero at room temperature. Thus, NMR spectroscopy is a very insensitive method requiring a highly concentrated sample and a high field strength.

In an NMR experiment, nuclei are placed in an external magnetic field and exposed to electromagnetic radiation, also called "pulse", produced by an induction coil in perpendicular field direction. When the radiation's frequency ν is in resonance with the Larmor frequency of a nucleus, it induces transitions between energy levels leading to a change in the macroscopic magnetization. The induced magnetization in the transverse plane and its reduction is measured as a function over time, the free induction decay (FID), by a detection coil surrounding the NMR sample. The signal-to-noise ratio is improved by $\sqrt{n}$, when applying the pulse and detecting the FID n times and averaging the acquired signal. It is decomposed into a function of frequency to separate the individual signals by Fourier transformation. This results in the NMR spectrum showing individual peaks at different frequencies. The actual resonance frequency of an individual nucleus depends on its chemical environment. When a nucleus is placed in a magnetic field B_0 an electronic current perpendicular to the magnetic field is induced by the surrounding electrons. This, in turn, induces a small local magnetic field opposed to the applied magnetic field, which modulates the magnetic field strength of the nucleus. These different local fields within one molecule influence each other. Therefore, the frequency varies for the same type of nucleus in a sample depending on its location in the molecule. Their positions are visualized by the chemical shift δ using a reference signal and expressed in parts per million (ppm)[255]:

$$\delta = \frac{\nu_{sample} - \nu_{ref}}{\nu_{ref}} \cdot 10^6$$

Equation 5.10: The chemical shift δ in [ppm] is calculated using the frequencies ν in [MHz] of the sample and the reference (tetramethylsilane (TMS) or 2,2-dimethyl-2-silapentane-5-sulfonic acid (DSS)).

5.2.16.2 Protein NMR

In protein NMR two-or multi-dimensional experiments are used to resolve the strong signal overlap in the first dimension[255–257]. For the second dimension an evolution time t_1 is added between the preparation time, consisting of the pulses, and the acquisition time. This evolution time is increased systematically

between each increment. Afterwards, all the FIDs are transformed using the same phase parameters. During the evolution time, the phase of the signals is modulated as a function of the t_1 evolution time, resulting in an interferogram similar to an FID, when the amplitude of a peak is plotted against t_1 after the initial Fourier transformation in the direct dimension. When this FID is Fourier transformed along t_2, this leads to a two-dimensional NMR spectrum with two frequency axes. The signal intensity is usually visualized by contour levels. More dimensions can be acquired by adding further evolution time periods.

In this work, the NMR studies mainly base on [^{1}H, ^{15}N]-Heteronuclear Single Quantum Coherence (HSQC) spectroscopy or the TROSY version of this experiment. A [^{1}H, ^{15}N]-HSQC is based on transferring magnetization from the proton to the less sensitive nitrogen and back after a certain time delay and subsequently recording the signal in the direct ^{1}H dimension[257]. By recording a series of experiments after different time delays, the chemical shift of both is detected and plotted against each other in the spectrum resulting in a signal for every H-N-bond. Thus, a signal for every backbone amide bond except proline is received for a protein. Additionally, each NH-group located in amino acid side chains gives a signal. The signals can be assigned to the corresponding amino acids by a third dimension that supplies the sequential connectivities, usually in the ^{13}C dimension. These connectivities can either be monitored by measuring spin-spin interactions that are mediated by the electrons in chemical bonds or through space. The interactions occurring through bonds are measured by the following measurements in this work, HNCO, HN(CA)CO, HNCA, HN(CO)CA and HNCACB. All these experiments are based on a [^{1}H, ^{15}N]-HSQC with the carbon dimension in the third dimension. In the HN(CA)CO signals for the carbonyl carbons are seen for the corresponding residue in the HSQC and the preceding backbone amide group. In the HNCO only the carbonyl carbon signal of the preceding backbone amide is detectable. Likewise, in the HNCA the alpha carbons are seen for the corresponding residue in the HSQC and the preceding backbone amide group, while the HN(CO)CA only shows the preceding alpha carbon. The HNCACB detects both alpha and beta carbons for both the immediate and the preceding backbone residues. Experiments to detect the ^{13}Cα, ^{13}Cβ and the ^{13}CO must be run to identify all the connectivities and unambiguously assign the backbone residues. For helical structures nuclear overhauser effect spectroscopy (NOESY)-based methods, which detect residues close in space, can assist the assignment. The ^{15}N-edited [^{1}H, ^{1}H]-/ [^{1}H, ^{15}N]-NOESY experiments show cross-peaks for the preceding and following NH-group, as both are close in space in an α-helical structure. In general, cross-peaks are seen to other protons or nitrogens, which are in a close range (< 5 Å)[258]. These information are essential for structure determination. For structure calculations, the NOE's can be classified in distance restraint ranges. Together with the TALOS$^+$-derived[176] backbone angles and the h-bonds defined by the lack of a water exchange peak, these data can be used to calculate a protein's structure using programs like XPlor-NIH[221].

5.2.16.3 Protein backbone dynamics

Internal protein dynamics can strongly influence the structure, stability and function of a protein and therefore, are of key interest[259]. NMR spectroscopy is unique in directly enabling the study of these dynamical processes, as spin relaxation is sensitive to both the physical environment of the nuclei and the motion of the molecule[257,260]. The set of R_1-, R_2-relaxation rates and {^{1}H}-^{15}N-heteronuclear NOE is generally used to study the mobility of protein backbones in the ns-ps time scale[261].

After a 90°$_x$ pulse is applied and the macroscopic magnetization is rotated onto the y-axis and precesses in the xy-plane, spin relaxation occurs by two distinct processes[255,257]. The T_1-relaxation, also called longitudinal or spin-lattice relaxation, describes the process by which the macroscopic magnetization returns to the Boltzmann equilibrium aligned along the z-axis of the external magnetic field. T_1-relaxation results from energy exchange with the surrounding lattice and occurs at the timescale of seconds in proteins. The T_2-relaxation, also called transverse or spin-spin relaxation, describes the entropic process by which the transverse magnetization returns to its equilibrium value of zero. T_2 relaxation is faster than T_1-relaxation. As relaxation is sensitive to the motion of a nuclei in the ns to ps time scale, these measurements enable the study of dynamics for individual residues within the molecule.

For the heteronuclear NOE (hetNOE), the difference in intensity of the ^{15}N-signal is detected with and without saturating the attached protons[255]. The saturation is transferred from one nucleus to the other by dipolar interactions and depends on the ns to ps dynamics of the bonds.

The rotational correlation time τ_c of a protein can be derived from the T_1 and T_2-relaxation rates and describes the average time needed to change the position by one radian[257]. For rigid protein molecules ($\tau_c \gg 0.5\ ns$) and a high magnetic field (≥ 500 MHz) it can be calculated as follows[256]:

$$\tau_c = \frac{\sqrt{\frac{6T_1}{T_2}} - 7}{4\pi\nu_N}$$

Equation 5.11: Calculation of the rotational correlation time τ_c using the T_1 and T_2 relaxation time constants. ν_N is the corresponding ^{15}N resonance frequency.

Using the Debye-Stoke-Einstein equation, the hydrodynamic radius can be calculated by averaging τ_c for the rigid protein parts[256].

$$\tau_c = \frac{4\pi\eta r^3}{3k_B T}$$

Equation 5.12: The Debye-Stoke-Einstein equation explains the relationship between the rotational correlation time τ_c and the hydrodynamic radius r. η=buffer viscosity, k_B=Boltzmann constant, T=temperature.

The dependence of the three parameters used for deriving dynamics in the ns-ps timescale on the correlation time is shown in **Fig. 5.1**. For very fast motions, the R_1-rate ($\frac{1}{T_1}$) and R_2-rate ($\frac{1}{T_2}$) are equal and increase with τ_c. For larger systems with slower motions, such as proteins, the relaxation rates drift apart. While the longitudinal relaxation rate reaches a maximum and then decreases, the transverse relaxation rate increases continuously. In contrast, the {^{1}H}-^{15}N-heteronuclear NOE has negative values in very dynamic systems and values close to 1 in rigid systems.

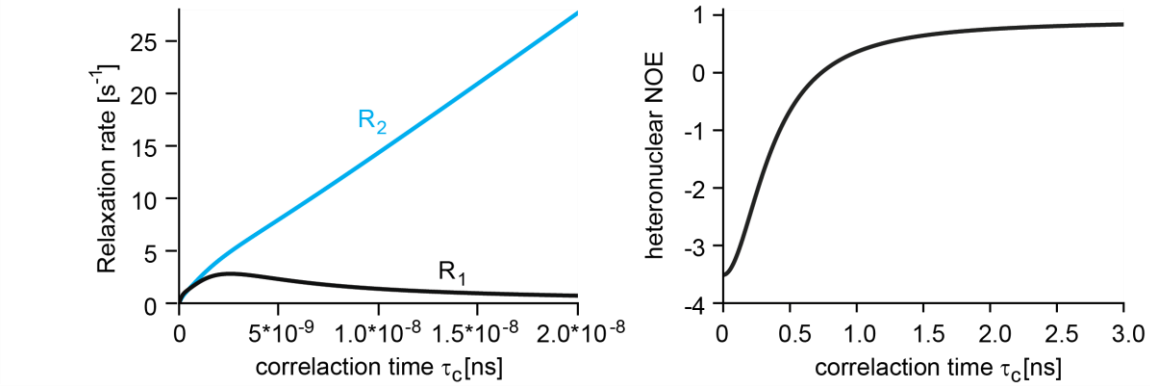

Figure 5.1: Correlation of the R_1/R_2-relaxation rates (left) and the hetNOE for a ^{15}N-nucleus (right) to the correlation time τ_c at a magnetic field of 14.1 T.

5.2.16.4 The TROSY-effect and deuteration

Transverse relaxation-optimized spectroscopy (TROSY) and deuteration are used for large protein systems to reduce line-broadening caused by slower tumbling rates, resulting in faster T_2-relaxation[262–264].

In a two-state spin system, where two spins, I and S, couple to each other through bonds, their corresponding peaks will split into doublets, described by the scalar coupling constant J_{IS}[263]. The T_2-relaxation of this system is mainly influenced by dipole-dipole (DD) interactions of I and S and chemical shift anisotropy (CSA) of the individual spins. The cross correlation between these two parameters leads to individual linewidths of the two peaks forming the doublet. When the correlation between the two spins is detected, as in an HSQC experiment, the cross peak corresponding to the two doublets would theoretically be split into four peaks, each with a different line shape **(Fig. 5.2)**. By decoupling the spins, the doublet is averaged to a single peak in both dimensions, resulting in a single cross-peak with an averaged line width and, thus, a reduced signal-to-noise ratio in the HSQC method conventionally used. Instead, in a TROSY experiment, the heteronuclear coupling remains active and the cross peak with the slowest relaxation properties for both nuclei resulting from destructive interference of the DD and CSA components is selected. As the CSA relaxation increases with the magnetic field strength for both ^{1}H and ^{15}N nuclei, the TROSY effect is especially pronounced at higher fields (> 700 MHz).

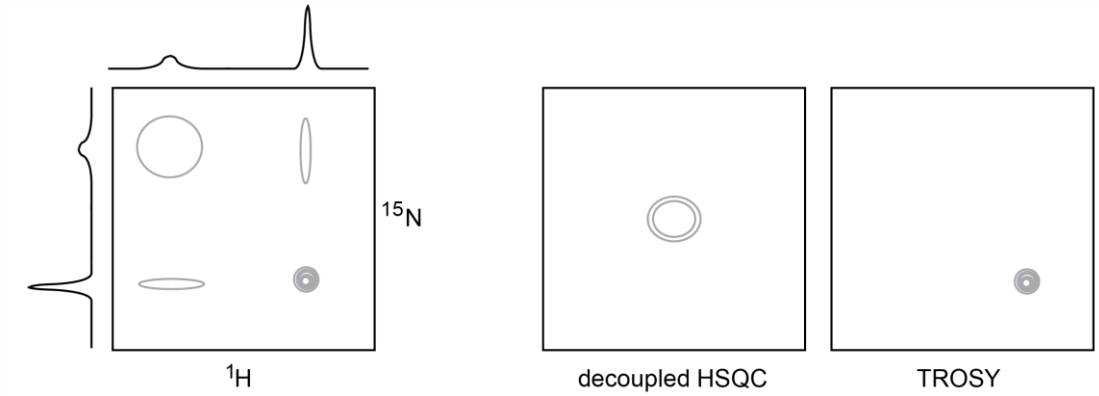

Figure 5.2: Depiction of the TROSY-effect.

The pulse sequence used for the TROSY experiment is derived from the HSQC pulse sequence **(Fig. 5.3)**[257]. Both pulse sequences start on the proton because it has a larger gyromagnetic ratio leading to a larger energy difference (see **Equation 5.9**) and, thus, a stronger signal. The coherence is transferred to the nitrogen spin with an INEPT sequence. The ^{15}N-signal evolves for the time period t_1. In the HSQC pulse sequence, a 180° pulse on protons is placed in the middle of t_1 forming a spin echo. This refocuses the evolution of coupling. The magnetization is transferred back to the proton and a second spin echo enables the anti-phase signals to become in-phase, so that they are detectable. Finally, the signal is acquired using broad band nitrogen decoupling during the acquisition time t_2. In the TROSY experiment coupling is desired, so the proton coupling is not refocused during t_1 by a 180° pulse and no broadband decoupling is performed on spin S during the acquisition time t_2. The TROSY pulse sequence selects for the spin transition with the most favorable line shape.

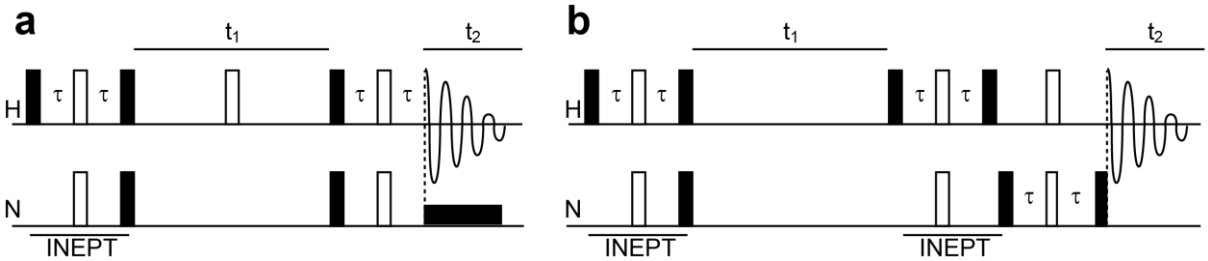

Figure 5.3: Decoupled HSQC (a) and TROSY (b) pulse sequences. The black vertical rectangles show 90° pulses, while the white rectangles show 180° pulses. The optimum value for τ is $1/(4J_{NH})$. In (a), the horizontal black rectangle during t_2 indicates broadband decoupling

Additionally, deuteration can improve the signal-to-noise ratio of an NMR spectrum[262]. While the labile NH-protons back-exchange with the aqueous solvent and are detectable, the non-exchangeable side chain protons remain deuterated. When a large amount of the protons is exchanged for deuterium in the sample, dipolar couplings are reduced, leading to a reduction of the relaxation rates of ^{13}C and ^{15}N spins, which are strongly influenced by directly bound protons.

5.2.16.5 Paramagnetic relaxation enhancement (PRE)

A nucleus in close proximity to an unpaired electron spin experiences a paramagnetic relaxation enhancement (PRE) due to the magnetic moment of the electron spin[265,266]. The magnetic dipolar interaction between the electrons and a nucleus nearby (< 35 Å) leads to increased T_2-relaxation rates and thus, extensive line broadening. The effect is distance-dependent and decreases with the power of r^6 (r = distance). This method is employed to study the binding of ligands, partner proteins or membrane surfaces. In this work, the fatty acid 16-doxyl-stearic acid (DSA) and water-soluble Gd^{3+}-chelated DOTA were used to study, which parts of a membrane protein are located inside and outside the detergent micelle **(Fig. 5.4)**.

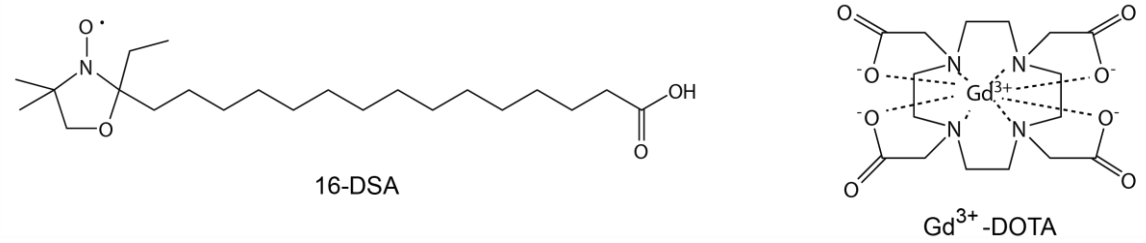

Figure 5.4: The PRE-labels 16-DOXYL-stearylic acid and Gd^{3+}-chelated DOTA.

5.2.16.6 Residual dipolar couplings (RDC)

While the NOE is limited to detecting distances up to 5 Å and PREs can pick up distances up to 35 Å, residual dipolar couplings (RDCs) provide relative orientations between internuclei vectors independent of their distance[267]. In solution state NMR, dipolar couplings are usually averaged to zero because the molecules occupy all possible orientations with equal probability. However, when the molecules are weakly aligned relative to the magnetic field an anisotropic condition is generated and RDCs evolve. The magnitude of this measurable RDC depends on the distance between the nuclei and the angle between the internuclei vector and the external magnetic field. A weak alignment of the protein can be induced by different methods. Either the direct weak alignment of the protein by the external magnetic field is used or a mechanical alignment is induced by the addition of media which can be aligned with the magnetic field and weakly interact with the protein. In this work, the second approach was chosen and the protein was mixed with filamentous Pf1-phages[268].

When two nuclei I and S experience an RDC, this leads to an additional splitting of the signal, which is the sum of the secular part of the dipole-dipole interaction D_{IS} and the coupling constant J_{IS}. The dipolar interaction can be described as follows[267].

$$D_{IS} = D_{max} \langle \frac{3cos^2\theta - 1}{2} \rangle$$

$$D_{max} = \frac{-\mu_0 \hbar \gamma_I \gamma_S}{8\pi^3 r_{IS}^3}$$

Equation 5.13: The dipole-dipole interaction D_{IS} depends on the dipole-dipole coupling constant D_{max} and the angle between the internuclei vector and the external magnetic field θ; μ_0 = vacuum permeability; ħ = Planck constant; γ = gyromagnetic ratio of the respective nucleus; r = distance between the nuclei.

When the spins I and S are connected by a chemical bond, D_{IS} depends on the dipole-dipole coupling constant D_{max} and the angle between the internuclei vector and the external magnetic field. Time or population averaging indicated by the angular brackets is necessary because the direction of the internuclei vector fluctuates due to rotational diffusion. Without an alignment, the term within the angular brackets averages to zero. D_{max} depends on the bond type, it decreases with the power of r^3 and is usually in the order of 10^3 Hz [267].

RDC's deliver additional information for structure calculations or can be used to determine the quality of a calculated structure by comparing calculated and experimentally derived RDCs.

5.2.16.7 Experimental procedures

All NMR experiments were performed on Bruker Avance III instruments operating at 600, 800, 900 and 950 MHz proton frequency, respectively, equipped with cryogenic probes and controlled by Topspin 3.5 (Bruker Biospin). All NUS-3D spectra were processed with NMRpipe [269]. All other spectra were processed with Topspin3.5 (Bruker Biospin). The resonance assignment and NMR data analysis was done with NMRFAM-Sparky [220]. Chemical shift-based order parameters were calculated with the program TALOS$^+$ [176]. Chemical shift perturbations were calculated as ^{1}H,^{15}N-averaged values, as described in Ref. [270] using the perturbation analysis module in NMRFAM-Sparky [220].

<u>Bak</u>

The NMR experiments on BakΔTM were performed in 20 mM NaPi pH 6.8, 1 mM EDTA, 2 mM DTT, while those on the Bak-TMH were recorded in 20 mM NaPi pH 7, 50 mM NaCl, 1 mM EDTA. If Ni-NTA-lipids were used for nanodisc assembly, no EDTA was added and DTT was exchanged for 5 mM BME. For the soluble domain, HSQC-type triple resonance experiments[271] were recorded for obtaining backbone resonance assignments. When nanodiscs or detergents were present, TROSY-type 3D-triple resonance experiments were recorded [264]. The soluble domain was measured at 30 °C both in solution (200-300 µM) and when bound to membrane mimetics (approximately 50-150 µM). Bak-TMH (300 µM) was measured at 37 °C in DPC micelles (~300 mM DPC) and at 42 °C in MSP1D1ΔH5 nanodiscs (75 % DMPC + 25 % DMPG). For the assignment of the Bak-TMH, 3D-TROSY-HNCA and HNCO experiments with *U*-[^{2}H, ^{13}C, ^{15}N]-labeled Bak-TMH in DPC as well as ^{15}N-edited [^{1}H, ^{1}H]-NOESY-TROSY- and ^{15}N-edited [^{1}H, ^{15}N]-NOESY experiments for *U*-[^{2}H, ^{15}N]-labeled Bak-TMH in DPC and lipid nanodiscs were recorded. For NOESY experiments, a mixing time of 200 ms was used. Structure calculations were done with XPlor-NIH[221] using standard protocols. Structural statistics of the ensemble were obtained by utilizing the 20 structures with the lowest restraint violation energies. Ramachandran map analysis was performed with the RAMPAGE webserver[272]. The T_1-, T_2-relaxation and {^{1}H}-^{15}N heteronuclear NOE experiments were recorded in a fully interleaved manner. For the T_1-

and T_2-relaxation experiments of Bak-TMH in DPC-micelles 8 delays were recorded ranging from 10 ms to 1200 ms and from 16 ms to 204 ms, respectively. 1024 complex points in the direct dimension and 130 complex points in the indirect dimension were recorded for each. The {^{1}H}-^{15}N heteronuclear NOE was measured with and without proton saturation. The proton saturation time was 2 seconds for activated BakΔTM in MSP1D1ΔH5 nanodiscs using a TROSY-based experiment [273] and 2.5 seconds for inactive BakΔTM using a HSQC-based experiment. 1024 complex points in the direct dimension and 128 complex points in the indirect dimension were recorded. Amide residual dipolar couplings (RDCs) were measured with 2D-TROSY and semi-TROSY [263] experiments in the isotropic case and in the presence of 10 mg/mL Pf1 phage (Asla Biotech, Riga, Latvia). Fitting of the RDC alignment tensor was done with PALES [274]. Refinement of the Bak crystal structure (PDB: 2IMS [114]) using NMR chemical shift and HN-RDC restraints was done with XPlor-NIH.

BclxL

NMR experiments on BclxLΔTM and its derivatives (400 µM -1.5mM) were performed in 20 mM NaPi pH 7, 50 mM NaCl, 1 mM EDTA, 2 mM DTT at 30 °C using either a protonated or deuterated ^{15}N-labeled protein. When BclxLΔTM was bound to ΔH5-nanodiscs via [Ni^{2+}]-caged lipids, EDTA and DTT were omitted and the protein was reduced using 5 mM BME. For the assignment of *U*- [^{2}H, ^{13}C, ^{15}N]-BclxLΔLΔTM-BakH1 3D-TROSY-HNCA, HNCACO, HNCO, HNCOCA and HNCACB experiments were recorded as well as ^{15}N-edited [^{1}H, ^{1}H]-NOESY-TROSY- and ^{15}N-edited [^{1}H, ^{15}N]-NOESY experiments. For the NOESY experiments a mixing time of 200 ms was used. The T_2-relaxation and {^{1}H}-^{15}N heteronuclear NOE experiments were recorded in a fully interleaved manner with 1024 complex points in the direct dimension and 256 complex points in the indirect dimension. 8 delays were recorded ranging from 16 to 160 ms for the T_2-relaxation experiments. The {^{1}H}-^{15}N heteronuclear NOE was measured with and without proton saturation. The proton saturation time was 2 seconds.

MPV17

For the backbone resonance assignments, a set of TROSY-type 3D-experiments was recorded [264] as well as a 3D-^{15}N-edited-[^{1}H, ^{1}H]-NOESY-TROSY (200 ms mixing time) with ~ 400 µM *U*-^{2}H,^{13}C,^{15}N-labeled MPV17 samples (wt, cysteine-free, MMTS methylated) in 20 mM NaPi, pH 7.0, 50 mM NaCl, 0.5 mM EDTA, 5 mM DTT (only wt MPV17), 300 mM DPC (Anatrace, F308). They were run in a non-uniformly sampled (NUS) manner with 15-20 % sampling density. The NUS sampling schedule was obtained by the Poisson-gap method [275]. For rapid spectra reconstruction, an iterative soft thresholding (IST) was employed [276].

{^{1}H},^{15}N-heteronuclear NOE was measured with a 400 µM ^{2}H,^{15}N-labeled sample at 310K with a 2 s proton saturation time, 96 transients and 128 complex points in the indirect ^{15}N dimension in a fully interleaved manner. Paramagnetic relaxation enhancement (PRE) experiments were conducted with a series of 2D-[^{15}N,^{1}H]-TROSY experiments (recycle delay 2 s) with or without the paramagnetic agent.

For probing membrane locations, the spin-labeled 16-doxyl-stearic acid (16-DSA) was added to a $^{2}H,^{15}N$-labeled MPV17 sample in DPC micelles at 1 to 5 mM concentration. For measuring solvent PREs, soluble Gd^{3+}-DOTA was stepwise added to the MPV17 sample in DPC micelles at a final concentration of 2 to 8 mM. At each sample, a 2D-[$^{15}N,^{1}H$]-TROSY experiment was recording with a recycle delay of 2 s.

For the assignment of the methyl groups, the 290 µM ILVAFYM-labeled sample was measured at 950 MHz and 310 K. Beside a 2D-[^{1}H, ^{15}N]-TROSY and a 2D-[^{1}H, ^{13}C]-HMQC several 3D-NOESY experiments were recorded: a TROSY-based HNH-NOESY, a HSQC-based HCH- and CNH-NOESY and a HMQC-based CCH-NOESY experiment was performed. A mixing time of 250 ms was applied.

6 References

1. Kühlbrandt W. Structure and function of mitochondrial membrane protein complexes. *BMC Biol*. 2015;13(1):1-11. doi:10.1186/s12915-015-0201-x

2. Kummer E, Ban N. Mechanisms and regulation of protein synthesis in mitochondria. *Nat Rev Mol Cell Biol*. 2021;22(5):307-325. doi:10.1038/s41580-021-00332-2

3. Althoff T, Mills DJ, Popot JL, Kühlbrandt W. Arrangement of electron transport chain components in bovine mitochondrial supercomplex I 1 III 2 IV 1. *EMBO J*. 2011;30(22):4652-4664. doi:10.1038/emboj.2011.324

4. Murphy MP, Brand MD. Membrane- potential- dependent changes in the stoichiometry of charge translocation by the mitochondrial electron transport chain. *Eur J Biochem*. 1988;173(3):637-644. doi:10.1111/j.1432-1033.1988.tb14046.x

5. Anderson AC. The Process of Structure-Based Drug Design. *Chem Biol*. 2003;10(9):787-797. doi:10.1016/J.CHEMBIOL.2003.09.002

6. Almén MS, Nordström KJV, Fredriksson R, Schiöth HB. Mapping the human membrane proteome: A majority of the human membrane proteins can be classified according to function and evolutionary origin. *BMC Biol*. 2009;7(1):50. doi:10.1186/1741-7007-7-50

7. Ravula T, Hardin NZ, Ramamoorthy A. Polymer nanodiscs: Advantages and limitations. *Chem Phys Lipids*. 2019;219:45-49. doi:10.1016/j.chemphyslip.2019.01.010

8. Alberts B, Johnson A, Lewis J, Raff M, Roberts K, Peter Walter. Molecular Biology of the Cell. In: *Molecular Biology of the Cell*. 4th ed. New York: Garland Science; 2002:1-12.

9. Watson H. Biological membranes. *Essays Biochem*. 2015;59:43-70. doi:10.1042/BSE0590043

10. Harvey Lodish, Arnold Berk, S Lawrence Zipursky, Paul Matsudaira, David Baltimore and JD. *Molecular Cell Biology*. 4th ed. New York: Freeman, W. H.; 2000.

11. Singer SJ, Nicolson GL. The Fluid Mosaic Model of the Structure of Cell Membranes. *Science (80-).* 1972;175(4023):720-731. doi:10.1126/SCIENCE.175.4023.720

12. Waechter CJ. Flippases. *Encycl Biol Chem*. January 2004:123-127. doi:10.1016/B0-12-443710-9/00231-3

13. Mesmin B. Mitochondrial lipid transport and biosynthesis: A complex balance. *J Cell Biol*. 2016;214(1):9-11. doi:10.1083/JCB.201606069

14. Horvath SE, Daum G. Lipids of mitochondria. *Prog Lipid Res*. 2013;52(4):590-614.

doi:10.1016/j.plipres.2013.07.002

15. Akopian D, Shen K, Zhang X, Shan S. Signal Recognition Particle: An essential protein targeting machine. *Annu Rev Biochem*. 2013;82:693. doi:10.1146/ANNUREV-BIOCHEM-072711-164732

16. Shan S, Schmid SL, Zhang X. Signal recognition particle (SRP) and SRP receptor: A new paradigm for multi-state regulatory GTPases. *Biochemistry*. 2009;48(29):6696. doi:10.1021/BI9006989

17. Ferguson MA. The structure, biosynthesis and functions of glycosylphosphatidylinositol anchors, and the contributions of trypanosome research. *J Cell Sci*. 1999;112(Pt 17):2799-2809.

18. Chou KC, Elrod DW. Prediction of membrane protein types and subcellular locations. *Proteins Struct Funct Genet*. 1999;34(1):137-153. doi:10.1002/(SICI)1097-0134(19990101)34:1<137::AID-PROT11>3.0.CO;2-O

19. Guha R. On exploring structure-activity relationships. *Methods Mol Biol*. 2013;993:81-94. doi:10.1007/978-1-62703-342-8_6

20. Sakakibara D, Sasaki A, Ikeya T, et al. Protein structure determination in living cells by in-cell NMR spectroscopy. *Nat 2009 4587234*. 2009;458(7234):102-105. doi:10.1038/nature07814

21. Bartesaghi A, Subramaniam S. Membrane protein structure determination using cryo-electron tomography and 3D image averaging. *Curr Opin Struct Biol*. 2009;19(4):402-407. doi:10.1016/J.SBI.2009.06.005

22. Lee SC, Knowles TJ, Postis VLG, et al. A method for detergent-free isolation of membrane proteins in their local lipid environment. *Nat Protoc 2016 117*. 2016;11(7):1149-1162. doi:10.1038/nprot.2016.070

23. AJ L, TH B, AN B, BA S, SG S. Functional reconstitution of Beta2-adrenergic receptors utilizing self-assembling Nanodisc technology. *Biotechniques*. 2006;40(5):601-612. doi:10.2144/000112169

24. Grisshammer R. Understanding recombinant expression of membrane proteins. *Curr Opin Biotechnol*. 2006;17(4):337-340. doi:10.1016/j.copbio.2006.06.001

25. Palmer I, Wingfield PT. Preparation and extraction of insoluble (Inclusion-body) proteins from Escherichia coli. *Curr Protoc Protein Sci*. 2012;1(SUPPL.70):1-20. doi:10.1002/0471140864.ps0603s70

26. Aroca JD, Sánchez-Piñera P, Corbalán-García S, Conesa-Zamora P, De Godos A, Gómez-

Fernández JC. Correlation between the effect of the anti-neoplastic ether lipid 1-O-octadecyl-2-O-methyl-glycero-3-phosphocholine on the membrane and the activity of protein kinase Cα. *Eur J Biochem*. 2001;268(24):6369-6378. doi:10.1046/j.0014-2956.2001.02554.x

27. Maire M le, Champeil P, Moeller J V. Interaction of membrane proteins and lipids with solubilizing detergents. *Biochim Biophys Acta*. 2000;1508(2):86-111. doi:10.1016/S0304-4157(00)00010-1

28. Neugebauer JM. Detergents: An overview. *Methods Enzymol*. 1990;182(C):239-253. doi:10.1016/0076-6879(90)82020-3

29. Linke D. *Detergents : An Overview*. Vol 463. 1st ed. Elsevier Inc.; 2009. doi:10.1016/S0076-6879(09)63034-2

30. Opella SJ. Structure Determination of Membrane Proteins in Their Native Phospholipid Bilayer Environment by Rotationally Aligned Solid-State NMR Spectroscopy. *Acc Chem Res*. 2013;46(9):2145. doi:10.1021/AR400067Z

31. Moraes I, Evans G, Sanchez-Weatherby J, Newstead S, Stewart PDS. Membrane protein structure determination - The next generation. *Biochim Biophys Acta - Biomembr*. 2014;1838(1 PARTA):78-87. doi:10.1016/j.bbamem.2013.07.010

32. Y C. Membrane protein structural biology in the era of single particle cryo-EM. *Curr Opin Struct Biol*. 2018;52:58-63. doi:10.1016/J.SBI.2018.08.008

33. Bowie JU. Stabilizing membrane proteins. *Curr Opin Struct Biol*. 2001;11(4):397-402. doi:10.1016/S0959-440X(00)00223-2

34. Seddon AM, Curnow P, Booth PJ. Membrane proteins, lipids and detergents: not just a soap opera. *BBA*. 2004;1666:105-117.

35. Klöpfer K, Hagn F. Beyond detergent micelles: The advantages and applications of non-micellar and lipid-based membrane mimetics for solution-state NMR. *Prog Nucl Magn Reson Spectrosc*. 2019;114-115:271-283. doi:10.1016/j.pnmrs.2019.08.001

36. Malia TJ, Wagner G. NMR structural investigation of the mitochondrial outer membrane protein VDAC and its interaction with antiapoptotic Bcl-XL. *Biochemistry*. 2007;46(2):514-525. doi:10.1021/bi061577h

37. Losonczi JA, Olejniczak ET, Betz SF, Harlan JE, Mack J, Fesik SW. NMR studies of the anti-apoptotic protein Bcl-x(L) in micelles. *Biochemistry*. 2000;39(36):11024-11033. doi:10.1021/bi000919v

38. Glover KJ, Whiles JA, Wu G, et al. *Structural Evaluation of Phospholipid Bicelles for Solution-State Studies of Membrane-Associated Biomolecules*.; 2001.

39. Wu H, Su K, Guan X, Sublette ME, Stark RE. Assessing the Size, Stability, and Utility of Isotropically Tumbling Bicelle Systems for Structural Biology. *Biochim Biophys Acta*. 2010;1798(3):482. doi:10.1016/J.BBAMEM.2009.11.004

40. Zoonens M, Zito F, Martinez KL, Popot J-L. Chapter 7 Amphipols: A General Introduction and Some Protocols. In: Mus-Veteau I, ed. *Membrane Proteins Production for Structural Analysis*. New York: Springer Science + Business Media; 2014:173-203. doi:10.1007/978-1-4939-0662-8

41. Tribet C, Audebert R, Popot JL. Amphipols: Polymers that keep membrane proteins soluble in aqueous solutions. *Proc Natl Acad Sci U S A*. 1996;93(26):15047-15050. doi:10.1073/pnas.93.26.15047

42. Tassadite Dahmane, Giusti F, Catoire LJ, Popot J-L. Sulfonated amphipols: Synthesis, properties, and applications. *Biopolymers*. 2011;95(12):811-823. doi:10.1002/BIP.21683

43. Chetty PS, Mayne L, Kan ZY, Lund-Katz S, Englander SW, Phillips MC. Apolipoprotein A-I helical structure and stability in discoidal high-density lipoprotein (HDL) particles by hydrogen exchange and mass spectrometry. *Proc Natl Acad Sci U S A*. 2012;109(29):11687-11692. doi:10.1073/pnas.1209305109

44. Denisov IG, Grinkova Y V., Lazarides AA, Sligar SG. Directed Self-Assembly of Monodisperse Phospholipid Bilayer Nanodiscs with Controlled Size. *J Am Chem Soc*. 2004;126(11):3477-3487. doi:10.1021/ja0393574

45. Hagn F, Etzkorn M, Raschle T, Wagner G. Optimized phospholipid bilayer nanodiscs facilitate high-resolution structure determination of membrane proteins. *J Am Chem Soc*. 2013;135(5):1919-1925. doi:10.1021/ja310901f

46. Miehling J, Goricanec D, Hagn F. A Split-Intein-Based Method for the Efficient Production of Circularized Nanodiscs for Structural Studies of Membrane Proteins. *ChemBioChem*. 2018;19(18):1927-1933. doi:10.1002/cbic.201800345

47. Nasr ML, Baptista D, Strauss M, et al. Covalently circularized nanodiscs for studying membrane proteins and viral entry. *Nat Methods*. 2016;14(1):49-52. doi:10.1038/nmeth.4079

48. Martinez D, Decossas M, Kowal J, et al. Lipid Internal Dynamics Probed in Nanodiscs. *ChemPhysChem*. 2017;18(19):2651-2657. doi:10.1002/CPHC.201700450

49. Midtgaard SR, Pedersen MC, Kirkensgaard JJK, et al. Self-assembling peptides form nanodiscs

that stabilize membrane proteins. *Soft Matter*. 2014;10(5):738-752. doi:10.1039/C3SM51727F

50. Ravula T, Hardin NZ, Ramadugu SK, Ramamoorthy A. pH Tunable and Divalent Metal Ion Tolerant Polymer Lipid Nanodiscs. *Langmuir*. 2017;33(40):10655-10662. doi:10.1021/ACS.LANGMUIR.7B02887

51. Ravula T, Hardin NZ, Ramadugu SK, Cox SJ, Ramamoorthy A. pH resistant monodispersed polymer-lipid nanodiscs. *Angew Chem Int Ed Engl*. 2018;57(5):1342. doi:10.1002/ANIE.201712017

52. Bruhn H. A short guided tour through functional and structural features of saposin-like proteins. *Biochem J*. 2005;389(Pt 2):249. doi:10.1042/BJ20050051

53. B O, B G-Á, J P-G. Structure-function correlations of pulmonary surfactant protein SP-B and the saposin-like family of proteins. *Eur Biophys J*. 2013;42(2-3):209-222. doi:10.1007/S00249-012-0858-9

54. Frauenfeld J, Löving R, Armache JP, et al. A saposin-lipoprotein nanoparticle system for membrane proteins. *Nat Methods*. 2016;13(4):345-351. doi:10.1038/nmeth.3801

55. Lloris-Garcerá P, Klinter S, Chen L, Skynner MJ, Löving R, Frauenfeld J. DirectMX – One-Step Reconstitution of Membrane Proteins From Crude Cell Membranes Into Salipro Nanoparticles. *Front Bioeng Biotechnol*. 2020;0:215. doi:10.3389/FBIOE.2020.00215

56. LA M, JP S, H Y. Constant pressure-controlled extrusion method for the preparation of Nano-sized lipid vesicles. *J Vis Exp*. 2012;(64). doi:10.3791/4151

57. ZL J, SY L. Liposome reconstitution and transport assay for recombinant transporters. *Methods Enzymol*. 2015;556:373-383. doi:10.1016/BS.MIE.2014.11.048

58. Kale J, Chi X, Leber B, Andrews D. Examining the molecular mechanism of bcl-2 family proteins at membranes by fluorescence spectroscopy. In: *Methods in Enzymology*. Vol 544. Academic Press Inc.; 2014:1-23. doi:10.1016/B978-0-12-417158-9.00001-7

59. CA M. Structure and dynamics of the mitochondrial inner membrane cristae. *Biochim Biophys Acta*. 2006;1763(5-6):542-548. doi:10.1016/J.BBAMCR.2006.04.006

60. Wiedemann N, Pfanner N. Mitochondrial Machineries for Protein Import and Assembly. *Annu Rev Biochem*. 2017;86(1):685-714. doi:10.1146/annurev-biochem-060815-014352

61. Friedman JR, Nunnari J. Mitochondrial form and function. *Nature*. 2014;505(7483):335-343. doi:10.1038/nature12985

62. Grevel A, Becker T. Porins as helpers in mitochondrial protein translocation. *Biol Chem*.

2020;401(6-7):699-708. doi:10.1515/hsz-2019-0438

63. Hu J, Dong L, Outten CE. The redox environment in the mitochondrial intermembrane space is maintained separately from the cytosol and matrix. *J Biol Chem*. 2008;283(43):29126-29134. doi:10.1074/jbc.M803028200

64. Peleh V, Riemer J, Dancis A, Herrmann JM. Protein oxidation in the intermembrane space of mitochondria is substrate-specific rather than general. *Microb Cell*. 2014;1(3):81-93. doi:10.15698/mic2014.01.130

65. Böttinger L, Gornicka A, Czerwik T, et al. In vivo evidence for cooperation of Mia40 and Erv1 in the oxidation of mitochondrial proteins. *https://doi.org/101091/mbc.e12-05-0358*. 2012;23(20):3957-3969. doi:10.1091/MBC.E12-05-0358

66. Anderson S, Bankier AT, Barrell BG, et al. Sequence and organization of the human mitochondrial genome. *Nature*. 1981;290(5806):457-465. doi:10.1038/290457a0

67. Herrmann JM, Neupert W. Protein insertion into the inner membrane of mitochondria. *IUBMB Life*. 2003;55(4-5):219-225. doi:10.1080/1521654031000123349

68. Chacinska A, Koehler CM, Milenkovic D, Lithgow T, Pfanner N. Importing Mitochondrial Proteins: Machineries and Mechanisms. *Cell*. 2009;138(4):628-644. doi:10.1016/j.cell.2009.08.005

69. MAHLKE K, PFANNER N, MARTIN J, HORWICH AL, HARTL F - U, NEUPERT W. Sorting pathways of mitochondrial inner membrane proteins. *Eur J Biochem*. 1990;192(2):551-555. doi:10.1111/j.1432-1033.1990.tb19260.x

70. Youle RJ, Van Der Bliek AM. Mitochondrial Fission, Fusion, and Stress. *Science (80-)*. 2012;337(6098):1062-1065. doi:10.1126/science.1219855.Mitochondrial

71. Yoneda M, Miyatake T, Attardi G. Complementation of mutant and wild-type human mitochondrial DNAs coexisting since the mutation event and lack of complementation of DNAs introduced separately into a cell within distinct organelles. *Mol Cell Biol*. 1994;14(4):2699. doi:10.1128/MCB.14.4.2699

72. A C, J N, PM V. Enzymic characterization and lipid composition of rat liver subcellular membranes. *Biochim Biophys Acta*. 1971;249(2):462-492. doi:10.1016/0005-2736(71)90123-4

73. Falabella M, Vernon HJ, Hanna MG, Claypool SM, Pitceathly RDS. Cardiolipin, Mitochondria, and Neurological Disease. *Trends Endocrinol Metab*. 2021;32(4):224-237. doi:10.1016/J.TEM.2021.01.006

74. Schlame M, Greenberg ML. Biosynthesis, remodeling and turnover of mitochondrial cardiolipin. *Biochim Biophys Acta - Mol Cell Biol Lipids*. 2017;1862(1):3-7. doi:10.1016/j.bbalip.2016.08.010

75. Chu CT, Ji J, Dagda RK, et al. Cardiolipin externalization to the outer mitochondrial membrane acts as an elimination signal for mitophagy in neuronal cells. *Nat Cell Biol*. 2013;15(10):1197. doi:10.1038/NCB2837

76. Lutter M, Fang M, Luo X, Nishijima M, Xie XS, Wang X. Cardiolipin provides specificity for targeting of tBid to mitochondria. *Nat Cell Biol*. 2000;2(10):754-756. doi:10.1038/35036395

77. Adams JM, Cory S. Bcl-2-regulated apoptosis: mechanism and therapeutic potential. *Curr Opin Immunol*. 2007;19(5):488-496. doi:10.1016/j.coi.2007.05.004

78. Dewson G, Kluck RM. Mechanisms by which Bak and Bax permeabilise mitochondria during apoptosis. *J Cell Sci*. 2009;122(16):2801-2808. doi:10.1242/jcs.038166

79. Elmore S. Apoptosis: A Review of Programmed Cell Death. *Toxicol Pathol*. 2007;35(4):495. doi:10.1080/01926230701320337

80. Crimi M, Esposti MD. Apoptosis-induced changes in mitochondrial lipids. *Biochim Biophys Acta - Mol Cell Res*. 2011;1813(4):551-557. doi:10.1016/j.bbamcr.2010.09.014

81. Uren RT, Iyer S, Kluck RM. Pore formation by dimeric Bak and Bax: An unusual pore? *Philos Trans R Soc B Biol Sci*. 2017;372(1726):20160218. doi:10.1098/rstb.2016.0218

82. Czabotar PE, Lessene G, Strasser A, Adams JM. Control of apoptosis by the BCL-2 protein family: implications for physiology and therapy. *Nat Rev Mol Cell Biol 2014 151*. 2013;15(1):49-63. doi:10.1038/NRM3722

83. Delbridge ARD, Grabow S, Strasser A, Vaux DL. Thirty years of BCL-2: translating cell death discoveries into novel cancer therapies. *Nat Rev Cancer 2016 162*. 2016;16(2):99-109. doi:10.1038/NRC.2015.17

84. Mihalyova J, Jelinek T, Growkova K, Hrdinka M, Simicek M, Hajek R. Venetoclax: A new wave in hematooncology. *Exp Hematol*. 2018;61:10-25. doi:10.1016/J.EXPHEM.2018.02.002

85. Willis SN, Fletcher JI, Kaufmann T, et al. Apoptosis initiated when BH3 ligands engage multiple Bcl-2 homologs, not Bax or Bak. *Science (80-).* 2007;315(5813):856-859. doi:10.1126/science.1133289

86. Chipuk JE, Moldoveanu T, Llambi F, Parsons MJ, Green DR. The BCL-2 Family Reunion. *Mol Cell*. 2010;37(3):299. doi:10.1016/J.MOLCEL.2010.01.025

87. Chipuk JE, Green DR. How do BCL-2 proteins induce mitochondrial outer membrane permeabilization? *Trends Cell Biol*. 2008;18(4):157-164. doi:10.1016/j.tcb.2008.01.007

88. Westphal D, Kluck RM, Dewson G. Building blocks of the apoptotic pore: How Bax and Bak are activated and oligomerize during apoptosis. *Cell Death Differ*. 2014;21(2):196-205. doi:10.1038/cdd.2013.139

89. Kluck RM, Bossy-Wetzel E, Green DR, Newmeyer DD. The Release of Cytochrome c from Mitochondria: A Primary Site for Bcl-2 Regulation of Apoptosis. *Science (80-)*. 1997;275(5303):1132-1136. doi:10.1126/SCIENCE.275.5303.1132

90. Elkholi R, Floros K V., Chipuk JE. The Role of BH3-Only Proteins in Tumor Cell Development, Signaling, and Treatment: *Genes and Cancer*. 2011;2(5):523-537. doi:10.1177/1947601911417177

91. Westphal D, Dewson G, Czabotar PE, Kluck RM. Molecular biology of Bax and Bak activation and action. *Biochim Biophys Acta - Mol Cell Res*. 2011;1813(4):521-531. doi:10.1016/j.bbamcr.2010.12.019

92. Kvansakul M, Hinds MG. The Bcl-2 family: Structures, interactions and targets for drug discovery. *Apoptosis*. 2015;20(2):136-150. doi:10.1007/s10495-014-1051-7

93. Sattler M, Liang H, Nettesheim D, et al. Structure of Bcl-x(L)-Bak peptide complex: Recognition between regulators of apoptosis. *Science (80-)*. 1997;275(5302):983-986. doi:10.1126/science.275.5302.983

94. Czabotar PE, Lee EF, Delft MF van, et al. Structural insights into the degradation of Mcl-1 induced by BH3 domains. *Proc Natl Acad Sci*. 2007;104(15):6217-6222. doi:10.1073/PNAS.0701297104

95. Liu X, Dai S, Zhu Y, Marrack P, Kappler JW. The structure of a Bcl-xL/Bim fragment complex: Implications for Bim function. *Immunity*. 2003;19(3):341-352. doi:10.1016/S1074-7613(03)00234-6

96. Hinds MG, Smits C, Fredericks-Short R, et al. Bim, Bad and Bmf: intrinsically unstructured BH3-only proteins that undergo a localized conformational change upon binding to prosurvival Bcl-2 targets. *Cell Death Differ*. 2006;14(1):128-136. doi:10.1038/sj.cdd.4401934

97. Chou JJ, Li H, Salvesen GS, Yuan J, Wagner G. Solution structure of BID, an intracellular amplifier of apoptotic signaling. *Cell*. 1999;96(5):615-624. doi:10.1016/S0092-8674(00)80572-3

98. Kelekar A, Thompson CB. Bcl-2-family proteins: the role of the BH3 domain in apoptosis.

Trends Cell Biol. 1998;8:324-330. doi:10.1517/13543784.2012.717930

99. Popgeorgiev N, Jabbour L, Gillet G. Subcellular Localization and Dynamics of the Bcl-2 Family of Proteins. *Front Cell Dev Biol*. 2018;6(FEB). doi:10.3389/FCELL.2018.00013

100. Brouwer JM, Lan P, Cowan AD, et al. Conversion of Bim-BH3 from Activator to Inhibitor of Bak through Structure-Based Design. *Mol Cell*. 2017;68(4):659-672. doi:10.1016/j.molcel.2017.11.001

101. Letai A, Bassik MC, Walensky LD, Sorcinelli MD, Weiler S, Korsmeyer SJ. Distinct BH3 domains either sensitize or activate mitochondrial apoptosis, serving as prototype cancer therapeutics. *Cancer Cell*. 2002;2(3):183-192. doi:10.1016/S1535-6108(02)00127-7

102. Hockings C, Anwari K, Ninnis RL, et al. Bid chimeras indicate that most BH3-only proteins can directly activate Bak and Bax, and show no preference for Bak versus Bax. *Cell Death Dis*. 2015;6(4):1-9. doi:10.1038/cddis.2015.105

103. Moldoveanu T, Grace CR, Llambi F, et al. BID-induced structural changes in BAK promote apoptosis. *Nat Struct Mol Biol*. 2013;20(5):589-597. doi:10.1038/nsmb.2563

104. Kim H, Tu HC, Ren D, et al. Stepwise Activation of BAX and BAK by tBID, BIM, and PUMA Initiates Mitochondrial Apoptosis. *Mol Cell*. 2009;36(3):487-499. doi:10.1016/j.molcel.2009.09.030

105. Fletcher JI, Meusburger S, Hawkins CJ, et al. Apoptosis is triggered when prosurvival Bcl-2 proteins cannot restrain Bax. *Proc Natl Acad Sci*. 2008;105(47):18081-18087. doi:10.1073/PNAS.0808691105

106. Llambi F, Moldoveanu T, Tait SWG, et al. A Unified Model of Mammalian BCL-2 Protein Family Interactions at the Mitochondria. *Mol Cell*. 2011;44(4):517-531. doi:10.1016/j.molcel.2011.10.001

107. O'neill KL, Huang K, Zhang J, Chen Y, Luo X. Inactivation of prosurvival Bcl-2 proteins activates Bax/Bak through the outer mitochondrial membrane. *Genes Dev*. 2016;30(8):973-988. doi:10.1101/gad.276725.115

108. Bleicken S, Hantusch A, Das KK, Frickey T, Garcia-Saez AJ. Quantitative interactome of a membrane Bcl-2 network identifies a hierarchy of complexes for apoptosis regulation. *Nat Commun*. 2017;8(1):1-15. doi:10.1038/s41467-017-00086-6

109. Jonas EA, Hickman JA, Chachar M, et al. Proapoptotic N-truncated BCL-xL protein activates endogenous mitochondrial channels in living synaptic terminals. *Proc Natl Acad Sci U S A*. 2004;101(37):13590-13595. doi:10.1073/pnas.0401372101

110. Todt F, Cakir Z, Reichenbach F, et al. Differential retrotranslocation of mitochondrial Bax and Bak. *EMBO J*. 2015;34(1):67-80. doi:10.15252/embj.201488806

111. Ferrer PE, Frederick P, Gulbis JM, Dewson G, Kluck RM. Translocation of a bak C-Terminus mutant from cytosol to mitochondria to mediate cytochrome c release: Implications for bak and bax apoptotic function. *PLoS One*. 2012;7(3). doi:10.1371/journal.pone.0031510

112. Leshchiner ES, Braun CR, Bird GH, Walensky LD. Direct activation of full-length proapoptotic BAK. *Proc Natl Acad Sci U S A*. 2013;110(11):E986. doi:10.1073/pnas.1214313110

113. Edlich F, Banerjee S, Suzuki M, et al. Bcl-xL retrotranslocates Bax from the mitochondria into the cytosol. *Cell*. 2011;145(1):104. doi:10.1016/J.CELL.2011.02.034

114. Moldoveanu T, Liu Q, Tocilj A, Watson M, Shore G, Gehring K. The X-Ray Structure of a BAK Homodimer Reveals an Inhibitory Zinc Binding Site. *Mol Cell*. 2006;24(5):677-688. doi:10.1016/j.molcel.2006.10.014

115. Wang H, Takemoto C, Akasaka R, et al. Novel dimerization mode of the human Bcl-2 family protein Bak, a mitochondrial apoptosis regulator. *J Struct Biol*. 2009;166(1):32-37. doi:10.1016/j.jsb.2008.12.003

116. Gräslund S, Sagemark J, Berglund H, et al. The use of systematic N- and C-terminal deletions to promote production and structural studies of recombinant proteins. *Protein Expr Purif*. 2008;58(2):210-221. doi:10.1016/j.pep.2007.11.008

117. Suzuki M, Youle RJ, Tjandra N. Structure of bax: Coregulation of dimer formation and intracellular localization. *Cell*. 2000;103(4):645-654. doi:10.1016/S0092-8674(00)00167-7

118. Muchmore SW, Sattler M, Liang H, et al. X-ray and NMR structure of human Bcl-xL, an inhibitor of programmed cell death. *Nature*. 1996;381(6580):335-341. doi:10.1038/381335a0

119. Czabotar PE, Westphal D, Dewson G, et al. Bax crystal structures reveal how BH3 domains activate Bax and nucleate its oligomerization to induce apoptosis. *Cell*. 2013;152(3):519-531. doi:10.1016/j.cell.2012.12.031

120. Dai H, Smith A, Meng XW, Schneider PA, Pang YP, Kaufmann SH. Transient binding of an activator BH3 domain to the Bak BH3-binding groove initiates Bak oligomerization. *J Cell Biol*. 2011;194(1):39-48. doi:10.1083/jcb.201102027

121. Wei MC, Lindsten T, Mootha VK, et al. tBid, a membrane targeted death ligand , oligomerizes BAK to release cytochrome c. *Genes Dev*. 2000;14(16):2060-2071. doi:10.1101/GAD.14.16.2060

122. Kale J, Osterlund EJ, Andrews DW. BCL-2 family proteins: Changing partners in the dance towards death. *Cell Death Differ*. 2018;25(1):65-80. doi:10.1038/cdd.2017.186

123. Gavathiotis E, Suzuki M, Davis ML, et al. BAX Activation is Initiated at a Novel Interaction Site. *Nature*. 2008;455(7216):1076. doi:10.1038/NATURE07396

124. Peng R, Tong J-S, Li H, et al. Targeting Bax interaction sites reveals that only homo-oligomerization sites are essential for its activation. *Cell Death Differ 2013 205*. 2013;20(5):744-754. doi:10.1038/cdd.2013.4

125. Garner TP, Reyna DE, Priyadarshi A, et al. An Autoinhibited Dimeric Form of BAX Regulates the BAX Activation Pathway. *Mol Cell*. 2016;63(3):485-497. doi:10.1016/j.molcel.2016.06.010

126. Dengler MA, Robin AY, Gibson L, Westphal D, Dewson G, Correspondence JMA. BAX Activation: Mutations Near Its Proposed Non-canonical BH3 Binding Site Reveal Allosteric Changes Controlling Mitochondrial Association. *CellReports*. 2019;27:359-373.e6. doi:10.1016/j.celrep.2019.03.040

127. Brouwer JM, Westphal D, Dewson G, et al. Bak Core and Latch Domains Separate during Activation, and Freed Core Domains Form Symmetric Homodimers. *Mol Cell*. 2014;55(6):938-946. doi:10.1016/j.molcel.2014.07.016

128. Griffiths GJ, Dubrez L, Morgan CP, et al. Cell damage-induced conformational changes of the pro-apoptotic protein Bak in vivo precede the onset of apoptosis. *J Cell Biol*. 1999;144(5):903-914. doi:10.1083/jcb.144.5.903

129. Dewson G, Kratina T, Czabotar P, Day CL, Adams JM, Kluck RM. Bak Activation for Apoptosis Involves Oligomerization of Dimers via Their α6 Helices. *Mol Cell*. 2009;36(4):696-703. doi:10.1016/j.molcel.2009.11.008

130. Alsop AE, Fennell SC, Bartolo RC, Tan IKL, Dewson G, Kluck RM. Dissociation of Bak α 1 helix from the core and latch domains is required for apoptosis. *Nat Commun*. 2015;6:1-13. doi:10.1038/ncomms7841

131. Dewson G, Kratina T, Sim HW, et al. To Trigger Apoptosis, Bak Exposes Its BH3 Domain and Homodimerizes via BH3:Groove Interactions. *Mol Cell*. 2008;30(3):369-380. doi:10.1016/j.molcel.2008.04.005

132. Bleicken S, Classen M, Padmavathi PVL, et al. Molecular details of Bax activation, oligomerization, and membrane insertion. *J Biol Chem*. 2010;285(9):6636-6647. doi:10.1074/jbc.M109.081539

133. G D, S M, P F, et al. Bax dimerizes via a symmetric BH3:groove interface during apoptosis. *Cell*

Death Differ. 2012;19(4):661-670. doi:10.1038/CDD.2011.138

134. Zhang J, Huang K, O'neill KL, Pang X, Luo X. Bax/bak activation in the absence of Bid, Bim, Puma, and p53. *Cell Death Dis*. 2016;7(6):e2266-e2266. doi:10.1038/cddis.2016.167

135. Uren RT, O'Hely M, Iyer S, et al. Disordered clusters of Bak dimers rupture mitochondria during apoptosis. *Elife*. 2017;6:1-23. doi:10.7554/elife.19944

136. Iyer S, Bell F, Westphal D, et al. Bak apoptotic pores involve a flexible C-terminal region and juxtaposition of the C-terminal transmembrane domains. *Cell Death Differ*. 2015;22(10):1665-1675. doi:10.1038/cdd.2015.15

137. Aluvila S, Mandal T, Hustedt E, Fajer P, Choe JY, Oh KJ. Organization of the mitochondrial apoptotic BAK pore: Oligomerization of the BAK homodimers. *J Biol Chem*. 2014;289(5):2537-2551. doi:10.1074/jbc.M113.526806

138. Ader NR, Hoffmann PC, Ganeva I, et al. Molecular and topological reorganizations in mitochondrial architecture interplay during bax-mediated steps of apoptosis. *Elife*. 2019;8. doi:10.7554/ELIFE.40712

139. Salvador- Gallego R, Mund M, Cosentino K, et al. Bax assembly into rings and arcs in apoptotic mitochondria is linked to membrane pores. *EMBO J*. 2016;35(4):389-401. doi:10.15252/embj.201593384

140. McArthur K, Whitehead LW, Heddleston JM, et al. BAK/BAX macropores facilitate mitochondrial herniation and mtDNA efflux during apoptosis. *Science (80-)*. 2018;359(6378). doi:10.1126/science.aao6047

141. Mandal T, Shin S, Aluvila S, et al. Assembly of Bak homodimers into higher order homooligomers in the mitochondrial apoptotic pore. *Sci Rep*. 2016;6(1):1-14. doi:10.1038/srep30763

142. López CA, Swift MF, Xu XP, Hanein D, Volkmann N, Gnanakaran S. Biophysical Characterization of a Nanodisc with and without BAX: An Integrative Study Using Molecular Dynamics Simulations and Cryo-EM. *Structure*. 2019;27(6):988-999.e4. doi:10.1016/j.str.2019.03.013

143. Basanez G, Nechushtan A, Drozhinin O, et al. Bax, but not Bcl-x L , decreases the lifetime of planar phospholipid bilayer membranes at subnanomolar concentrations. *Proc Natl Acad Sci*. 1999;96:5492-5497. www.pnas.org. Accessed January 12, 2021.

144. Flores- Romero H, Ros U, Garcia- Saez AJ. Pore formation in regulated cell death. *EMBO J*. 2020;39(23). doi:10.15252/embj.2020105753

145. Cowan AD, Smith NA, Sandow JJ, et al. BAK core dimers bind lipids and can be bridged by them. *Nat Struct Mol Biol*. 2020;27:1024-1031. doi:10.1038/s41594-020-0494-5

146. Westphal D, Dewson G, Menard M, et al. Apoptotic pore formation is associated with in-plane insertion of Bak or Bax central helices into the mitochondrial outer membrane. *Proc Natl Acad Sci U S A*. 2014;111(39):E4076-E4085. doi:10.1073/pnas.1415142111

147. Bleicken S, Jeschke G, Stegmueller C, Salvador-Gallego R, García-Sáez AJ, Bordignon E. Structural Model of Active Bax at the Membrane. *Mol Cell*. 2014;56(4):496-505. doi:10.1016/j.molcel.2014.09.022

148. Bleicken S, Assafa TE, Stegmueller C, Wittig A, Garcia-Saez AJ, Bordignon E. Topology of active, membrane-embedded Bax in the context of a toroidal pore. *Cell Death Differ*. 2018;25(10):1717-1731. doi:10.1038/s41418-018-0184-6

149. Weiher H, Noda T, Gray DA, Sharpe AH, Jaenisch R. Transgenic mouse model of kidney disease: Insertional inactivation of ubiquitously expressed gene leads to nephrotic syndrome. *Cell*. 1990;62(3):425-434. doi:10.1016/0092-8674(90)90008-3

150. Zwacka RM, Reuter A, Pfaff E, et al. The glomerulosclerosis gene Mpv17 encodes a peroxisomal protein producing reactive oxygen species. *EMBO J*. 1994;13(21):5129-5134. doi:10.1002/j.1460-2075.1994.tb06842.x

151. Karasawa M, Zwacka RM, Reuter A, et al. The human homolog of the glomerulosclerosis gene Mpv17: structure and genomic organization. *Hum Mol Genet*. 1993;2(11):1829-1834. doi:10.1093/hmg/2.11.1829

152. Spinazzola A, Viscomi C, Fernandez-Vizarra E, et al. MPV17 encodes an inner mitochondrial membrane protein and is mutated in infantile hepatic mitochondrial DNA depletion. *Nat Genet*. 2006;38(5):570-576. doi:10.1038/ng1765

153. Spinazzola A, Santer R, Akman OH, et al. Hepatocerebral Form of Mitochondrial DNA Depletion Syndrome. *Arch Neurol*. 2008;65(8):1108-1113. doi:10.1001/archneur.65.8.1108

154. Bottani E, Giordano C, Civiletto G, et al. AAV-mediated liver-specific MPV17 expression restores mtdna levels and prevents diet-induced liver failure. *Mol Ther*. 2014;22(1):10-17. doi:10.1038/mt.2013.230

155. El-Hattab AW, Wang J, Dai H, et al. MPV17-related mitochondrial DNA maintenance defect: New cases and review of clinical, biochemical, and molecular aspects. *Hum Mutat*. 2018;39(4):461-470. doi:10.1002/humu.23387

156. Holve S, Hu D, Shub M, Tyson RW, Sokol RJ. Liver disease in Navajo neuropathy. *J Pediatr*.

1999;135(4):482-493. doi:10.1016/S0022-3476(99)70172-1

157. Karadimas CL, Vu TH, Holve SA, et al. Navajo neurohepatopathy is caused by a mutation in the MPV17 gene. *Am J Hum Genet*. 2006;79(3):544-548. doi:10.1086/506913

158. Löllgen S, Weiher H. The role of the Mpv17 protein mutations of which cause mitochondrial DNA depletion syndrome (MDDS): Lessons from homologs in different species. *Biol Chem*. 2015;396(1):13-25. doi:10.1515/hsz-2014-0198

159. Wong L-JC, Brunetti-Pierri N, Zhang Q, et al. Mutations in theMPV17 gene are responsible for rapidly progressive liver failure in infancy. *Hepatology*. 2007;46(4):1218-1227. doi:10.1002/hep.21799

160. Choi Y-R, Hong Y Bin, Jung S-C, et al. A novel homozygous MPV17 mutation in two families with axonal sensorimotor polyneuropathy. *BMC Neurol*. 2015;15(1):179. doi:10.1186/s12883-015-0430-1

161. Baumann M, Schreiber H, Schlotter- Weigel B, et al. MPV17mutations in juvenile- and adult-onset axonal sensorimotor polyneuropathy. *Clin Genet*. 2019;95(1):182-186. doi:10.1111/cge.13462

162. Blakely EL, Butterworth A, Hadden RDM, et al. MPV17 mutation causes neuropathy and leukoencephalopathy with multiple mtDNA deletions in muscle. *Neuromuscul Disord*. 2012;22(7):587-591. doi:10.1016/J.NMD.2012.03.006

163. Garone C, Rubio JC, Calvo SE, et al. MPV17 Mutations Causing Adult-Onset Multisystemic Disorder With Multiple Mitochondrial DNA Deletions. *Arch Neurol*. 2012;69(12):1648. doi:10.1001/ARCHNEUROL.2012.405

164. Copeland W. Defects in Mitochondrial DNA Replication and Human Disease. *Crit Rev Biochem Mol Biol*. 2012;47(1):64-74. doi:10.1161/CIRCULATIONAHA.110.956839

165. El-Hattab AW, Craigen WJ, Scaglia F. Mitochondrial DNA maintenance defects. *Biochim Biophys Acta - Mol Basis Dis*. 2017;1863(6):1539-1555. doi:10.1016/j.bbadis.2017.02.017

166. Alonzo JR, Venkataraman C, Field MS, Stover PJ. The mitochondrial inner membrane protein MPV17 prevents uracil accumulation in mitochondrial DNA. *J Biol Chem*. 2018;293(52):20285-20294. doi:10.1074/jbc.RA118.004788

167. Dalla Rosa I, Cámara Y, Durigon R, et al. MPV17 Loss Causes Deoxynucleotide Insufficiency and Slow DNA Replication in Mitochondria. *PLoS Genet*. 2016;12(1). doi:10.1371/journal.pgen.1005779

168. Antonenkov VD, Isomursu A, Mennerich D, et al. The human mitochondrial DNA depletion syndrome gene MPV17 encodes a non-selective channel that modulates membrane potential. *J Biol Chem*. 2015;290(22):13840-13861. doi:10.1074/jbc.M114.608083

169. Dallabona C, Marsano RM, Arzuffi P, et al. Sym1, the yeast ortholog of the MPV17 human disease protein, is a stress-induced bioenergetic and morphogenetic mitochondrial modulator. *Hum Mol Genet*. 2010;19(6):1098-1107. doi:10.1093/hmg/ddp581

170. Trott A, Morano KA. SYM1 is the stress-induced Saccharomyces cerevisiae ortholog of the mammalian kidney disease gene Mpv17 and is required for ethanol metabolism and tolerance during heat shock. *Eukaryot Cell*. 2004;3(3):620-631. doi:10.1128/EC.3.3.620-631.2004

171. Reinhold R, Kruger V, Meinecke M, et al. The Channel-Forming Sym1 Protein Is Transported by the TIM23 Complex in a Presequence-Independent Manner. *Mol Cell Biol*. 2012;32(24):5009-5021. doi:10.1128/mcb.00843-12

172. Krauss J, Astrinides P, Frohnhöfer HG, Walderich B, Nüsslein-Volhard C. Transparent, a gene affecting stripe formation in Zebrafish, encodes the mitochondrial protein Mpv17 that is required for iridophore survival. *Biol Open*. 2013;2(7):703-710. doi:10.1242/bio.20135132

173. Franke B, Opitz C, Isogai S, et al. Production of isotope-labeled proteins in insect cells for NMR. *J Biomol NMR*. 2018;71(3):173-184. doi:10.1007/s10858-018-0172-7

174. Ye K, Meng WX, Sun H, et al. Characterization of an alternative BAK-binding site for BH3 peptides. *Nat Commun*. 2020;11(1):1-14. doi:10.1038/s41467-020-17074-y

175. Martinez-Senac M del M, Senena C-G, Gomez-Fernandez JC. The Structure of the C-Terminal Domain of the Pro-Apoptotic Protein Bak. *Biophys J*. 2002;81(January):233-243.

176. Yang Shen, Frank Delaglio, Gabriel Cornilescu and AB. TALOS+: A hybrid method for predicting protein backbone torsion angles from NMR chemical shifts. *J Biomol NMR*. 2009;44(4):213-223. doi:10.1007/s10858-009-9333-z

177. Raltchev K, Pipercevic J, Hagn F. Production and Structural Analysis of Membrane-Anchored Proteins in Phospholipid Nanodiscs. *Chem - A Eur J*. 2018;24(21):5493-5499. doi:10.1002/chem.201800812

178. Häusler E, Fredriksson K, Goba I, et al. Quantifying the insertion of membrane proteins into lipid bilayer nanodiscs using a fusion protein strategy. *Biochim Biophys Acta - Biomembr*. 2020;1862(4):183190. doi:10.1016/j.bbamem.2020.183190

179. Hagn F, Nasr ML, Wagner G. Assembly of phospholipid nanodiscs of controlled size for structural studies of membrane proteins by NMR. *Nat Protoc*. 2018;13(1):79-98.

doi:10.1038/nprot.2017.094

180. Kallick DA, Tessmer MR, Watts CR, Li C-Y. The Use of Dodecylphosphocholie Micelles in Solution NMR. *J Magn Reson*. 1995;Series B(109):60-65. doi:doi.org/10.1006/jmrb.1995.1146

181. Chen I, Dorr BM, Liu DR. A general strategy for the evolution of bond-forming enzymes using yeast display. *Proc Natl Acad Sci U S A*. 2011;108(28):11399-11404. doi:10.1073/pnas.1101046108

182. Yethon JA, Epand RF, Leber B, Epand RM, Andrews DW. Interaction with a membrane surface triggers a reversible conformational change in Bax normally associated with induction of apoptosis. *J Biol Chem*. 2003;278(49):48935-48941. doi:10.1074/jbc.M306289200

183. Oh KJ, Singh P, Lee K, et al. Conformational changes in BAK, a pore-forming proapoptotic Bcl-2 family member, upon membrane insertion and direct evidence for the existence of BH3-BH3 contact interface in BAK homo-oligomers. *J Biol Chem*. 2010;285(37):28924-28937. doi:10.1074/jbc.M110.135293

184. Pogmore J, Pemberton J, Chi X, Andrews D. Using FRET to measure protein interactions between Bcl-2 family proteins on mitochondrial membranes. *Progr cell death methods Protoc Mol Biol*. 2016;1419:197-212. doi:10.1007/978-1-4939-3581-9

185. Dai H, Ding H, Meng XW, et al. Constitutive BAK activation as a determinant of drug sensitivity in malignant lymphohematopoietic cells. *Genes Dev*. 2015;29(20):2140-2152. doi:10.1101/gad.267997.115

186. Lai YC, Li CC, Sung TC, Chang CW, Lan YJ, Chiang YW. The role of cardiolipin in promoting the membrane pore-forming activity of BAX oligomers. *Biochim Biophys Acta - Biomembr*. 2019;1861(1):268-280. doi:10.1016/j.bbamem.2018.06.014

187. Schafer B, Quispe J, Choudhary V, et al. Mitochondrial outer membrane proteins assist Bid in Bax-mediated lipidic pore formation. *Mol Biol Cell*. 2009;20(8):2276-2285. doi:10.1091/mbc.e08-10-1056

188. Landeta O, Landajuela A, Gil D, et al. Reconstitution of proapoptotic BAK function in liposomes reveals a dual role for mitochondrial lipids in the BAK-driven membrane permeabilization process. *J Biol Chem*. 2011;286(10):8213-8230. doi:10.1074/jbc.M110.165852

189. Dai H, Pang YP, Ramirez-Alvarado M, Kaufmann SH. Evaluation of the BH3-only protein Puma as a direct Bak activator. *J Biol Chem*. 2014;289(1):89-99. doi:10.1074/jbc.M113.505701

190. Vargas-Uribe M, Rodnin M V., Ladokhin AS. Comparison of membrane insertion pathways of the apoptotic regulator Bcl-xL and the diphtheria toxin translocation domain. *Biochemistry*.

2013;52(45):7901-7909. doi:10.1021/bi400926k

191. Pagliari LJ, Kuwana T, Bonzon C, et al. The multidomain proapoptotic molecules Bax and Bak are directly activated by heat. *Proc Natl Acad Sci U S A*. 2005;102(50):17975-17980. doi:10.1073/pnas.0506712102

192. Bleicken S, Zeth K. Conformational changes and protein stability of the pro-apoptotic protein Bax. *J Bioenerg Biomembr*. 2009;41(1):29-40. doi:10.1007/s10863-009-9202-1

193. Kuwana T, Bouchier-Hayes L, Chipuk JE, et al. BH3 domains of BH3-only proteins differentially regulate Bax-mediated mitochondrial membrane permeabilization both directly and indirectly. *Mol Cell*. 2005;17(4):525-535. doi:10.1016/j.molcel.2005.02.003

194. Royer CA. Probing protein folding and conformational transitions with fluorescence. *Chem Rev*. 2006;106(5):1769-1784. doi:10.1021/cr0404390

195. Huynh K, Partch CL. Analysis of protein stability and ligand interactions by thermal shift assay. *Curr Protoc protein Sci*. 2015;79:28.9.1-28.9.14. doi:10.1002/0471140864.ps2809s79

196. Pedrote MM, De Oliveira GAP, Felix AL, et al. Aggregation-primed molten globule conformers of the p53 core domain provide potential tools for studying p53C aggregation in cancer. *J Biol Chem*. 2018;293(29):11374-11387. doi:10.1074/jbc.RA118.003285

197. Bodenhausen G, Ruben DJ. Natural abundance nitrogen-15 NMR by enhanced heteronuclear spectroscopy. *Chem Phys Lett*. 1980;69(1):185-189. doi:10.1016/0009-2614(80)80041-8

198. Follis AV, Chipuk JE, Fisher JC, et al. PUMA binding induces partial unfolding within BCL-xL to disrupt p53 binding and promote apoptosis. *Nat Chem Biol*. 2013;9(3):163-168. doi:10.1038/nchembio.1166

199. Cosentino K, García-Sáez AJ. Bax and Bak Pores: Are We Closing the Circle? *Trends Cell Biol*. 2017;27(4):266-275. doi:10.1016/j.tcb.2016.11.004

200. Moldoveanu T, Czabotar PE. BAX, BAK, and BOK: A coming of age for the BCL-2 family effector proteins. *Cold Spring Harb Perspect Biol*. 2020;12(4):1-19. doi:10.1101/cshperspect.a036319

201. Iyer S, Uren RT, Dengler MA, et al. Robust autoactivation for apoptosis by BAK but not BAX highlights BAK as an important therapeutic target. *Cell Death Dis*. 2020;11(4):1-13. doi:10.1038/s41419-020-2463-7

202. Kuwana T, Mackey MR, Perkins G, et al. Bid, Bax, and lipids cooperate to form supramolecular openings in the outer mitochondrial membrane. *Cell*. 2002;111(3):331-342. doi:10.1016/S0092-

8674(02)01036-X

203. Tan Y, Wu C, De Veyra T, Greer PA. Ubiquitous calpains promote both apoptosis and survival signals in response to different cell death stimuli. *J Biol Chem*. 2006;281(26):17689-17698. doi:10.1074/jbc.M601978200

204. Kuwana T, King LE, Cosentino K, et al. Mitochondrial residence of the apoptosis inducer BAX is more important than BAX oligomerization in promoting membrane permeabilization. *J Biol Chem*. 2020;295(6):1623-1636. doi:10.1074/jbc.RA119.011635

205. Xiao K, Zhao W, Zhou L, Chang DC. Alpha 5/6 helix domains together with N-terminus determine the apoptotic potency of the Bcl-2 family proteins. *Apoptosis*. 2016;21(11):1214-1226. doi:10.1007/s10495-016-1283-9

206. Riehn M, Klopocki E, Molkentin M, Reinhardt R, Burmeister T. A BACH2-BCL2L1 Fusion Gene Resulting from a Lymphoma Cell Line BLUE-1. *Cancer*. 2011;396(January):389-396. doi:10.1002/gcc

207. Kholoussi NM, El-Nabi SEH, Esmaiel NN, Abd El-Bary NM, El-Kased AF. Evaluation of Bax and Bak gene mutations and expression in breast cancer. *Biomed Res Int*. 2014;2014. doi:10.1155/2014/249372

208. Marcotte EL, Pankratz N, Amatruda JF, et al. Variants in BAK1, SPRY4, and GAB2 are associated with pediatric germ cell tumors: A report from the children's oncology group. *Genes Chromosom Cancer*. 2017;56(7):548-558. doi:10.1002/gcc.22457

209. Griffiths GJ, Corfe BM, Savory P, et al. Cellular damage signals promote sequential changes at the N-terminus and BH-1 domain of the pro-apoptotic protein Bak. *Oncogene*. 2001;20(52):7668-7676. doi:10.1038/sj.onc.1204995

210. Du X, Li Y, Xia Y-L, et al. Insights into Protein–Ligand Interactions: Mechanisms, Models, and Methods. *Int J Mol Sci*. 2016;17(2). doi:10.3390/IJMS17020144

211. Zhou P, Wagner G. Overcoming the solubility limit with solubility-enhancement tags: Successful applications in biomolecular NMR studies. *J Biomol NMR*. 2010;46(1):23-31. doi:10.1007/s10858-009-9371-6

212. Kurauskas V, Hessel A, Ma P, et al. How Detergent Impacts Membrane Proteins: Atomic-Level Views of Mitochondrial Carriers in Dodecylphosphocholine. *J Phys Chem Lett*. 2018;9:933-938. doi:10.1021/acs.jpclett.8b00269

213. Sun H, Ming QIAN Z. *Membrane-Inserted Conformation of Transmembrane Domain 4 of Divalent-Metal Transporter*. Vol 372.; 2003. http://lamar. Accessed June 28, 2021.

214. Gohon Y, Giusti F, Prata C, et al. Well-defined nanoparticles formed by hydrophobic assembly of a short and polydisperse random terpolymer, amphipol A8-35. *Langmuir*. 2006;22(3):1281-1290. doi:10.1021/la052243g

215. Raschle T, Hiller S, Yu TY, Rice AJ, Walz T, Wagner G. Structural and functional characterization of the integral membrane protein VDAC-1 in lipid bilayer nanodiscs. *J Am Chem Soc*. 2009;131(49):17777-17779. doi:10.1021/ja907918r

216. Kobashi K. Catalytic oxidation of sulfhydryl groups by o-phenanthroline copper complex. *BBA - Gen Subj*. 1968;158(2):239-245. doi:10.1016/0304-4165(68)90136-0

217. Uusimaa J, Evans J, Smith C, et al. Clinical, biochemical, cellular and molecular characterization of mitochondrial DNA depletion syndrome due to novel mutations in the MPV17 gene. *Eur J Hum Genet*. 2014;22(2):184-191. doi:10.1038/ejhg.2013.112

218. Gilberti M, Baruffini E, Donnini C, Dallabona C. Pathological alleles of MPV17 modeled in the yeast Saccharomyces cerevisiae orthologous gene SYM1 reveal their inability to take part in a high molecular weight complex. *PLoS One*. 2018;13(10). doi:10.1371/journal.pone.0205014

219. Kovermann M, Rogne P, Wolf-Watz M. Protein dynamics and function from solution state NMR spectroscopy. *Q Rev Biophys*. 2016;49:e6. doi:10.1017/S0033583516000019

220. Lee W, Tonelli M, Markley JL. NMRFAM-SPARKY: Enhanced software for biomolecular NMR spectroscopy. *Bioinformatics*. 2015;31(8):1325-1327. doi:10.1093/bioinformatics/btu830

221. Schwieters CD, Kuszewski JJ, Tjandra N, Clore GM. The Xplor-NIH NMR molecular structure determination package. *J Magn Reson*. 2003;160(1):65-73. doi:10.1016/S1090-7807(02)00014-9

222. Corpet F. Multiple sequence alignment with hierarchical clustering. *Nucleic Acids Res*. 1988;16(22):10881-10890. doi:10.1093/nar/16.22.10881

223. Chen GJ, Qiu N, Karrer C, Caspers P, Page MGP. Restriction site-free insertion of PCR products directionally into vectors. *Biotechniques*. 2000;28(3):498-505. doi:10.2144/00283st08

224. Wu Z, Hong H, Zhao X, Wang X. Efficient expression of sortase A from Staphylococcus aureus in Escherichia coli and its enzymatic characterizations. *Bioresour Bioprocess*. 2017;4(1):13. doi:10.1186/s40643-017-0143-y

225. Plevin M, Hamelin O, Boisbouvier J, Gans P. A simple biosynthetic method for stereospecific resonance assignment of prochiral methyl groups in proteins. *J Biomol NMR*. 2011;49(2):61-67. doi:10.1007/S10858-010-9463-3

226. Gans P, Hamelin O, Sounier R, et al. Stereospecific Isotopic Labeling of Methyl Groups for NMR Spectroscopic Studies of High-Molecular-Weight Proteins. *Angew Chemie Int Ed*. 2010;49(11):1958-1962. doi:10.1002/ANIE.200905660

227. Goto N, Gardner K, Mueller G, Willis R, E. Kay L. A robust and cost-effective method for the production of Val, Leu, Ile (delta 1) methyl-protonated 15N-, 13C-, 2H-labeled proteins. *J Biomol NMR*. 1999;13(4):369-374. doi:10.1023/A:1008393201236

228. Pak, William L. KS, Joseph G, Arnold. Cleavage of Structural Proteins during the Assembly of the Head of Bacteriophage T4. *Nat Publ Gr*. 1970;227:680-685. http://www.mendeley.com/research/discreteness-conductance-chnge-n-bimolecular-lipid-membrane-presence-certin-antibiotics/.

229. Teijido O, Ujwal R, Hillerdal CO, Kullman L, Rostovtseva TK, Abramson J. Affixing N-terminal α-helix to the wall of the voltage-dependent anion channel does not prevent its voltage gating. *J Biol Chem*. 2012;287(14):11437-11445. doi:10.1074/jbc.M111.314229

230. Schmid F. Spectroscopic Techniques to Study Protein Folding and Stability. In: Buchner J, Kiefhaber T, eds. *Protein Folding Handbook*. Weinheim: WILEY-VCH Verlag GnbH & Co. KGaA; 2005:22-44.

231. Sambrook J, Fritsch E, Maniatis T. *Molecular Cloning: A Laboratory Manual*. Cold Spring Harbor, New York: Cold Spring Harbor Laboratory Press; 1989.

232. Stoscheck CM. Quantitation of protein. *Methods Enzymol*. 1990;182(C):50-68. doi:10.1016/0076-6879(90)82008-P

233. Kelly SM, Jess TJ, Price NC. How to study proteins by circular dichroism. *Biochim Biophys Acta - Proteins Proteomics*. 2005;1751(2):119-139. doi:10.1016/j.bbapap.2005.06.005

234. Greenfield NJ. Using circular dichroism spectra to estimate protein secondary structure. *Nat Protoc*. 2006;1(6):2876-2890. doi:10.1038/nprot.2006.202.Using

235. Aillard B, Kilburn JD, Blaydes JP, et al. Synthesis and evaluation of a (3R,6S,9S)-2-oxo-1-azabicyclo[4.3.0]nonane scaffold as a mimic of Xaa-trans-Pro in poly-l-proline type II helix conformation. *Org Biomol Chem*. 2015;13(15):4562-4569. doi:10.1039/c5ob00180c

236. Morrisett JD, David JSK, Pownall HJ, Gotto AM. Interaction of an Apolipoprotein (ApoLP-Alanine) with Phosphatidylcholine. *Biochemistry*. 1973;12(7):1290-1299. doi:10.1021/bi00731a008

237. Jiskoot W, Hlady V, Naleway JJ, Herron JN. Application of fluorescence spectroscopy for determining the structure and function of proteins. *Pharm Biotechnol*. 1995;7:1-63.

doi:10.1007/978-1-4899-1079-0_1

238. Sapienza PJ, Li L, Williams T, Lee AL, Carter CW. An Ancestral Tryptophanyl-tRNA Synthetase Precursor Achieves High Catalytic Rate Enhancement without Ordered Ground-State Tertiary Structures. *ACS Chem Biol*. 2016;11(6):1661-1668. doi:10.1021/acschembio.5b01011

239. Johnson CM. Differential scanning calorimetry as a tool for protein folding and stability. *Arch Biochem Biophys*. 2013;531(1-2):100-109. doi:10.1016/j.abb.2012.09.008

240. Holdgate GA, Ward WHJ, Ward WHJ. Measurements of binding thermodynamics in drug discovery. *Drug Discov Today*. 2005;10(22):1543-1550. doi:10.1016/S1359-6446(05)03610-X

241. Velazquez-Campoy A, Leavitt SA, Freire E. Characterization of protein-protein interactions by isothermal titration calorimetry. *Methods Mol Biol*. 2004;261:35-54. doi:10.1385/1-59259-762-9:035

242. Stetefeld J, McKenna SA, Patel TR. Dynamic light scattering: a practical guide and applications in biomedical sciences. *Biophys Rev*. 2016;8(4):409-427. doi:10.1007/s12551-016-0218-6

243. Konermann L, Pan J, Liu YH. Hydrogen exchange mass spectrometry for studying protein structure and dynamics. *Chem Soc Rev*. 2011;40(3):1224-1234. doi:10.1039/c0cs00113a

244. Englander SW, Kallenbach NR. Hydrogen exchange and structural dynamics of proteins and nucleic acids. *Q Rev Biophys*. 1983;16(4):521-655. doi:10.1017/S0033583500005217

245. Smith DL, Deng Y, Zhang Z. Probing the Non- covalent Structure of Proteins by Amide Hydrogen Exchange and Mass Spectrometry. *J Mass Spectrom*. 1997;32(2):135-146. doi:10.1002/(sici)1096-9888(199702)32:2<135::aid-jms486>3.3.co;2-d

246. Vadas O, Jenkins ML, Dornan GL, Burke JE. *Using Hydrogen–Deuterium Exchange Mass Spectrometry to Examine Protein–Membrane Interactions*. Vol 583. 1st ed. Elsevier Inc.; 2017. doi:10.1016/bs.mie.2016.09.008

247. Wales TE, Engen JR. Hydrogen exchange mass spectrometry for the analysis of protein dynamics. *Mass Spectrom Rev*. 2006;25(1):158-170. doi:10.1002/mas.20064

248. Hollingsworth SA, Dror RO. Molecular Dynamics Simulation for All. *Neuron*. 2018;99(6):1129-1143. doi:10.1016/j.neuron.2018.08.011

249. Dawe GB, Musgaard M, Aurousseau MRP, et al. Distinct Structural Pathways Coordinate the Activation of AMPA Receptor-Auxiliary Subunit Complexes. *Neuron*. 2016;89(6):1264-1276. doi:10.1016/j.neuron.2016.01.038

250. Dror RO, Green HF, Valant C, et al. Structural basis for modulation of a G-protein-coupled

receptor by allosteric drugs. *Nature*. 2013;503(7475):295-299. doi:10.1038/nature12595

251. Jo S, Kim T, Iyer VG, Im W. CHARMM-GUI: A web-based graphical user interface for CHARMM. *J Comput Chem*. 2008;29(11):1859-1865. doi:10.1002/jcc.20945

252. Phillips JC, Braun R, Wang W, et al. Scalable molecular dynamics with NAMD. *J Comput Chem*. 2005;26(16):1781-1802. doi:10.1002/jcc.20289

253. Darden T, York D, Pedersen L. Particle mesh Ewald: An N·log(N) method for Ewald sums in large systems. *J Chem Phys*. 1993;98(12):10089-10092. doi:10.1063/1.464397

254. Humphrey W, Dalke A, Schulten K. VMD: Visual molecular dynamics. *J Mol Graph*. 1996;14(1):33-38. doi:10.1016/0263-7855(96)00018-5

255. Teng Q. *Structural Biology: Practical NMR Applications*. Springer Science + Business Media; 2005.

256. John Cavanagh, Wayne J. Fairbrother, Arthur G. Palmer, III NJS. *Protein NMR Spectroscopy: Principles and Practice*. 2nd ed. London: Elsevier Academic Press; 2007. https://books.google.de/books?hl=de&lr=&id=85rYGWiBJ1kC&oi=fnd&pg=PP1&dq=protein+nmr+spectroscopy+principles+and+practice&ots=L6htzm62tv&sig=QnpFYRJLDO6RvN6cyAfLHMBUV7E#v=onepage&q&f=false. Accessed July 2, 2021.

257. Keeler J. *Understanding NMR Spectroscopy*. 2nd ed. West Sussex, UK: John Wiley and Sons, Ltd; 2011.

258. Cheng C-Y, Franck JM, Han S, et al. *Protein NMR. Modern Techniques and Biomedial Applications*. (Berliner L, ed.). Springer Science + Business Media; 2015. doi:10.1007/978-1-4899-7621-5

259. Wand AJ. Dynamic activation of protein function: A view emerging from NMR spectroscopy. *Nat Struct Biol*. 2001;8(11):926-931. doi:10.1038/nsb1101-926

260. Chao FA, Byrd RA. Protein dynamics revealed by NMR relaxation methods. *Emerg Top Life Sci*. 2018;2(1):93-105. doi:10.1042/ETLS20170139

261. Kharchenko V, Nowakowski M, Jaremko M, Ejchart A, Jaremko Ł. Dynamic 15N{1H} NOE measurements: a tool for studying protein dynamics. *J Biomol NMR*. 2020;74(12):707-716. doi:10.1007/s10858-020-00346-6

262. Sattler M, Fesik SW. Use of deuterium labeling in NMR: Overcoming a sizeable problem. *Structure*. 1996;4(11):1245-1249. doi:10.1016/S0969-2126(96)00133-5

263. Pervushin K, Riek R, Wider G, Wüthrich K. Attenuated T2 relaxation by mutual cancellation of

dipole-dipole coupling and chemical shift anisotropy indicates an avenue to NMR structures of very large biological macromolecules in solution. *Proc Natl Acad Sci U S A*. 1997;94(23):12366-12371. doi:10.1073/pnas.94.23.12366

264. Salzmann M, Pervushin K, Wider G, Senn H, Wüthrich K. Trosy in triple-resonance experiments: New perspectives for sequential NMR assignment of large proteins. *Proc Natl Acad Sci U S A*. 1998;95(23):13585-13590. doi:10.1073/pnas.95.23.13585

265. Softley CA, Bostock MJ, Popowicz GM, Sattler M. Paramagnetic NMR in drug discovery. *J Biomol NMR*. 2020;74(6):287-309. doi:10.1007/s10858-020-00322-0

266. Clore GM, Junji Iwahara. Theory, Practice, and Applications of Paramagnetic Relaxation Enhancement for the Characterization of Transient Low-Population States of Biological Macromolecules and Their Complexes. *Chem Rev*. 2009;109:4106-4139.

267. Cheng K, Tjandra N. The Use of Residual Dipolar Coupling in Studying Proteins by NMR. *Top Curr Chem*. 2011;326:47-68. doi:10.1007/128_2011_215

268. Hansen MR, Mueller L, Pardi A. Tunable alignment of macromolecules by filamentous phage yields dipolar coupling interactions. *Nat Struct Biol*. 1998;5(12):1065-1074. doi:10.1038/4176

269. Delaglio F, Grzesiek S, Vuister GW, Zhu G, Pfeifer J, Bax A. NMRPipe: a multidimensional spectral processing system based on UNIX pipes. *J Biomol NMR*. 1995;6(3):277-293.

270. Hagn F, Klein C, Demmer O, et al. BclxL changes conformation upon binding to wild-type but not mutant p53 DNA binding domain. *J Biol Chem*. 2010;285(5). doi:10.1074/jbc.M109.065391

271. Sattler M, Schleucher J, Griesinger C. Heteronuclear multidimensional NMR experiments for the structure determination of proteins in solution employing pulsed field gradients. *Prog Nucl Magn Reson Spectrosc*. 1999;34:93-158.

272. Lovell SC, Davis IW, Arendall WB, et al. Structure validation by Cα geometry: φ,ψ and Cβ deviation. *Proteins Struct Funct Genet*. 2003;50(3):437-450. doi:10.1002/prot.10286

273. Zhu G, Xia Y, Nicholson LK, Sze KH. Protein Dynamics Measurements by TROSY-Based NMR Experiments. *J Magn Reson*. 2000;143(2):423-426. doi:10.1006/jmre.2000.2022

274. Zweckstetter M, Bax A. Prediction of sterically induced alignment in a dilute liquid crystalline phase: Aid to protein structure determination by NMR [11]. *J Am Chem Soc*. 2000;122(15):3791-3792. doi:10.1021/ja0000908

275. Hyberts SG, Takeuchi K, Wagner G. Poisson-gap sampling and forward maximum entropy reconstruction for enhancing the resolution and sensitivity of protein NMR data. *J Am Chem Soc*.

2010;132(7):2145-2147. doi:10.1021/ja908004w

276. Hyberts SG, Milbradt AG, Wagner AB, Arthanari H, Wagner G. Application of iterative soft thresholding for fast reconstruction of NMR data non-uniformly sampled with multidimensional Poisson Gap scheduling. *J Biomol NMR*. 2012;52(4):315-327. doi:10.1007/s10858-012-9611-z

277. Laskowski RA, Rullmann JAC, MacArthur MW, Kaptein R, Thornton JM. AQUA and PROCHECK-NMR: Programs for checking the quality of protein structures solved by NMR. *J Biomol NMR*. 1996;8(4):477-486. doi:10.1007/BF00228148

7 Appendix

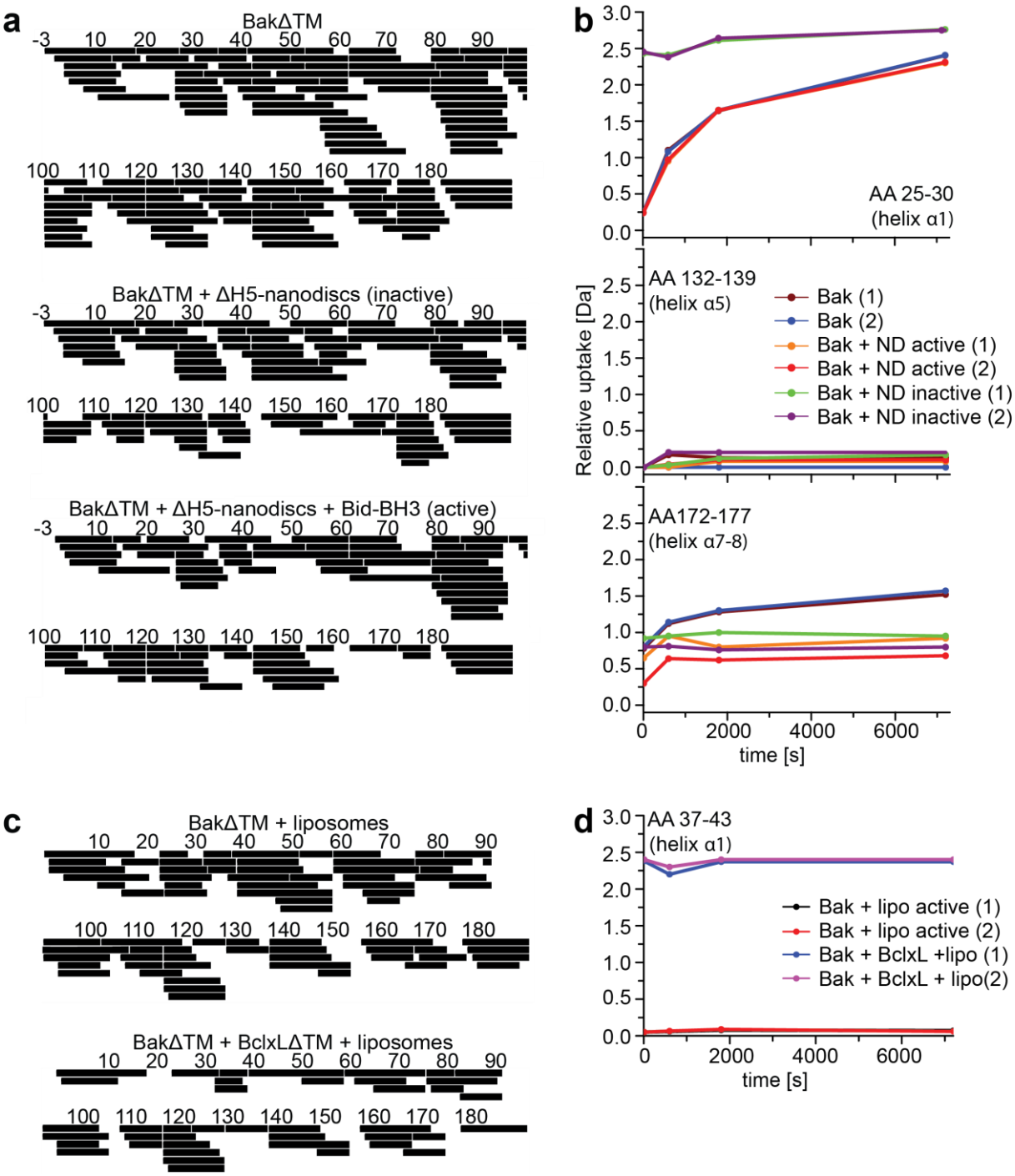

Figure 7.1: (a) HDX peptide coverage maps. BakΔTM: Total coverage was 100 % with 126 peptides and a redundancy of 6.96. BakΔTM + ΔH5-nanodiscs (inactive): Total coverage was 99 % with 83 peptides and a redundancy of 4.47. BakΔTM + ΔH5-nanodiscs + Bid-BH3 (active): Total coverage was 97 % with 76 peptides and a redundancy of 4.25. (b) HDX graphs of three peptides, located in different helices as indicated, displaying the relative deuterium uptake during the reaction time. Two biological replicates were measured for each state. (ND = ΔH5-nanodiscs). (c) HDX peptide coverage maps. BakΔTM + liposomes: Total coverage was 97.5 % with 73 peptides and a redundancy of 4.19. BakΔTM + BclxLΔTM + liposomes: Total coverage was 92.4 % with 41 peptides and a redundancy of 2.37. (d) HDX graphs of a peptide stretch located in the Bak helix 1, displaying the relative deuterium uptake during the reaction time. Two biological replicates were measured for each state. (lipo = liposomes).

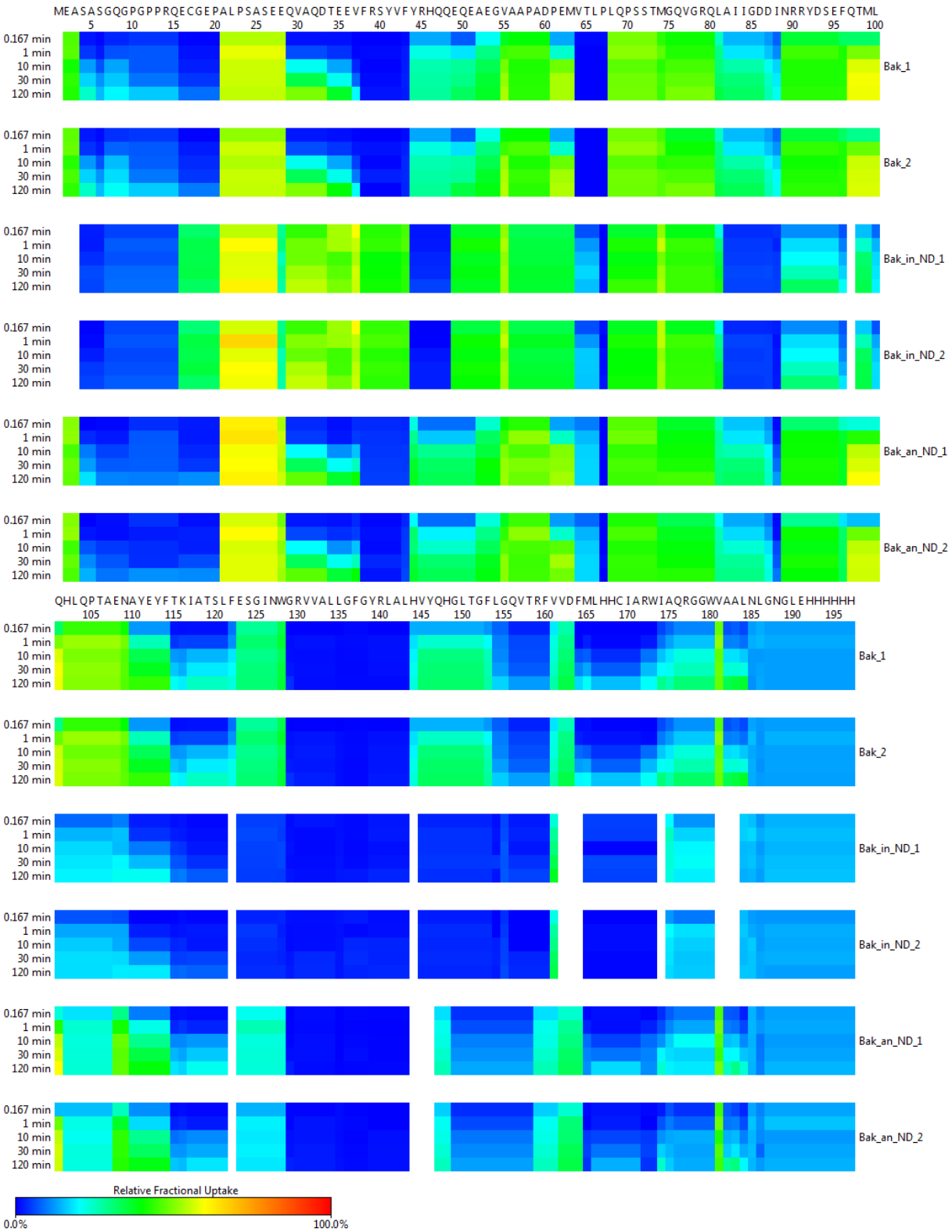

Figure 7.2: HDX-MS: heat maps of the relative fractional uptake of soluble BakΔTM (Bak_x), inactive BakΔTM bound to nanodiscs (Bak_an_ND_x) and active BakΔTM in nanodiscs after Bid-BH3 induced activation (Bak_in_ND_x).

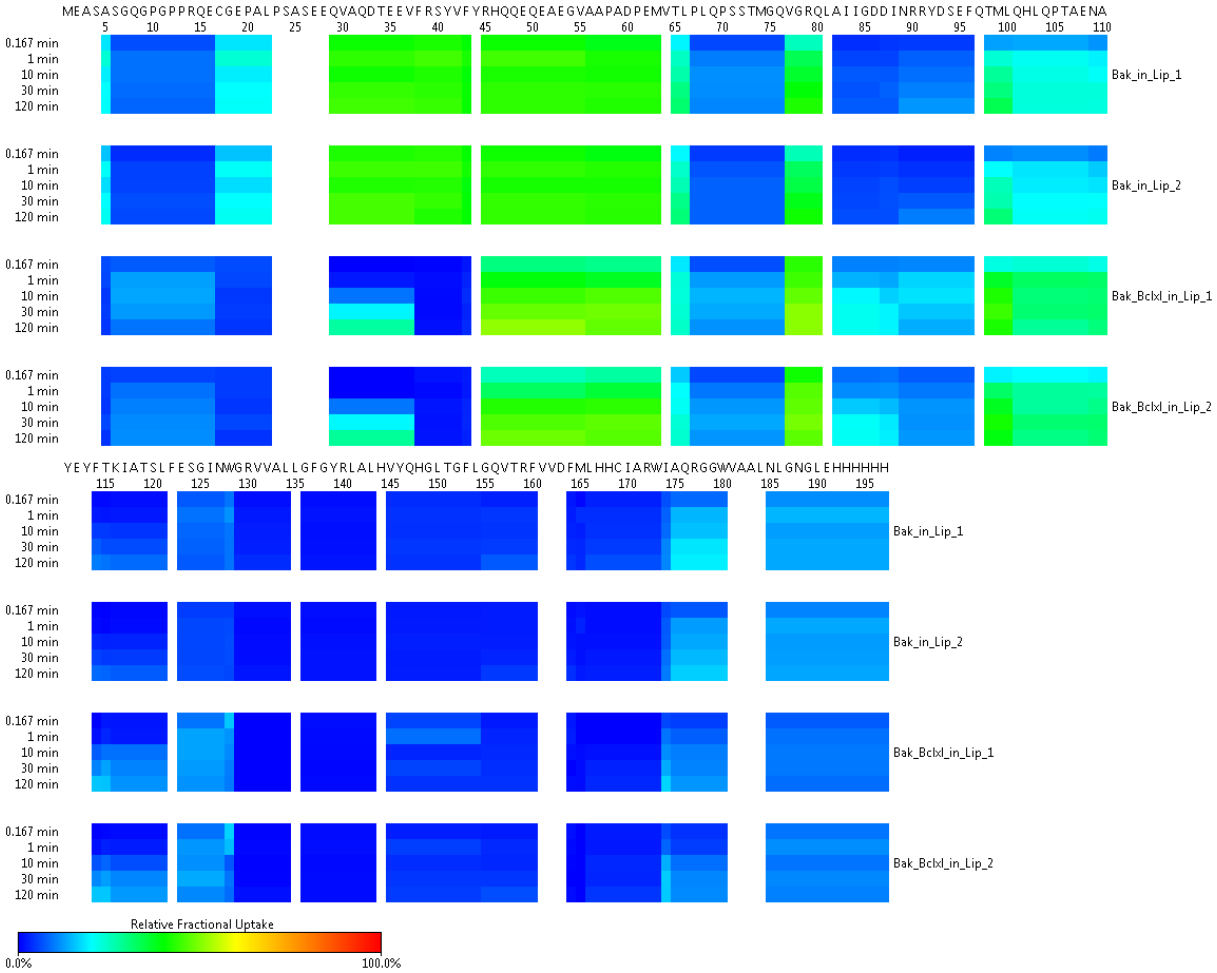

Figure 7.3: HDX-MS: heat maps of the relative fractional uptake of BakΔTM in liposomes (Bak_in_Lip_x) and BakΔTM and BclxLΔTM in liposomes (Bak_BclxL_in_Lip_x).

Table 7.1: Protein sequences of the constructs used in this work. Bold lettering: protein of interest; red: His-tag; magenta: Sortase A recognition site; blue: GB1; orange: thrombin cleavage site; green: TEV cleavage site

Bcl2-protein constructs
BakΔTM
MEAS**ASGQGPGPPRQECGEPALPSASEEQVAQDTEEVFRSYVFYRHQQEQEAEGVAAPADPE MVTLPLQPSSTMGQVGRQLAIIGDDINRRYDSEFQTMLQHLQPTAENAYEYFTKIATSLFESGINW GRVVALLGFGYRLALHVYQHGLTGFLGQVTRFVVDFMLHHCIARWIAQRGGWVAALNLGNG**LEH HHHHH
BakΔTM-xL-link
MEAS**ASGQGPGPPRQECGEPALPSASEEQVAQDTEEVFRSYVFYRHQQEQEAEGVAAPADPE MVTLPLQPSSTMGQVGRQLAIIGDDINRRYDSEFQTMLQHLQPTAENAYEYFTKIATSLFESGINW GRVVALLGFGYRLALHVYQHGLTGFLGQVTRFVVDFMLHHCIARWIAQRGGWVAALN**YGNNAA AESRKGQERFNRHHHHHH
BakΔTM-Sor
MEAS**ASGQGPGPPRQECGEPALPSASEEQVAQDTEEVFRSYVFYRHQQEQEAEGVAAPADPE MVTLPLQPSSTMGQVGRQLAIIGDDINRRYDSEFQTMLQHLQPTAENAYEYFTKIATSLFESGINW GRVVALLGFGYRLALHVYQHGLTGFLGQVTRFVVDFMLHHCIARWIAQRGGWVAALN**LPETGGH HHHHH
BclxLΔTM
**MSQSNRELVVDFLSYKLSQKGYSWSQFSDVEENRTEAPEGTESEMETPSAINGNPSWHLADSPA VNGATGHSSSLDAREVIPMAAVKQALREAGDEFELRYRRAFSDLTSQLHITPGTAYQSFEQVVNE

LFRDGVNWGRIVAFFSFGGALCVESVDKEMQVLVSRIAAWMATYLNDHLEPWIQENGGWDTFVE LYGNNAAAESRKGQERLEHHHHHH
BclxLΔLΔTM
MSQSNRELVVDFLSYKLSQKGYSWSQFSDVEENRTEAPEGTESEAVKQALREAGDEFELRYRR AFSDLTSQLHITPGTAYQSFEQVVNELFRDGVNWGRIVAFFSFGGALCVESVDKEMQVLVSRIAA WMATYLNDHLEPWIQENGGWDTFVELYGNNAAAESRKGQERLEHHHHHH
BclxLΔLΔTM-BakH1
MSQSNRELVVDFLSYKLSQKGYSWSQFSDVEENRTEAPEGTESEAVKQALREAGDEFELRYRR AFSDLTSQLHITPGTAYQSFEQVVNELFRDGVNWGRIVAFFSFGGALCVESVDKEMQVLVSRIAA WMATYLNDHLEPWIQENGGWDTFVELYGNNAAAESRKGQERLEGGEEQVAQDTEEVFRSYVFY RHQQGGHHHHHH
cBid
MDCEXNNGSSLRDECITNLLVFGFLQSCSDNSFRRELDALGHELPVLAPQWEGYDELVPR/GS**RS SHSRLGRIEADSESQEDIIRNIARHLAQVGDSMDRSIPPGLVNGLALQLRNTSRSEEDRNRDLATA LEQLLQAYPRDMEKEKTMLVLALLLAKKVASHTPSLLRDVFHTTVNFINQNLRTYVRSLARNGMD** LEHHHHHH
Sortase A
M**QAKPQIPKDKSKVAGYIEIPDADIKEPVYPGPATREQLNRGVSFAEENESLDDQNISIAGHTFIDR PNYQFTNLKAAKKGSMVYFKVGNETRKYKMTSIRNVKPTAVEVLDEQKGKDKQLTLITCDDYNEE TGVWETRKIFVATEVK**LEHHHHHH
Bak-TMH
MSYYHHHHHHDYDIPTTAMEYKLILNGKTLKGETTTEAVDAATAEKVFKQYANDNGVDGEWTYDD ATKTFTVTEIPTTLVPR/GSGS**LGNGPILNVLVVLGVVLLGQFVVRRFFKS**
Bak-TMH-Sor
MSYYHHHHHHDYDIPTTAMEYKLILNGKTLKGETTTEAVDAATAEKVFKQYANDNGVDGEWTYDD ATKTFTVTEIPTTLVPR/GSGSGSGSGS**LGNGPILNVLVVLGVVLLGQFVVRRFFKS**
BclxL-TMH
MSYYHHHHHHDYDIPTTAMEYKLILNGKTLKGETTTEAVDAATAEKVFKQYANDNGVDGEWTYDD ATKTFTVTEIPTTLVPR/GSG**ESRKGQERFNRWFLTGMTVAGVVLLGSLFSRK**
GlyA-TMH
MSYYHHHHHHDYDIPTTAMEYKLILNGKTLKGETTTEAVDAATAEKVFKQYANDNGVDGEWTYDD ATKTFTVTEIPTTLVPR/GSGSG**SEPEITLIIFGVMAGVIGTILLISYGIRRLIKK**
MPV17 constructs
MPV17wt
MSYYHHHHHHDYDIPTTAMEYKLILNGKTLKGETTTEAVDAATAEKVFKQYANDNGVDGEWTYDD ATKTFTVTEIPTTLVPR/GSGGSS**MALWRAYQRALAAHPWKVQVLTAGSLMGLGDIISQQLVERR GLQEHQRGRTLTMVSLGCGFVGPVVGGWYKVLDRFIPGTTKVDALKKMLLDQGGFAPCFLGCF LPLVGALNGLSAQDNWAKLQRDYPDALITNYYLWPAVQLANFYLVPLHYRLAVVQCVAVIWNSY LSWKAHRL**
MPV17-cHis
MEYKLILNGKTLKGETTTEAVDAATAEKVFKQYANDNGVDGEWTYDDATKTFTVTEIPTTLVPR/GS GGSS**MALWRAYQRALAAHPWKVQVLTAGSLMGLGDIISQQLVERRGLQEHQRGRTLTMVSLGC GFVGPVVGGWYKVLDRFIPGTTKVDALKKMLLDQGGFAPCFLGCFLPLVGALNGLSAQDNWAK LQRDYPDALITNYYLWPAVQLANFYLVPLHYRLAVVQCVAVIWNSYLSWKAHR**LEHHHHHHHHH H
MSP-constructs

MSP1D1ΔH5
MGSSHHHHHHENLYFQ/G**STFSKLREQLGPVTQEFWDNLEKETEGLRQEMSKDLEEVKAKVQPY LDDFQKKWQEEMELYRQKVEPLGEEMRDRARAHVDALRTHLAPYSDELRQRLAARLEALKENG GARLAEYHAKATEHLSTLSEKAKPALEDLRQGLLPVLESFKVSFLSALEEYTKKLNTQ**
MSP1D1ΔH5-ΔnG
M**STFSKLREQLGPVTQEFWDNLEKETEGLRQEMSKDLEEVKAKVQPYLDDFQKKWQEEMELYR QKVEPLGEEMRDRARAHVDALRTHLAPYSDELRQRLAARLEALKENGGARLAEYHAKATEHLS TLSEKAKPALEDLRQGLLPVLESFKVSFLSALEEYTKKLNTQ**ENLYFQ/GGNNAAAESRKGQERL EHHHHHH
MSP1D1
MGSSHHHHHHHDYDIPTTENLYFQ/G**STFSKLREQLGPVTQEFWDNLEKETEGLRQEMSKDLEEV KAKVQPYLDDFQKKWQEEMELYRQKVEPLRAELQEGARQKLHELQEKLSPLGEEMRDRARAH VDALRTHLAPYSDELRQRLAARLEALKENGGARLAEYHAKATEHLSTLSEKAKPALEDLRQGLL PVLESFKVSFLSALEEYTKKLNTQ**
MSP1E3D1
MGSSHHHHHHHDYDIPTTENLYFQ/G**STFSKLREQLGPVTQEFWDNLEKETEGLRQEMSKDLEEV KAKVQPYLDDFQKKWQEEMELYRQKVEPLRAELQEGARQKLHELQEKLSPLGEEMRDRARAH VDALRTHLAPYLDDFQKKWQEEMELYRQKVEPLRAELQEGARQKLHELQEKLSPLGEEMRDRA RAHVDALRTHLAPYSDELRQRLAARLEALKENGGARLAEYHAKATEHLSTLSEKAKPALEDLRQ GLLPVLESFKVSFLSALEEYTKKLNTQ**

Table 7.2: Protein parameters used to calculate concentrations by UV/Vis and the mean residual weight ellipticity. The extinction coefficients at 280 nm are in units of M^{-1} cm^{-1}. The parameters are given for the final constructs after cleavage.

Protein construct	**Molecular mass [Da]**	**No. of AA**	**Extinction coefficient**
BakΔTM	21966	197	26930
BakΔTM-xL-link	23257	209	28420
BakΔTM_1	21938	197	26930
BakΔTM_2	21968	197	26930
BakΔTM_3	21810	197	26930
BakΔTM-Sor	21937	197	26930
BclxLΔTM	24432	217	41940
BclxLΔLΔTM	20360	177	36440
BclxLΔTM-BakH1	27420	243	44920
BclxLΔLΔTM-BakH1	23360	203	39420
cBid	23053	203	9970
Sortase A	17853	156	14440
Bak-TMH[1]	3443	33	0
Bak-TMH-Sor[1]	3876	39	0
BclxL-TMH[1]	3872	35	5500
GlyA-TMH[1]	3961	38	1490
MPV17wt[1]	20166	182	50420

MPV17-cHis[1]	21666	193	50420
MPV17-Cysfree[1]	20037	182	50420
MPV17-R50W[1]	20196	182	55920
MPV17-Q93P[1]	20135	182	50420
MPV17-N166K[1]	20180	182	50420
MSP ΔH5[2]	19488	168	18450
MSP ΔH5-nΔG[3]	20357	174	19940
MSP 1D1[2]	22043	190	18450
MSP 1E3D1[2]	29 982 Da	256	26600

[1]before cleavage 82 AA, 9328 Da and an extinction coefficient of 14440 M^{-1} cm^{-1} must be added
[2]before cleavage 24 AA, 2924 Da and an extinction coefficient of 2980 M^{-1} cm^{-1} must be added
[3]before cleavage 23 AA, 2592 Da and an extinction coefficient of 0 M^{-1} cm^{-1} must be added

Table 7.3: NMR Structural Statistics of the Bak-TMH in MSP1D1ΔH5-nanodiscs and DPC micelles[1]

	Bak-TMH in MSP- 1D1ΔH5-nanodiscs	**Bak-TMH in DPC micelles**
Structural Information		
Number of NOEs restraints	54 (1.8/ aa)	56 (1.87/ aa)
Number of hydrogen bond restraints	18	18
Dihedral angle restraints (TALOS)	-	26
Backbone/heavy atom rmsd for all residues [Å][2]	2.6 ± 0.5 / 3.3 ± 0.7	2.3 ± 0.5 / 3.2 ± 0.67
Backbone/heavy atom rmsd for ordered secondary structure elements [Å][3]	0.25 ± 0.07 / 1.0 ± 0.1	0.2 ± 0.06/1.0 ± 0.08
Ramachandran Map Analysis [4]		
Most favored regions	95.7 %	100.0 %
Additionally allowed regions	0.0 %	0.0 %
Generously allowed regions	4.3 %	0.0 %
Disallowed regions	0.0 %	0.0 %
Deviation from Restraints and Idealized Geometry		
Distance restraints [Å]	0.0097 ± 0.00070	0.018 ± 0.0018
Dihedral angle restraints [deg]	0.023 ± 0.021	0.014 ± 0.017
Bonds [Å]	0.0018 ± 0.000087	0.0018 ± 0.000062

Angles [deg]	0.50 ± 0.017	0.49 ± 0.015
Impropers [deg]	1.03 ± 0.097	0.99 ± 0.092

[1] Analysis of the 20 lowest total-energy structures
[2] r.m.s.d. values are calculated relative to a non-minimized average structure of the ensemble
[3] α-helical region: residues 187-209
[4] Ramachandran analysis with PROCHECK-NMR[277] was performed with the lowest-energy structure

Table 7.4: Accession codes to entries in the Biological Magnetic Resonance Bank (BMRB) or the Protein Data Bank (PDB) data banks generated in this work.

Protein construct	**BMRB**	**PDB**
Bak-TMH in DPC-micelles	34621	7OFM
Bak-TMH in ΔH5 nanodiscs	34622	7OFO
BakΔTM	50942	-
MPV17wt in DPC-micelles	50889	-
MPV17ΔCys in DPC-micelles	50890	-
Met-MPV17wt in DPC-micelles	50891	-

Table 7.5: Resonance list of the assignment of BakΔTM in ΔH5-nanodiscs after activation by a Bid-BH3 peptide. The standard deviation (SDev) is calculated from all available chemical shifts for the individual atom. The corresponding amount of shifts is indicated under "Assignments".

Group	Atom	Nuc	Shift	SDev	Assignments
A2	H	1H	8,447	0	1
A2	N	15N	126,417	0	1
G4	C	13C	174,05	0	1
Q5	C	13C	176,14	0	1
Q5	CA	13C	55,64	0,041	3
Q5	H	1H	8,108	0,004	3
Q5	N	15N	120,06	0,001	3
G6	CA	13C	44,44	0	1
G6	H	1H	8,219	0,002	5
G6	N	15N	110,768	0,021	5
P7	C	13C	177,29	0,01	2
P7	CA	13C	63,259	0,028	2
P7	CB	13C	32,167	0	1
G8	C	13C	181,076	0	1
G8	CA	13C	44,252	0,016	2
G8	H	1H	8,179	0,001	9
G8	N	15N	109,762	0,006	9
P10	C	13C	176,825	0,011	2
P10	CA	13C	62,829	0,009	2
R11	C	13C	176,202	0,019	2
R11	CA	13C	55,945	0,048	2

R11	H	1H	8,321	0,001	7
R11	N	15N	121,993	0,011	7
Q12	C	13C	175,883	0,026	2
Q12	CA	13C	55,79	0,037	3
Q12	H	1H	8,416	0,002	5
Q12	N	15N	122,753	0,02	5
E13	C	13C	176,349	0	1
E13	CA	13C	56,612	0	1
E13	CB	13C	29,897	0	1
E13	H	1H	8,535	0,001	7
E13	N	15N	123,28	0,024	7
C14	C	13C	174,766	0	1
C14	CA	13C	58,436	0	1
C14	H	1H	8,345	0,005	2
C14	N	15N	120,321	0,019	2
G15	C	13C	173,486	0,003	2
G15	CA	13C	45,009	0,04	4
G15	H	1H	8,326	0,003	3
G15	N	15N	111,706	0,029	3
E16	C	13C	174,45	0	1
E16	CA	13C	54,223	0	1
E16	CB	13C	29,611	0	1
E16	H	1H	8,099	0,001	9
E16	N	15N	122,251	0,017	9
P17	C	13C	176,367	0,012	2
P17	CA	13C	62,903	0	1
P17	CB	13C	31,938	0	1
A18	C	13C	177,362	0,012	3
A18	CA	13C	51,922	0,011	3
A18	CB	13C	19,203	0,026	2
A18	H	1H	8,238	0,001	8
A18	N	15N	124,94	0,028	8
L19	C	13C	175,36	0	1
L19	CA	13C	52,787	0	1
L19	CB	13C	41,706	0	1
L19	H	1H	8,14	0,001	9
L19	N	15N	123,55	0,013	9
P20	C	13C	176,911	0,006	2
P20	CA	13C	63,059	0,016	2
P20	CB	13C	31,828	0	1
S21	C	13C	174,356	0,004	2
S21	CA	13C	58,105	0,006	3
S21	CB	13C	63,76	0	1
S21	H	1H	8,249	0,002	9
S21	N	15N	116,482	0,012	9

A22	C	13C	177,707	0,004	3
A22	CA	13C	52,529	0,008	3
A22	CB	13C	19,125	0	1
A22	H	1H	8,28	0,001	7
A22	N	15N	126,711	0,036	7
S23	C	13C	174,625	0,004	2
S23	CA	13C	58,37	0,005	3
S23	CB	13C	63,689	0,016	2
S23	H	1H	8,168	0,001	7
S23	N	15N	115,517	0,02	7
E24	C	13C	176,464	0,011	2
E24	CA	13C	56,739	0	1
E24	CB	13C	30,133	0	1
E24	H	1H	8,328	0,002	9
E24	N	15N	123,133	0,016	9
E25	CA	13C	56,69	0	1
E25	CB	13C	30,125	0	1
E25	H	1H	8,247	0,001	4
E25	N	15N	122,038	0,027	4
Q26	C	13C	175,815	0,005	2
Q26	CA	13C	55,667	0,008	3
Q26	CB	13C	29,357	0	1
Q26	H	1H	8,254	0	3
Q26	N	15N	122,253	0,008	3
V27	C	13C	175,83	0,005	3
V27	CA	13C	62,165	0,016	3
V27	CB	13C	32,728	0,01	2
V27	H	1H	8,068	0,001	8
V27	N	15N	122,278	0,017	8
A28	C	13C	177,533	0,008	3
A28	CA	13C	52,408	0,005	3
A28	CB	13C	19,111	0,022	2
A28	H	1H	8,285	0,001	9
A28	N	15N	128,486	0,017	9
Q29	C	13C	175,7	0,015	3
Q29	CA	13C	55,692	0,004	3
Q29	CB	13C	29,734	0,015	2
Q29	H	1H	8,272	0,001	9
Q29	N	15N	120,553	0,015	9
D30	C	13C	176,498	0,02	3
D30	CA	13C	54,414	0,009	3
D30	CB	13C	41,045	0,017	2
D30	H	1H	8,355	0,003	9
D30	N	15N	122,238	0,025	9
T31	C	13C	174,783	0,004	2

T31	CA	13C	62,214	0,01	3
T31	CB	13C	69,596	0,041	2
T31	H	1H	7,985	0,002	9
T31	N	15N	114,547	0,01	9
E32	C	13C	176,811	0,005	2
E32	CA	13C	57,089	0	1
E32	CB	13C	30,076	0	1
E32	H	1H	8,308	0,002	8
E32	N	15N	123,033	0,036	8
E33	C	13C	176,935	0,022	2
E33	CA	13C	57,248	0,027	3
E33	CB	13C	29,976	0	1
E33	H	1H	8,225	0,001	4
E33	N	15N	122,135	0,007	4
V34	C	13C	176,372	0,004	2
V34	CA	13C	63,236	0,026	2
V34	CB	13C	47,787	15,467	2
V34	H	1H	7,875	0,001	8
V34	N	15N	120,925	0,01	8
F35	C	13C	175,921	0	1
F35	CA	13C	58,232	0,035	3
F35	CB	13C	39,007	0	1
F35	H	1H	8,044	0,002	6
F35	N	15N	122,815	0,015	6
R36	CA	13C	56,355	0	1
R36	H	1H	7,919	0,001	5
R36	N	15N	122,551	0,04	5
Y38	C	13C	175,699	0	1
Y38	CA	13C	58,29	0,008	2
V39	C	13C	175,518	0,006	2
V39	CA	13C	62,845	0,01	3
V39	H	1H	7,682	0,002	6
V39	N	15N	121,53	0,021	6
F40	C	13C	175,419	0,026	2
F40	CA	13C	58,005	0,011	2
F40	CB	13C	39,573	0	1
F40	H	1H	7,875	0,002	7
F40	N	15N	123,078	0,035	7
Y41	CA	13C	58,09	0	1
Y41	H	1H	7,889	0,002	4
Y41	N	15N	122,076	0,03	4
Q44	C	13C	175,867	0	1
Q44	CA	13C	56,307	0	1
Q45	C	13C	176,234	0	1
Q45	CA	13C	56,284	0,016	3

Q45	CB	13C	29,56	0	1
Q45	H	1H	8,294	0,001	5
Q45	N	15N	121,52	0,032	5
E46	C	13C	176,608	0,006	2
E46	CA	13C	57,018	0,01	3
E46	H	1H	8,345	0,002	5
E46	N	15N	122,261	0,017	5
Q47	C	13C	176,079	0,011	3
Q47	CA	13C	55,997	0,014	3
Q47	CB	13C	29,568	0	1
Q47	H	1H	8,201	0,001	8
Q47	N	15N	120,963	0,009	8
E48	C	13C	176,3	0,009	3
E48	CA	13C	56,72	0,007	3
E48	CB	13C	30,05	0,032	2
E48	H	1H	8,295	0,002	8
E48	N	15N	122,646	0,027	8
A49	C	13C	177,618	0,01	3
A49	CA	13C	52,479	0,009	3
A49	CB	13C	19,234	0	1
A49	H	1H	8,162	0,001	8
A49	N	15N	125,296	0,024	8
E50	C	13C	177,041	0,016	3
E50	CA	13C	56,739	0,007	3
E50	CB	13C	30,163	0,026	2
E50	H	1H	8,232	0,002	9
E50	N	15N	120,585	0,007	9
G51	C	13C	173,895	0,021	3
G51	CA	13C	45,256	0,009	5
G51	H	1H	8,27	0,001	9
G51	N	15N	110,426	0,011	9
V52	C	13C	175,673	0,004	3
V52	CA	13C	61,921	0,012	3
V52	CB	13C	32,754	0,003	2
V52	H	1H	7,799	0,002	9
V52	N	15N	119,813	0,023	9
A53	C	13C	176,799	0,006	3
A53	CA	13C	51,97	0,005	3
A53	CB	13C	19,266	0	1
A53	H	1H	8,23	0,001	9
A53	N	15N	128,69	0,016	9
A54	C	13C	175,34	0	1
A54	CA	13C	50,184	0	1
A54	CB	13C	18,018	0	1
A54	H	1H	8,16	0,001	8

A54	N	15N	125,667	0,016	8
P55	C	13C	176,368	0	1
P55	CA	13C	62,928	0	1
P55	CB	13C	31,938	0	1
A56	C	13C	177,141	0,003	3
A56	CA	13C	51,974	0,038	2
A56	CB	13C	19,261	0,032	2
A56	H	1H	8,239	0,002	7
A56	N	15N	124,952	0,032	7
D57	C	13C	174,785	0	1
D57	CA	13C	52,145	0	1
D57	CB	13C	41,018	0	1
D57	H	1H	8,149	0,001	8
D57	N	15N	121,62	0,011	8
P58	C	13C	177,1	0,006	2
P58	CA	13C	63,437	0,016	2
P58	CB	13C	32,037	0	1
E59	C	13C	176,594	0,006	3
E59	CA	13C	56,647	0,008	3
E59	CB	13C	29,892	0,003	2
E59	H	1H	8,358	0,001	9
E59	N	15N	120,017	0,011	9
M60	C	13C	175,88	0,007	2
M60	CA	13C	55,377	0,005	3
M60	CB	13C	32,806	0	1
M60	H	1H	8,051	0,002	9
M60	N	15N	121,413	0,009	9
V61	C	13C	175,963	0,003	2
V61	CA	13C	62,295	0,014	3
V61	CB	13C	32,727	0,045	2
V61	H	1H	7,977	0,001	7
V61	N	15N	122,266	0,014	7
T62	C	13C	173,974	0,003	2
T62	CA	13C	61,531	0,003	3
T62	CB	13C	69,685	0,025	2
T62	H	1H	8,118	0,002	8
T62	N	15N	119,276	0,022	8
L63	C	13C	174,998	0	1
L63	CA	13C	52,957	0	1
L63	CB	13C	41,779	0	1
L63	H	1H	8,164	0,003	8
L63	N	15N	127,136	0,011	8
P64	C	13C	176,566	0	1
P64	CA	13C	62,794	0,006	2
L65	C	13C	177,161	0,003	2

L65	CA	13C	54,99	0	1
L65	H	1H	8,138	0,001	6
L65	N	15N	122,68	0,004	6
Q66	CA	13C	53,424	0	1
Q66	H	1H	8,278	0,001	3
Q66	N	15N	122,6	0,019	3

Table 7.6: Resonance list of the assignment of BclxLΔLΔTM-BakH1. The standard deviation (SDev) is calculated from all available chemical shifts for the individual atom. The corresponding amount of shifts is indicated under "Assignments".

Residue	Atom	Nuclues	Shift	SDev	Assignments
Q3	C	13C	173,834	0	1
Q3	CA	13C	56,132	0,009	2
S4	C	13C	173,389	0	1
S4	CA	13C	58,615	0,011	3
S4	CB	13C	62,47	0,087	2
S4	H	1H	8,51	0,002	6
S4	N	15N	117,147	0,018	6
N5	C	13C	174,772	0,014	2
N5	CA	13C	55,593	0,005	3
N5	CB	13C	37,39	0,031	2
N5	H	1H	8,45	0,002	8
N5	N	15N	122,409	0,042	8
R6	C	13C	174,744	0,017	3
R6	CA	13C	59,159	0,009	2
R6	CB	13C	28,394	0	1
R6	H	1H	8,114	0,003	8
R6	N	15N	120,329	0,024	8
E7	C	13C	176,754	0,012	3
E7	CA	13C	58,735	0,01	3
E7	CB	13C	28,323	0,009	2
E7	H	1H	7,862	0,003	7
E7	N	15N	118,117	0,022	7
L8	C	13C	175,817	0,011	2
L8	CA	13C	57,468	0,008	3
L8	CB	13C	40,493	0,002	2
L8	H	1H	7,63	0,003	9
L8	N	15N	120,125	0,021	9
V9	C	13C	174,55	0,011	3
V9	CA	13C	66,993	0,002	3
V9	CB	13C	31,07	0	1
V9	H	1H	7,656	0,003	8
V9	N	15N	118,077	0,03	8
V10	C	13C	175,963	0,009	3

V10	CA	13C	66,274	0,003	3
V10	CB	13C	30,049	0	1
V10	H	1H	8,217	0,003	7
V10	N	15N	117,443	0,015	7
D11	C	13C	174,844	0,015	2
D11	CA	13C	58,305	0,009	3
D11	CB	13C	42,444	0,016	2
D11	H	1H	7,976	0,003	8
D11	N	15N	121,223	0,03	8
F12	C	13C	175,498	0,007	3
F12	CA	13C	62,555	0,001	3
F12	CB	13C	38,992	0	1
F12	H	1H	8,227	0,003	8
F12	N	15N	120,658	0,03	8
L13	C	13C	176,881	0,006	3
L13	CA	13C	57,658	0,017	3
L13	CB	13C	40,412	0,016	2
L13	H	1H	8,802	0,003	9
L13	N	15N	117,124	0,017	9
S14	C	13C	174,646	0	1
S14	CA	13C	62,106	0,048	3
S14	CB	13C	61,652	0,004	2
S14	H	1H	8,397	0,003	8
S14	N	15N	114,442	0,02	8
Y15	C	13C	175,591	0,012	2
Y15	CA	13C	59,647	0,005	3
Y15	CB	13C	36,778	0,02	2
Y15	H	1H	8,142	0,002	8
Y15	N	15N	125,265	0,04	8
K16	C	13C	177,588	0,022	3
K16	CA	13C	56,415	0,005	3
K16	CB	13C	38,9	0	1
K16	H	1H	8,231	0,003	8
K16	N	15N	120,532	0,037	8
L17	C	13C	177,324	0,008	3
L17	CA	13C	58,005	0,01	3
L17	CB	13C	39,878	0,018	2
L17	H	1H	8,596	0,003	8
L17	N	15N	118,722	0,031	8
S18	C	13C	175,984	0	1
S18	CA	13C	61,12	0,005	3
S18	CB	13C	61,791	0,028	2
S18	H	1H	8,264	0,002	8
S18	N	15N	117,917	0,036	8
Q19	C	13C	174,609	0,014	3

Q19	CA	13C	57,825	0,012	3
Q19	CB	13C	27,802	0,016	2
Q19	H	1H	7,616	0,003	8
Q19	N	15N	123,241	0,026	8
K20	C	13C	172,979	0,011	3
K20	CA	13C	53,43	0,014	3
K20	CB	13C	31,38	0,011	2
K20	H	1H	7,158	0,003	9
K20	N	15N	116,75	0,017	9
G21	C	13C	171,358	0,009	3
G21	CA	13C	44,656	0,009	5
G21	H	1H	7,504	0,003	9
G21	N	15N	105,973	0,016	9
Y22	C	13C	172,36	0,019	3
Y22	CA	13C	55,093	0,023	3
Y22	CB	13C	39,85	0,003	2
Y22	H	1H	7,814	0,003	9
Y22	N	15N	120,301	0,021	9
S23	C	13C	171,772	0,015	3
S23	CA	13C	56,199	0,012	3
S23	CB	13C	63,809	0,003	2
S23	H	1H	8,455	0,003	9
S23	N	15N	115,695	0,014	9
W24	C	13C	174,197	0,01	2
W24	CA	13C	59,242	0,011	2
W24	CB	13C	29,764	0	1
W24	H	1H	8,89	0,003	9
W24	HE1	1H	9,927	0	1
W24	N	15N	127,681	0,029	9
W24	NE1	15N	129,239	0	1
S25	C	13C	172,443	0	1
S25	CA	13C	59,34	0,014	3
S25	CB	13C	62,179	0,014	2
S25	H	1H	8,1	0,002	5
S25	N	15N	112,869	0,04	5
N26	C	13C	173,403	0,019	3
N26	CA	13C	56,327	0,014	2
N26	CB	13C	27,653	0,011	2
N26	H	1H	7,349	0,003	8
N26	N	15N	119,83	0,029	8
F27	C	13C	172,467	0,018	3
F27	CA	13C	56,103	0,027	3
F27	CB	13C	38,819	0,001	2
F27	H	1H	7,268	0,003	8
F27	N	15N	117,097	0,021	8

S28	C	13C	171,068	0,018	2
S28	CA	13C	57,07	0,024	3
S28	CB	13C	63,065	0,027	2
S28	H	1H	7,269	0,003	9
S28	N	15N	114,547	0,033	9
D29	C	13C	173,641	0,022	2
D29	CA	13C	53,678	0,013	3
D29	CB	13C	40,3	0	2
D29	H	1H	8,253	0,003	8
D29	N	15N	122,925	0,02	8
V30	C	13C	173,581	0,015	3
V30	CA	13C	61,747	0,003	3
V30	CB	13C	31,834	0,029	2
V30	H	1H	7,844	0,003	8
V30	N	15N	119,471	0,018	8
E31	C	13C	173,889	0,011	3
E31	CA	13C	56,017	0,004	2
E31	CB	13C	29,215	0	1
E31	H	1H	8,369	0,003	9
E31	N	15N	124,659	0,037	9
E32	C	13C	173,52	0,02	3
E32	CA	13C	56,115	0,013	3
E32	CB	13C	29,31	0,024	2
E32	H	1H	8,306	0,003	7
E32	N	15N	122,437	0,021	7
N33	C	13C	172,311	0,02	3
N33	CA	13C	52,771	0,011	3
N33	CB	13C	37,992	0,048	2
N33	H	1H	8,38	0,003	9
N33	N	15N	119,914	0,019	9
R34	C	13C	173,839	0,01	2
R34	CA	13C	55,594	0,005	2
R34	CB	13C	29,66	0	1
R34	H	1H	8,207	0,002	6
R34	N	15N	122,346	0,031	6
T35	C	13C	171,769	0,011	3
T35	CA	13C	61,47	0,002	3
T35	CB	13C	69,089	0,002	2
T35	H	1H	8,152	0,003	9
T35	N	15N	116,164	0,017	9
E36	C	13C	173,017	0,012	2
E36	CA	13C	55,72	0,008	3
E36	CB	13C	29,291	0,007	2
E36	H	1H	8,276	0,002	9
E36	N	15N	123,382	0,031	9

E36'	H	1H	8,364	0	1
E36'	N	15N	124,155	0	1
A37	C	13C	172,813	0	1
A37	CA	13C	49,841	0	1
A37	CB	13C	17,332	0	1
A37	H	1H	8,191	0,003	8
A37	N	15N	126,471	0,023	8
A37'	H	1H	8,156	0	1
A37'	N	15N	125,676	0	1
P38	C	13C	174,454	0	1
P38	CA	13C	62,63	0,002	2
P38	CB	13C	30,917	0	1
E39	C	13C	174,459	0,013	3
E39	CA	13C	56,233	0,001	3
E39	CB	13C	29,276	0,017	2
E39	H	1H	8,501	0,002	8
E39	N	15N	121,433	0,023	8
G40	C	13C	171,947	0,019	3
G40	CA	13C	44,877	0,059	4
G40	H	1H	8,392	0,003	8
G40	N	15N	110,577	0,025	8
T41	C	13C	172,846	0,008	3
T41	CA	13C	61,732	0,001	3
T41	CB	13C	69,156	0,004	2
T41	H	1H	8,146	0,003	9
T41	N	15N	113,627	0,019	9
E42	C	13C	174,546	0,013	3
E42	CA	13C	56,791	0,013	3
E42	CB	13C	28,702	0,01	2
E42	H	1H	8,738	0,003	9
E42	N	15N	123,462	0,022	9
S43	C	13C	173,041	0,018	2
S43	CA	13C	58,239	0,001	2
S43	CB	13C	62,825	0,005	2
S43	H	1H	8,397	0,003	9
S43	N	15N	115,988	0,032	9
E44	C	13C	175,317	0,011	3
E44	CA	13C	58,335	0,011	3
E44	CB	13C	28,265	0,005	2
E44	H	1H	8,225	0,002	7
E44	N	15N	123,316	0,017	7
A45	C	13C	177,972	0,015	3
A45	CA	13C	54,513	0,002	3
A45	CB	13C	17,337	0,002	2
A45	H	1H	8,096	0,003	9

A45	N	15N	121,23	0,024	9
V46	C	13C	174,118	0,009	3
V46	CA	13C	65,435	0,003	3
V46	CB	13C	30,414	0	1
V46	H	1H	7,453	0,003	9
V46	N	15N	119,183	0,039	9
K47	C	13C	176,239	0,016	3
K47	CA	13C	59,104	0,008	3
K47	CB	13C	31,038	0,078	2
K47	H	1H	7,311	0,003	8
K47	N	15N	118,084	0,027	8
Q48	C	13C	174,932	0,017	3
Q48	CA	13C	58,267	0,008	3
Q48	CB	13C	27,04	0,003	2
Q48	H	1H	8,014	0,003	9
Q48	N	15N	116,588	0,017	9
A49	C	13C	176,716	0,014	2
A49	CA	13C	54,362	0,005	3
A49	CB	13C	17,574	0	1
A49	H	1H	7,672	0,003	9
A49	N	15N	120,778	0,023	9
L50	C	13C	176,744	0,012	3
L50	CA	13C	57,845	0,011	3
L50	CB	13C	40,941	0,012	2
L50	H	1H	8,308	0,003	7
L50	N	15N	120,001	0,041	7
R51	C	13C	175,984	0,014	3
R51	CA	13C	60,133	0,004	3
R51	CB	13C	29,674	0	1
R51	H	1H	8,002	0,003	9
R51	N	15N	118,679	0,019	9
E52	C	13C	177,342	0,008	3
E52	CA	13C	58,785	0,005	3
E52	CB	13C	28,718	0,021	2
E52	H	1H	7,824	0,003	8
E52	N	15N	117,069	0,031	8
A53	C	13C	178,305	0,018	2
A53	CA	13C	54,505	0,007	3
A53	CB	13C	18,058	0	2
A53	H	1H	8,867	0,003	9
A53	N	15N	123,835	0,034	9
G54	C	13C	172,868	0,018	2
G54	CA	13C	46,47	0,05	4
G54	H	1H	8,994	0,003	8
G54	N	15N	108,227	0,035	8

D55	CA	13C	57,128	0	1
D55	CB	13C	38,843	0	1
D55	H	1H	8,035	0,005	5
D55	N	15N	122,636	0,061	6
R63	C	13C	175,183	0	1
R63	CA	13C	57,896	0	1
A64	C	13C	177,559	0	1
A64	CA	13C	54,085	0	1
A64	CB	13C	17,443	0	1
A64	H	1H	7,674	0,004	6
A64	N	15N	122,228	0,023	6
L68	C	13C	173,665	0	1
L68	CA	13C	55,324	0,008	2
T69	C	13C	171,59	0	1
T69	CA	13C	61,443	0	1
T69	CB	13C	69,095	0	1
T69	H	1H	8,222	0,002	7
T69	N	15N	117,127	0,017	7
S70	C	13C	172,909	0	1
S70	CA	13C	59,846	0,016	3
S70	CB	13C	62,436	0	1
S70	H	1H	7,629	0,002	2
S70	N	15N	116,058	0,029	2
Q71	C	13C	173,326	0,022	2
Q71	CA	13C	56,602	0,018	3
Q71	CB	13C	28,632	0	1
Q71	H	1H	7,587	0,003	8
Q71	N	15N	118,833	0,017	8
L72	CA	13C	54,507	0	1
L72	CB	13C	43,049	0	1
L72	H	1H	7,342	0,004	6
L72	N	15N	118,584	0,033	6
P76	C	13C	174,627	0,014	2
P76	CA	13C	57,106	0,006	2
P76	CB	13C	29,126	0	1
G77	C	13C	172,002	0,022	3
G77	CA	13C	45,032	0,013	4
G77	H	1H	8,468	0,003	9
G77	N	15N	109,929	0,026	9
T78	C	13C	173,07	0	1
T78	CA	13C	62,016	0	1
T78	CB	13C	69,087	0	1
T78	H	1H	8,022	0,003	8
T78	N	15N	113,669	0,032	8
F83	C	13C	172,608	0	1

F83	CA	13C	60,757	0,006	2
F83	CB	13C	38,353	0	1
E84	C	13C	174,617	0,017	3
E84	CA	13C	58,415	0,013	2
E84	CB	13C	28,959	0,022	2
E84	H	1H	8,57	0,002	8
E84	N	15N	119,928	0,019	8
Q85	C	13C	176,001	0,009	2
Q85	CA	13C	58,512	0,017	3
Q85	CB	13C	27,566	0	1
Q85	H	1H	7,571	0,003	8
Q85	N	15N	115,809	0,033	8
V86	C	13C	175,473	0	1
V86	CA	13C	65,385	0	1
V86	CB	13C	30,443	0	1
V86	H	1H	7,041	0,004	7
V86	N	15N	118,901	0,024	7
N88	C	13C	176,374	0	1
N88	CA	13C	54,809	0,002	2
N88	CB	13C	36,281	0	1
E89	C	13C	176,363	0	1
E89	CA	13C	58,181	0	1
E89	CB	13C	27,743	0	1
E89	H	1H	7,205	0,003	8
E89	N	15N	119,091	0,019	8
F91	C	13C	173,969	0,005	2
F91	CA	13C	57,088	0,019	2
F91	CB	13C	38,267	0	1
R92	C	13C	174,583	0,01	3
R92	CA	13C	59,191	0,013	3
R92	CB	13C	28,763	0,001	2
R92	H	1H	7,184	0,003	9
R92	N	15N	124,541	0,027	9
D93	C	13C	173,029	0,012	3
D93	CA	13C	53,515	0,012	3
D93	CB	13C	39,879	0,011	2
D93	H	1H	8,65	0,002	9
D93	N	15N	117,124	0,016	9
G94	C	13C	169,953	0,015	2
G94	CA	13C	43,236	0,054	5
G94	H	1H	7,463	0,003	9
G94	N	15N	109,172	0,01	9
V95	C	13C	171,908	0,022	3
V95	CA	13C	62,113	0,002	3
V95	CB	13C	30,841	0,006	2

V95	H	1H	8,164	0,002	8
V95	N	15N	121,601	0,024	8
N96	C	13C	172,471	0,013	3
N96	CA	13C	51,384	0,008	3
N96	CB	13C	38,962	0,013	2
N96	H	1H	6,253	0,003	9
N96	N	15N	115,918	0,021	9
W97	C	13C	175,444	0	1
W97	CA	13C	60,292	0	1
W97	CB	13C	29,804	0	1
W97	H	1H	8,421	0,003	9
W97	HE1	1H	10,217	0	1
W97	N	15N	118,797	0,018	9
W97	NE1	15N	129,263	0	1
I100	C	13C	175,566	0	1
I100	CA	13C	66,47	0,006	2
I100	CB	13C	38,892	0	1
V101	C	13C	175,151	0	1
V101	CA	13C	67,322	0,034	3
V101	CB	13C	29,901	0,008	2
V101	H	1H	8,233	0,004	7
V101	N	15N	121,621	0,035	7
A102	C	13C	175,643	0	1
A102	CA	13C	54,595	0	1
A102	CB	13C	17,472	0	1
A102	H	1H	7,754	0,004	8
A102	N	15N	122,111	0,029	8
F103	C	13C	172,856	0	1
F103	CA	13C	57,433	0	1
F104	CA	13C	57,766	0	1
F104	H	1H	7,879	0,002	4
F104	N	15N	120,821	0,041	4
S105	C	13C	175,095	0	1
F106	C	13C	173,833	0	1
F106	CA	13C	59,486	0,023	3
F106	CB	13C	37,671	0,009	2
F106	H	1H	9,116	0,004	4
F106	N	15N	124,907	0,029	4
G107	C	13C	173,96	0,022	2
G107	CA	13C	47,283	0,021	3
G107	H	1H	7,989	0,003	8
G107	N	15N	106,803	0,017	8
G108	C	13C	171,923	0,011	3
G108	CA	13C	47,136	0,045	5
G108	H	1H	8,899	0,003	6

G108	N	15N	108,137	0,026	6
A109	C	13C	178,42	0,029	2
A109	CA	13C	54,398	0,003	2
A109	CB	13C	17,352	0,077	2
A109	H	1H	8,224	0,003	9
A109	N	15N	125,022	0,028	9
L110	C	13C	177,411	0,016	2
L110	CA	13C	56,794	0,036	3
L110	CB	13C	40,983	0,007	2
L110	H	1H	8,15	0,004	7
L110	N	15N	119,47	0,032	7
C111	C	13C	173,347	0,021	2
C111	CA	13C	63,855	0,007	3
C111	CB	13C	25,642	0,006	2
C111	H	1H	8,099	0,003	8
C111	N	15N	119,605	0,039	8
V112	C	13C	174,762	0	1
V112	CA	13C	66,543	0,003	3
V112	CB	13C	30,69	0,019	2
V112	H	1H	8,038	0,003	8
V112	N	15N	119,465	0,019	8
E113	C	13C	175,648	0,009	2
E113	CA	13C	58,644	0,017	3
E113	CB	13C	28,228	0,003	2
E113	H	1H	8,094	0,003	7
E113	N	15N	119,781	0,036	7
S114	C	13C	172,903	0	1
S114	CA	13C	62,572	0,01	3
S114	CB	13C	61,245	0,022	2
S114	H	1H	7,645	0,003	7
S114	N	15N	114,066	0,023	7
V115	C	13C	176,837	0,011	3
V115	CA	13C	65,938	0,005	3
V115	CB	13C	30,13	0	1
V115	H	1H	7,299	0,003	8
V115	N	15N	121,212	0,027	8
D116	?	13C	56,887	0	1
D116	C	13C	175,352	0,011	3
D116	CA	13C	56,857	0,012	2
D116	CB	13C	40,15	0,011	2
D116	H	1H	8,27	0,003	7
D116	N	15N	123,333	0,035	7
K117	C	13C	172,473	0,015	3
K117	CA	13C	55,079	0,02	3
K117	CB	13C	30,89	0,003	2

K117	H	1H	7,584	0,003	9
K117	N	15N	116,31	0,018	9
E118	C	13C	173,385	0,02	3
E118	CA	13C	57,178	0,01	3
E118	CB	13C	25,509	0,021	2
E118	H	1H	7,832	0,003	9
E118	N	15N	114,655	0,016	9
M119	C	13C	174,226	0,01	3
M119	CA	13C	53,144	0,008	3
M119	CB	13C	31,355	0,012	2
M119	H	1H	8,454	0,003	9
M119	N	15N	119,685	0,02	9
Q120	C	13C	174,892	0,013	3
Q120	CA	13C	59,354	0,012	3
Q120	CB	13C	26,586	0	1
Q120	H	1H	8,607	0,002	9
Q120	N	15N	119,87	0,019	9
V121	C	13C	173,196	0,015	3
V121	CA	13C	63,02	0,003	3
V121	CB	13C	30,294	0,019	2
V121	H	1H	7,853	0,003	8
V121	N	15N	117,595	0,03	8
L122	C	13C	175,372	0,011	3
L122	CA	13C	54,974	0,01	3
L122	CB	13C	39,936	0,012	2
L122	H	1H	7,775	0,003	9
L122	N	15N	117,839	0,024	9
V123	C	13C	174,445	0,014	2
V123	CA	13C	67,034	0,006	3
V123	CB	13C	29,766	0,006	2
V123	H	1H	7,337	0,003	9
V123	N	15N	120,174	0,024	9
S124	C	13C	174,506	0	1
S124	CA	13C	60,58	0,016	3
S124	CB	13C	61,642	0,012	2
S124	H	1H	8,176	0,002	7
S124	N	15N	111,278	0,014	7
R125	C	13C	173,064	0,01	3
R125	CA	13C	58,07	0,007	3
R125	CB	13C	28,395	0,03	2
R125	H	1H	6,601	0,002	8
R125	N	15N	123,582	0,034	8
I126	C	13C	175,413	0,013	3
I126	CA	13C	64,169	0,005	3
I126	CB	13C	36,332	0,018	2

I126	H	1H	7,944	0,003	9
I126	N	15N	118,914	0,024	9
A127	C	13C	176,84	0,011	3
A127	CA	13C	54,44	0,018	2
A127	CB	13C	17,102	0	1
A127	H	1H	7,59	0,003	9
A127	N	15N	119,715	0,02	9
A128	C	13C	178,407	0,033	2
A128	CA	13C	54,524	0,011	3
A128	CB	13C	16,572	0,043	2
A128	H	1H	7,231	0,002	7
A128	N	15N	120,982	0,022	7
W129	C	13C	176,924	0	1
W129	CA	13C	57,24	0	1
W129	CB	13C	27,722	0	1
W129	H	1H	8,929	0,003	8
W129	HE1	1H	9,999	0	1
W129	N	15N	122,064	0,03	8
W129	NE1	15N	127,134	0	1
A131	C	13C	176,504	0,009	3
A131	CA	13C	55,347	0,036	3
A131	CB	13C	16,463	0,004	2
A131	H	1H	8,224	0,004	4
A131	N	15N	121,148	0,023	4
T132	C	13C	172,323	0	1
T132	CA	13C	66,622	0	1
T132	CB	13C	68,419	0	1
T132	H	1H	8,572	0,003	9
T132	N	15N	117,174	0,016	9
L134	C	13C	175,632	0,005	2
L134	CA	13C	58,698	0	2
L134	CB	13C	41,5	0	1
N135	C	13C	173,765	0,013	3
N135	CA	13C	56,221	0,006	2
N135	CB	13C	38,288	0,015	2
N135	H	1H	8,36	0,003	9
N135	N	15N	117,621	0,017	9
D136	C	13C	175,047	0,013	3
D136	CA	13C	55,877	0,021	2
D136	CB	13C	39,836	0,006	2
D136	H	1H	8,463	0,003	8
D136	N	15N	116,336	0,016	8
H137	C	13C	173,293	0,022	3
H137	CA	13C	56,023	0,007	3
H137	CB	13C	30,372	0,002	2

H137	H	1H	7,985	0,003	8
H137	N	15N	112,726	0,021	8
L138	C	13C	173,92	0,009	3
L138	CA	13C	55,137	0,013	3
L138	CB	13C	42,07	0,014	2
L138	H	1H	7,188	0,003	9
L138	N	15N	117,686	0,032	9
E139	C	13C	171,26	0	1
E139	CA	13C	60,021	0	1
E139	CB	13C	26,589	0	1
E139	H	1H	8,593	0,004	9
E139	N	15N	122,176	0,019	9
P140	C	13C	176,614	0	1
P140	CA	13C	65,812	0,001	2
P140	CB	13C	29,454	0	1
W141	C	13C	176,716	0,06	2
W141	CA	13C	61,474	0,002	3
W141	CB	13C	27,787	0,014	2
W141	H	1H	7,081	0,003	8
W141	HE1	1H	9,402	0	1
W141	N	15N	118,655	0,021	8
W141	NE1	15N	156,698	0	1
I142	C	13C	176,346	0,013	3
I142	CA	13C	65,504	0,036	3
I142	CB	13C	36,946	0,005	2
I142	H	1H	8,395	0,002	8
I142	N	15N	122,909	0,033	8
Q143	C	13C	176,948	0,009	3
Q143	CA	13C	57,876	0,008	3
Q143	CB	13C	26,907	0,014	2
Q143	H	1H	8,428	0,004	9
Q143	N	15N	117,109	0,019	9
E144	C	13C	174,181	0,01	3
E144	CA	13C	57,323	0,013	3
E144	CB	13C	28,663	0,004	2
E144	H	1H	7,556	0,003	9
E144	N	15N	119,976	0,03	9
N145	C	13C	171,253	0,016	3
N145	CA	13C	53,124	0,006	3
N145	CB	13C	37,237	0,014	2
N145	H	1H	7,099	0,003	9
N145	N	15N	117,148	0,021	9
G146	C	13C	173,251	0,018	3
G146	CA	13C	45,127	0,011	4
G146	H	1H	7,315	0,003	8

G146	N	15N	105,551	0,018	8
G147	C	13C	170,702	0,02	3
G147	CA	13C	43,811	0,06	5
G147	H	1H	8,487	0,004	9
G147	N	15N	109,323	0,018	9
W148	C	13C	175,943	0,01	3
W148	CA	13C	60,093	0,004	3
W148	CB	13C	28,843	0,039	2
W148	H	1H	8,599	0,003	9
W148	HE1	1H	10,436	0	1
W148	N	15N	118,746	0,031	9
W148	NE1	15N	129,516	0	1
D149	C	13C	176,948	0,007	3
D149	CA	13C	57,201	0,008	3
D149	CB	13C	39,443	0,016	2
D149	H	1H	8,785	0,002	9
D149	N	15N	118,165	0,025	9
T150	C	13C	172,656	0,015	3
T150	CA	13C	65,774	0,002	3
T150	CB	13C	67,518	0,002	2
T150	H	1H	7,524	0,003	9
T150	N	15N	117,4	0,018	9
F151	C	13C	173,678	0,026	3
F151	CA	13C	60,955	0,008	3
F151	CB	13C	36,721	0	1
F151	H	1H	6,508	0,003	9
F151	N	15N	122,703	0,027	9
V152	C	13C	175,853	0,015	2
V152	CA	13C	66,089	0,005	3
V152	H	1H	7,644	0,002	6
V152	N	15N	117,719	0,043	6
E153	C	13C	175,643	0	1
E153	CA	13C	58,498	0	1
E153	CB	13C	28,877	0	1
E153	H	1H	7,321	0,004	8
E153	N	15N	120,133	0,031	8
N157	C	13C	172,967	0	1
N157	CA	13C	53,196	0	1
N158	C	13C	173	0,025	3
N158	CA	13C	53,702	0,015	3
N158	CB	13C	38,137	0,136	2
N158	H	1H	8,211	0,003	6
N158	N	15N	119,764	0,034	6
A159	C	13C	175,925	0,011	2
A159	CA	13C	53,092	0,005	3

A159	CB	13C	17,617	0	1
A159	H	1H	8,077	0,003	9
A159	N	15N	123,741	0,023	9
A160	C	13C	175,923	0,009	3
A160	CA	13C	52,536	0,018	3
A160	CB	13C	17,607	0	1
A160	H	1H	7,99	0,002	7
A160	N	15N	122,12	0,032	7
A161	C	13C	176,376	0,017	3
A161	CA	13C	53,099	0,006	3
A161	CB	13C	17,706	0,033	2
A161	H	1H	7,916	0,003	8
A161	N	15N	122,67	0,023	8
E162	C	13C	174,977	0,021	3
E162	CA	13C	57,069	0,007	3
E162	CB	13C	28,733	0,013	2
E162	H	1H	8,192	0,003	9
E162	N	15N	119,063	0,021	9
S163	C	13C	172,558	0,017	2
S163	CA	13C	58,781	0,007	3
S163	CB	13C	62,707	0,027	2
S163	H	1H	8,004	0,003	9
S163	N	15N	115,732	0,016	9
R164	C	13C	174,115	0,011	3
R164	CA	13C	56,079	0,01	2
R164	CB	13C	29,3	0,006	2
R164	H	1H	7,951	0,004	8
R164	N	15N	122,279	0,027	8
K165	C	13C	174,878	0,021	3
K165	CA	13C	56,537	0,019	3
K165	CB	13C	31,605	0,018	2
K165	H	1H	7,979	0,003	8
K165	N	15N	121,629	0,049	8
G166	C	13C	171,8	0,017	3
G166	CA	13C	45,014	0,023	5
G166	H	1H	8,319	0,004	9
G166	N	15N	109,883	0,032	9
Q167	C	13C	173,55	0,019	3
Q167	CA	13C	55,414	0,019	3
Q167	CB	13C	28,338	0	1
Q167	H	1H	8,035	0,003	9
Q167	N	15N	120,084	0,021	9
E168	C	13C	173,851	0,016	3
E168	CA	13C	56,46	0,021	3
E168	CB	13C	28,865	0	1

E168	H	1H	8,404	0,003	8
E168	N	15N	122,107	0,031	8
R169	C	13C	173,487	0,021	3
R169	CA	13C	55,452	0,018	3
R169	CB	13C	29,396	0,069	2
R169	H	1H	8,189	0,052	9
R169	N	15N	122,047	0,029	8
L170	C	13C	174,864	0,018	3
L170	CA	13C	54,666	0,015	3
L170	CB	13C	41,025	0	1
L170	H	1H	8,197	0,003	9
L170	N	15N	124,143	0,017	9
E171	C	13C	174,358	0,014	3
E171	CA	13C	56,163	0,009	3
E171	CB	13C	29,258	0	1
E171	H	1H	8,364	0,003	7
E171	N	15N	121,879	0,027	7
G172	C	13C	172,068	0,024	3
G172	CA	13C	44,832	0,052	3
G172	H	1H	8,353	0,003	9
G172	N	15N	110,45	0,018	9
G173	C	13C	171,653	0,009	3
G173	CA	13C	44,666	0,015	5
G173	H	1H	8,165	0,003	7
G173	N	15N	109,166	0,015	7
E174	C	13C	174,086	0,012	3
E174	CA	13C	56,26	0,012	2
E174	CB	13C	29,272	0	1
E174	H	1H	8,349	0,003	9
E174	N	15N	120,937	0,024	9
E175	C	13C	173,834	0,016	3
E175	CA	13C	56,243	0,015	3
E175	CB	13C	29,218	0	1
E175	H	1H	8,435	0,002	7
E175	N	15N	121,837	0,016	7
Q176	C	13C	173,242	0,019	2
Q176	CA	13C	55,215	0,013	3
Q176	CB	13C	28,477	0,109	2
Q176	H	1H	8,263	0,003	8
Q176	N	15N	121,92	0,028	8
V177	C	13C	173,282	0,015	2
V177	CA	13C	61,653	0,002	3
V177	CB	13C	31,723	0,024	2
V177	H	1H	8,042	0,002	7
V177	N	15N	121,797	0,021	7

A178	C	13C	174,965	0,019	3
A178	CA	13C	51,926	0,009	3
A178	CB	13C	18,165	0,001	2
A178	H	1H	8,271	0,003	9
A178	N	15N	127,928	0,028	9
Q179	C	13C	173,185	0,015	3
Q179	CA	13C	55,298	0,014	3
Q179	CB	13C	28,996	0,24	2
Q179	H	1H	8,273	0,002	9
Q179	N	15N	120,182	0,029	9
D180	C	13C	173,882	0,017	3
D180	CA	13C	54,041	0,015	3
D180	CB	13C	40,668	0,278	2
D180	H	1H	8,359	0,006	9
D180	N	15N	121,812	0,03	9
T181	C	13C	172,096	0,022	2
T181	CA	13C	61,713	0,003	3
T181	CB	13C	69,064	0,008	2
T181	H	1H	7,955	0,003	9
T181	N	15N	114,268	0,019	9
E182	C	13C	172,069	0	1
E182	CA	13C	56,469	0	1
E182	CB	13C	29,22	0	1
E182	H	1H	8,298	0,006	8
E182	N	15N	122,965	0,031	8